

2013

# Momentum, energy and scalar transport in polydisperse gas-solid flows using particle-resolved direct numerical simulations

Sudheer Tenneti  
Iowa State University

Follow this and additional works at: <https://lib.dr.iastate.edu/etd>

 Part of the [Mechanical Engineering Commons](#)

## Recommended Citation

Tenneti, Sudheer, "Momentum, energy and scalar transport in polydisperse gas-solid flows using particle-resolved direct numerical simulations" (2013). *Graduate Theses and Dissertations*. 12997.  
<https://lib.dr.iastate.edu/etd/12997>

This Dissertation is brought to you for free and open access by the Iowa State University Capstones, Theses and Dissertations at Iowa State University Digital Repository. It has been accepted for inclusion in Graduate Theses and Dissertations by an authorized administrator of Iowa State University Digital Repository. For more information, please contact [digirep@iastate.edu](mailto:digirep@iastate.edu).

**Momentum, energy and scalar transport in polydisperse gas–solid flows using  
particle–resolved direct numerical simulations**

by

Sudheer Tenneti

A dissertation submitted to the graduate faculty  
in partial fulfillment of the requirements for the degree of  
**DOCTOR OF PHILOSOPHY**

Major: Mechanical Engineering

Program of Study Committee:

Shankar Subramaniam, Major Professor

Rodney O. Fox

Xinwei Wang

Theodore Heindel

Hailiang Liu

Iowa State University

Ames, Iowa

2013

Copyright © Sudheer Tenneti, 2013. All rights reserved.

## DEDICATION

I would like to dedicate this thesis to my wife Rohini and to my parents without whose support I would not have been able to complete this work. I would also like to thank my friends and family for their loving guidance during the writing of this work.

## TABLE OF CONTENTS

<b>LIST OF TABLES</b> . . . . .	viii
<b>LIST OF FIGURES</b> . . . . .	x
<b>ABSTRACT</b> . . . . .	xxvii
<b>CHAPTER 1. Introduction</b> . . . . .	1
1.1 Background . . . . .	1
1.2 Statistical approaches . . . . .	3
1.2.1 Random-field Theory . . . . .	4
1.2.2 Point Process Theory . . . . .	5
1.2.3 Use of PR-DNS for modeling gas-solid flow . . . . .	6
1.3 PR-DNS approaches . . . . .	7
1.4 Research objectives . . . . .	10
1.4.1 Modeling mean interphase momentum transfer in polydisperse gas-solid flow . . . . .	11
1.4.2 Quantifying the level of gas-phase velocity fluctuations . . . . .	13
1.4.3 Develop a fomulation to study convective heat transfer in gas-solid flow	14
1.4.4 Effect of particle velocity distribution and closure at the level of the one- particle distribution function . . . . .	15
1.4.5 Particle-resolved DNS on peta scale computers . . . . .	16
1.5 Report outline . . . . .	17
<b>CHAPTER 2. Drag law for monodisperse gas-solid systems using particle- resolved direct numerical simulation of flow past fixed assemblies of spheres</b>	18
2.1 Introduction . . . . .	19

2.2	Governing Equations . . . . .	26
2.2.1	Ensemble-averaged two-fluid equations . . . . .	28
2.2.2	Quantifying average interphase momentum transfer from particle-resolved DNS . . . . .	30
2.2.3	Fixed particle assemblies . . . . .	32
2.3	Solution Approach . . . . .	33
2.3.1	Conservation of mean momentum in the fluid-phase . . . . .	36
2.4	Simulation Methodology . . . . .	38
2.4.1	Numerical parameters . . . . .	39
2.4.2	Estimation of mean drag from simulations . . . . .	40
2.5	Numerical Convergence . . . . .	42
2.6	Numerical Tests . . . . .	45
2.6.1	Stokes flow . . . . .	46
2.6.2	Moderate Reynolds numbers . . . . .	48
2.7	Comparison of simulation setups to extract computational drag laws . . . . .	49
2.8	Results . . . . .	54
2.8.1	Comparison of PReIBM with body-fitted grid simulations . . . . .	59
2.8.2	Relative contributions of pressure and viscous drag . . . . .	62
2.8.3	Local profiles of pressure and viscous contributions to the fluid-particle drag force . . . . .	64
2.9	A new correlation for the average fluid-particle drag . . . . .	67
2.10	Summary . . . . .	69
 <b>CHAPTER 3. Quantification of gas-phase velocity fluctuations in statisti-</b>		
<b>cally homogeneous gas-solid flow using particle-resolved direct numerical</b>		
<b>simulation . . . . .</b>		
3.1	Introduction . . . . .	71
3.2	Ensemble-averaged quantities . . . . .	72
3.2.1	Quantifying gas-phase velocity variance from particle-resolved DNS . . . . .	78
3.3	Numerical Method . . . . .	81

3.4	Validation . . . . .	84
3.5	Simulation Setup . . . . .	86
3.6	Results . . . . .	91
3.7	Implications for modeling the dissipation of kinetic energy . . . . .	93
3.8	Eddy viscosity for gas–solid flow . . . . .	97
3.9	Conclusions . . . . .	98
<b>CHAPTER 4. Heat transfer in dense gas–solid flow as revealed by particle–</b>		
<b>resolved direct numerical simulation . . . . .</b>		
4.1	Introduction . . . . .	100
4.2	Problem description . . . . .	101
4.3	Formulation of the heat transfer problem . . . . .	105
4.4	Governing Equations . . . . .	106
4.5	Solution Approach . . . . .	107
4.6	Results and Discussion . . . . .	110
4.7	Conclusions . . . . .	112
<b>CHAPTER 5. Particle–resolved direct numerical simulation of freely evol-</b>		
<b>ving gas-solid suspensions at moderate Reynolds number . . . . .</b>		
5.1	Introduction . . . . .	120
5.2	Statistical models . . . . .	121
5.2.1	One-particle distribution function . . . . .	124
5.2.2	Moment equations . . . . .	125
5.2.3	Closure for high Stokes number particles undergoing elastic collisions in Stokes flow . . . . .	127
5.3	Direct numerical simulation approach . . . . .	131
5.3.1	Hydrodynamic solver . . . . .	133
5.3.2	Fixed particle assemblies . . . . .	135
5.3.3	Freely evolving suspensions . . . . .	135
5.4	Results . . . . .	138

5.4.1	Fixed particle assemblies . . . . .	139
5.4.2	Freely moving suspensions . . . . .	142
5.5	Conclusions . . . . .	145
<b>CHAPTER 6. Stochastic acceleration model for inertial particles in gas–</b>		
	<b>solid suspensions . . . . .</b>	<b>153</b>
6.1	Introduction . . . . .	154
6.2	Numerical Method . . . . .	162
6.3	Instantaneous particle acceleration model . . . . .	163
6.4	Results . . . . .	164
6.5	Verification of Langevin model . . . . .	165
6.6	Specification of the model coefficients . . . . .	167
6.7	Conclusions . . . . .	171
<b>CHAPTER 7. Interphase momentum transfer and the level of gas–phase</b>		
	<b>velocity fluctuations in polydisperse gas–solid suspensions . . . . .</b>	<b>173</b>
7.1	Discrete representation of a polydisperse suspension . . . . .	174
7.2	Interphase momentum transfer in a polydisperse suspension . . . . .	175
7.3	Drag and gas–phase velocity fluctuations from PReIBM simulations . . . . .	177
7.4	Bi-disperse suspensions with relative velocity between size classes . . . . .	179
<b>CHAPTER 8. Parallelization and scale-up of PReIBM (Particle-resolved</b>		
	<b>Uncontaminated–fluid Reconcilable Immersed Boundary Method) for di-</b>	
	<b>rect numerical simulation of gas-solid flows on petascale computers . . . . .</b>	<b>182</b>
8.1	Serial algorithm . . . . .	183
8.2	Validation . . . . .	188
8.3	Performance . . . . .	188
<b>CHAPTER 9. Future work . . . . .</b>		
9.1	Stability of gas–solid suspensions with finite fluid inertia . . . . .	193
9.2	Instabilities in the averaged equations . . . . .	195
9.3	Mechanism of generation of instabilities . . . . .	198

9.3.1	PR–DNS of freely evolving suspensions with finite fluid inertia . . . . .	199
9.4	Multiscale metrics for characterizing statistically homogeneous gas–solid flows .	202
9.4.1	Local volume fraction fluctuations in statistically homogeneous gas–solid flows . . . . .	202
9.5	Correct governing equations for stability analysis . . . . .	207
<b>CHAPTER 10. Conclusions . . . . .</b>		<b>208</b>
<b>APPENDIX A. Simplification of the covariance of fluctuating velocity and gradient of stress tensor to dissipation in statistically homogeneous gas– solid flow . . . . .</b>		<b>210</b>
<b>APPENDIX B. Regime of applicability of the assumptions in PR–DNS of gas–solid heat transfer . . . . .</b>		<b>212</b>
<b>APPENDIX C. Equations of motion in an accelerating frame of reference . .</b>		<b>215</b>
<b>APPENDIX D. Identification of source and dissipation of granular temper- ature from PR–DNS . . . . .</b>		<b>222</b>
<b>APPENDIX E. Equations of motion for a polydisperse suspension in an accelerating frame of reference . . . . .</b>		<b>227</b>
<b>BIBLIOGRAPHY . . . . .</b>		<b>231</b>

## LIST OF TABLES

Table 2.1	Summary of various simulation setups. . . . .	51
Table 2.2	Comparison of the numerical parameters (number of particles $N_p$ , number of MIS $\mathcal{M}$ , particle diameter in grid units $D_m$ and the ratio of the length of the box to the particle diameter $L/D$ ) used for random arrays in PReIBM simulations with the past LBM simulations of HKL and BVK. For each entry, first and second rows correspond, respectively, to the LBM simulations of HKL and BVK, and the third row corresponds to the current PReIBM simulations. For the PReIBM simulations, different numerical parameters are used for $Re_m \leq 100$ and $Re_m > 100$ . These are separated by “/”. Numbers before the “/” correspond to $Re_m \leq 100$ while numbers after the “/” correspond to $Re_m > 100$ . At volume fraction 0.5 PReIBM simulations are performed only up to a Reynolds number of 100. . . . .	55
Table 3.1	Numerical parameters (number of particles $N_p$ , number of MIS $\mathcal{M}$ , particle diameter in grid units $D_m$ and the ratio of the length of the box to the particle diameter $L/D$ ) used for random arrays in PReIBM simulations. Different numerical parameters are used for $Re_m \leq 100$ and $Re_m > 100$ . These are separated by “/”. Numbers before the “/” correspond to $Re_m \leq 100$ while numbers after the “/” correspond to $Re_m > 100$ . At volume fraction 0.5 PReIBM simulations are performed only up to a Reynolds number of 100. . . . .	88

Table 4.1	Comparison of Nusselt number obtained from PReIBM simulation of duct flow for three different Reynolds numbers with the Nusselt number derived from an analytical calculation. . . . .	113
Table 8.1	Error in the velocity and pressure fields between the serial and parallel versions of the PReIBM code for different configurations. . . . .	188
Table 8.2	Variation of the problem size and number of particles with increasing the number of processors with $N_x = 8$ . . . . .	190
Table 8.3	Comparison of the performance of PReIBM with $N_x = 8$ and $N_x = 4$ . The numbers in the paranthesis denote the number of processors. . . .	190

## LIST OF FIGURES

Figure 1.1	Role of PR–DNS in gas–solid flow model development. . . . .	7
Figure 1.2	Schematic showing the research objectives of this work. PR–DNS will be used to probe the effects of particle size distribution, gas–phase velocity fluctuations and particle velocity distribution. The data obtained from carefully performed DNS will be used to propose models for the mean interphase momentum transfer, turbulent kinetic energy and heat transfer. Another objective of this work is to use PR–DNS to provide a closure at the level of the one–particle distribution function, which is the starting point of kinetic theory for gas–solid flows (KTGF) and quadrature method of moments (QMOM). The improved models and kinetic theory closures can be used in more accurate EE and LE gas–solid CFD simulations. . . . .	10

Figure 2.1 A schematic of a realization of gas-solid flow showing a statistically homogeneous assembly of particles in a representative region  $\mathcal{V}$ , bounded by surface  $\partial\mathcal{V}$ . The region  $\mathcal{V}$  is composed of the region  $\mathcal{V}_f$  occupied by the fluid phase that is bounded by the surface  $\partial\mathcal{V}_f$ , and the region  $\mathcal{V}_s$  occupied by the solid phase that is bounded by the surface  $\partial\mathcal{V}_s$ , such that  $\mathcal{V} = \mathcal{V}_s \cup \mathcal{V}_f$ . The boundary  $\partial\mathcal{V}$  is decomposed as  $\partial\mathcal{V} = \partial\mathcal{V}_s^{\text{ext}} \cup \partial\mathcal{V}_f^{\text{ext}}$ , where  $\partial\mathcal{V}_s^{\text{ext}} = \partial\mathcal{V} \cap \partial\mathcal{V}_s$  (shown by curly braces) is the domain boundary cut by the solid particles, and  $\partial\mathcal{V}_f^{\text{ext}} = \partial\mathcal{V} \cap \partial\mathcal{V}_f$  (shown by dashed lines) is the remaining domain boundary. The boundary of the solid-phase can be expressed as the union of external and internal boundaries  $\partial\mathcal{V}_s = \partial\mathcal{V}_s^{\text{ext}} \cup \partial\mathcal{V}_s^{\text{int}}$ , where  $\partial\mathcal{V}_s^{\text{int}}$  (shown by solid lines) is the bounding surface of the solid particles in contact with the fluid. Similarly, the boundary of the fluid-phase can be expressed as  $\partial\mathcal{V}_f = \partial\mathcal{V}_f^{\text{ext}} \cup \partial\mathcal{V}_f^{\text{int}}$ . . . . . 26

Figure 2.2 A schematic showing the computation of the immersed boundary forcing for a stationary particle. The solid circle represents the surface of the particle at  $r$ . Open dot shows the location of one exterior point at  $r + \Delta r$  (only one exterior point is shown for clarity, although there is one exterior point for each interior point) and filled dots show the location of interior points at  $r - \Delta r$  where the immersed boundary forcing is computed. For the special case of a stationary particle, the velocity at the interior points is forced to be the opposite of the velocity at the corresponding exterior points. In the schematic,  $u_n \mathbf{e}_n$  represents the normal velocity and  $u_t \mathbf{e}_t$  represents the tangential velocity at the exterior point. . . . . 34

Figure 2.3 Convergence characteristics of drag force due to fluctuating pressure gradient (open symbols) and viscous stresses (filled symbols) for FCC arrays at  $Re_m = 40$  with grid resolution  $D_m$  for two CFL values of 0.2 (squares) and 0.05 (triangles). Volume fraction  $\phi$  is equal to 0.2 in (a) and 0.4 in (b). . . . . 42

Figure 2.4 Convergence characteristics of drag force due to fluctuating pressure (open symbols) and viscous stresses (filled symbols) for FCC arrays at  $Re_m = 300$  with grid resolution  $D_m$ . Volume fraction  $\phi$  is equal to 0.2. . . . . 43

Figure 2.5 Decay of the fluid velocity autocorrelation function (cf. Eq. 3.17) obtained from PReIBM simulation of steady flow past a random configuration of spheres at a solid volume fraction of 0.2 and mean flow Reynolds numbers 20 (squares) and 300 (triangles). In these simulations  $L/D$  ratios of 6 and 4.5 are used for Reynolds numbers 20 and 300 respectively. . . . . 45

Figure 2.6 Variation of the normalized drag force as a function of the solid volume fraction  $\phi$  in Stokes flow past SC, FCC and random arrangements of spheres. In figure 2.6(a) drag values obtained from PReIBM simulations (open symbols) of Stokes flow in SC and FCC arrangements are compared with the results Zick and Homsy (1982) (filled symbols). In figure 2.6(b) drag values from PReIBM simulations of Stokes flow in random arrays of spheres are compared with the Stokes drag correlation proposed by van der Hoef et al. (2005). For each volume fraction the normalized force from PReIBM simulations is reported by averaging over 5 MIS and the error bars on the symbols in this figure represent 95% confidence intervals in the estimation of the normalized force. . . . . 47

Figure 2.7 Variation of the normalized drag force as a function of both the solid volume fraction and mean flow Reynolds number for flow past SC and FCC arrays. In all these cases, the mean flow is directed along the positive  $x$ -axis. In figure 2.7(a) drag obtained from PReIBM simulations (open symbols) for SC arrangements is shown while in figure 2.7(b) drag obtained for FCC arrangement is shown. In both figures, PReIBM drag values (open symbols) are compared with those reported by Hill et al. (2001b) (closed symbols). . . . . 48

Figure 2.8 Schematic comparing various simulation setups. . . . . 51

Figure 2.9 Plot comparing the velocity contours obtained from the different simulation set ups. The contours shown in this figure are for a simple cubic arrangement at a volume fraction of 0.4 and mean flow Reynolds number of 150. . . . . 52

Figure 2.10 Plot comparing the evolution of normalized pressure and viscous forces obtained from the different simulation setups shown in figure 2.8. The volume fraction is 0.4 and the mean flow Reynolds number is 150. Pressure force is plotted in Figure 2.10(a) while the viscous force is plotted in Figure 2.10(b). Since the results obtained from setups A, A' and B are identical, only two (A and A') are shown in these plots for clarity. . . . . 53

Figure 2.11 Variation of normalized force with Reynolds number for random assembly of fixed particles. Drag values obtained from PReIBM simulations (open symbols) are compared with those reported by HKL (filled symbols) and BVK. In left panel (a)  $\phi = 0.1, 0.2, 0.3$  and in the right panel (b)  $\phi = 0.4, 0.5$ . The error bars on the symbols in this figure represent 95% confidence intervals in the estimation of the normalized force. . . . . 56

Figure 2.12 Plot showing the variation of normalized fluid–particle force with mean slip Reynolds number for a random array at two different volume fractions ( $\phi = 0.2, 0.3$ ). Results obtained from both setups A and C are shown. The BVK drag correlation (lines) is also shown for comparison. . . . . 58

Figure 2.13 Plots showing the grid convergence of ANSYS–FLUENT software and PReIBM. Grid resolution of ANSYS–FLUENT (squares) corresponds to the bottom  $x$ -axis while the grid resolution of PReIBM simulations (triangles) is shown in the top  $x$ -axis. The drag value reported by BVK at this volume fraction (0.4) and Reynolds number (100) is also shown for reference. . . . . 60

Figure 2.14 Plots comparing the contours of the Reynolds number based on the streamwise component of the instantaneous fluid velocity obtained from PReIBM (2.14(a)) with those obtained from ANSYS-FLUENT software (2.14(b)). . . . . 61

Figure 2.15 Plots comparing the contours of instantaneous dimensionless pressure ( $p^* = p/(\frac{1}{2}\rho_f |\langle \mathbf{W} \rangle|^2)$ ) obtained from PReIBM (2.15(a)) with those obtained from ANSYS-FLUENT software (2.15(b)). . . . . 61

Figure 2.16 Plots showing the pressure and viscous drag force in a random configuration. . . . . 63

Figure 2.17 Schematic of the spherical coordinate system used to define the local pressure and viscous drags. The polar angle in our convention is  $\theta$  ( $0 \leq \theta \leq \pi$ ) and the azimuthal angle is  $\alpha$  ( $0 \leq \alpha \leq 2\pi$ ). . . . . 64

Figure 2.18 Profiles of local coefficient of pressure and coefficient of friction along the polar angle. Figure 2.18(a) shows the local pressure profiles for different volume fractions at a Reynolds number of 100 while figure 2.18(b) shows the local pressure profiles for various mean flow Reynolds numbers at a volume fraction of 0.2. Similarly figure 2.18(c) shows the local viscous drag profiles for different volume fractions at a Reynolds number of 100 while figure 2.18(d) shows the local viscous drag profiles for various mean flow Reynolds numbers at a volume fraction of 0.2. . . . . 66

Figure 2.19 DingDong Plot comparing the normalized force values obtained from the PReIBM drag law (cf. 3.24) with those obtained from the drag laws of HKL, BVK, Gidaspow (1986) and Syamlal and O'Brien (1987) for four different solid volume fractions. The volume fraction at which the drag values are computed is shown at the top of each panel. For every volume fraction, the HKL drag law terminates at  $Re_m = 100$  since it is not valid beyond that Reynolds number. . . . . 68

Figure 3.1 Schematic of a CFD simulation of gas–solid flow. In every computational grid cell, governing equations for the averaged quantities in both phases are solved. Here  $\langle \mathbf{u}^{(f)} \rangle$  is the average gas–phase velocity and  $\langle \mathbf{u}^{(s)} \rangle$  is the average solid–phase velocity. The average interphase momentum transfer  $\langle \mathbf{S}_M^{(f)} \rangle = -\langle \mathbf{S}_M^{(s)} \rangle$  that represents the coupling between the solid and the gas–phase appears as an unclosed term in both equations. Also, the transport of Reynolds stress in each phase is an unclosed term in the average momentum equation of that phase. Here  $\mathbf{u}''^{(f)}$  denotes the fluctuating velocity in the gas–phase. . . . . 73

Figure 3.2 Schematic showing the concept of the average fluid–phase velocity. The average fluid–phase velocity that is solved in gas–solid CFD simulations is obtained by averaging over all possible realizations. . . . . 79

Figure 3.3 A schematic showing the computation of the immersed boundary forcing for a stationary particle. The solid circle represents the surface of the particle at  $r$ . Open dot shows the location of one exterior point at  $r + \Delta r$  (only one exterior point is shown for clarity, although there is one exterior point for each interior point) and filled dots show the location of interior points at  $r - \Delta r$  where the immersed boundary forcing is computed. For the special case of a stationary particle, the velocity at the interior points is forced to be the opposite of the velocity at the corresponding exterior points. In the schematic,  $u_n \mathbf{e}_n$  represents the normal velocity and  $u_t \mathbf{e}_t$  represents the tangential velocity at the exterior point. . . . . 82

Figure 3.4 (a) Variation of the coefficient of pressure  $C_p$  along the surface of the sphere. Symbols are the data obtained from PReIBM simulations for a Reynolds number of 10, while the solid line is that reported in the book authored by Clift, Grace and Weber (CGW) Clift et al. (1978). (b) Comparison of the velocity profile in a square duct obtained from PReIBM simulations at a Reynolds number of 20 with analytical solution Cornish (1928). It is worthwhile to note that the walls are generated using the immersed boundary method. . . . . 86

Figure 3.5 Contours of local kinetic energy ( $k^{(f)} = \frac{1}{2}u_i''^{(f)}u_i''^{(f)}$ ) in the gas-phase normalized by the mean energy for steady flow past random assembly of spheres at a solid volume fraction of 0.05 and mean flow Reynolds number of 50. . . . . 87

Figure 3.6 Convergence characteristics of  $k_f/E_f$  with grid resolution  $D/\Delta x$  for flow past random arrays of spheres at  $\phi = 0.3$  and  $Re_m = 20$ . The error bars denote 95% confidence intervals in the estimation of the average  $k_f$  from 5 independent realizations. . . . . 89

Figure 3.7 (a) Convergence of the fluid-phase velocity autocorrelation function with grid resolution as well as box size for a random configuration of particles at a solid volume fraction of 0.2 and Reynolds number of 20. (b) Decay of the fluid velocity autocorrelation function obtained from PReIBM simulation of steady flow past a random configuration of spheres at a solid volume fraction of 0.2 and mean flow Reynolds numbers 20 (squares) and 300 (triangles). In these simulations  $L/D$  ratios of 6 and 4.5 are used for Reynolds numbers 20 and 300 respectively. 90

- Figure 3.8 Variation of the turbulent kinetic energy normalized by  $E_f = \frac{1}{2} \langle \mathbf{u}^{(f)} \rangle \cdot \langle \mathbf{u}^{(f)} \rangle$  with  $Re_m$  and  $\phi$ . Figure 3.8(a) shows the behavior of  $k_f/E_f$  with  $\phi$  for different mean flow Reynolds numbers while Fig. 3.8(b) shows the behavior of  $k_f/E_f$  with  $Re_m$  for different solid volume fractions. For each volume fraction  $k_f$  obtained from PReIBM simulations is reported by averaging over 5 MIS and the error bars on the symbols in this figure represent 95% confidence intervals in the estimation of  $k_f$ . . . . . 91
- Figure 3.9 State of anisotropy of the gas-phase Reynolds stress tensor in the Lumley plane. Color of the symbol indicates the volume fraction going from  $\phi = 0.1$  (blue) to  $\phi = 0.5$  (red). For each volume fraction the invariants of the gas-phase Reynolds stress tensor are shown:  $Re_m = 0.01$  (squares),  $Re_m = 20$  (circles),  $Re_m = 100$  (diamonds) and  $Re_m = 200$  (triangles) are shown. . . . . 93
- Figure 3.10 Variation of dissipation length scales with Reynolds number for solid volume fractions 0.1 and 0.2. Dashed lines are obtained by modeling the dissipation term as  $k_f^{3/2}/l_K$  while the solid lines are obtained by modeling the dissipation as  $2\nu_f k_f/l_T^2$ . . . . . 97
- Figure 3.11 Behavior of the ratio  $k_f^2/(\varepsilon_f \nu_f)$  with mean flow Reynolds number for different solid volume fractions. . . . . 98
- Figure 4.1 Schematic of a CFD simulation of gas–solid flow. In every computational grid cell, governing equations for the averaged quantities in both phases are solved. Here,  $\langle \mathbf{u}^{(f)} \rangle$  is the average fluid–phase velocity,  $\langle T^{(f)} \rangle$  is the average fluid–phase temperature,  $\langle \mathbf{u}^{(s)} \rangle$  is the average solid–phase velocity and  $\langle T^{(s)} \rangle$  is the average solid–phase temperature. In this schematic,  $\langle Q_{g-s} \rangle$  denotes the average gas–solid interphase heat transfer. . . . . 102

Figure 4.2 Schematic showing contours of steady temperature field in a flow through fixed bed of particles (solid volume fraction 0.1 and Reynolds number 20). In this schematic,  $\langle \mathbf{W} \rangle$  is the mean slip velocity between the solid and the fluid-phase. The fluid enters the domain at a bulk temperature of  $T_{m,in}$  and all the particles are held at a uniform constant temperature  $T_s$ . . . . . 105

Figure 4.3 A schematic showing the computation of the immersed boundary forcing  $f_\phi$  for an isothermal particle. The solid circle represents the surface of the particle at  $r$ . Open dot shows the location of one exterior point at  $r + \Delta r$  (only one exterior point is shown for clarity, although there is one exterior point for each interior point) and filled dots show the location of interior points at  $r - \Delta r$  where the immersed boundary forcing is computed. In the schematic,  $\phi_e$  represents the temperature at the exterior point,  $\phi_s$  is the surface temperature while  $\phi_i$  is the temperature at the interior point. . . . . 111

Figure 4.4 (a) Convergence characteristics of Nusselt number with grid resolution for internal duct flow at a Reynolds number of 100 are shown in. In this plot  $Nu_a$  refers to the analytical value of the Nusselt number obtained by Shah and London (1978),  $\Delta x$  is the size of the grid cell and  $H$  is the channel height. (b) Contours of the scaled temperature  $\theta$  are shown in three planes along the direction of the flow shown by the arrow. . . . . 114

Figure 4.5 Variation of Nusselt number and the area occupied by the fluid-phase along the direction of the mean flow, obtained from PUREIBM simulations of heat transfer in a fixed bed at a volume fraction of 0.4 and mean flow Reynolds number of 100. The local Nusselt number is reported by averaging over (a) 50 and (b) 5 MIS. . . . . 115

Figure 4.6 Behavior of the average Nusselt number  $\langle Nu \rangle$  with mean flow Reynolds number for two solid volume fractions. Symbols indicate data obtained from PReIBM simulations while the solid lines are obtained from Gunn’s correlation (Gunn, 1978). The average Nusselt number from PReIBM simulations is reported by averaging over 5 MIS and the error bars on the symbols in this figure represent 95% confidence intervals in the estimation of Nusselt number. . . . . 117

Figure 4.7 (a) Variation of the nondimensional bulk fluid temperature along the axial direction for two mean flow Reynolds numbers (1 and 100) and two solid volume fractions (0.2 and 0.4). (b) Behavior of heat ratio with Reynolds number for two solid volume fractions (0.2 and 0.4). . . . . 118

Figure 5.1 Figure shows the comparison of the mean drag obtained from PReIBM simulations with the drag correlation reported by Hill et al. (2001b) at a solid volume fraction of 0.2 for the baseline case of zero particle velocity fluctuations. . . . . 139

Figure 5.2 Scatter plot of streamwise component of fluctuating acceleration versus the streamwise component of fluctuating velocity. Square symbols ( $\square$ ) show fluctuations in the particle acceleration obtained from DNS using PReIBM simulations, while upper triangles ( $\triangle$ ) show fluctuations in the particle acceleration predicted by simple extension of a mean drag law to its instantaneous counterpart. . . . . 141

- Figure 5.3 Schematic of the flow setup. The mean velocity of the fluid phase  $\langle \mathbf{u}^{(f)} \rangle$  is directed along the positive  $x$  axis as shown. The mean velocity  $\langle \mathbf{v} \rangle$  of the particles is zero and so the mean slip velocity  $\langle \mathbf{W} \rangle = \langle \mathbf{v} \rangle - \langle \mathbf{u}^{(f)} \rangle$  is along the negative  $x$  axis. The solid particle shown in this figure has a positive velocity fluctuation  $\mathbf{v}'$  along the positive  $x$  axis. The schematic illustrates that a positive fluctuation about the mean velocity of the particles implies a reduced instantaneous slip velocity,  $\mathbf{v}' - \langle \mathbf{u}^{(f)} \rangle$  between the particle and the fluid. . . . . 142
- Figure 5.4 Figure 5.4(a) shows the evolution of the normalized mean drag at a volume fraction of 0.2 and a mean flow Reynolds number of 20 for three different particle to fluid density ratios:  $\rho_p/\rho_f = 10$  (red), 100 (blue), and 1000 (purple). The black solid line indicates the drag in a static bed at the same mean flow Reynolds number and volume fraction. The dashed lines represent 95% confidence limits on the mean drag for the static bed. Figure 5.4(b) shows the evolution of the standard deviation of fluctuations in the particle acceleration relative to the mean drag at a volume fraction of 0.2 and a mean flow Reynolds number of 20 for different density ratios. In this plot, data for  $\rho_p/\rho_f = 10$  are shown on the right hand side  $y$ -axis. The standard deviation in the acceleration obtained for a fixed bed is 0.22 . . . . . 143
- Figure 5.5 Evolution of the particle granular temperature at a volume fraction of 0.2 and a mean flow Reynolds number of 20 for different density ratios. 145

- Figure 6.1 Illustration of different contributions to the instantaneous gas-solid force in a suspension with a mean fluid velocity  $\langle \mathbf{u}^{(f)} \rangle$  and a mean particle velocity  $\langle \mathbf{v} \rangle$  is shown in top left panel (a). Pressure contours are shown for (b) a single particle far away from its neighbors and moving with a velocity equal to the mean particle velocity (top right panel), (c) a particle moving in a different direction than the mean fluid flow and far from its neighbors (bottom left panel), and (d) a collection of particles moving in different directions (bottom right panel). The pressure contours are obtained from particle-resolved direct numerical simulations (PR-DNS) for a gas-solid suspension that corresponds to a solid volume fraction of 0.2 and mean flow Reynolds number 0.01. . . . . 157
- Figure 6.2 Scatter plot of streamwise component of particle acceleration fluctuations  $\mathbf{A}''$  (normalized by the standard deviation in the particle acceleration distribution  $\sigma_A$ ) versus the streamwise component of particle velocity fluctuations  $\mathbf{v}''$  (normalized by the standard deviation in the particle acceleration distribution  $\sigma_v$ ). Square symbols ( $\square$ ) denote the fluctuations in the particle acceleration obtained from PR-DNS of a freely evolving gas-solid suspension corresponding to a solid volume fraction of 0.2, mean flow Reynolds number of 1.0 and solid to fluid density ratio of 1000. Upper triangles ( $\triangle$ ) denote the fluctuations in the particle acceleration predicted by using a model for the fluid-particle acceleration of the form  $\langle \mathbf{A} | \mathbf{x}, \mathbf{v}; t \rangle = \beta(\mathbf{u}^{(f)} - \mathbf{v})$ . . . . . 160
- Figure 6.3 Plot showing the evolution of the Reynolds number based on granular temperature ( $\text{Re}_T$ ) for a freely evolving suspension of elastic particles at a volume fraction of 0.1 and solid to fluid density ratio of 100. . . . 165

- Figure 6.4 (a) Comparison of the particle velocity autocorrelation function extracted from the DNS of freely evolving suspension (solid volume fraction of 0.2, mean slip Reynolds number 20 and solid to fluid density ratio of 10) with the exponential decay predicted by the Langevin model. (b) Same as Fig. 6.4(a) for a suspension with solid to fluid density of 100. 166
- Figure 6.5 Plot showing the scaling of source and dissipation with granular temperature in nondimensional phase space. Red squares denote the source and blue triangles denote dissipation. The solid lines are the curve fits for source and dissipation given by Eqs. 6.6 and 6.7 respectively. . . . . 168
- Figure 6.6 Plot in 6.6(a) shows the variation of steady granular temperature with volume fraction and mean flow Reynolds number for a density ratio of 100. Symbols are data obtained from PReIBM DNS and the solid lines indicate the fit given by Eq. 6.8. Plot in 6.6(b) shows the variation of steady granular temperature with solid to fluid density ratio for a solid volume fraction of 0.1 and mean flow Reynolds number 20. Symbols denote the data obtained from PReIBM DNS and the solid line indicates the function  $\left(\frac{\rho_p}{\rho_f}\right)^{-1}$  . . . . . 169
- Figure 6.7 Plot showing the behavior of steady source with volume fraction and Reynolds number for a solid to fluid density ratio of 100. Symbols indicate PReIBM DNS data and solid lines indicate the fit given by Eq. 6.11 . . . . . 170

Figure 7.1	Plot showing the normalized force obtained from PReIBM simulations of flow past bi-disperse particle assemblies at a total volume fraction of (a) 0.3 and (b) 0.4 for two mean flow Reynolds numbers ( $Re_m = 50$ and 75). Solid lines are obtained by substituting the monodisperse drag correlation obtained from PReIBM simulations performed by Tenneti et al. (2011) for $F(\phi, Re_m)$ in Eq. (7.12). Dashed lines are obtained by substituting the monodisperse drag correlation given by Beetstra et al. (2007) for $F(\phi, Re_m)$ in Eq. (7.12). The normalized force is reported by averaging over 5 MIS and the error bars show 95% confidence intervals in the estimation of the normalized force. . . . .	178
Figure 7.2	Behavior of $k_f/E_f$ for bidisperse suspension with diameter ratio for two solid volume fractions (0.3 and 0.4) at a mean flow Reynolds number of 50. . . . .	178
Figure 7.3	Evolution of slip velocity between size classes and granular temperature of each size class for a bi-disperse freely evolving suspension at a total solid volume fraction of 0.2, mean flow Reynolds number 20 and solid to fluid density ratio 100. In this simulation the volume fractions of the size classes are taken to be equal. Red symbols denote the streamwise component of the slip velocity while purple and black represent the cross-stream components of the slip velocity between the size classes. . . . .	181
8.1	Schematic showing the serial algorithm of the PReIBM solver . . . . .	183
8.2	Schematic showing the partition of the domain in the PReIBM solver. . . . .	184

8.3	Figure shows the parallelization strategy for the immersed boundary method with two processors. The domain is partitioned in the $x$ -direction. The partition boundary is shown by the green dashed line. A particle that cuts across two processors is handled by the processors in parallel. In IBM, the particle surface is represented by a finite number of points. These are shown by the crosses. The red crosses are the points which are handled by the processor $P_0$ and the blue crosses are handled by the processor $P_1$ . The points which belong to the grid cell that contains the partition boundary (shown by pink circles) are processed by both the processors. . . . .	185
8.4	Form of the tridiagonal matrix that is inverted in the PReIBM solver. The horizontal blue lines show the partition boundaries. . . . .	186
8.5	Schematic showing the transpose strategy used to solve the interface system. In this figure $N_y^2$ denotes the number of grid points in the $yz$ plane and $N$ denotes the total number of processors. . . . .	187
8.6	Schematic of the test case chosen to assess the performance of the parallel PReIBM code . . . . .	189
Figure 8.7	Weak scaling of the parallel PReIBM code with number of processors for the case of $N_x = 8$ . Symbols show the time obtained from the PReIBM code while the dashed line shows the ideal behavior with no communication. . . . .	191
Figure 9.1	Plot showing the various regions of validity of Koch's analysis. . . . .	194

Figure 9.2 (a) Pair correlation function obtained from PR-DNS of freely evolving gas-solid suspensions corresponding to a solid volume fraction of 0.2, mean flow Reynolds number of 20 and solid to fluid density ratio of 100. These parameters correspond to a Stokes number of 278. These simulations have been performed for three different coefficients of restitution. ((b))Pair correlation function at three different times obtained from PR-DNS of gas-solid suspension at a solid volume fraction of 0.05, mean flow Reynolds number of 50 and solid to fluid density ratio of 100. The Stokes number of the suspension is 694. Initial configuration is taken from an inelastic granular gas simulation and the later times are one and two flow through times of the periodic box respectively. . . . . 201

9.3 Schematic showing the intersection of solid particles with the measurement region. The region of space occupied by the solids is hatched with vertical lines. The region of intersection of the solid particles with the measurement region is hatched with horizontal lines. . . . . 203

C.1 Schematic of the physical domain. Hatched lines represent the volume  $\mathcal{V}_f$  occupied by the fluid phase, solid fill represents the volume  $\mathcal{V}_s$  occupied by the solid particle, and  $\mathcal{V} = \mathcal{V}_f + \mathcal{V}_s$  is the total volume.  $\partial\mathcal{V}$  and  $\partial\mathcal{V}_s$  represent, respectively, the areas of the computational box and the solid particle. . . . . 215

Figure C.2 Evolution of the mean solids velocity and mean fluid velocity in the moving frame and the frame velocity with respect to the laboratory frame obtained from the DNS of a freely evolving suspension of volume fraction 0.2,  $Re_m = 20$ . Figure C.2(a) shows the results for a solid to fluid density ratio of 10 while Figure C.2(b) shows the results for a solid to fluid density ratio of 1000. In both figures, the mean solids velocity (open circles), the mean fluid velocity ( $\square$ ) and the frame velocity ( $\nabla$ ) are scaled by the desired mean slip velocity. . . . . 221

- Figure D.1 Scatter plot showing the the fluctuating particle acceleration versus the fluctuating particle velocity obtained from the DNS of flow past a fixed particle assembly at a volume fraction of 0.2, mean flow Reynolds number of 20 and Reynolds number based on granular temperature of 16. From the analysis on the extraction of source and dissipation from the DNS, we can see that the symbols that lie in the first and the third quarter contribute to source and the symbols that lie in the second and the fourth quadrant contribute to the dissipation. . . . . 224
- Figure D.2 Phase space plot showing the variation of source and dissipation with granular temperature. DNS data for two different suspensions is shown here. The volume fraction, mean flow Reynolds number and solid to fluid density ratio are 0.2, 20 and 100 respectively. Triangles denote the source (filled symbols) and dissipation (hollow symbols) and dissipation for a suspension initialized with zero granular temperature. Squares denote the data for a suspension initialized with a finite granular temperature corresponding to  $Re_T = 4$ . . . . . 225

## ABSTRACT

Gas-solid flows are commonly encountered in Nature and in several industrial applications. Emerging carbon-neutral or carbon negative technologies such as chemical looping combustion and CO<sub>2</sub> capture are examples of gas-solid flows in power generation industry. Computational fluid dynamics (CFD) simulations are increasingly being seen as a cost-effective tool in the design of technological applications in power generation industry. Device-scale CFD calculations that involve gas-solid flow are based on statistical descriptions that require closure models for the exchange of mass, momentum, energy and heat transfer between the dispersed solid phase and the gas phase. The predictive capability of multiphase flow CFD simulations strongly depends on the accuracy of the models used for the interphase exchange terms. Particle-resolved direct numerical simulation (PR-DNS) is a first-principles approach to develop accurate models for interphase momentum, energy and heat transfer in gas-solid flow. The primary objective of this work is the development of accurate models for the interphase exchange of momentum, kinetic energy and heat transfer in polydisperse gas-solid flows using PR-DNS.

A novel computational tool named Particle-resolved Uncontaminated-fluid Reconcilable Immersed Boundary Method (PUReIBM) has been developed as a part of this work to perform PR-DNS of flow past fixed and freely moving spherical particles. We designed the appropriate numerical experiment that can be used to develop closure models for interphase momentum transfer and formally established the connection between PR-DNS and statistical theory of multiphase flow for which the models are intended. Using PUReIBM we developed an improved drag correlation to model interphase momentum transfer in gas-solid flow. The solution fields obtained from PUReIBM PR-DNS have been used to quantify the velocity fluctuations in the gas-phase and a simple eddy viscosity model for the gas-phase pseudo-turbulent kinetic energy has been developed. A novel PR-DNS methodology to study heat transfer in gas-solid flow has been developed. These results provide insight into the role of fluid heating in gas-solid flow and

motivate the development of better models for gas-solid flow heat transfer. From PR-DNS of freely evolving gas-solid suspensions we developed a stochastic model for particle acceleration that accounts for the particle velocity distribution. In addition to model development, the implementation of a parallel algorithm that enables PR-DNS of gas-solid flow on petascale supercomputers is also discussed.

## CHAPTER 1. Introduction

### 1.1 Background

Gas-solid flows occur in many industrial applications such as energy generation, as well as food, chemical, and pharmaceutical processing. Quantitative understanding of gas-solid flows in fluidized beds is crucial for efficient operation of processes such as fluid catalytic cracking (FCC), which is now a worldwide trillion dollar industry (Avidan, 1997). Emerging technologies such as chemical looping combustion (Shen et al., 2008), and CO<sub>2</sub> capture from flue gases using dry sorbents (Yi et al., 2007; Abanades et al., 2004) offer the promise of carbon-neutral energy generation (Azar et al., 2006). The success of these technologies and their commercialization depends on the ability of designers to rationally choose from a plethora of design options using reliable and predictive computer simulations of gas-solid flow in industrial devices.

Gas-solid flow in energy applications is characterized by changing random configurations of a large number of particles of different sizes, turbulence in the gas-phase, gas-solid heat transfer as well as particle-particle interactions. Due to the inherent randomness in gas-solid flows, statistical descriptions are useful to predict the overall behavior of the system. Moreover, Computational Fluid Dynamics (CFD) simulations of device-scale gas-solid flow applications are primarily based on such statistical descriptions. Interphase exchanges of mass, momentum and energy play a pivotal role in determining the overall behavior of gas-solid flow. These interphase exchanges appear as unclosed terms in the averaged conservation equations for mass, momentum and energy. Developing accurate models for the average interphase exchange terms is the primary focus of this dissertation.

Developing predictive models for gas-solid flow in industrial applications is challenging due to many reasons. Some of the major challenges that are dealt with in this work are listed below:

1. *Polydispersity*: The presence of particles of different sizes, or polydispersity, may be a property of the starting material itself or it may be intentionally utilized in order to improve process performance. The presence of particles of different sizes introduces a range of length and time scales and the interaction of these length and time scales with the gas-phase gives rise to interesting phenomena such as segregation. Polydispersity also affects interphase transfer of mean interphase momentum, kinetic energy, and heat transfer, which in turn affect the overall flow behavior.
2. *Gas-phase velocity fluctuations*: The diameters of the particles found in industrial devices such as fluidized beds are typically in the range of 50–150  $\mu\text{m}$  and are usually larger than the Kolmogorov length scale of gas-phase turbulence (Moran and Glicksman, 2003). The interaction of such finite sized particles with the gas-phase gives rise to fluctuations in the gas velocity, in addition to the inherent turbulent motions of the gas-phase. These gas-phase velocity fluctuations play an important role in the transport of the particles to and from the walls of the device as well as in the mixing of chemical species and interphase heat transfer.
3. *Particle velocity distribution*: It is clear from visual observation as well as experimental measurements that particles have a range of velocities. The particle velocity fluctuations characterized by the particle granular temperature (particle velocity variance) affect the mean interphase momentum transfer (Wylie et al., 2003) and also play an important role in phenomena such as the core-annular structure in riser flows. It is now established that the prediction of core-annular structure in riser flows requires solving the transport equation for the particle granular temperature (Hrenya and Sinclair, 1997). Hence, there is a need for models that accurately predict the particle granular temperature, which in turn should lead to a better prediction of the mean fields such as solid volume fraction.

In addition to the aforementioned challenges, the nonlinear and multiscale interactions in gas-solid flow result in a rich variety of flow phenomena spanning many flow regimes. One of the principal features of gas-solid flow that distinguish it from advection and diffusion of chemical species in multicomponent flows is the inertia of dispersed phase particles. Outside the Stokes

flow regime, particle inertia results in a nonlinear dependence of particle acceleration on particle velocity and this nonlinearity is important in many applications where the particle Reynolds number is finite. The influence of the dispersed phase on carrier-phase momentum balance is another source of nonlinear behavior in the system. Unlike molecular gases, not all multiphase flows are collision-dominated, and hence it is possible for the probability density function (PDF) of the particle velocity to depart significantly from equilibrium. These nonlinearities, multiscale interactions and nonequilibrium effects lead to the emergence of new phenomena such as preferential concentration and clustering that have a significant impact on gas-solid flow applications. It is worthwhile to note that the nonequilibrium and multiscale nature of gas-solid flows cannot be adequately dealt with using existing modeling approaches. In this work we focus on modeling the unclosed terms that arise in the existing statistical approaches. The novel feature of the present work is the use of particle-resolved direct numerical simulation (PR-DNS) to develop closure models for gas-solid flow by establishing an explicit connection between the quantities computed from PR-DNS solution fields and the unclosed terms that arise in the statistical approaches.

## 1.2 Statistical approaches

A complete description of a gas-solid flow requires the state of each particle and each fluid point at each time instant. However, such level of description contains much more information than is required for practical applications. Therefore, a statistical description of the gas-solid flow that provides information on macroscopic average quantities that describe the flow is more useful for engineers in the design process. Computational fluid dynamics (CFD) simulations that are based on such statistical descriptions of gas-solid flow are being increasingly used as a cost-effective approach for rapid evaluation of designs (Halvorsen et al., 2003).

Statistical approaches to multiphase flow can be classified on the basis of three criteria: (i) whether each phase is represented using a *random field* or *stochastic point process*<sup>1</sup> description, (ii) whether each phase is represented in an Eulerian or Lagrangian reference frame, and (iii)

<sup>1</sup>The term point process should not be confused with the 'point particle' assumption. Stochastic point processes are mathematical descriptors of non-contiguous objects in space that can be spheres of finite radius.

the level of closure in the statistical theory. The two principal statistical approaches are: (i) the *random field* approach in which both dispersed and carrier phases are represented as random fields in the Eulerian frame, and (ii) the *point process* approach in which the dispersed phase is represented as a stochastic point process in the Lagrangian frame and the carrier phase is represented as a random field in the Eulerian frame.

### 1.2.1 Random-field Theory

In statistical theories of turbulent single-phase flow, the Eulerian velocity field is represented as a random vector field (Pope, 2000). A similar approach can be adopted for gas–solid flows, but in addition to the velocity field it is also necessary to specify the location and shape of the dispersed-phase elements. The velocity field  $\mathbf{U}(\mathbf{x}, t)$ , which is defined in both thermodynamic phases, is a vector field which is defined at each point  $\mathbf{x}$  in the flow domain in physical space. The dispersed–phase elements are described by a dispersed–phase indicator *field*  $I_d(\mathbf{x}, t)$ , which is unity for all points inside the dispersed–phase elements that are contained in the flow domain, and zero outside (see Fig. 1.1). Statistical theories based on random–field representations require the consideration of multipoint joint probability density functions, and these have not resulted in tractable engineering models even for single–phase turbulent flow (Pope, 2000; Monin and Yaglom, 1975).

The simplest statistical theory based on the random–field representation that is useful to modelers is a single–point representation. Figure 1.1 shows the hierarchy of the level of description in the random–field representation. The single–point representation results in the single–point Eulerian–Eulerian (EE) two–fluid theory. In this case the statistics of the velocity field and the dispersed–phase indicator field are considered at a single space–time location, i.e., the indicator field reduces to an indicator function. The velocity and indicator function can be treated as random variables (or random vector in the case of velocity) *parametrized* by space and time variables. The averaged equations resulting from this approach are described in Drew (1983), and Drew and Passman (1998). The single–point Eulerian–Eulerian theory can be developed at the more fundamental level of probability density functions also, and this theory is described in Pai and Subramaniam (2009).

### 1.2.2 Point Process Theory

Stochastic point process theory (Daley and Vere-Jones, 1988; Stoyan et al., 1995; Stoyan and Stoyan, 1995) enables the statistical description of points that are distributed in space. This provides the necessary mathematical foundation to describe the statistics of solid particles. The theory of marked point processes allows us to assign the size of the particle as a “mark” or tag to the particle location. From this it is clear that stochastic point process theory does not require that particles are modeled as point-particles that correspond to delta-function sources of mass and momentum. The statistical representation of a spray as a point process has been formulated by Subramaniam (2000). It is shown that the complete characterization of all multi-particle events requires consideration of the Liouville probability density function (pdf).

The simplest point-process theory (Williams, 1958; Subramaniam, 2000, 2001), also known as the Lagrangian–Eulerian (LE) statistical approach considers the evolution equation of the one-particle distribution function. The one-particle distribution function is also commonly known as the droplet distribution function (ddf) in spray literature. The one-particle distribution function is a function of the sample space of particle positions, velocity, and radius. There are several approaches that are available to obtain a solution for the distribution function. The moments of the distribution function imply various average quantities such as the average solid volume fraction, average solid-phase velocity etc. Therefore, by taking the moments of the evolution equation for the ddf, one can derive conservation equations for the average mass, momentum and energy of the solid phase. This is the approach taken in the classical theory of molecular gases (Liboff, 2003) as well as in the kinetic theory of granular flows (KTGF) (Jenkins and Savage, 1983; Lun et al., 1984; Serero et al., 2006; Sela and Goldhirsch, 1998; Garzo et al., 2007a).

Another approach to solve the evolution equation of the distribution function is via the Quadrature Based Moment Methods (QBMM) introduced by Fox (2008). In this approach, the distribution function is represented as a sum of  $\delta$ -functions at time-varying abscissa locations with corresponding weights that also evolve in time. Transport equations for the moments are derived in a fashion similar to the KTGF approach, which results in unclosed terms. The

moments of the distribution function are related to the quadrature abscissae and the moment transport equations are closed in terms of the quadrature abscissae.

There are also a suite of simulation techniques, commonly termed as the LE simulation methods (Amsden et al., 1989) that solve for the distribution function in an indirect way. In the LE simulation approach, the solid phase is represented by an ensemble of computational particles and the velocities and positions of these computational particles are evolved in time. This methodology is popularly known as Lagrangian particle tracking and it requires models for the acceleration of the particles in order to evolve the particle velocities.

Both random-field and point-process statistical descriptions of gas-solid flow result in a closure problem similar to that encountered in the statistical theory of single-phase turbulence. The averaging procedure results in unclosed terms that need to be modeled. Recently, Pai and Subramaniam (2009) established equivalence relations between the unclosed terms in the EE and LE statistical representations. For instance, in the random field description, the mean momentum conservation equation in the particle phase requires closure of the average fluid-particle interaction force (mean drag force) and the average stress in the solid particle phase. Similarly, in the point process description, closure model for the acceleration of the particles in terms of the particle velocity is required. Therefore, it is clear that accurate models for the unclosed terms are needed for the effective use of gas-solid CFD simulations that are based on statistical descriptions.

### 1.2.3 Use of PR-DNS for modeling gas-solid flow

From the foregoing discussion of the modeling challenges, it is clear that a first-principles approach is needed to develop accurate physics-based models. Theoretical approaches become intractable due to the randomness in the particle configuration as well as the nonlinearity of the governing equations at finite Reynolds numbers that are encountered in practical applications. Although experiments provide valuable insights for modeling, it is difficult to obtain detailed information of the flow fields and particle velocities needed for accurate model development due to poor optical access in gas-solid systems. The exponential rise in computing power provides the application of advanced numerical methods as an attractive option to obtain detailed and

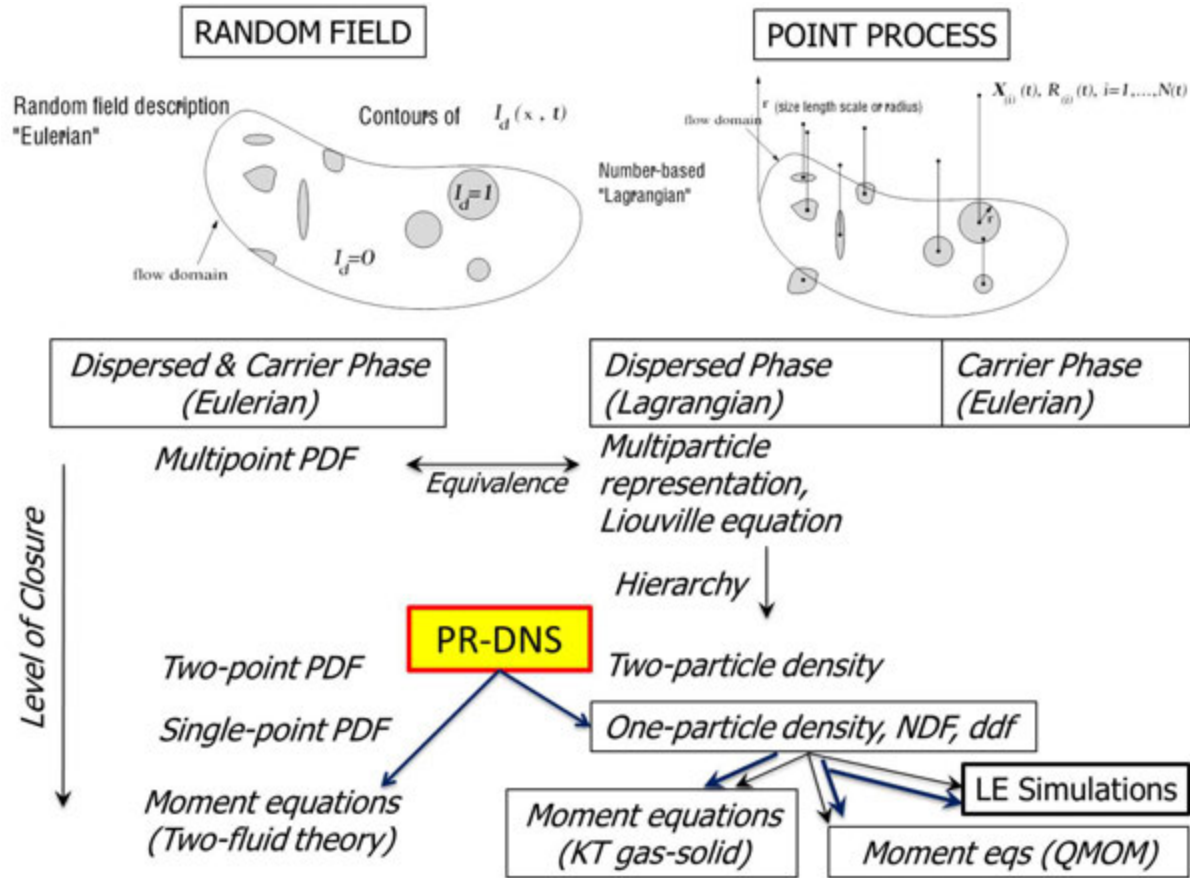


Figure 1.1 Role of PR–DNS in gas–solid flow model development.

accurate information in gas–solid flow. Figure 1.1 depicts the role of PR–DNS in gas–solid flow model development. The attractive aspect of PR–DNS is that it can be used to develop models in the context of both the random field and stochastic point process descriptions. In the following section we discuss recent advances in using PR–DNS for gas–solid flow model development.

### 1.3 PR–DNS approaches

PR–DNS is a first–principles approach to developing accurate models for interphase momentum, energy and heat transfer in gas–solids flow. In the PR–DNS approach the governing Navier–Stokes (NS) equations are solved with exact boundary conditions at each particle surface. It produces a model–free solution with complete three–dimensional time–dependent ve-

locity, pressure and temperature fields. It is worthwhile to note that the PR–DNS approach is significantly different from the *point particle* direct numerical simulation methodology (Squires and Eaton, 1991; Elghobashi and Truesdell, 1993; Boivin et al., 1998; Sundaram and Collins, 1999; Mashayek and Taulbee, 2002) (DNS) in which the particles are treated as points and the effect of the particles on the gas–phase is represented by a force applied at the particle center. Clearly the point particle approach is valid only when the particle size is much smaller compared to the Kolmogorov length scale. When the particle size is larger or comparable to the Kolmogorov length scale, the effects of the wake generated by the particles become important and hence it is important to resolve the boundary layers around the particle.

Recently, a variety of numerical approaches have been developed to perform PR–DNS of gas–solid flow. These can be broadly classified as those that rely on a body–fitted mesh to impose boundary conditions at particle surfaces, and those that employ regular Cartesian grids. The body–fitted methods include the arbitrary Lagrangian Eulerian (ALE) approach (Hu et al., 2001; Nomura and Hughes, 1992) as well as the method used by Balachandar and co-workers (Bagchi and Balachandar, 2003, 2004). Also Burton and Eaton (2005) used the overset grid technique to study the interaction between a fixed particle and decaying homogeneous isotropic turbulence. The principal disadvantage with approaches based on body-fitted meshes is that repeated re-meshing and solution projection are required for moving interfaces.

For methods that employ regular Cartesian grids, this need for re-meshing and projection is eliminated, resulting in much faster solution times for moving particle simulations. The wide range of parameters encountered in gas–solids flow and the need to perform multiple independent simulations (MIS) (due to the random arrangements of the particles) makes it impractical to use body–fitted meshes. However, because the grid does not conform to the particle surface, special attention is needed to generate an accurate solution. Popular methods based on regular Cartesian grids include the fictitious domain method (Patankar et al., 2000; Glowinski et al., 2001; Sharma and Patankar, 2005; Apte et al., 2009), the lattice Boltzmann method (LBM) (Hill et al., 2001a,b; Ladd and Verberg, 2001; Ten Cate et al., 2004; van der Hoef et al., 2005; Beetstra et al., 2007), and the immersed boundary method (IBM) (Peskin, 1981; Yusof, 1996; Uhlmann, 2005; Garg, 2009; Kim and Choi, 2006; Lucci et al., 2010). Besides these

widely used techniques, there are other methods such as PHYSALIS (Oguz and Prosperetti, 2001; Takagi et al., 2005; Zhang and Prosperetti, 2003, 2005) that use a general analytic solution of the Stokes equation in the flow domain close to particle boundaries to impose the no-slip velocity boundary condition on the particle surface.

In this work we employ a DNS approach based on the Particle-resolved Uncontaminated-fluid Reconcilable Immersed Boundary Method (PUREIBM) that is used to solve for flow past arbitrary arrangements of solid spherical particles. PUREIBM is a particle-resolved direct numerical simulation approach for gas-solid flow where the Navier-Stokes equations with no-slip and no-penetration boundary conditions on each particle's surface are solved using a forcing term that is added to the momentum equation. The salient features that distinguish PUREIBM from other immersed boundary method approaches are as follows:

1. Uncontaminated fluid: In PUREIBM the immersed boundary (IB) forcing is solely restricted to those grid points that lie in the solid phase, and therefore the flow solution in the fluid phase is uncontaminated by the IB forcing. Consequently the velocity and pressure in the fluid phase is a solution to the unmodified Navier-Stokes equations (in contrast to IB implementations that smear the IB forcing on to grid points in the fluid phase adjoining solid boundaries, resulting in solution fields that do not correspond to unmodified Navier-Stokes equations).
2. Reconcilable: In PUREIBM the hydrodynamic force experienced by a particle is computed directly from the stress tensor at the particle surface that is obtained from this uncontaminated fluid flow solution (in contrast to IB implementations that calculate the hydrodynamic force from the IB forcing field). This feature of PUREIBM enables us to directly compare the DNS solution with any random-field theory of multiphase flow. In particular, for statistically homogeneous suspensions it is shown in Tenneti et al. (2011) that PUREIBM DNS reconciles with multiphase flow theory.

It is also shown that PUREIBM is a numerically convergent and accurate particle-resolved DNS method for gas-solids flow and its performance has been validated in a comprehensive suite of tests. The PR-DNS tool developed in this work is used to achieve the research objectives

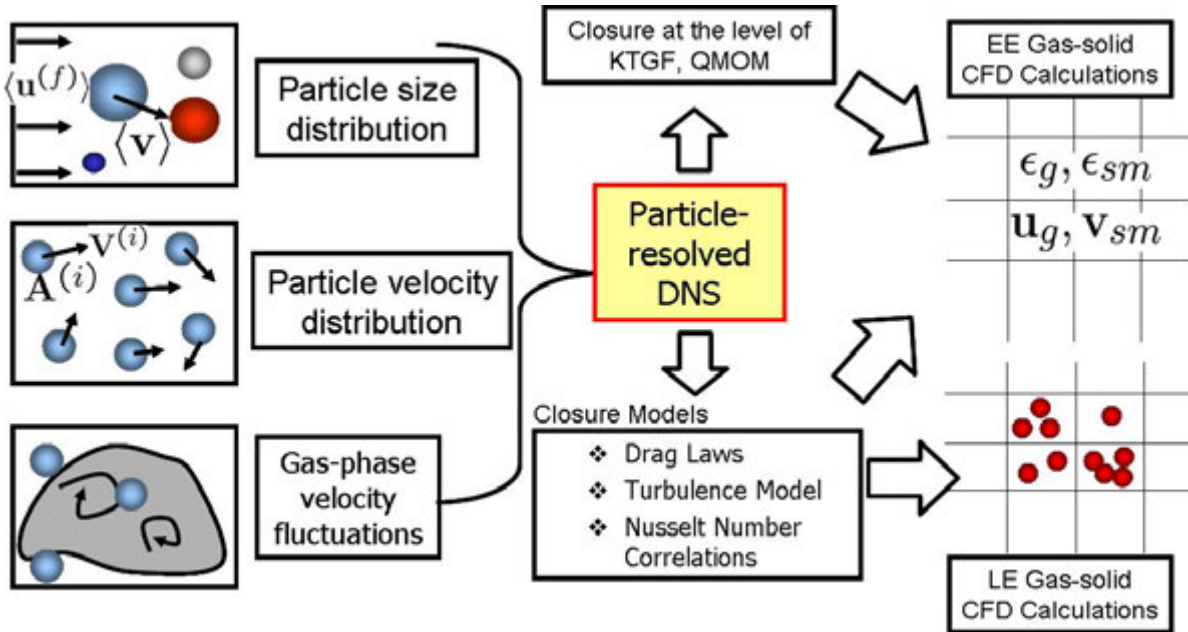


Figure 1.2 Schematic showing the research objectives of this work. PR-DNS will be used to probe the effects of particle size distribution, gas-phase velocity fluctuations and particle velocity distribution. The data obtained from carefully performed DNS will be used to propose models for the mean interphase momentum transfer, turbulent kinetic energy and heat transfer. Another objective of this work is to use PR-DNS to provide a closure at the level of the one-particle distribution function, which is the starting point of kinetic theory for gas-solid flows (KTGF) and quadrature method of moments (QMOM). The improved models and kinetic theory closures can be used in more accurate EE and LE gas-solid CFD simulations.

described in the next section.

#### 1.4 Research objectives

The principal objective of this work is to use PR-DNS to achieve the following goals (see figure 1.2):

1. Develop a model for mean interphase momentum transfer in polydisperse gas-solid flow
2. Quantify the level of gas-phase velocity fluctuations and develop a model to account for gas velocity fluctuations in polydisperse gas-solid flow
3. Develop a formulation to study heat transfer due to forced convection in gas-solid flow

4. Account for the distribution of particle velocities and provide a closure at the level of the one-particle distribution function.

These principal research objectives are discussed below in further detail.

#### 1.4.1 Modeling mean interphase momentum transfer in polydisperse gas–solid flow

A gas–solid flow with a particle size distribution is usually represented in terms of a collection of particles belonging to discrete classes of different sizes. In the EE approach, conservation equations for the mean momentum are written for each size class, and the mean interphase momentum transfer between particles belonging to a size class and the gas–phase appears as an unclosed term in the mean momentum conservation equation of that size class. Even in LE simulations, the total force acting on the particles in a computational grid cell is needed in order to solve the momentum equation in the gas–phase. Therefore, an accurate model for the mean interphase momentum transfer is needed in terms of the average properties namely the solid volume fraction  $\phi$  and the Reynolds number  $Re_m$  based on the relative or slip velocity between the solid and the gas–phase. The closure for the mean interphase momentum transfer is popularly known as a “drag law”.

The average force acting on the particles belonging to a size class in a polydisperse gas–solid flow is usually modeled in terms of the average force acting on an equivalent monodisperse suspension. Hence, the accuracy of polydisperse drag models depends on the accuracy of the monodisperse drag law. Several drag correlations have been proposed for monodisperse gas–solid suspensions by simulating steady flow past random arrangements of stationary spheres (Hill et al., 2001a,b; van der Hoef et al., 2005; Beetstra et al., 2007). Hill, Koch and Ladd (Hill et al., 2001a,b) referred to collectively as HKL in this work, studied the steady flow past ordered and random arrays of monodisperse spheres using the lattice Boltzmann method (LBM). While van der Hoef et al. (2005) extended HKL’s LBM simulations to account for polydispersity in the Stokes flow regime, Beetstra et al. (2007) collectively referred to as BVK in this work, proposed a drag correlation for mono– and bi–disperse random arrays at higher

Reynolds numbers. Yin and Sundaresan (2009a) proposed a new drag correlation for Stokes flow in fixed assemblies of monodisperse spheres to account for particle–particle relative motion. All the computational drag laws for flow past random arrays of spheres discussed so far are based on the lattice Boltzmann code SUSP3D developed by Ladd (1994a,b).

In the SUSP3D code used by HKL and BVK, a spherical particle is represented by a stair–step lattice approximation and so the exact value of the particle diameter is not known *a priori*. The drag values obtained from SUSP3D simulations are assumed to correspond to an effective hydrodynamic diameter that is obtained *a posteriori* by calibrating the simulations against the analytical solution of Hasimoto (1959) for Stokes flow in a dilute simple cubic arrangement of spheres. This hydrodynamic diameter depends on the fluid viscosity as well as the particle size. So the momentum transfer at boundary lattice nodes does not correspond to the force density at the surface of the particle and the magnitude of this surface force density is calibrated. It must be noted here that recent developments in LBM have removed the need for calibrating the hydrodynamic diameter (Ginzburg and d’Humières, 2003). It has not been demonstrated that solutions obtained from SUSP3D reconcile with the random–field multiphase flow theory. Furthermore, in the study of BVK a constant grid resolution of 21.5 lattice units was used to simulate Reynolds numbers ranging from 21 to 1000 at a given volume fraction while the boundary layer thickness  $\delta$  reduces by 30–fold. The grid resolution should be increased with increasing Reynolds number to properly resolve the boundary layers as the boundary layer thickness  $\delta \sim D/\sqrt{\text{Re}_m}$ . This casts doubt on the accuracy of the monodisperse drag correlation proposed by BVK at higher Reynolds numbers.

In this work, we study the flow past fixed random assemblies of monodisperse spheres using PReIBM. We present a comprehensive set of drag data for mono and bidisperse gas–solid suspensions using an incompressible Navier–Stokes solver. The normalized average gas–solid force  $F$  is obtained as a function of solid volume fraction  $\phi$  ( $0.1 \leq \phi \leq 0.5$ ) and mean flow Reynolds number  $\text{Re}_m$  ( $0.01 \leq \text{Re}_m \leq 300$ ) for random assemblies of monodisperse spheres. Differences between the drag values obtained from PReIBM and the drag correlation of Beetstra et al. (2007) are as high as 30% for  $\text{Re}_m$  in the range 100–300. An improved correlation for  $F$  in terms of  $\phi$  and  $\text{Re}_m$  is proposed that corrects the existing correlations in  $\text{Re}_m$  range 100–300.

This new monodisperse drag correlation has been used to propose an improved polydisperse drag correlation.

#### 1.4.2 Quantifying the level of gas-phase velocity fluctuations

The transport of the second moment of fluctuating gas velocity (the gas-phase Reynolds stress) appears as an unclosed term in the mean momentum conservation equation of the gas phase. In industrial applications of gas-solids flow such as fluidized beds (Moran and Glicksman, 2003), the particle diameter  $D$  is usually larger than the Kolmogorov length scale  $\eta$ . However, the vast majority of existing work (Squires and Eaton, 1991; Elghobashi and Truesdell, 1993; Boivin et al., 1998; Sundaram and Collins, 1999; Mashayek and Taulbee, 2002) on particle-turbulence interaction addresses particles with  $D < \eta$ . There are relatively few studies (Uhlmann, 2008; Xu and Subramaniam, 2010; Lucci et al., 2011) for particles with  $D > \eta$ . Unlike in single-phase turbulence, the mean slip velocity is an important parameter in gas-solid flows with  $D > \eta$ . This is because the mean slip velocity results in an asymmetric pressure distribution around the particles and the also in the formation of boundary layers on particle surfaces. The pressure asymmetry in turn results in the formation of wakes behind the particles, which contribute to gas-phase velocity fluctuations even in “laminar” gas-solid flows. It is important to note that the gas-phase Reynolds stress is due to the inherent turbulent fluctuations in the gas-phase as well as the pseudo-turbulent velocity fluctuations arising due to the presence of particles. Since the mechanisms for the generation and dissipation of these fluctuations are different, it is important to distinguish the pseudo-turbulent gas-phase velocity fluctuations from the inherent turbulent fluctuations in the gas-phase. The gas-phase Reynolds stress arising from pseudo-turbulent velocity fluctuations has not been quantified over a range of solids volume fraction and Reynolds number based on the mean slip velocity between the solid and gas-phase. In the absence of such comprehensive quantification, the gas-phase Reynolds stress term is sometimes neglected in CFD simulations of dense gas-solid flow on the grounds that the dominant forces in the gas-phase momentum balance are the pressure drop and drag force (Hrenya and Sinclair, 1997). However, recent intrusive hot wire measurements have been performed (Moran and Glicksman, 2003) that indicate that the level of gas-phase velocity

fluctuations can be significant in a circulating fluidized bed riser at dilute solids volume fraction.

The gas-phase Reynolds stress arising from both turbulent and pseudo-turbulent velocity fluctuations, is usually modeled using an eddy viscosity model that accounts for the presence of solid particles (Ahmadi and Ma, 1990b,a; Bolio and Sinclair, 1995; Balzer et al., 1998; Benyahia et al., 2005). In order to use this model, the turbulent kinetic energy (TKE)  $k_f$  and the dissipation rate  $\varepsilon_f$  in the fluid phase have to be quantified. Because of the absence of such quantification, transport equations for  $k_f$  and  $\varepsilon_f$  are written by modifying the single-phase turbulence models. In particular the models used for the dissipation of turbulent kinetic energy are based on the Kolmogorov scaling ( $k_f^{3/2}/l_{\text{diss}}$ ) used in single-phase turbulence, but their validity in particle-laden flows is not verified.

For particles of size comparable to or larger than the Kolmogorov length scale, the appropriate numerical approach is the particle-resolved DNS methodology in which all the scales of the inherent turbulence and the flow scales introduced by the presence of large particles are resolved. In this work we use PReIBM DNS to quantify the strength of gas-phase velocity fluctuations in steady flow through a statistically homogeneous fixed assembly of monodisperse spheres. Using the data obtained from PReIBM DNS, we analyzed the implications for modeling the dissipation of kinetic energy in the gas-phase by considering the energy balance equation and proposed an eddy viscosity model to account for the transport of average gas-phase Reynolds stress.

#### 1.4.3 Develop a formulation to study convective heat transfer in gas-solid flow

Accurate prediction of the average fluid phase temperature is crucial for applications such as Chemical Looping Combustion (CLC). Average interphase heat transfer and transport of the the covariance of temperature and gas velocity are the unclosed terms that appear in the conservation equation of the average gas-phase temperature. The average interphase heat flux  $\langle Q_{g-s} \rangle$  is modeled in terms of an average Nusselt number and the difference between the average fluid and solid-phase temperature ( $\langle T^{(f)} \rangle - \langle T^{(s)} \rangle$ ) averaged. This Nusselt number is usually given by a correlation that depends only on solid volume fraction  $\phi$ , mean slip Reynolds number  $Re_m$  and the Prandtl number  $Pr$ . In applying this model for the average interphase heat flux

in gas–solid CFD codes, it is assumed that the heat transfer problem is locally homogeneous. The average Nusselt number and the average fluid and solid–phase temperatures are assumed to be constant in the grid cell. This implies that the fluid does not get heated up (or cooled down) as it flows past the solid particles. In this work we use particle–resolved direct numerical simulation (DNS) to show that fluid heating can become important, especially at high solid volume fraction and low mean flow Reynolds numbers, and hence the assumption of statistical homogeneity of the average temperature field may not be used. We develop a novel DNS methodology that gives a statistically homogeneous average Nusselt number, even though the temperature field is inhomogeneous.

#### **1.4.4 Effect of particle velocity distribution and closure at the level of the one–particle distribution function**

In the multifluid theory, the second moment of particle velocity represents the strength of particle velocity fluctuations. It is now established that the prediction of core–annular structure in riser flows requires solving the transport equation for the particle granular temperature (Hrenya and Sinclair, 1997). This informs us that a closure at the level of mean quantities is not adequate to predict important flow characteristics such as core–annular structure, but a closure at the level of second moments is necessary. An alternative approach to the closure of moment transport equations is to consider the evolution of the one–particle distribution function. Just as closure at the level of the transport equation for the probability density function (PDF) in single–phase turbulent reactive flow implies a closure for all moment equations, similarly a kinetic equation that achieves a closure for the one–particle distribution function in kinetic theory implies a closure for all moment equations. In particular, a closure at the one–particle distribution level automatically implies closure of the mean momentum and particle velocity second moment equations. Furthermore, closures at the one–particle distribution level are guaranteed to satisfy realizability criteria, whereas special care is needed to ensure the same in the case of moment closures. These considerations motivate the development of models for the unclosed terms in the transport equation for the one–particle distribution function corresponding to gas–solid flow. Such closures can also be used directly with Quadrature

Based Moment Methods (QBMM).

In statistically homogeneous suspensions undergoing elastic collisions, the particle acceleration–velocity covariance alone governs the evolution of granular temperature. This acceleration–velocity covariance can be decomposed into a source and dissipation of granular temperature due to hydrodynamic forces. Koch and co-workers (Koch, 1990; Koch and Sangani, 1999) quantified the hydrodynamic source and dissipation terms in the granular temperature evolution using a combination of kinetic theory closure and multipole expansion simulations at very low Reynolds numbers (Stokes flow regime). In this work, DNS of freely evolving gas–solid suspensions are performed using PReIBM. Analysis of DNS results shows that the fluctuations in the particle acceleration that are aligned with the fluctuations in the particle velocity give rise to source in the granular temperature. It is found that simple extension of a class of mean particle acceleration models to their corresponding instantaneous versions does not predict the correct joint acceleration–velocity statistics that are obtained from DNS. Also such models do not give rise to any source in the granular temperature due to hydrodynamic effects. It is found that a Langevin equation for the increment in the particle velocity reproduces the DNS results for particle velocity autocorrelation in freely evolving suspensions. Modeling the increment in the particle velocity using a Langevin equation implies a closure for the evolution of the one-particle distribution function in terms of the Fokker–Planck equation. Particle–resolved simulations of freely evolving gas–solid suspensions are performed over a range of solid volume fraction ( $0.1 \leq \phi \leq 0.4$ ), Reynolds number based on the slip velocity between the solid and the fluid–phase ( $10 \leq \text{Re}_m \leq 100$ ) and solid to fluid density ratio ( $100 \leq \frac{\rho_p}{\rho_f} \leq 2000$ ). Based on the data obtained from the simulations, correlations for the model coefficients are proposed.

#### 1.4.5 Particle–resolved DNS on peta scale computers

Gas–solid flows exhibit several multiscale phenomenon such as formation of particle clusters and streamers. Such phenomenon can be studied using particle–resolved DNS by performing simulations in large computational domains. Therefore, there is a need to perform these highly resolved simulations on peta scale super computers in order to obtain detailed information on the mechanism of formation of particle clusters. In this work we developed a strategy for

the parallelization of PReIBM on the petascale computer Jaguarpf at Oak Ridge Leadership Computing Facility (OLCF). Several test cases are presented that confirm the accuracy of the parallel solver. An idealized riser with a solid volume fraction of 1% has been chosen to assess the weak scaling behavior of the solver. The parallel PReIBM solver shows an excellent scaling with increasing number of processors.

## 1.5 Report outline

The description of the PReIBM methodology and the development of the monodisperse drag correlation are described in chapter 2. Quantification of the gas-phase velocity fluctuations and modeling of the average gas-phase Reynolds stress is discussed in chapter 3. Chapter 4 describes the PR-DNS formulation to study heat transfer in gas-solid flow. The PR-DNS methodology to perform simulations of freely evolving suspensions is presented in chapter 5, while the details of the particle acceleration model are given in chapter 6. Quantification of interphase momentum transfer and the level of gas-phase velocity fluctuations in fixed and freely evolving polydisperse gas-solid flow is described in chapter 7. Details of the parallelization strategy are given in chapter 8 and the current effort towards characterizing the stability of gas-solid flows and possible future work is presented in chapter 9.

## CHAPTER 2. Drag law for monodisperse gas–solid systems using particle–resolved direct numerical simulation of flow past fixed assemblies of spheres

This chapter is an article (Tenneti et al., 2011) titled “Drag law for monodisperse gas–solid systems using particle–resolved direct numerical simulation of flow past fixed assemblies of spheres” published in the International Journal of Multiphase Flows’. This article is authored by S. Tenneti, R. Garg and S. Subramaniam.

### Abstract

Gas–solid momentum transfer is a fundamental problem that is characterized by the dependence of normalized average fluid–particle force  $F$  on solid volume fraction  $\phi$  and the Reynolds number based on the mean slip velocity  $Re_m$ . In this work we report particle–resolved direct numerical simulation (DNS) results of interphase momentum transfer in flow past fixed random assemblies of monodisperse spheres with finite fluid inertia using a continuum Navier–Stokes solver. This solver is based on a new formulation we refer to as the Particle–resolved Uncontaminated–fluid Reconcilable Immersed Boundary Method (PUREIBM). The principal advantage of this formulation is that the fluid stress at the particle surface is calculated directly from the flow solution (velocity and pressure fields), which when integrated over the surfaces of all particles yields the average fluid–particle force. We demonstrate that PUREIBM is a consistent numerical method to study gas–solid flow because it results in a force density on particle surfaces that is reconcilable with the averaged two–fluid theory. The numerical convergence and accuracy of PUREIBM are established through a comprehensive suite of validation tests. The normalized average fluid–particle force  $F$  is obtained as a function of solid volume

fraction  $\phi$  ( $0.1 \leq \phi \leq 0.5$ ) and mean flow Reynolds number  $Re_m$  ( $0.01 \leq Re_m \leq 300$ ) for random assemblies of monodisperse spheres. These results extend previously reported results of Hill et al. (2001a,b) to a wider range of  $\phi$ ,  $Re_m$ , and are more accurate than those reported by Beetstra et al. (2007). Differences between the drag values obtained from PReIBM and the drag correlation of Beetstra et al. (2007) are as high as 30% for  $Re_m$  in the range 100-300. We take advantage of PReIBM's ability to directly calculate the relative contributions of pressure and viscous stress to the total fluid-particle force, which is useful in developing drag correlations. Using a scaling argument, Hill et al. (2001b) proposed that the viscous contribution is independent of  $Re_m$  but the pressure contribution is linear in  $Re_m$  (for  $Re_m > 50$ ). However, from PReIBM simulations we find that the viscous contribution is not independent of the mean flow Reynolds number, although the pressure contribution does indeed vary linearly with  $Re_m$  in accord with the analysis of Hill et al. (2001b). An improved correlation for  $F$  in terms of  $\phi$  and  $Re_m$  is proposed that corrects the existing correlations in  $Re_m$  range 100-300. Since this drag correlation has been inferred from simulations of fixed particle assemblies, it does not include the effect of mobility of the particles. However, the fixed-bed simulation approach is a good approximation for high Stokes number particles, which are encountered in most gas-solid flows. This improved drag correlation can be used in CFD simulations of fluidized beds that solve the average two-fluid equations where the accuracy of the drag law affects the prediction of overall flow behavior.

## 2.1 Introduction

Gas-solid flows occur in many industrial applications such as energy generation, as well as food, chemical, and pharmaceutical processing. A fundamental understanding of gas-solid flows continues to be important, especially due to increasing interest in technologies such as carbon-neutral energy generation (Azar et al., 2006), chemical looping combustion (Shen et al., 2008), and CO<sub>2</sub> capture from flue gases using dry sorbents (Yi et al., 2007; Abanades et al., 2004).

Computational fluid dynamics (CFD) simulations (Syamlal et al., 1993; Kashiwa and Gaffney, 2003; Sun et al., 2007) that solve the averaged equations of multiphase flow are increasingly be-

ing used as an efficient alternative for design optimization because experiments are often costly and time-consuming. CFD simulations of multiphase flow are based on either the Lagrangian–Eulerian (LE) or the Eulerian–Eulerian (EE) two–fluid approach (Anderson and Jackson, 1967; Drew and Passman, 1998). In the EE approach that forms the basis for popular gas–solid CFD codes (Syamlal et al., 1993; Kashiwa and Gaffney, 2003), averaged equations for mass, momentum and energy are written for both the solid and fluid phases, with coupling terms that represent interphase interactions. These coupling terms are unclosed and need to be modeled. For instance, the mean momentum conservation equation in the particle phase requires closure of the average fluid–particle interaction force (mean drag force) in terms of average quantities like the solids volume fraction  $\phi$  and the mean flow Reynolds number  $Re_m$ . This closure for the average fluid–particle force is popularly known as a “drag law” and is typically obtained from a combination of theoretical, experimental and computational studies.

Several studies (Bokkers et al., 2004; Benyahia et al., 2005; Leboireiro et al., 2008) point out the importance of the fluid–particle drag in determining the characteristics of monodisperse fluidized beds. Patil et al. (2005) observe that the prediction of injected bubbles in a bubbling, gas–fluidized bed operated by a jet depends on the choice of the drag law. Also, drag laws for polydisperse gas–solid suspensions are based on the drag law for an equivalent monodisperse suspension (van der Hoef et al., 2005; Beetstra et al., 2007; Yin and Sundaresan, 2009a,b; Holloway et al., 2010). Therefore, the predictive capability of CFD simulations of polydisperse gas–solid suspensions depend on the accuracy of the monodisperse drag law. Besides CFD simulations, the functional dependence of drag on volume fraction is important in the stability analysis of the two–fluid equations and in predicting the stability limits of fluidized beds (Koch, 1990; Koch and Sangani, 1999).

Theoretical studies to predict the average fluid–particle force or the drag force are limited to dilute solid volume fractions and low mean flow Reynolds numbers (Stokes flow regime). Hasegawa (1959) obtained an expression for the drag force in Stokes flow past dilute ordered arrangement of spheres by deriving periodic fundamental solutions of the Stokes equations. Later Sangani and Acrivos (1982) calculated the drag force in Stokes flow past ordered arrays of spheres over the complete range of volume fraction. In the Stokes flow regime, the Kozeny–Carman

relation (Carman, 1937) is widely used for packed beds of monodisperse spherical particles. At low Reynolds numbers Hill et al. (2001a) used lattice Boltzmann simulations to propose an expression for the drag force in random arrangements of spheres that is valid at all volume fractions.

At higher Reynolds numbers the nonlinearity of the governing Navier–Stokes equations together with the randomness in particle configurations make the theoretical analysis of this problem very difficult. Widely used closures for the average fluid–particle force in engineering practice are either obtained from pressure drop measurements in packed beds (Ergun, 1952) or measurements of terminal velocity in sedimenting suspensions (Richardson and Zaki, 1954). A limitation of these studies is that they are applicable only in the dense regime. Another closure equation for the drag force that is widely used in CFD simulations of gas–solid flow is given by Wen and Yu (1966). This drag correlation is convenient to use in CFD simulations where a range of solid volume fractions and Reynolds numbers are encountered within the computational domain. Further modifications to the Wen–Yu equation are proposed by various researchers (Gidaspow, 1986; Syamlal and O’Brien, 1987).

The exponential rise of computing power and advances in numerical methods have made it possible to perform detailed and accurate numerical simulations of flow past random particle assemblies at higher Reynolds numbers. Particle–resolved direct numerical simulation (DNS) is a first–principles approach to developing accurate models for interphase momentum transfer in gas–solids flow. Since DNS solves the governing Navier–Stokes (NS) equations with exact boundary conditions at each particle surface, it produces a model–free solution with complete three–dimensional time–dependent velocity and pressure fields.

Recently, a variety of numerical approaches have been developed for particle–resolved DNS. These can be broadly classified as those that rely on a body–fitted mesh to impose boundary conditions at particle surfaces, and those that employ regular Cartesian grids. The body–fitted methods include the arbitrary Lagrangian Eulerian (ALE) approach (Hu et al., 2001; Nomura and Hughes, 1992) as well as the method used by Balachandar and co–workers (Bagchi and Balachandar, 2003, 2004). Also Burton and Eaton (2005) used the overset grid technique to study the interaction between a fixed particle and decaying homogeneous isotropic turbulence.

The principal disadvantage with approaches based on body-fitted meshes is that repeated re-meshing and solution projection are required for moving interfaces.

For methods that employ regular Cartesian grids this need for re-meshing and projection is eliminated, resulting in much faster solution times for moving particle simulations. Even for fixed particle assemblies, the wide range of parameters encountered in gas–solids flow and the need to perform multiple independent simulations (MIS) (due to the random arrangements of the particles) makes it impractical to use body–fitted meshes. However, because the grid does not conform to the particle surface, special attention is needed to generate an accurate solution. Popular methods based on regular Cartesian grids include the fictitious domain method, the lattice Boltzmann method (LBM), and the immersed boundary method (IBM). The fictitious domain method with Lagrange multipliers has been developed to solve flow past many moving particles by several research groups (Patankar et al., 2000; Glowinski et al., 2001; Sharma and Patankar, 2005; Apte et al., 2009). LBM has been used to simulate flow through a fixed bed of spheres (Hill et al., 2001a,b; van der Hoef et al., 2005; Beetstra et al., 2007). and for particulate flows (Ladd and Verberg, 2001; Ten Cate et al., 2004). The immersed boundary method first proposed by Peskin (1981) is used to simulate flexible boundaries in a flow field. More recently, several researchers (Uhlmann, 2005; Yusof, 1996; Garg, 2009; Kim and Choi, 2006; Lucci et al., 2010) have modified IBM to study the interaction between flow and rigid particles. Besides these widely used techniques, there are other methods such as PHYSALIS (Oguz and Prosperetti, 2001; Takagi et al., 2005; Zhang and Prosperetti, 2003, 2005) that use a general analytic solution of the Stokes equation in the flow domain close to particle boundaries to impose the no-slip velocity boundary condition on the particle surface. In this work we describe a particle–resolved DNS methodology based on the immersed boundary method.

In order to specify a closure for the interphase momentum transfer term, it is natural to simulate a statistically homogeneous suspension flow with freely moving particles and to then compute volume–averaged estimates of the average fluid–particle force from the particle acceleration data. Imposing a pressure gradient that balances the weight of the suspension leads to a steady momentum balance. In this setup the particle positions and velocities sample a trajectory in the phase space that corresponds to the specified non–equilibrium steady state of

the system. However, such freely moving suspensions are computationally prohibitive because in order to propose drag laws these simulations need to be performed over a range of solid volume fractions and mean flow Reynolds numbers. However, we note that the Stokes numbers encountered in typical gas–solid flow applications (e.g., coal particles in air) are usually very high ( $\sim O(10^5)$ ). A convenient simplification for high Stokes number suspensions is to replace the ensemble of particle positions and velocities sampled by the system in its nonequilibrium steady state, by a set of particle configurations and velocities that would result from a granular gas simulation. Steady flow is simulated past fixed assemblies of particles in configurations (and with velocities) sampled from this set, and drag laws are obtained by averaging over this ensemble. The idea of extracting computational drag laws from steady flow past fixed random assemblies of spheres has been successfully exploited by several researchers (Hill et al., 2001a,b; van der Hoef et al., 2005; Beetstra et al., 2007).

Hill, Koch and Ladd (Hill et al., 2001a,b) referred to collectively as HKL from hereon, studied the steady flow past ordered and random arrays of monodisperse spheres. While van der Hoef et al. (2005) extended HKL’s LBM simulations to account for polydispersity in the Stokes flow regime, Beetstra et al. (2007) collectively referred to as BVK from hereon, proposed a drag correlation for mono– and bi–disperse random arrays at higher Reynolds numbers. Yin and Sundaresan (2009a) proposed a new drag correlation for Stokes flow in fixed assemblies of monodisperse spheres to account for particle–particle relative motion. All the computational drag laws for flow past random arrays of spheres discussed so far are based on the lattice Boltzmann code SUSP3D developed by Ladd (1994a,b).

It is worthwhile to examine the requirements that any particle–resolved DNS approach should satisfy for specifying a closure for the average interphase momentum transfer term in gas–solids flow. One of these requirements is the consistency of the DNS approach with the two–fluid theory of multiphase flow. On each realization of a multiphase flow, the fluid stress at the particle surfaces generates a surface force density  $\tau_{ji}n_j\delta(\mathbf{x} - \mathbf{x}^{(I)})$  where,  $\boldsymbol{\tau}$  is the fluid stress tensor and  $\mathbf{n}$  is the normal vector pointing into the fluid at a point  $\mathbf{x}^{(I)}$  on the particle surface. A similar term appears in the so called whole–domain formulation (Scardovelli and Zaleski, 1999). Averaging over several realizations (particle configurations) results in the

expected value of the surface force density which is the average interphase momentum transfer term  $\langle \tau_{ji} n_j \delta(\mathbf{x} - \mathbf{x}^{(I)}) \rangle$  appearing in the two-fluid theory (Drew, 1983). Consistency of DNS approach with two-fluid theory requires that the method used to estimate the surface force density in the DNS should be consistent with the definition of the average interphase momentum transfer term. Otherwise, the model (drag law) inferred from DNS may not be consistent with the EE equations that arise from the two-fluid theory.

In the SUSP3D code used by HKL and BVK, a spherical particle is represented by a stair-step lattice approximation and so the exact value of the particle diameter is not known *a priori*. The drag values obtained from SUSP3D simulations are assumed to correspond to an effective hydrodynamic diameter that is obtained *a posteriori* by calibrating the simulations against the analytical solution of Hasimoto (1959) for Stokes flow in a dilute simple cubic arrangement of spheres. This hydrodynamic diameter depends on the fluid viscosity as well as the particle size. So the momentum transfer at boundary lattice nodes does not correspond to the force density at the surface of the particle and the magnitude of this surface force density is calibrated. It has not been demonstrated that solutions obtained from SUSP3D reconcile with the random-field multiphase flow theory. It must be noted here that recent developments in LBM have removed the need for calibrating the hydrodynamic diameter (Ginzburg and d’Humières, 2003).

Another requirement of a particle-resolved DNS approach is to ensure that the simulation approach results in grid independent solutions. If we take steady incompressible flow past a single particle at a specified  $Re_m$ , then the flow solution and drag force should converge as the grid is progressively refined. It is not established by HKL or BVK that for a given physical problem corresponding to a fixed  $Re_m$  and fixed level of compressibility their simulations result in numerically converged solutions as the lattice spacing is reduced progressively.

In any particle-resolved DNS approach, the grid resolution should be increased with increasing Reynolds number to properly resolve the boundary layers as the boundary layer thickness  $\delta \sim D/\sqrt{Re_m}$ . Respecting the resolution restrictions of LBM, HKL simulated only unto a Reynolds number of 100 and progressively refined their grid with increasing Reynolds numbers. However, BVK used a constant grid resolution of 21.5 lattice units to simulate Reynolds numbers ranging from 21 to 1000 at a given volume fraction while the boundary layer thickness

$\delta$  reduces by 30-fold. Clearly, the boundary layers cannot be resolved at this resolution.

Besides consistency and numerical convergence, it is necessary to ensure that the simulation setup using which the drag law is inferred corresponds to a Galilean-Invariant (GI) transformation of the original physical problem. Moreover, any DNS code used to infer the drag law should ensure that the total fluid-particle force obtained by solving the physical problem in various GI simulation setups should be the same. We discuss the various GI simulation setups to extract computational drag laws in section 2.7 and show that PReIBM gives the same solution for all GI setups. We also show that using a non-GI simulation setup leads to erroneous results and these errors are compounded with increasing Reynolds numbers.

In this work, we study the flow past fixed random assemblies of monodisperse spheres using a Particle-resolved Uncontaminated-fluid Reconcilable Immersed Boundary Method (PReIBM). We present a comprehensive set of drag data for monodisperse gas-solid suspensions using an incompressible NS solver. In PReIBM flow solution is obtained on a structured Cartesian grid but, the particle surface is discretized in spherical coordinates and the total force exerted by the fluid on the particle is computed directly from the stress tensor at the particle surface. This feature enables us to compare the DNS solution with any random-field theory of multiphase flow. In section 2.2 we derive the ensemble-averaged two-fluid equations and in section 2.3 we show that the numerical equations solved in PReIBM are consistent and can be reconciled with the equations of two-fluid theory. We describe the simulation methodology and the relevant numerical parameters in section 2.4. In section 2.5 we establish the spatial and temporal convergence of PReIBM solutions. The PReIBM solver is validated for several test cases in section 2.6. We compare various Galilean Invariant simulation setups that can be used to extract computational drag laws in section 2.7 and show that PReIBM results in a Galilean Invariant solution to the physical problem of flow past a fixed assembly of spheres. In section 2.8.1 we compare the average fluid-particle force and the velocity and pressure fields obtained from PReIBM simulation of flow past a random configuration of spheres ( $\phi = 0.4$  and  $Re_m = 100$ ) with those obtained from solving the same problem with a body-fitted grid using the ANSYS-FLUENT CFD package.

As discussed earlier, in PReIBM the force acting on the sphere is computed by integrating

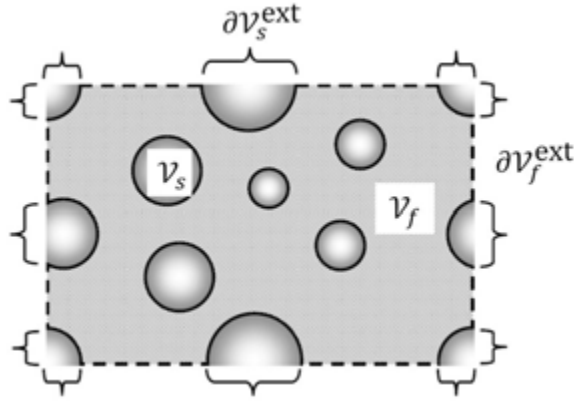


Figure 2.1 A schematic of a realization of gas-solid flow showing a statistically homogeneous assembly of particles in a representative region  $\mathcal{V}$ , bounded by surface  $\partial\mathcal{V}$ . The region  $\mathcal{V}$  is composed of the region  $\mathcal{V}_f$  occupied by the fluid phase that is bounded by the surface  $\partial\mathcal{V}_f$ , and the region  $\mathcal{V}_s$  occupied by the solid phase that is bounded by the surface  $\partial\mathcal{V}_s$ , such that  $\mathcal{V} = \mathcal{V}_s \cup \mathcal{V}_f$ . The boundary  $\partial\mathcal{V}$  is decomposed as  $\partial\mathcal{V} = \partial\mathcal{V}_s^{\text{ext}} \cup \partial\mathcal{V}_f^{\text{ext}}$ , where  $\partial\mathcal{V}_s^{\text{ext}} = \partial\mathcal{V} \cap \partial\mathcal{V}_s$  (shown by curly braces) is the domain boundary cut by the solid particles, and  $\partial\mathcal{V}_f^{\text{ext}} = \partial\mathcal{V} \cap \partial\mathcal{V}_f$  (shown by dashed lines) is the remaining domain boundary. The boundary of the solid-phase can be expressed as the union of external and internal boundaries  $\partial\mathcal{V}_s = \partial\mathcal{V}_s^{\text{ext}} \cup \partial\mathcal{V}_s^{\text{int}}$ , where  $\partial\mathcal{V}_s^{\text{int}}$  (shown by solid lines) is the bounding surface of the solid particles in contact with the fluid. Similarly, the boundary of the fluid-phase can be expressed as  $\partial\mathcal{V}_f = \partial\mathcal{V}_f^{\text{ext}} \cup \partial\mathcal{V}_f^{\text{int}}$ .

the pressure and viscous stresses separately over the particle surface and it is possible to investigate their relative contributions to the drag force. In section 2.8.2 we discuss the normalized pressure and viscous contributions to the total drag and their dependence on volume fraction and mean flow Reynolds number. We also investigate the local profiles of pressure and viscous forces along the surface of the sphere. A new correlation for the average fluid-particle force in random arrays of monodisperse spheres is presented in section 2.9. Finally, section 2.10 summarizes the principal findings of this work.

## 2.2 Governing Equations

A schematic describing the problem of flow past a random assembly of particles is shown in figure 2.1.

For incompressible flows, the mass and momentum conservation equations for the fluid-phase are

$$\frac{\partial u_i}{\partial x_i} = 0, \quad (2.1)$$

and

$$\rho_f \frac{\partial u_i}{\partial t} + \rho_f \frac{\partial u_i u_j}{\partial x_j} = -g_i + \frac{\partial \tau_{ji}}{\partial x_j}, \quad (2.2)$$

respectively, where  $\rho_f$  is the thermodynamic density of the fluid-phase. In (2.2),  $\mathbf{g}$  represents the body forces (hydrostatic pressure gradient, acceleration due to gravity etc) acting throughout the volume of an infinitesimal fluid element, while  $\boldsymbol{\tau}$  represents the surface stresses (both pressure and viscous stresses) acting on the surface of an infinitesimal fluid element, so that

$$\frac{\partial \tau_{ji}}{\partial x_j} = -g'_i + \mu_f \frac{\partial^2 u_i}{\partial x_j \partial x_j} \quad (2.3)$$

where,  $\mu_f$  is the dynamic viscosity of the fluid and  $\mathbf{g}'$  is the gradient in the pressure acting on the surface of a fluid element. At the particle-fluid interface, the no-slip and no-penetration (for impermeable surfaces) boundary conditions require the relative velocity between fluid and solid to be zero. We note that equations (2.1) and (2.2) together with the boundary conditions are true for a single realization of a gas-solid flow, and are valid only in the region  $\mathcal{V}_f$  occupied by the fluid.

It is worthwhile to derive equations that are valid in the whole region  $\mathcal{V}$  because such equations are the starting point for the derivation of ensemble-averaged equations. Since particle-resolved DNS methods that employ Cartesian grids solve the governing equations in the entire computational domain, we can relate the numerical formulation with the governing equations that are valid in the entire physical domain.

The momentum conservation equation valid in the entire domain is obtained by multiplying equation (2.2) by the fluid-phase indicator function  $I_f(\mathbf{x}, t)$  which is unity if the point  $\mathbf{x}$  lies in the fluid-phase and zero otherwise. The indicator function obeys the topological equation (Drew, 1983):

$$\frac{\partial I_f}{\partial t} + U_j^{(I)} \frac{\partial I_f}{\partial x_j} = 0 \quad (2.4)$$

where,  $\mathbf{U}^{(I)}$  is the velocity of the fluid-particle interface. This equation simply states that the indicator function is convected by the velocity of the fluid-particle interface. Using the

topological equation (2.4) and multiplying (2.2) with  $I_f$  one obtains:

$$\rho_f \frac{\partial I_f u_i}{\partial t} + \rho_f \frac{\partial I_f u_i u_j}{\partial x_j} = -I_f g_i + \rho_f u_i \left( u_j - U_j^{(I)} \right) \frac{\partial I_f}{\partial x_j} + \frac{\partial I_f \tau_{ji}}{\partial x_j} - \tau_{ji} \frac{\partial I_f}{\partial x_j}. \quad (2.5)$$

The second term on the right hand side of (2.5) represents momentum source due to the difference between the interface velocity and the velocity of the fluid at the fluid–particle interface, which occurs in two–phase flows with interphase mass transfer, e.g. vaporization. Since we consider gas–solids flow with no mass transfer at the interface, this term is zero. The gradient of the indicator function  $\partial I_f / \partial x_j$  can be expressed as  $-n_j^{(f)} \delta(\mathbf{x} - \mathbf{x}^{(I)})$  (Drew, 1983), where  $\mathbf{n}^{(f)}$  is the unit normal vector pointing outward from the fluid surface into the particle, and  $\delta(\mathbf{x} - \mathbf{x}^{(I)})$  is a generalized delta function<sup>1</sup> at the fluid–particle interface  $\mathbf{x}^{(I)}$ . Substituting the definition of the gradient of the indicator function into (2.5), the momentum conservation equation valid in the entire domain is:

$$\rho_f \frac{\partial I_f u_i}{\partial t} + \rho_f \frac{\partial I_f u_i u_j}{\partial x_j} = -I_f g_i + \frac{\partial I_f \tau_{ji}}{\partial x_j} - \tau_{ji} n_j^{(s)} \delta(\mathbf{x} - \mathbf{x}^{(I)}). \quad (2.6)$$

In the above equation  $\mathbf{n}^{(s)}$  is the normal vector pointing outward from the particle surface into the fluid, i.e.  $\mathbf{n}^{(s)} = -\mathbf{n}^{(f)}$ . The last term on the right hand side of (2.6) namely,  $-\tau_{ji} n_j^{(s)} \delta(\mathbf{x} - \mathbf{x}^{(I)})$  is the surface force density and it represents momentum transfer at the fluid–particle interface. We will show in the following section that the average of the surface force density appears as an unclosed term in the ensemble–averaged equations that can be quantified by particle–resolved DNS. Equation (2.6) is similar to the momentum conservation equation solved in the whole–domain formulation of Scardovelli and Zaleski (1999). There are several ways to solve (2.6) and particle–resolved DNS methodologies differ in the procedure used to compute the surface force density. We now derive the ensemble–averaged two–fluid equations corresponding to mass and momentum conservation and identify the unclosed terms.

### 2.2.1 Ensemble–averaged two–fluid equations

In the Eulerian two–fluid theory, phasic averages are defined as averages conditional on the presence of fluid or solid phase. If  $Q(\mathbf{x}, t)$  is any field, then its phasic average  $\langle Q^{(f)} \rangle(\mathbf{x}, t)$

<sup>1</sup>The generalized delta function  $\delta^{(d),(k)}(\mathbf{x} - \mathbf{x}^{(I)})$  allows the representation in  $\mathcal{R}^{(d)}$  of quantities defined in  $\mathcal{R}^{(k)}$ ,  $k < d$ . The dimensions of the generalized delta functions are  $L^{k-d}$ . In this case  $d = 3$  and  $k = 2$ , so the delta function has dimensions  $L^{-1}$  and hence it allows the surface force density to be written as an interphase momentum transfer term in  $\mathcal{R}^{(3)}$ .

referred to as its fluid-phase mean, is defined as:

$$\langle Q^{(f)} \rangle (\mathbf{x}, t) = \frac{\langle I_f(\mathbf{x}, t) Q(\mathbf{x}, t) \rangle}{\langle I_f(\mathbf{x}, t) \rangle} \quad (2.7)$$

where  $I_f$  is the indicator function described earlier. The solid-phase mean  $\langle Q^{(s)} \rangle (\mathbf{x}, t)$  is similarly defined.

The mean momentum conservation equation in the fluid phase (Drew, 1983; Pai and Subramaniam, 2009) can be derived by ensemble-averaging (2.6) resulting in

$$\begin{aligned} \frac{\partial}{\partial t} \left\{ \rho_f (1 - \phi) \langle u_i^{(f)} \rangle \right\} + \frac{\partial}{\partial x_j} \left\{ \rho_f (1 - \phi) \langle u_i^{(f)} \rangle \langle u_j^{(f)} \rangle \right\} \\ = - (1 - \phi) \langle g_i^{(f)} \rangle - \frac{\partial}{\partial x_j} \left\{ \rho_f \langle I_f u_i^{(f)} u_j^{(f)} \rangle \right\} \\ + \left\langle \frac{\partial I_f \tau_{ji}}{\partial x_j} \right\rangle - \left\langle \tau_{ji} n_j^{(s)} \delta(\mathbf{x} - \mathbf{x}^{(I)}) \right\rangle, \end{aligned} \quad (2.8)$$

where,  $u_i^{(f)} = u_i - \langle u_i^{(f)} \rangle$  denotes the fluctuations in the fluid velocity field with respect to the phase-averaged fluid velocity and  $\phi = \langle I_s \rangle$  is the average volume fraction of the solid phase and  $(1 - \phi)$  is the average volume fraction of the fluid phase. The terms on the right hand side are the average body force density, the transport of fluid-phase velocity fluctuations, and the average interphase momentum transfer respectively, of which the last two are the unclosed terms that need to be modeled.

In this work we perform particle-resolved DNS of statistically homogeneous suspensions to model the average interphase momentum transfer. For a statistically homogeneous suspension the average quantities do not depend on  $\mathbf{x}$  and hence the convective term on the left hand side of (2.8), and the transport of fluid-phase velocity fluctuations on the right hand side are zero. Therefore, the phasic averaged fluid velocity evolves as:

$$\frac{\partial}{\partial t} \left\{ \rho_f (1 - \phi) \langle u_i^{(f)} \rangle \right\} = - (1 - \phi) \langle g_i^{(f)} \rangle - \left\langle \tau_{ji} n_j^{(s)} \delta(\mathbf{x} - \mathbf{x}^{(I)}) \right\rangle. \quad (2.9)$$

The mean fluid velocity reaches a steady state when the average interphase momentum transfer balances the body forces like gravity or an imposed pressure gradient:

$$(1 - \phi) \langle g_i^{(f)} \rangle = - \left\langle \tau_{ji} n_j^{(s)} \delta(\mathbf{x} - \mathbf{x}^{(I)}) \right\rangle. \quad (2.10)$$

As noted earlier  $\langle \tau_{ji} n_j^{(s)} \delta(\mathbf{x} - \mathbf{x}^{(I)}) \rangle$  is the unclosed average interphase momentum transfer. We now describe how this quantity can be computed from solution of flow past statistically homogeneous suspensions using particle-resolved DNS.

### 2.2.2 Quantifying average interphase momentum transfer from particle-resolved DNS

In particle-resolved DNS, statistically homogeneous suspension is approximated by flow past a random configuration of particles in a periodically repeating unit cell. Let  $\mathbf{u}(\mathbf{x}, t; \omega)$  be the velocity field obtained from particle-resolved DNS of flow past a random configuration of particles represented by the positions and velocities  $\{\mathbf{X}^{(i)}, \mathbf{V}^{(i)}, i = 1, \dots, N_p\}$  of  $N_p$  particles. This configuration represents a realization  $\omega$  in the sample space  $\Omega$  of all possible configurations. The ensemble-averaged velocity field or the mathematical expectation is defined as (Subramaniam, 2000):

$$\langle \mathbf{u} \rangle(\mathbf{x}, t) = \int_{\Omega} \mathbf{u}(\mathbf{x}, t; \omega) dP_{\omega}, \quad (2.11)$$

where  $P_{\omega}$  is the probability measure that is defined on  $\Omega$ . If the flow is statistically homogeneous, ensemble-averaged quantities can be approximated by taking the volumetric mean of the solution fields, e.g. the volumetric mean of the velocity field over the fluid region is defined as:

$$\langle \mathbf{u}^{(f)} \rangle_{\mathcal{V}}(t; \omega) = \frac{1}{V_f} \int_{\mathcal{V}} I_f(\mathbf{x}, t; \omega) \mathbf{u}(\mathbf{x}, t; \omega) dV, \quad (2.12)$$

where  $V_f$  is the volume of the region occupied by the fluid-phase. The volumetric mean approaches the ensemble average in the limit of infinite box size (i.e.,  $V \rightarrow \infty$ ). A reasonable approximation is obtained with finite box size provided the two-point correlations in the particle and the fluid phases decay to zero within the box length<sup>2</sup>. However, in order to account for the statistical variability arising from different particle configurations, we require very large box sizes. Especially for dilute suspensions, since average quantities in the particle phase

<sup>2</sup>This is simply the two-phase extension of the criterion given by Pope (2000) for single-phase turbulent flows.

(such as the average fluid–particle force) converge to their expected values as  $1/\sqrt{N_P}$ , this requirement can be computationally prohibitive. In order to accurately estimate the ensemble–averaged interphase momentum transfer from finite box sizes, two approaches are available: (i) simulate freely evolving suspensions and use time–averaging to calculate estimates with statistically stationary flows or, (ii) simulate fixed particle assemblies and average over different configurations. The choice of approach depends on the nature of the problem.

For fixed particle assemblies, the ensemble–average can be estimated by averaging over different configurations or realizations i.e.,

$$\left\{ \mathbf{u}^{(f)} \right\}_{\mathcal{V}, \mathcal{M}}(t) = \frac{1}{\mathcal{M}} \sum_{\mu=1}^{\mathcal{M}} \left\langle \mathbf{u}^{(f)} \right\rangle_{\mathcal{V}}(t; \omega_{\mu}). \quad (2.13)$$

In the above equation  $\left\{ \mathbf{u}^{(f)} \right\}_{\mathcal{V}, \mathcal{M}}$  denotes an estimate to the true expectation  $\left\langle \mathbf{u}^{(f)} \right\rangle$  and  $\mathcal{M}$  denotes the number of independent configurations. For freely evolving suspensions of statistically stationary flow, the ensemble–averaged quantities can be estimated using time–averaging:

$$\left\{ \mathbf{u}^{(f)} \right\}_{\mathcal{V}, T} = \frac{1}{T} \int_{t_0}^{t_0+T} \left\langle \mathbf{u}^{(f)} \right\rangle_{\mathcal{V}}(t'); dt'. \quad (2.14)$$

In either case, the evolution equation for the volumetric mean fluid velocity can be derived by integrating (2.6) over the entire region  $\mathcal{V}$  to give:

$$\begin{aligned} \rho_f V_f \frac{d \left\langle u_i^{(f)} \right\rangle_{\mathcal{V}}}{dt} + \rho_f \oint_{\partial \mathcal{V}} (I_f u_i u_j) n_j dA = - V_f \left\langle g_i^{(f)} \right\rangle_{\mathcal{V}} + \oint_{\partial \mathcal{V}} (I_f \tau_{ji}) n_j dA \\ - \oint_{\partial \mathcal{V}^{\text{int}}} \tau_{ji} n_j^{(s)} dA \end{aligned} \quad (2.15)$$

where  $\mathbf{n}$  is the unit normal vector pointing away from the domain. In deriving the above equation, we used the Gauss–divergence theorem and properties of the gradient of the indicator function under the integral operator (Drew, 1983). The second term on the left hand side denotes the net convective flux entering the domain while the second term on the right hand side side denotes the net diffusive flux and surface pressure acting on the domain. Due to periodic boundaries these terms are zero. Thus the conservation of momentum averaged over the fluid region reads:

$$\rho_f (1 - \phi) \frac{d \left\langle u_i^{(f)} \right\rangle_{\mathcal{V}}}{dt} = - (1 - \phi) \left\langle g_i^{(f)} \right\rangle_{\mathcal{V}} - \frac{1}{V} \oint_{\partial \mathcal{V}^{\text{int}}} \tau_{ji} n_j^{(s)} dA. \quad (2.16)$$

In writing this equation we used the property that for a statistically homogeneous suspension, the volume fraction of the fluid phase is given by  $(1 - \phi) = V_f/V$ . The volumetric mean fluid velocity attains a steady value when the surface stresses acting on the fluid–particle interface balance the body forces i.e.,

$$(1 - \phi) \langle g_i^{(f)} \rangle_{\mathcal{V}} = -\frac{1}{V} \oint_{\partial\mathcal{V}^{\text{int}}} \tau_{ji} n_j^{(s)} dA. \quad (2.17)$$

Equation (2.17) is the DNS counterpart of the ensemble–averaged momentum balance (2.10), and it is clear that under the assumption of statistical homogeneity the average interphase momentum transfer term can be estimated using the volumetric mean of surface stresses. We now describe how this momentum balance is accomplished for flow past fixed particle assemblies neglecting the effect of gravity. The corresponding formulation for flow past freely evolving gas–solid suspensions has been discussed by Tenneti et al. (2010b).

### 2.2.3 Fixed particle assemblies

There are two approaches to set up the problem of flow past fixed particle assemblies. We can impose a constant pressure gradient across the domain, in which case,  $\langle \mathbf{g}^{(f)} \rangle_{\mathcal{V}}$  is known *a priori* and the volume–averaged fluid velocity evolves to reach a steady state corresponding to the imposed pressure gradient. Another approach is to specify a desired volumetric flow rate and the volume–averaged pressure gradient  $\langle \mathbf{g}^{(f)} \rangle_{\mathcal{V}}$  is adjusted to maintain the specified flow rate. The physical problem corresponding to both these approaches can be simulated in any particle–resolved DNS methodology. Hill et al. (2001b) proposed their LBM–based drag correlation by imposing a known constant pressure gradient. In our simulations using PUREIBM DNS, we specify the desired flow rate and obtain the pressure gradient as an output. In the following section we describe the governing equations in our numerical method and show that the volume–average estimate of the average interphase momentum transfer obtained from the simulations is consistent with the two–fluid theory.

### 2.3 Solution Approach

In PReIBM, we employ Cartesian grids and solve the mass and momentum conservation equations on all the grid points (including those lying inside the particles). A fictitious flow is generated inside the particles that does not affect the exterior flow solution. The mass and momentum conservation equations that are solved in PReIBM are

$$\frac{\partial u_i}{\partial x_i} = 0, \quad (2.18)$$

and

$$\rho_f \frac{\partial u_i}{\partial t} + \rho_f S_i = -g_{\text{IBM},i} + \mu_f \frac{\partial^2 u_i}{\partial x_j \partial x_j} + f_{\text{u},i}, \quad (2.19)$$

respectively, where  $\mathbf{g}_{\text{IBM}}$  is the pressure gradient,  $\mathbf{S} = \nabla \cdot (\mathbf{u}\mathbf{u})$  is the convective term in conservative form, and  $\mathbf{u}$  is the instantaneous velocity field. In the momentum conservation equation (cf. 3.10),  $\mathbf{f}_{\text{u}}$  is the additional immersed boundary (IB) force term that accounts for the presence of solid particles in the fluid-phase by ensuring the no-slip and no-penetration boundary conditions at the particle-fluid interface.

The surface of the solid particle is represented by a discrete number of points called boundary points. For spherical particles, the boundary points are specified by discretizing the sphere in spherical coordinates. In figure 3.3, a schematic describing the computation of the IB forcing is shown for the equatorial plane passing through the spherical particle. Another set of points called exterior points are generated by projecting these boundary points onto a sphere of radius  $r + \Delta r$ , where  $r$  is the radius of the particle (see exterior point represented by an open circle on the dashed line in figure 3.3). Similarly, the boundary points are projected onto a smaller sphere of radius  $r - \Delta r$  and these points are called interior points. In our simulations  $\Delta r$  is taken to be same as the grid spacing. The IB force is computed at the interior points. At these points the fluid velocity is forced in a manner similar to the ghost cell approach used in standard finite-difference/finite-volume based methods (Patankar, 1980). Specifically for the case of zero solid particle velocity, the velocity at the interior points is forced to be equal in magnitude but opposite in direction of the fluid velocity at the corresponding exterior points. Velocities at the exterior and interior points are obtained by interpolating the velocities from

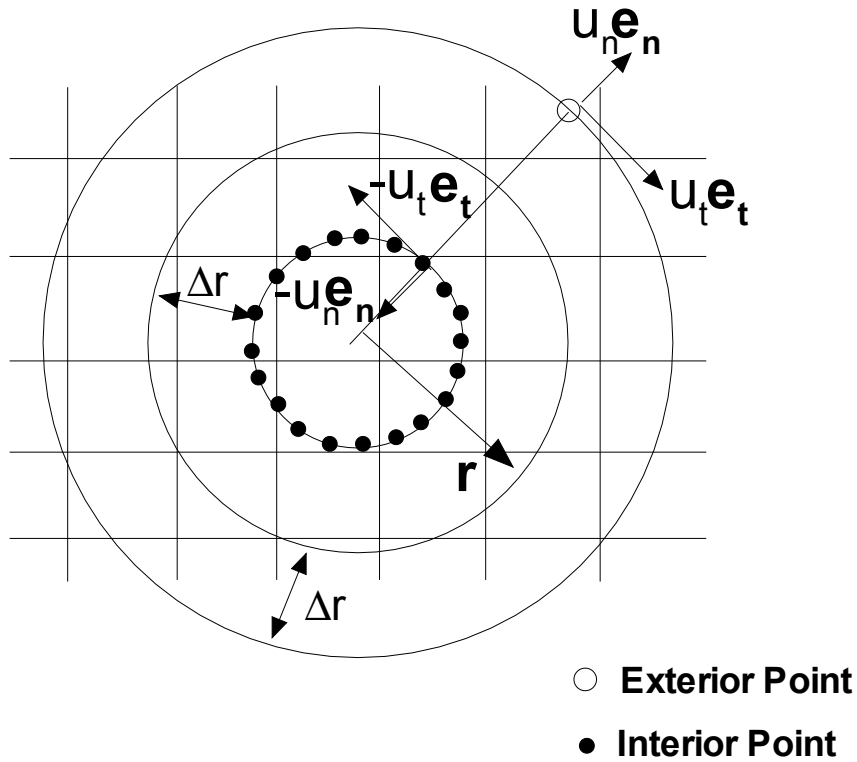


Figure 2.2 A schematic showing the computation of the immersed boundary forcing for a stationary particle. The solid circle represents the surface of the particle at  $r$ . Open dot shows the location of one exterior point at  $r + \Delta r$  (only one exterior point is shown for clarity, although there is one exterior point for each interior point) and filled dots show the location of interior points at  $r - \Delta r$  where the immersed boundary forcing is computed. For the special case of a stationary particle, the velocity at the interior points is forced to be the opposite of the velocity at the corresponding exterior points. In the schematic,  $u_n \mathbf{e}_n$  represents the normal velocity and  $u_t \mathbf{e}_t$  represents the tangential velocity at the exterior point.

the neighboring grid nodes. The computation of IB forcing is similar to the direct forcing method proposed by Yusof (1996). The IB forcing at the  $n + 1^{\text{th}}$  time-step is specified to cancel the remaining terms in the momentum conservation, and to force the velocity to its desired value  $\mathbf{u}^d$  at the interior points:

$$f_{\mathbf{u},i}^{n+1} = \rho_f \frac{u_i^d - u_i^n}{\Delta t} + \rho_f S_i^n + g_{\text{IBM},i}^n - \mu_f \frac{\partial^2}{\partial x_j \partial x_j} u_i^n. \quad (2.20)$$

The IB forcing at the interior points is then interpolated to the neighboring grid nodes that do not include grid nodes in the fluid phase. It is noteworthy that the discretization of the sphere in spherical coordinates is independent of the grid resolution and hence to some extent, decouples the grid resolution from the accuracy with which the boundary condition is imposed.

The distinctive feature of PUREIBM is that the surface force density is directly calculated from the surface values of the velocity and pressure fields obtained from the unmodified Navier–Stokes equations in the fluid phase. This feature of PUREIBM distinguishes it from the so-called diffuse interface methods (Uhlmann, 2005; Yusof, 1996) where the IB forcing is computed on the surface of the particle and then interpolated to the neighboring grid nodes that could also lie in the fluid-phase. They are called diffuse–interface methods because the surface force density is smeared into the fluid–phase.

The governing equations in PUREIBM (cf. 3.9 and 3.10) are solved by imposing periodic boundary conditions on fluctuating variables that are now defined. The velocity field is decomposed into a spatially uniform mean flow that is purely time-dependent and a fluctuating velocity field  $\mathbf{u}'$  that is periodic, i.e.,

$$\mathbf{u}(\mathbf{x}, t) = \langle \mathbf{u} \rangle_{\mathcal{V}}(t) + \mathbf{u}'(\mathbf{x}, t), \quad (2.21)$$

where the volumetric mean velocity

$$\langle \mathbf{u} \rangle_{\mathcal{V}}(t) = \frac{1}{V} \int_{\mathcal{V}} \mathbf{u}(\mathbf{x}, t) d\mathcal{V}, \quad (2.22)$$

is obtained by averaging the velocity field over the entire computational domain. Similar decompositions can be written for the non-linear term  $\mathbf{S}$ , pressure gradient  $\mathbf{g}$ , and immersed boundary forcing  $\mathbf{f}_u$  terms. Substituting the above decompositions in the mass (cf. 3.9) and

momentum (cf. 3.10) conservation equations, followed by averaging over the entire computational domain yields the volume averaged mass and momentum conservation equations. Since the volumetric means are independent of spatial location, mean mass conservation is trivially satisfied. The mean momentum conservation equation in the whole domain becomes

$$\rho_f \frac{d\langle u_i \rangle_{\mathcal{V}}}{dt} = -\langle g_{\text{IBM},i} \rangle_{\mathcal{V}} + \langle f_{\text{u},i} \rangle_{\mathcal{V}}, \quad (2.23)$$

where the volume integrals of convective and diffusive terms are zero because of periodic boundary conditions. The mean IB forcing term  $\langle \mathbf{f}_{\text{u}} \rangle_{\mathcal{V}}$  is computed by volume-averaging the IB force specified by (3.11) over the region  $\mathcal{V}$ . As noted earlier, the mean pressure gradient  $\langle \mathbf{g}_{\text{IBM}} \rangle_{\mathcal{V}}$  is computed such that we obtain the desired flow rate.

While mean mass conservation is trivially satisfied, the fluctuating velocity field needs to be divergence free, i.e.,

$$\frac{\partial u'_i}{\partial x_i} = 0. \quad (2.24)$$

Subtracting the mean momentum conservation equation (3.14) from the instantaneous momentum conservation equation (3.10) yields the following equation for the fluctuating velocity:

$$\rho_f \frac{\partial u'_i}{\partial t} + \rho_f S'_i = -g'_i + \mu_f \frac{\partial^2 u_i}{\partial x_j \partial x_j} + f'_{\text{u},i} \quad (2.25)$$

Taking the divergence of the above equation and using equation (2.24) results in the following modified Poisson equation for the fluctuating pressure gradient:

$$\frac{\partial g'_{\text{IBM},i}}{\partial x_i} = \frac{\partial f'_{\text{u},i}}{\partial x_i} - \rho_f \frac{\partial S'_i}{\partial x_i} \quad (2.26)$$

The conservation equations (3.14)–(2.26) are solved on every grid point (including those inside the solid particles) to yield the flow around immersed bodies that satisfies the no-slip and no-penetration boundary conditions. In the following section we derive the evolution equation for the velocity averaged over the fluid-phase using the PReIBM governing equations and show that PReIBM is reconcilable with the two-fluid theory.

### 2.3.1 Conservation of mean momentum in the fluid-phase

The mean momentum conservation equation in the fluid-phase is derived by averaging the PReIBM momentum conservation equation (cf. 3.10) over the fluid region. When performing

volume-averaging one has to account for discontinuities in the stresses at the particle-fluid interfaces. The conservation of fluid-phase mean momentum reads:

$$\rho_f(1 - \phi) \frac{d \langle u_i^{(f)} \rangle_{\mathcal{V}}}{dt} = -(1 - \phi) \langle g_{\text{IBM},i} \rangle_{\mathcal{V}} - \frac{1}{V} \oint_{\partial \mathcal{V}^{\text{int}}} \tau_{ji} n_j^{(s)} dA. \quad (2.27)$$

We can see that the above equation is identical to (2.16) and thus we conclude that PReIBM is consistent with the two-fluid theory. Note that when we average the PReIBM momentum conservation equation (cf. 3.10) over the fluid region, the average of IB forcing over the fluid region is zero since the IB forcing is non-zero only inside the particles. In IBM implementations where the IB forcing is finite in the fluid-phase (Yusof, 1996; Uhlmann, 2005), an extra term in the form of fluid-phase volume average of the IB forcing  $\langle \mathbf{f}_u^{(f)} \rangle_{\mathcal{V}}$  will appear in (2.27).

The mean pressure gradient  $\langle \mathbf{g}_{\text{IBM}} \rangle_{\mathcal{V}}$  required to obtain a desired fluid-phase mean velocity  $\langle \mathbf{u}^{(f)} \rangle_{\mathcal{V}}^d$ , is computed using an explicit time discretization of (2.27) such that at the  $n^{\text{th}}$  time step the mean pressure gradient is given by

$$-\langle \mathbf{g}_{\text{IBM}} \rangle_{\mathcal{V}}^n = \rho_f \frac{\langle \mathbf{u}^{(f)} \rangle_{\mathcal{V}}^d - \langle \mathbf{u}^{(f)} \rangle_{\mathcal{V}}^n}{\Delta t} + \frac{1}{(1 - \phi)V} \left\{ \oint_{\partial \mathcal{V}^{\text{int}}} \tau_{ji}^{(n)} n_j^{(s)} \right\} dA, \quad (2.28)$$

where all quantities in the integrand are evaluated on the fluid side of the fluid-particle interface, and the superscript  $n$  implies the relevant quantities at the  $n^{\text{th}}$  time step. This equation is obtained by requiring that  $\langle \mathbf{u}^{(f)} \rangle_{\mathcal{V}}^{n+1} = \langle \mathbf{u}^{(f)} \rangle_{\mathcal{V}}^d$ , so that the first term on right hand side drives the volume-averaged mean fluid velocity to its desired value. The equations are evolved in time until the volume-averaged quantities reach a steady state, at which point the first term on the right hand side of (2.28) is negligible, and consequently (2.28) reduces to the numerical counterpart of (2.17). This establishes that the resulting numerical solution to the PReIBM governing equations is a valid numerical solution to steady flow past homogeneous particle assemblies.

The numerical scheme used in PReIBM is a primitive-variable, pseudo-spectral method, using a Crank-Nicholson scheme for the viscous terms, and an Adams-Bashforth scheme for the convective terms. A fractional time-stepping method that is based on Kim and Moin's approach (Kim and Moin, 1985) is used to advance the velocity and pressure fields in time.

Kim and Moin's algorithm involves a predictor step followed by a corrector step. The velocity field obtained from the predictor step need not be divergence free. Therefore, a corrector step is required so that the velocity is divergence free. Since PReIBM uses this approach, the maximum divergence of the velocity field obtained at any time step is of the order of machine precision. A common criticism of this method is that due to the divergence correction the corrected velocity field does not satisfy the desired boundary condition (Muldoon and Acharya, 2008). Although the divergence correction changes the velocity of the particle surface at every time step, the velocity correction at steady state is of the order of  $10^{-10}$ . Therefore, once steady state is reached the fluid velocity at the particle surface does not change at all. In our simulations, the maximum difference between the corrected surface velocity and the desired boundary velocity at steady state is found to be less than  $10^{-3}$ . Since only steady flows are considered in this work, it suffices to ensure that the velocity field obeys the continuity equation. The numerical method described in this work must be modified appropriately to obtain time-accurate solutions for unsteady flows.

## 2.4 Simulation Methodology

We now describe how the mean flow Reynolds number and solid volume fraction are specified in the simulation. For flow past homogeneous particle assemblies, a Reynolds number based on the magnitude of mean slip velocity between the two phases is defined as

$$\text{Re}_m = \frac{|\langle \mathbf{W} \rangle| (1 - \phi) D}{\nu_f}, \quad (2.29)$$

where  $|\langle \mathbf{W} \rangle| = |\langle \mathbf{u}^{(f)} \rangle - \langle \mathbf{u}^{(s)} \rangle|$  is the magnitude of the mean slip velocity,  $D$  is the particle diameter, and  $\langle \mathbf{u}^{(f)} \rangle$  and  $\langle \mathbf{u}^{(s)} \rangle$  are the mean velocities in the fluid and solid phases respectively. For the purpose of generating drag correlations it is more convenient to specify the mean flow Reynolds number as input to the simulations, rather than the mean pressure gradient. For fixed particle assemblies  $\langle \mathbf{u}^{(s)} \rangle = 0$  and the desired fluid-phase mean velocity  $\langle \mathbf{u}^{(f)} \rangle$  is known in terms of the input Reynolds number and other physical properties.

Particles are initialized corresponding to a specified mean solid volume fraction  $\phi$ . For ordered arrays (where a unit cell is simulated) this is accomplished by simply varying the ratio

of the computational box length  $L$  to the particle diameter  $D$ . For random assemblies, the particles are fixed in a random equilibrium configuration they attain following elastic collisions (in the absence of ambient fluid) starting from a lattice arrangement with a Maxwellian velocity distribution. The elastic collisions are simulated using a soft-sphere discrete element model (Cundall and Strack, 1979; Garg et al., 2010a). The pair correlation function at equilibrium specifies the particle configuration for random assemblies.

#### 2.4.1 Numerical parameters

The computational domain used is a cube with sides of length  $L$  which is discretized using a regular Cartesian grid with  $M$  grid cells in each direction so that  $\Delta x = L/M$  is the size of each grid cell. The spatial resolution is represented by the number of grid cells across the diameter of a particle, which is denoted  $D_m = D/\Delta x$ . For ordered arrays the ratio of computational box length  $L$  to the particle diameter  $D$  is not an independent parameter since  $L$  corresponds to a unit cell of the lattice arrangement and is determined by the volume fraction  $\phi$ . Thus  $D_m$  is the only relevant numerical parameter in the simulations of ordered arrays.

For random arrays, the ratio  $L/D$  is an independent parameter. The minimum box length is determined by the criterion that the spatial autocorrelation of flow statistics must decay to zero within the box. This is to prevent the periodicity of the numerical solution from leading to unphysical flow fields. The numerical parameter  $L/D$  also determines the number of particles  $N_p$  in the box such that for a given volume fraction  $\phi$  it is given by

$$N_p = \left[ \frac{6\phi}{\pi} \left( \frac{L}{D} \right)^3 \right] \quad (2.30)$$

where, the square brackets denote the nearest integer.

The number of grid cells  $M$  along each axis of the computational box determines the computational cost of the problem that scales as  $M^3$ . It is related to the grid resolution parameter  $D_m$  and the box length to particle diameter ratio,  $L/D$  as follows

$$M = \frac{L}{\Delta x} = \frac{L}{D} D_m. \quad (2.31)$$

This relation shows that for fixed computational cost, there is a tradeoff between spatial resolution and box size which determines the effect of periodic boundary conditions on the numerical

solution through  $L/D$ .

The solution algorithm is advanced in pseudo-time from specified initial conditions to steady state using a time step  $\Delta t$  that is chosen as the minimum of the convective and viscous time steps according to the criterion

$$\Delta t = \text{CFL} \times \min \left\{ \frac{\Delta x}{u_{\max}}, \frac{\Delta x^2 (1 - \phi)}{\nu_f} \right\}. \quad (2.32)$$

At the beginning of the simulation we set  $u_{\max} = |\langle \mathbf{u}^{(f)} \rangle|$ , and as the flow evolves  $u_{\max}$  is set to the magnitude of the maximum fluid velocity so that the time step adapts itself to satisfy the above criterion.

Both spatial and temporal discretization contribute to numerical error in the estimation of the drag force. However, for steady flows the numerical error is determined solely by the spatial resolution parameter  $\Delta x/D = 1/D_m$ , which must be sufficiently small to ensure numerically converged results. The influence of these numerical parameters—the grid resolution parameter  $D_m$ , the ratio of computational box length to particle diameter  $L/D$ , and the number of solid particles  $N_p$ —on the numerical convergence of PReIBM simulations is discussed in the next section.

#### 2.4.2 Estimation of mean drag from simulations

Direct numerical simulation of flow through a particle assembly using PReIBM results in velocity and pressure fields on a regular Cartesian grid. In PReIBM the drag force on the  $i^{\text{th}}$  particle,  $\mathbf{F}_d^{(i)} = m^{(i)} \mathbf{A}^{(i)}$ , is reported by integrating the viscous and pressure forces exerted by the fluid on the particle surface and not from the IB forcing. The average drag force on particles in a homogeneous suspension for  $\mu^{\text{th}}$  realization is computed as

$$\{\mathbf{F}_d\}_{\mathcal{V}}^{\mu} = \frac{1}{N_p} \left\{ -\langle \mathbf{g}_{\text{IBM}} \rangle_{\mathcal{V}} V_s - \oint_{\partial \mathcal{V}_s} \psi \mathbf{dA} + \mu_f \oint_{\partial \mathcal{V}_s} \nabla \mathbf{u} \cdot \mathbf{dA} \right\}. \quad (2.33)$$

In the above equation the first term on the right hand side is the body force due to mean pressure gradient, the second term is the drag force due to fluctuating pressure field, and the third term is the viscous contribution to the drag force. The pressure and viscous contributions to the drag force are obtained by integrating the pressure and viscous stresses over the surface

of each particle. To perform this integration, the pressure and viscous stresses are interpolated to the boundary points (see figure 3.3) from the surrounding grid nodes and the force acting on the boundary point is computed by multiplying the interpolated fluid stress with the area associated with the boundary point. Summation of the forces acting on all the boundary points of the particle gives the force acting on it. The sum of the last two terms on the right hand side of Eq. (2.33) is the exact numerical representation of the expectation of the surface force density. Thus, we conclude that the drag law inferred from PUREIBM simulations is consistent with the two-fluid theory. It should be noted that HKL proposed their correlation for the total fluid-particle force (cf. 2.33) whereas van der Hoef et al. (2005) and BVK subtracted the contribution of mean pressure gradient to propose their drag correlation.

The simulation is carried out until the average drag force per particle reaches a steady state. The difference in the drag values of successive time steps is monitored and a moving average of this difference is calculated over 10% of the time required for the fluid to travel the length of the box. If this moving average is less than a threshold ( $1 \times 10^{-6}$  in most of the simulations), we conclude that the drag has reached its steady value. Although some unsteadiness has been observed in the velocity field particularly for volume fractions less than 0.2, there is no noticeable unsteadiness in the mean drag.

The mean drag force represents an average over all particle configurations corresponding to the same volume fraction and pair correlation function. Therefore, the drag from a single realization (cf. 2.33) is averaged over multiple independent realizations (MIS) to obtain an estimate for the ensemble-averaged drag:

$$\{\mathbf{F}_d\}_{V,\mathcal{M}} = \frac{\sum_{\mu=1}^{\mathcal{M}} \{\mathbf{F}_d\}_{V}^{\mu}}{\mathcal{M}}. \quad (2.34)$$

which converges to the true expectation of the drag force in the limit  $N_p \mathcal{M} \rightarrow \infty$ . The ensemble-averaged drag force is later reported as a normalized average drag force given by

$$F = \frac{\{\mathbf{F}_d\}_{V,\mathcal{M}}}{F_{\text{Stokes}}}, \quad (2.35)$$

where  $F_{\text{Stokes}} = 3\pi\mu_f D(1-\phi)|\langle \mathbf{W} \rangle|$  is the Stokes drag acting on an isolated sphere moving with a slip velocity of  $(1-\phi)|\langle \mathbf{W} \rangle|$ . The number of multiple independent simulations  $\mathcal{M}$  is

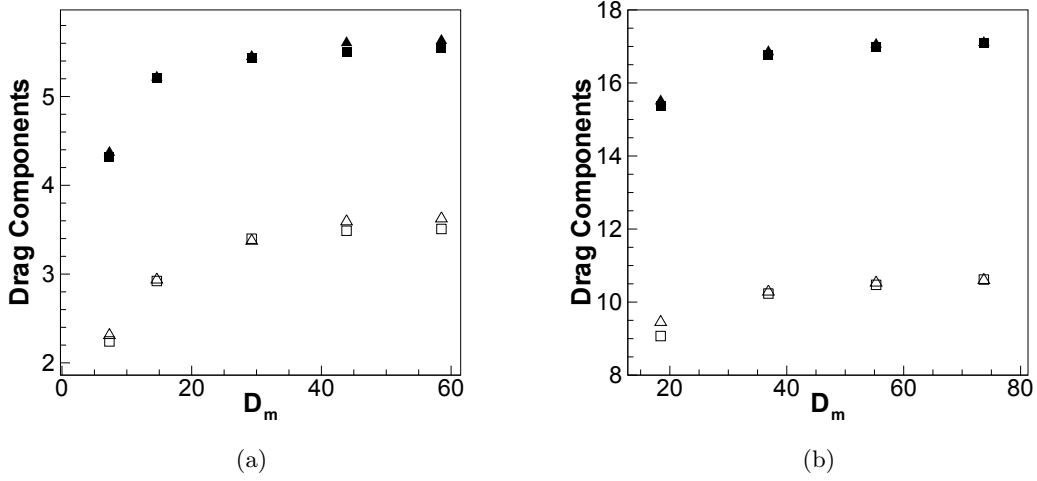


Figure 2.3 Convergence characteristics of drag force due to fluctuating pressure gradient (open symbols) and viscous stresses (filled symbols) for FCC arrays at  $Re_m = 40$  with grid resolution  $D_m$  for two CFL values of 0.2 (squares) and 0.05 (triangles). Volume fraction  $\phi$  is equal to 0.2 in (a) and 0.4 in (b).

determined by the requirement that the total number of samples  $\mathcal{M}N_p$  in the estimate for the average force given by (2.34) be sufficiently large to ensure low statistical variability.

## 2.5 Numerical Convergence

In this section we investigate the influence of the numerical parameters discussed in the previous section on PReIBM simulations. We first examine the influence of the grid resolution parameter  $D_m$  and the time step  $\Delta t$ . We study steady flow past an ordered array of particles in a FCC lattice arrangement, because for this case the only numerical parameter is the grid resolution  $D_m$ . Although we consider steady flows, we also verify that the steady value of the drag does not change with the time step chosen to evolve the flow in pseudo time from a uniform flow initial condition.

For a face centered cubic (FCC) arrangement of particles ( $\phi = 0.2$ ,  $Re_m = 40$ ), figure 2.3(a) shows the convergence characteristics of drag forces due to fluctuating pressure gradient (open symbols) and viscous stresses (filled symbols) as a function of grid resolution  $D_m$  for two different values of CFL equal to 0.2 (squares) and 0.05 (triangles). Figure 2.3(b) shows the

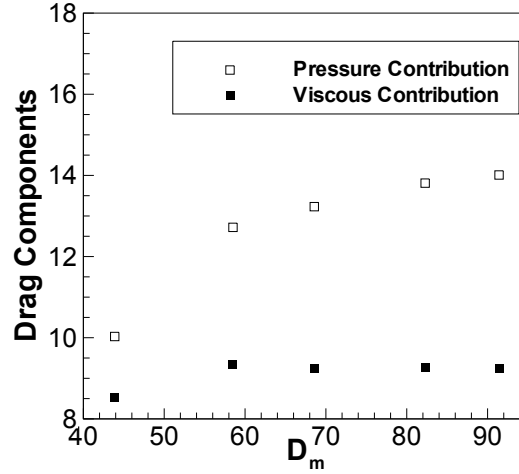


Figure 2.4 Convergence characteristics of drag force due to fluctuating pressure (open symbols) and viscous stresses (filled symbols) for FCC arrays at  $Re_m = 300$  with grid resolution  $D_m$ . Volume fraction  $\phi$  is equal to 0.2.

same convergence characteristics for a denser FCC arrangement with a solid volume fraction of 0.4 and  $Re_m = 40$ . In both figures it can be seen that the PReIBM simulation result is nearly independent of the time step (CFL). The figures show that the resolution requirements increase with increasing volume fraction. We conclude that a minimum resolution of  $D_m = 40$  is needed for converged results at  $\phi = 0.2$ , while a minimum resolution of  $D_m = 60$  is required for  $\phi = 0.4$ . These values are based on relative error in the normalized force that can be calculated based on the normalized force values obtained on the finest grid resolution. If the relative error is less than 2%, the values are considered grid converged. Based on this criterion,  $D_m = 40$  and  $D_m = 60$  are considered grid converged resolutions for solid volume fractions 0.2 and 0.4, respectively. It is noted that in the simulations for ordered arrays presented in section 2.6 we used much higher resolutions ( $D_m = 60$  for  $\phi = 0.2$   $D_m = 80$  for  $\phi = 0.4$ ). In addition to the dependence of grid resolution on volume fraction, higher mean flow Reynolds numbers require progressively higher grid resolution. Figure 2.4 shows the convergence characteristics for FCC arrays at a volume fraction of 0.2 and  $Re_m = 300$ . As expected the resolution required for a numerically converged result is higher compared to that required for  $Re_m = 40$  at the same volume fraction of 0.2.

For random arrays, in addition to errors arising from finite grid resolution, there is statistical variability between different realizations and the box length is an independent numerical parameter. The choice of  $L/D$  is determined by two requirements: (i) spatial autocorrelation of velocity should decay within the box length and (ii) there should be sufficient number of particles in the box for a statistically reliable estimate of the average normalized force.

An initial estimate for the minimum box length required can be found from the Brinkman screening length. Brinkman screening is the phenomenon whereby the fluid velocity disturbance produced by each particle is decreased due to the force exerted by the fluid on the neighboring particles. It plays a crucial role in limiting the range of fluid velocity correlations. The length scale  $l_b$  over which the fluid correlations decay is termed the Brinkman screening length (Hinch, 1977; Hill et al., 2001a) and it decreases with increasing volume fraction ( $l_b \sim O(D/(2\sqrt{\phi}))$ ).

Decay of the fluid velocity autocorrelation  $\rho_u(r)$  which is defined as

$$\rho_u(r) = \frac{\langle I_f(\mathbf{x}) \mathbf{u}''^{(f)}(\mathbf{x}) \cdot I_f(\mathbf{x} + \mathbf{r}) \mathbf{u}''^{(f)}(\mathbf{x} + \mathbf{r}) \rangle}{\langle I_f \mathbf{u}''^{(f)} \cdot \mathbf{u}''^{(f)} \rangle}, \quad (2.36)$$

for steady flow past a random configuration of spheres ( $\phi = 0.2$ ), is shown in figure 3.7(b) for two values of mean flow Reynolds numbers ( $Re_m = 20, 300$ ). For both Reynolds numbers, the fluid velocity autocorrelation function decays to zero around  $x = 0.2L$ , while the estimate for Brinkman screening length is  $0.15L$ . Thus the Brinkman screening length can be used as a good estimate to determine the required box length. However, if we choose a box length that is comparable to or slightly greater than the Brinkman screening length, we get very few spheres in the box and this leads to high statistical variability in the drag force. The box lengths that we choose to perform the PReIBM simulations are much larger than the Brinkman screening lengths and we have used values from past LBM simulations as a guideline.

In summary, these numerical convergence test results show that the PReIBM simulations yield grid-independent values for the mean drag. These results are also independent of the choice of time step used to advance the solution in pseudo time, provided the stability criterion is met. A satisfactory number of MIS should ideally be determined by determining the minimum number of samples for a given level of statistical error in the force estimate. However, this quantity is a strong function of  $Re_m$  and solid volume fraction. To report estimates for

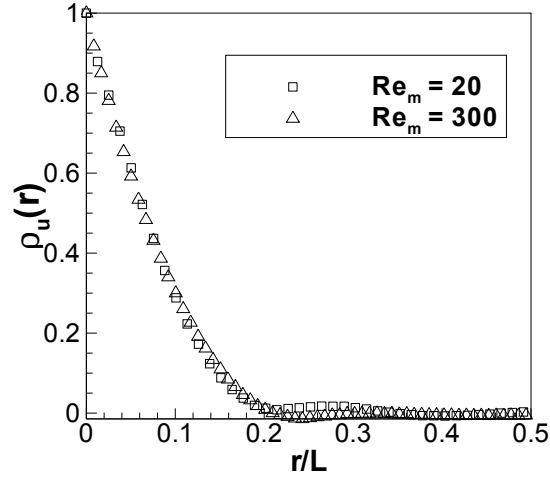


Figure 2.5 Decay of the fluid velocity autocorrelation function (cf. Eq. 3.17) obtained from PReIBM simulation of steady flow past a random configuration of spheres at a solid volume fraction of 0.2 and mean flow Reynolds numbers 20 (squares) and 300 (triangles). In these simulations  $L/D$  ratios of 6 and 4.5 are used for Reynolds numbers 20 and 300 respectively.

the average normalized force for random arrays, we used 5 MIS at all volume fractions and Reynolds numbers. Clearly, the requirements of minimum  $L/D$ , minimum  $D_m$ , and minimum  $\mathcal{M}$ , together dictate a trade-off for a fixed level of computational work. Of these parameters, our tests reveal that the numerical error in PReIBM exhibits the highest sensitivity to grid resolution  $D_m$ .

## 2.6 Numerical Tests

PReIBM has been validated by comparing the drag force obtained from simulations of flow past an isolated sphere with the single sphere drag correlation given by Schiller and Naumann (1935) (see Garg et al. (2011)). Since it is difficult to find an experimental data set to validate simulations of dense suspensions that use periodic boundary conditions, we compare our results with previous numerical or analytical works. We compare the drag force obtained from PReIBM simulations for the following test cases:

1. Stokes flow past simple cubic (SC) and face centered cubic (FCC) arrangements (ranging from dilute to close-packed limit) with the boundary-integral method of Zick and Homsy (1982)
2. Stokes flow past random arrays of monodisperse spheres with LBM simulations of van der Hoef et al. (2005)
3. moderate to high Reynolds ( $Re_m \leq 300$ ) in SC and FCC arrangements with LBM simulations of Hill et al. (2001b)
4. flow past random arrays of monodisperse spheres at  $Re_m = 100$  with ANSYS-FLUENT CFD package (see section 2.8.1)

### 2.6.1 Stokes flow

We first consider Stokes flow past ordered and random arrays of equisized spheres. Different analytical and numerical techniques, such as analytical solution to the Stokes equations (Hsimoto, 1959), Galerkin methods (Snyder and Stewart, 1966; Sorensen and Stewart, 1974a), and the boundary-integral method (Zick and Homsy, 1982) have been used to determine the drag force in Stokes flow past ordered arrays as a function of solid volume fraction. Since Zick and Homsy's results are within 6% of all the other studies, and include all three ordered configurations for the entire range of solid volume fraction, their results are used as a benchmark to compare with PReIBM simulations. Figure 2.6(a) shows that the PReIBM simulations are in excellent agreement with reported values from dilute to close-packed limits. Moreover, PReIBM is able to capture slightly different dependence of  $F(\phi)$  for SC (as compared to FCC) for  $\phi > 0.3$ . The grid resolution in the PReIBM simulations for the FCC cases is 25.24 and 104 grid points per particle diameter, for the minimum and maximum volume fractions of 0.01 and 0.698 considered, respectively. In the simple cubic cases,  $D_m$  is equal to 40.08 and 149, for the minimum and maximum volume fractions of 0.01 and 0.514, respectively.

Stokes flow past random arrays of spheres has been studied extensively by several researchers (Hill et al., 2001a; van der Hoef et al., 2005). In figure 2.6(b) we compare the Stokes drag obtained from PReIBM simulations of flow past random arrays of monodisperse spheres

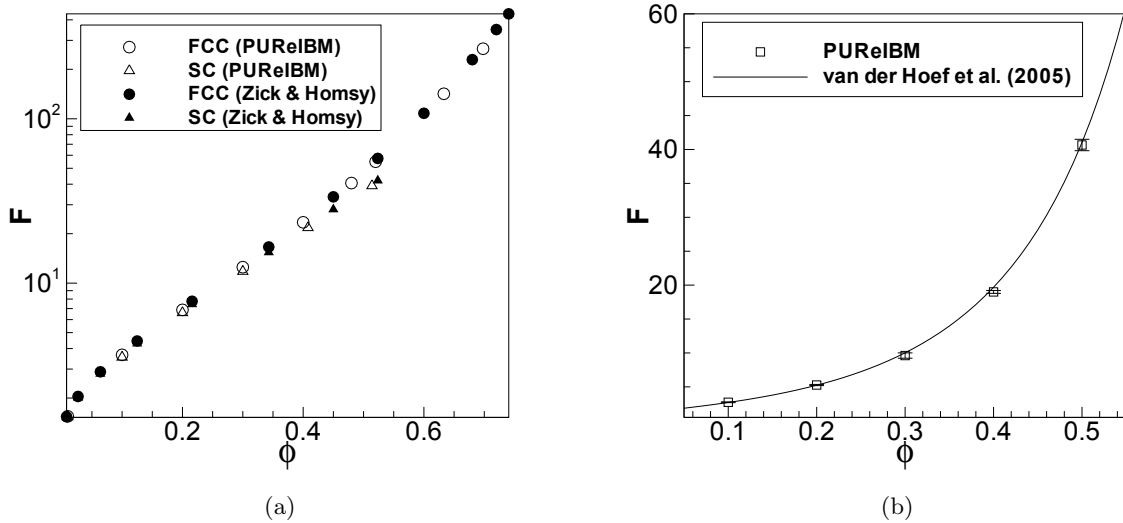


Figure 2.6 Variation of the normalized drag force as a function of the solid volume fraction  $\phi$  in Stokes flow past SC, FCC and random arrangements of spheres. In figure 2.6(a) drag values obtained from PReIBM simulations (open symbols) of Stokes flow in SC and FCC arrangements are compared with the results Zick and Homsy (1982) (filled symbols). In figure 2.6(b) drag values from PReIBM simulations of Stokes flow in random arrays of spheres are compared with the Stokes drag correlation proposed by van der Hoef et al. (2005). For each volume fraction the normalized force from PReIBM simulations is reported by averaging over 5 MIS and the error bars on the symbols in this figure represent 95% confidence intervals in the estimation of the normalized force.

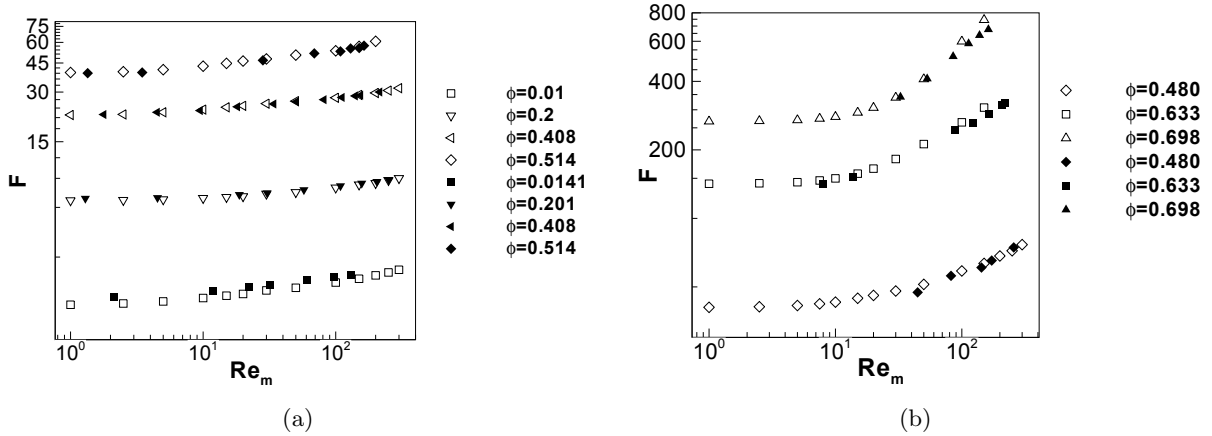


Figure 2.7 Variation of the normalized drag force as a function of both the solid volume fraction and mean flow Reynolds number for flow past SC and FCC arrays. In all these cases, the mean flow is directed along the positive  $x$ -axis. In figure 2.7(a) drag obtained from PUREIBM simulations (open symbols) for SC arrangements is shown while in figure 2.7(b) drag obtained for FCC arrangement is shown. In both figures, PUREIBM drag values (open symbols) are compared with those reported by Hill et al. (2001b) (closed symbols).

with the drag correlation of van der Hoef et al. (2005). From this figure we can see that the results from PUREIBM simulations are in excellent agreement with the LBM-based correlation for Stokes drag in random arrays.

## 2.6.2 Moderate Reynolds numbers

Hill et al. (2001b) performed an extensive study of flow past ordered SC and FCC arrangements at moderate Reynolds numbers using LBM simulations. We compare the drag values for moderate Reynolds number flow in SC and FCC arrangements obtained from PUREIBM simulations with those reported by Hill et al. (2001b) in figures 2.7(a) and 2.7(b) respectively. HKL note that the normalized drag force in ordered arrays is a strong function of the flow angle. To avoid additional parameterization of the problem by flow angle, the validation tests shown in this section are performed for the case where the mean flow is directed along the positive  $x$ -axis. These figures show that drag values for ordered arrays are in excellent agreement with those reported by Hill et al. (2001b).

The validation tests described in this section show that the PReIBM simulations faithfully reproduce many standard results published in literature. Before we present the results for flow past random arrays of spheres at moderate Reynolds numbers, it is important to understand the rationale behind choosing the simulation setup that we used. It is also important to compare the simulation setup used in this work with those used by HKL, BVK (and several other) for similar studies.

## 2.7 Comparison of simulation setups to extract computational drag laws

To specify a closure for the interphase momentum transfer term, it is natural to simulate a statistically homogeneous suspension flow with freely moving particles and to then compute volume-averaged estimates of the average fluid-particle force from the particle acceleration data. Due to the large number of parameters encountered in gas-solid flow, it is advantageous to use a fixed bed setup so that the parameter space can be explored relatively easily. Another advantage of using fixed bed setups is that it is easy to design an experimental setup that mimics the simulation setup. Use of fixed bed simulation methodology to extract computational drag laws for gas-solid flows is justified if the configuration of the particles changes very slowly compared to the time it takes to attain mean momentum balance. The time scale over which the particle configuration changes depends on  $\text{Re}_T = DT^{1/2}/\nu_f$ , which is the Reynolds number based on the particle fluctuating velocity that is characterized by the particle granular temperature  $T$ . The particle granular temperature  $T$  is a measure of the variance in the particle velocities and is defined as  $T = 1/3 \langle \mathbf{v}'' \cdot \mathbf{v}'' \rangle$  where,  $\mathbf{v}''$  is the fluctuation in the particle velocity defined with respect to the mean particle velocity. Particle-resolved simulations of freely evolving suspensions (Tenneti et al., 2010b) and recent high-speed imaging of particles (Cocco et al., 2010) show that this value of  $\text{Re}_T$  is low for high Stokes number suspensions.

Although fixed bed simulations can be used to infer drag laws for gas-solids flow, care must be taken when extending this setup to simulate problems with non-zero  $\text{Re}_T$  and bi-disperse suspensions with relative velocity between both size classes. If all particles move with the same velocity (i.e.,  $\text{Re}_T = 0$ ), a change of frame renders the fixed bed setup a Galilean-Invariant (GI) transformation of the physical problem. This is not the case for non-zero  $\text{Re}_T$ . Similarly for

bi-disperse suspensions with non-zero relative velocity between size classes, a Galilean change of frame can bring only particles of one size class to rest, unless particles belonging to both size classes move with the same mean velocity.

The simulation setup used in this work is flow past infinitely massive particles initially at rest in a fluid ( $\text{Re}_T = 0$ ). Particle velocities do not change in time due to the infinite inertia of the particles and hence they remain at rest throughout the simulation. The desired mean flow Reynolds number (or flow rate) is specified and the mean pressure gradient required to produce the desired flow rate evolves in time to balance the force acting on the particles. We denote this setup A as described in table 2.1.

The next simulation setup we consider is a GI equivalent of setup A, where the problem is solved in a frame moving with velocity equal to  $\langle \mathbf{u}^{(f)} \rangle$  with respect to the laboratory frame. In this frame, the mean fluid velocity is zero and all the particles move with the same constant velocity of  $-\langle \mathbf{u}^{(f)} \rangle$ . In setup A', if the equations of motion are written for a *fixed, non-deforming* control volume (CV), the positions of the particles must evolve in time due to the non-zero velocities of the particles. This setup A' (cf. Table 2.1) is used by van der Hoef et al. (2005) and BVK to propose their respective drag laws.

Setup A' can also be solved by considering a *moving, non-deforming* control volume that moves with the particle velocity  $\mathbf{V}^{(p)}$  such that particle positions do not change with respect to the control volume (note that all the particles move with the same velocity, i.e.,  $\text{Re}_T = 0$ ). We denote this approach as setup B (cf. figure 2.8). Although the control volume is moving in this setup, we must remember that the solution fields and particle velocities are with respect to the frame of setup A'. For a moving control volume the convective flux is written with respect to the control volume and hence the nonlinear term in setup B is different from that in setup A or A'.

All the setups A, A' (fixed CV) and B (moving CV) are GI transformations of the same physical problem and thus any computational method should yield the same solution when viewed in the appropriate reference frame. In particular, quantities such as the steady mean drag that are GI should be identically reproduced by any numerical method, irrespective of the chosen setup.

Setup	Average velocity	fluid	Particle velocity	Particle position	Control volume
A	$\langle \mathbf{u}^{(f)} \rangle$	0	0	Fixed	Fixed
A'	0		$-\langle \mathbf{u}^{(f)} \rangle$	Moving	Fixed
B	0		$-\langle \mathbf{u}^{(f)} \rangle$	Fixed	Moving
C(non GI)	0		$-\langle \mathbf{u}^{(f)} \rangle$	Fixed	Fixed

Table 2.1 Summary of various simulation setups.

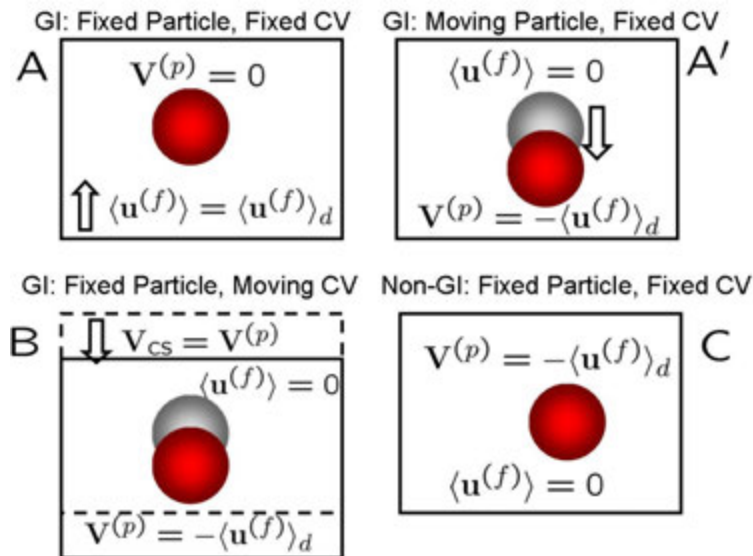


Figure 2.8 Schematic comparing various simulation setups.

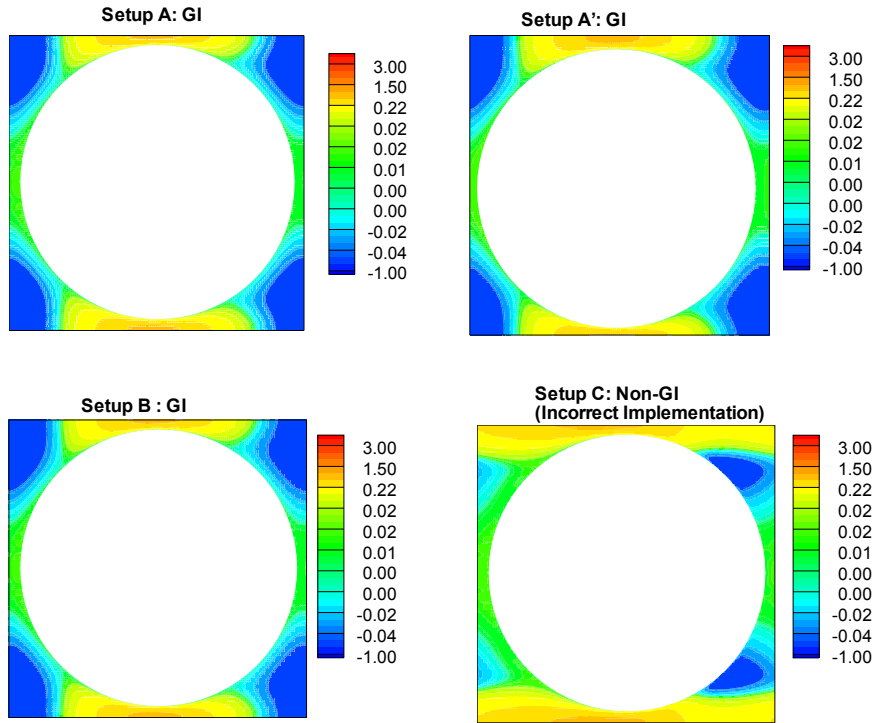


Figure 2.9 Plot comparing the velocity contours obtained from the different simulation set ups. The contours shown in this figure are for a simple cubic arrangement at a volume fraction of 0.4 and mean flow Reynolds number of 150.

Besides the setups discussed above, a *non-Galilean-invariant* setup is sometimes used to solve the physical problem. In this setup denoted C (cf. Table 2.1), the particles are all assigned the same velocity, but their positions are fixed to their initial locations and the equations of motion are written for a *fixed, non-deformable* control volume. Since setup C is not a GI transformation of the physical problem it is an *incorrect* setup, although the error incurred in the limit of Stokes flow the error incurred in the solution is negligible. In this section we show that we obtain GI solutions from PUnReIBM simulations of setups A, A' and B. We also show how the incorrect non-GI setup C leads to erroneous results at  $Re_m = 150$ .

We consider a simple cubic arrangement of spheres at a volume fraction of 0.4 and mean slip Reynolds number of 150. In figure 2.9, the steady state velocity field obtained from PUnReIBM simulations for the different setups (A, A', B and C) are compared. All these velocity fields are viewed in the reference frame of setup A (laboratory frame). From these figures we can see

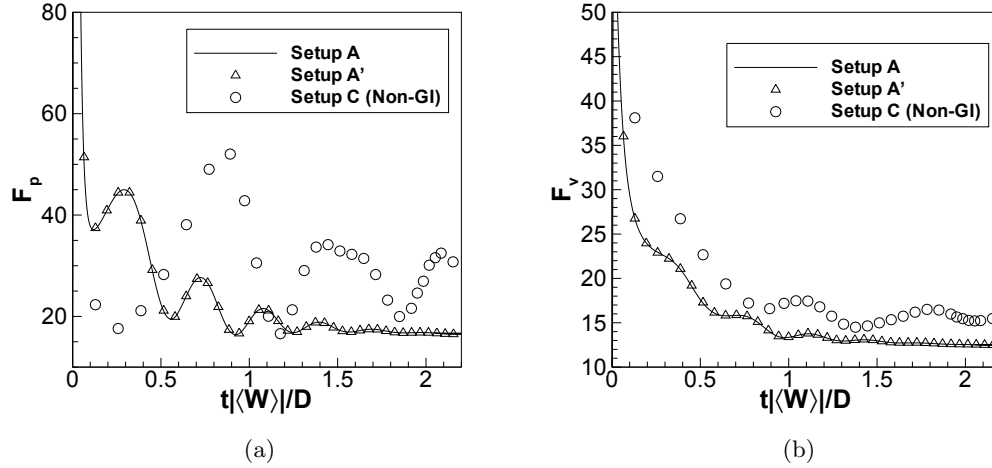


Figure 2.10 Plot comparing the evolution of normalized pressure and viscous forces obtained from the different simulation setups shown in figure 2.8. The volume fraction is 0.4 and the mean flow Reynolds number is 150. Pressure force is plotted in Figure 2.10(a) while the viscous force is plotted in Figure 2.10(b). Since the results obtained from setups A, A' and B are identical, only two (A and A') are shown in these plots for clarity.

that while setups A, A' and B give the same solution fields, the solution obtained from setup C is significantly different. So we expect that the drag force, which is obtained by integrating the pressure and viscous stress over the particle surface, will also be significantly different. Figure 2.10 compares the evolution of the normalized pressure and viscous forces for all the setups. As expected, the evolution of both pressure and viscous contributions to the drag force in the incorrect non-GI setup C is significantly different from those obtained from other GI setups.

In particular, setups A and B are very useful to extract computational drag laws for fixed beds because the motion of the particles need not be considered. But this simplification is possible as long as all the particles are initialized with the same velocity. When the particles have different velocities there exists no Galilean-invariant transformation such that all the particles appear fixed to their initial locations. Such problems can only be solved using setup A'. Recently Yin and Sundaresan (2009a,b) and Holloway et al. (2010) used setup C to propose LBM based drag correlations to account for the relative slip velocity between particles. The

work of Yin and Sundaresan (2009a,b) is limited to the Stokes flow regime and hence the use of setup C is a valid approximation because the particles might not even move one grid cell during the simulation. However, the applicability of setup C to the higher Reynolds number simulations of Holloway et al. (2010) needs to be examined more closely. PReIBM simulations of SC arrays using the non-GI setup C revealed that the drag obtained from setup C is in reasonable agreement with the drag obtained from the other GI setups only up to a Reynolds number of 50, and differs substantially beyond that. This clearly shows that simulations of high Reynolds number flow past particles using a non-GI setup will lead to wrong results. Holloway et al. (2010) did not perform any simulations beyond Reynolds number of 50 and so their results are probably within 10% of the results obtained from other GI setups. We now present the results obtained from PReIBM simulations of flow past random arrays of spheres at moderate Reynolds numbers using setup A.

## 2.8 Results

We performed PReIBM simulations of flow past fixed random configurations of particles at Reynolds numbers up to 300 and for solid volume fractions in the range of 0.1–0.5. The numerical resolutions used in PReIBM simulations are either comparable or higher than those used by HKL and BVK (cf. Table 3.1). Values of the normalized force obtained from PReIBM simulations are compared with those reported by HKL and BVK in figure 2.11. Normalized force values for volume fractions 0.1, 0.2 and 0.3 are shown in figure 2.11(a) while force values for volume fractions 0.4 and 0.5 are shown in figure 2.11(b). It can be seen that PReIBM simulations are in good agreement with the data reported by HKL. The average percentage difference between PReIBM and HKL drag values is about 8% while a maximum difference of 20% is observed at a volume fraction of 0.4 and a mean flow Reynolds number of 120. One reason for this discrepancy at  $\phi = 0.4$  is that although HKL reported their results for a nominal volume fraction of 0.4, the actual volume fraction that they simulated was 0.410 (Hill et al., 2001b). At higher Reynolds numbers the change in the force due to change in volume fraction can be quite significant. For instance, at  $Re_m = 100$ , the normalized force obtained at a  $\phi = 0.4$  is almost twice the normalized force obtained at  $\phi = 0.3$ .

$\phi$	$N_p$	$\mathcal{M}$	$D_m$	$L/D$
0.1	16	5	9.6	4.38
	54	20	17.5	6.6
	80/ 41	5	20/30	7.5/ 6
0.2	16	5	17.6	3.47
	54	20	17.5	5.2
	161/ 34	5	20/40	7.5/ 4.5
0.3	16	5	17.6	3.06
	54	20	21.5	3.07
	71/ 26	5	30/50	5/ 3.6
0.4	16	5	33.6	2.73
	54	20	21.5	4.13
	95/ 20	5	30/60	5/ 3
0.5	16	5	33.6	2.56
	54	20	21.5	3.84
	61/-	5	40/-	4/-

Table 2.2 Comparison of the numerical parameters (number of particles  $N_p$ , number of MIS  $\mathcal{M}$ , particle diameter in grid units  $D_m$  and the ratio of the length of the box to the particle diameter  $L/D$ ) used for random arrays in PReIBM simulations with the past LBM simulations of HKL and BVK. For each entry, first and second rows correspond, respectively, to the LBM simulations of HKL and BVK, and the third row corresponds to the current PReIBM simulations. For the PReIBM simulations, different numerical parameters are used for  $Re_m \leq 100$  and  $Re_m > 100$ . These are separated by “/”. Numbers before the “/” correspond to  $Re_m \leq 100$  while numbers after the “/” correspond to  $Re_m > 100$ . At volume fraction 0.5 PReIBM simulations are performed only up to a Reynolds number of 100.

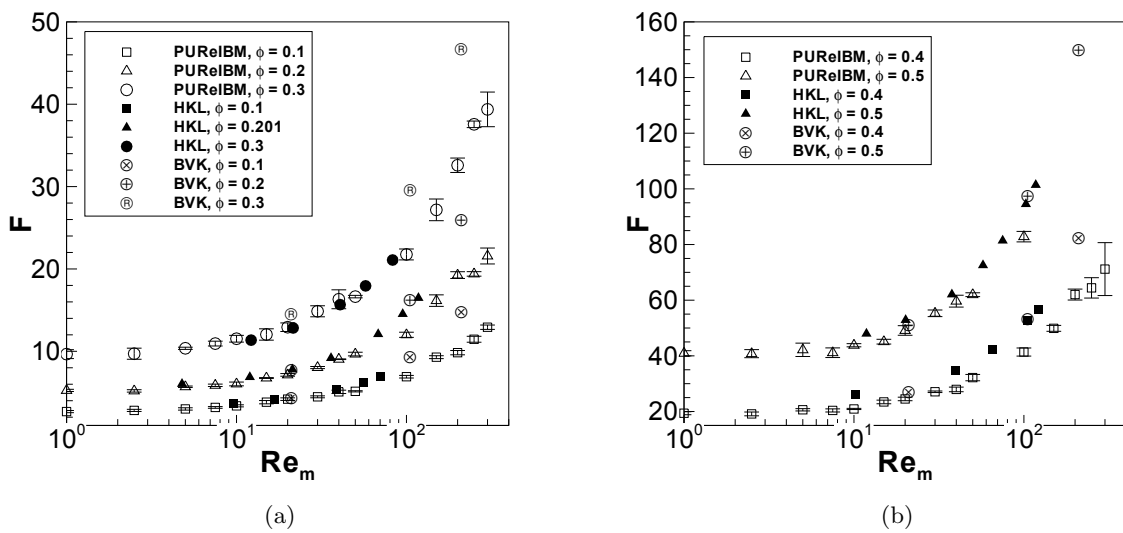


Figure 2.11 Variation of normalized force with Reynolds number for random assembly of fixed particles. Drag values obtained from PUREiBM simulations (open symbols) are compared with those reported by HKL (filled symbols) and BVK. In left panel (a)  $\phi = 0.1, 0.2, 0.3$  and in the right panel (b)  $\phi = 0.4, 0.5$ . The error bars on the symbols in this figure represent 95% confidence intervals in the estimation of the normalized force.

We can see from table 3.1 that the numerical resolution used by HKL and in PReIBM simulations are comparable up to  $Re_m = 100$ . The grid resolutions reported for HKL in table 3.1 are those used for the highest Reynolds numbers that they simulated. HKL used much coarser meshes to simulate lower Reynolds numbers. For  $Re_m > 100$  the PReIBM simulations are performed with much higher resolutions and HKL did not perform any simulations for  $Re_m > 100$  for most volume fractions. A comparison of the simulation data with the drag correlation proposed by HKL showed that beyond  $Re_m = 100$ , differences between the PReIBM simulation data and the HKL drag correlation increased with increasing  $Re_m$ . Since HKL did not explore a wider range of Reynolds numbers, this work provides a more accurate variation of the normalized force with Reynolds number.

From figure 2.11 we see that PReIBM drag values differ substantially from those reported by BVK. A difference of about 30% is consistently observed at a Reynolds number of 200 for all volume fractions while a difference of 20% is observed at a Reynolds number of 100. BVK used a constant resolution of 17.5 lattice units across a particle diameter was for  $\phi \leq 0.2$ , and for higher volume fractions, their results were obtained by averaging the drag obtained using two different resolutions of 17.5 and 25.5 lattice units. Therefore, in table 3.1, we have used the average value of 21.5 lattice units to report their resolutions for  $\phi \geq 0.3$ . At a given volume fraction, they used a constant grid resolution to simulate Reynolds numbers ranging from 21 to 1000. As the volume fraction increases, the number of grid/lattice nodes in the gaps between the spheres decrease and a progressively higher grid resolution is required. In the HKL study the particle resolution was increased from 9.6 lattice units per particle diameter for the lowest volume fraction of 0.1 to 41.6 lattice units for the highest volume fraction of 0.641, which is a four-fold increase. However, in the BVK study the particle resolution increased by only a fraction for a wide volume fraction range of 0.1-0.6. Table 3.1 shows that the PReIBM simulations are consistently better resolved in terms of the number of particles, grid resolution, and the box-size. BVK performed greater number of MIS but the scatter in PReIBM data does not point to a need for such high number of MIS. In addition to the numerical parameters, PReIBM and BVK simulations differ in the simulation setup. While PReIBM simulations are performed using setup A, the simulations of BVK are performed using setup A'.

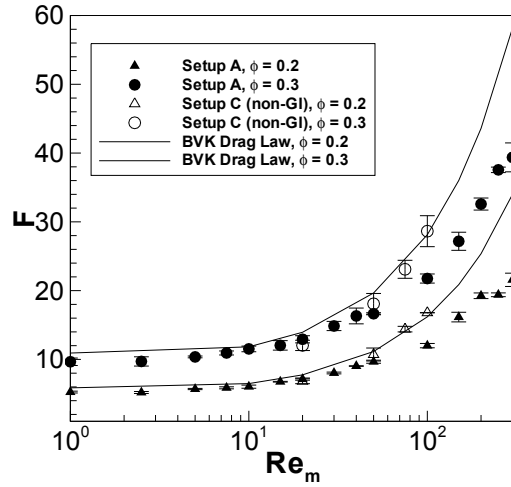


Figure 2.12 Plot showing the variation of normalized fluid–particle force with mean slip Reynolds number for a random array at two different volume fractions ( $\phi = 0.2, 0.3$ ). Results obtained from both setups A and C are shown. The BVK drag correlation (lines) is also shown for comparison.

We also studied the effect of using a non–GI setup to simulate flow past random arrays at higher Reynolds numbers. We performed PReIBM simulations of flow past random arrays using the setup C for two different volume fractions (0.2 and 0.3). Figure 2.12 shows the variation of the normalized fluid–particle force with Reynolds number obtained from setups A and C. It is interesting to note from this figure that the force obtained from setup C is in excellent agreement with the BVK drag correlation.

To summarize, PReIBM simulations show an excellent match with the drag correlations proposed by HKL and BVK for low Reynolds number for both dilute and moderately dense random arrays. However, PReIBM simulations show a significant departure from these correlations at higher  $Re_m$ . The drag law proposed by HKL is stated to be more reliable for all Reynolds numbers only at higher volume fraction. The BVK drag correlation is proposed based on a fit to the drag values obtained from simulating only 5 different Reynolds numbers between 20 and 1000, and their simulations are not as highly resolved as PReIBM simulations and they might not be grid independent. Owing to the differences in the solution approach and numerical resolutions between PReIBM and LBM based studies, an independent verification

with a body-fitted solver is required to assess the accuracy of PReIBM and LBM simulations of flow past fixed assemblies of randomly distributed particles with finite fluid inertia. In the following subsection we compare results from PReIBM simulations with those obtained from a body-fitted grid.

### 2.8.1 Comparison of PReIBM with body-fitted grid simulations

We assess the accuracy of PReIBM simulations by comparing the results obtained from PReIBM with those obtained by solving the same problem using ANSYS-FLUENT, which uses a body-fitted solver. We simulated flow past the same random configuration using PReIBM and ANSYS-FLUENT to directly compare pressure and velocity fields. This random configuration was taken from one of the 5 independent configurations that we simulated using PReIBM at a volume fraction of 0.4 and mean flow Reynolds number of 100.

We performed a grid refinement study of the ANSYS-FLUENT solver by simulating flow past the chosen random configuration using four different resolutions. The coarsest mesh we used has 60,000 tetrahedral cells while the finest mesh has 3.25 million tetrahedral cells. We used a second-order upwind method for the discretization the convective terms and the simulation was stopped after the scaled residuals dropped by six orders of magnitude and the drag acting on the suspension reached a steady state. In figure 2.13, we show the grid-convergence characteristics of the normalized force obtained from both ANSYS-FLUENT and PReIBM simulations. Grid resolution of ANSYS-FLUENT is shown on the bottom  $x$ -axis while that of PReIBM simulations (open triangles) is shown on the top. From the figure we conclude that the results obtained from PReIBM and ANSYS-FLUENT simulations are numerically converged. Moreover, the grid-independent drag value obtained from the PReIBM simulation on the finest mesh ( $D_m = 40$ ) is within 1% of the grid independent drag value that is obtained from the ANSYS-FLUENT simulation. We also show the drag predicted by the LBM simulations of BVK (open circle) on this plot. Their simulations correspond to  $D_m = 21.5$  and it is clear that the value predicted by the BVK drag law does not agree well with that predicted by PReIBM or ANSYS-FLUENT. Since the drag law of BVK is obtained by averaging over 20 different particle configurations, this difference in drag cannot be attributed

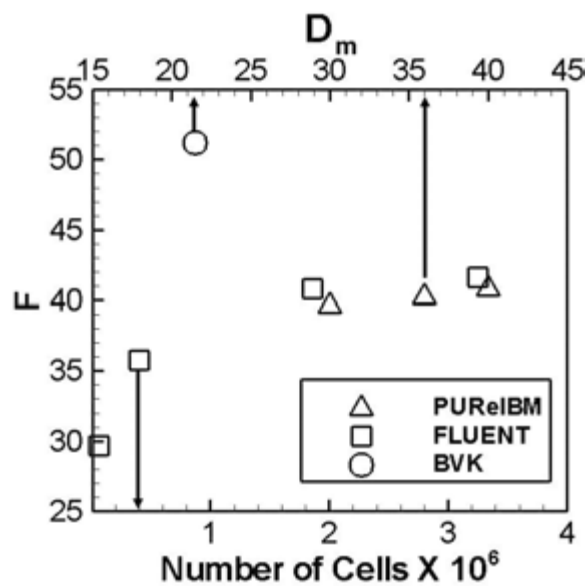


Figure 2.13 Plots showing the grid convergence of ANSYS–FLUENT software and PUReIBM. Grid resolution of ANSYS–FLUENT (squares) corresponds to the bottom  $x$ -axis while the grid resolution of PUReIBM simulations (triangles) is shown in the top  $x$ -axis. The drag value reported by BVK at this volume fraction (0.4) and Reynolds number (100) is also shown for reference.

to the dependence on particle configurations.

We also compared the velocity and pressure fields obtained from PUReIBM and ANSYS–FLUENT simulations. Figure 2.14 shows contours of the streamwise component of fluid velocity while figure 2.15 shows the contours of pressure on a cut–plane in the middle of the box. In this figure the flow is from left to right. It is important to remember that PUReIBM uses a pseudo–spectral method on Cartesian grids while ANSYS–FLUENT uses a finite volume method on a body–fitted mesh. Given the differences between the differencing operators and the nature of interpolation errors in the two codes, the agreement obtained in figures 2.14 and 2.15 is excellent. Thus we conclude that PUReIBM computes solutions to the governing equations for gas–solids flow with an accuracy comparable to that of a body–fitted solver.

Since the drag in PUReIBM is computed from this flow solution by calculating stress at the particle surface, this gives confidence that the surface force density that is used to calculate the total drag is indeed accurately computed. Using PUReIBM we can look at the relative contribution of pressure and viscous terms to the total drag and also the local profiles of

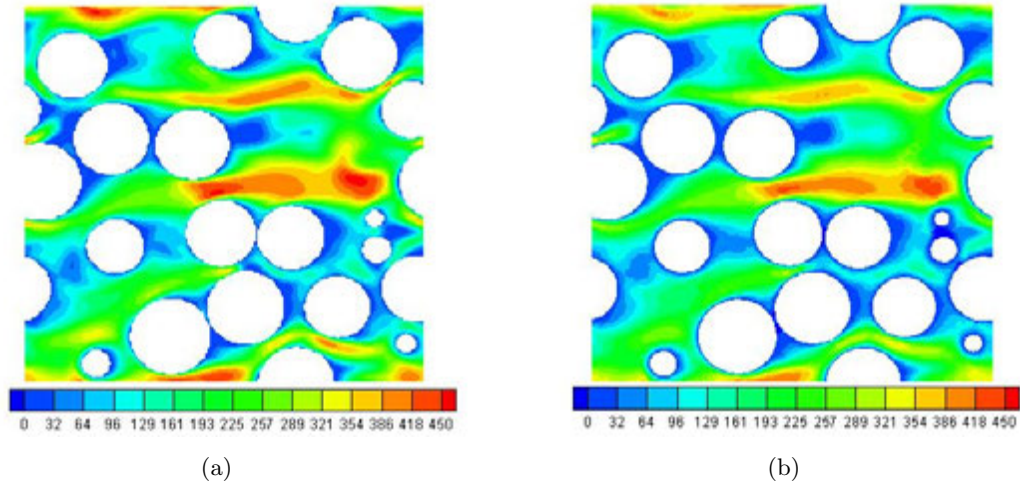


Figure 2.14 Plots comparing the contours of the Reynolds number based on the streamwise component of the instantaneous fluid velocity obtained from PUREIBM (2.14(a)) with those obtained from ANSYS-FLUENT software (2.14(b)).

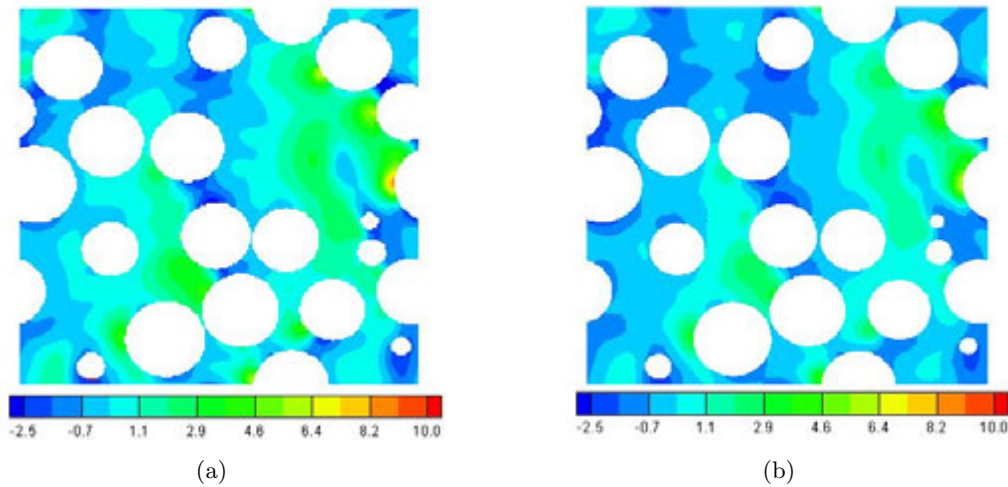


Figure 2.15 Plots comparing the contours of instantaneous dimensionless pressure ( $p^* = p/(\frac{1}{2}\rho_f |\langle \mathbf{W} \rangle|^2)$ ) obtained from PUREIBM (2.15(a)) with those obtained from ANSYS-FLUENT software (2.15(b)).

pressure and viscous drag forces.

### 2.8.2 Relative contributions of pressure and viscous drag

At steady state, the mean pressure gradient is balanced by the pressure and viscous forces acting on all the particles such that

$$-(1 - \phi) V \langle \mathbf{g}_{\text{IBM}} \rangle_{\mathcal{V}} = - \oint_{\partial \mathcal{V}_s} \psi \mathbf{n}^{(s)} dA + \mu_f \oint_{\partial \mathcal{V}_s} (\nabla \mathbf{u}') \cdot \mathbf{n}^{(s)} dA, \quad (2.37)$$

where the total force acting on the suspension is  $-\langle \mathbf{g}_{\text{IBM}} \rangle_{\mathcal{V}} V$ . The average force acting per particle,  $\langle \mathbf{f} \rangle$ , is obtained by dividing the total force by the total number of particles:

$$\langle \mathbf{f} \rangle = -\frac{1}{N_p} \langle \mathbf{g}_{\text{IBM}} \rangle_{\mathcal{V}} V.$$

Dividing equation (2.37) by  $N_p$ , the average force per particle is the sum of average pressure force per particle  $\langle \mathbf{f}_p \rangle$  and average viscous force per particle  $\langle \mathbf{f}_v \rangle$ , i.e.,

$$(1 - \phi) \langle \mathbf{f} \rangle = \langle \mathbf{f}_p \rangle + \langle \mathbf{f}_v \rangle. \quad (2.38)$$

While the vector equation 2.38 is always true, the following scalar equation for the normalized force  $F$  ( $F = |\langle \mathbf{f} \rangle|/F_{\text{Stokes}}$ )

$$(1 - \phi) F(\phi, \text{Re}_m) = F_p(\phi, \text{Re}_m) + F_v(\phi, \text{Re}_m) \quad (2.39)$$

holds only when the vectors  $\langle \mathbf{f}_p \rangle$  and  $\langle \mathbf{f}_v \rangle$  are collinear. Here  $F_p$  and  $F_v$  are the magnitudes of the average pressure and viscous forces per particle normalized by  $F_{\text{Stokes}}$ . We verified that the pressure and viscous forces are collinear over a wide range of volume fraction and Reynolds numbers and hence the sum of the normalized pressure and viscous forces give the total normalized force.

The scaling of normalized pressure and viscous forces with mean flow Reynolds number gives insight into the powers of  $\text{Re}_m$  that should be used in the drag law for the total force. Simple scaling arguments dictate that the pressure force  $|\langle \mathbf{f}_p \rangle| \sim \rho_f U_{\text{slip}}^2 D^2$  and the viscous force  $|\langle \mathbf{f}_v \rangle| \sim \mu_f U_{\text{slip}} D$ . Normalizing the magnitudes of pressure and viscous forces by  $F_{\text{Stokes}}$ , it is easy to see that the normalized pressure force varies linearly with Reynolds number and

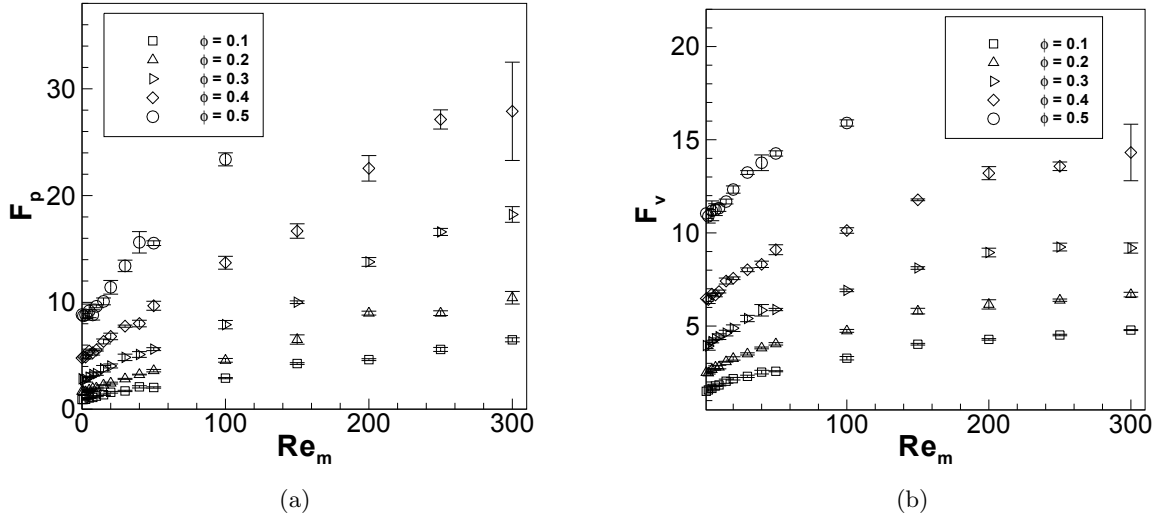


Figure 2.16 Plots showing the pressure and viscous drag force in a random configuration.

the normalized viscous force is independent of the Reynolds number. So taking  $F_p \sim Re_m$  and  $F_v$  independent of  $Re_m$  led HKL to propose the following form of the drag law at moderate Reynolds numbers:

$$F(\phi, Re_m) = F_2(\phi) + F_3(\phi) Re_m \quad (2.40)$$

where,  $F_2(\phi)$  represents  $F_v$  and  $F_3(\phi)$  represents the volume fraction dependence of  $F_p$ . HKL assumed that the viscous contribution to the drag force remains constant for all Reynolds numbers, but this was not verified from simulations. However, as figure 2.16 shows, the viscous drag is not independent of the Reynolds number but it is a sublinear power of the mean flow Reynolds number. Figure 2.16 confirms the assumption of HKL that the pressure drag is approximately linear for larger Reynolds numbers ( $Re_m > 40$ ).

From PUREIBM simulations we observe that at any given Reynolds number, the ratio  $F_p/F_v$  increases with increasing volume fraction. At a given volume fraction,  $F_p/F_v$  increases with Reynolds number as expected. However, the viscous contribution does not become negligible compared to pressure drag. In fact, for volume fractions 0.1 and 0.2 the ratio  $F_p/F_v$  exceeds 1 only when  $Re_m > 100$ . We also observed that the Reynolds number at which the pressure drag exceeds the viscous drag decreases with increasing volume fraction.

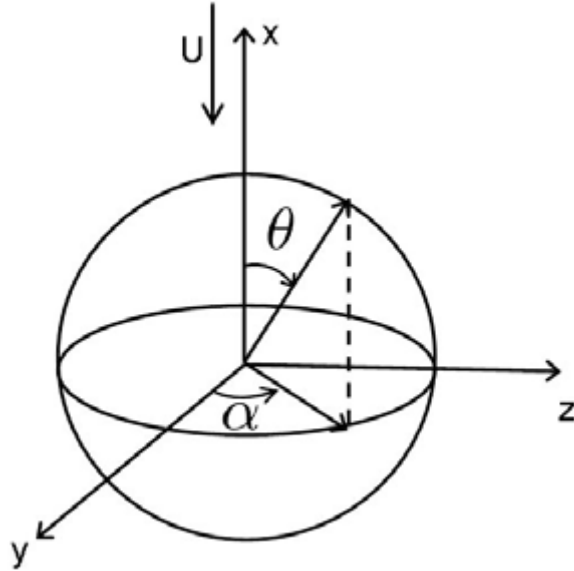


Figure 2.17 Schematic of the spherical coordinate system used to define the local pressure and viscous drags. The polar angle in our convention is  $\theta$  ( $0 \leq \theta \leq \pi$ ) and the azimuthal angle is  $\alpha$  ( $0 \leq \alpha \leq 2\pi$ ).

### 2.8.3 Local profiles of pressure and viscous contributions to the fluid–particle drag force

Profiles of the local pressure and viscous drag can provide insight into the behavior of the pressure and viscous drag with varying mean flow Reynolds numbers and volume fractions. We examine the local profiles of pressure and viscous forces to facilitate the development of a drag law and to see if any self–similar scaling would emerge.

We define the local pressure and viscous drags with respect to the spherical coordinate system shown in figure 2.17. It is useful to define a unit vector  $\mathbf{e}_{\parallel} = \langle \mathbf{W} \rangle / |\langle \mathbf{W} \rangle|$  along the mean slip direction. In this work since the mean slip is along the direction of the flow, we refer to the direction of the mean slip as the streamwise direction. We examine the profiles of the streamwise components of the average pressure and viscous forces per particle along the polar angle. For every particle in the  $\mu^{\text{th}}$  realization the variation of the streamwise component of pressure and viscous forces along the polar angle is computed by averaging out the dependence on the azimuthal angle. The variations of average pressure and viscous forces per particle along the polar angle are then computed by averaging the local profiles over all the particles.

The streamwise components of the average pressure and viscous forces per particle in the  $\mu^{\text{th}}$  realization can be expressed as:

$$\begin{aligned} F_{p,\mu}^{\text{loc}}(\theta) &= \frac{1}{N_p} \sum_{n=1}^{N_p} \left( \int_0^{2\pi} -\psi(\theta, \alpha) \mathbf{n}^{(n)} \cdot \mathbf{e}_{\parallel} d\alpha \right) 4\pi R^2, \\ F_{v,\mu}^{\text{loc}}(\theta) &= \frac{\mu_f}{N_p} \sum_{n=1}^{N_p} \left( \int_0^{2\pi} (\nabla \mathbf{u}'(\theta, \alpha) \cdot \mathbf{n}^{(n)}) \cdot \mathbf{e}_{\parallel} d\alpha \right) 4\pi R^2. \end{aligned} \quad (2.41)$$

In the above equations,  $\mathbf{n}^{(n)}$  is the unit normal vector pointing outward from the surface of the  $n^{\text{th}}$  particle and  $R = D/2$  is the radius of the particle. An ensemble-averaged estimate for the local pressure ( $F_p^{\text{loc}}$ ) and viscous ( $F_v^{\text{loc}}$ ) forces is then defined similar to equation (2.34). In figure 2.18 we plot the local coefficient of pressure  $C_p^{\text{loc}}(\theta)$  and the local skin friction coefficient  $C_f^{\text{loc}}(\theta)$  along the polar angle for different volume fractions and mean flow Reynolds numbers. The definitions of local coefficient of pressure and the local skin friction coefficient are similar to those used for a single sphere in an unbounded medium:

$$\begin{aligned} C_p^{\text{loc}}(\theta) &= \frac{F_p^{\text{loc}}(\theta)}{\frac{1}{2} \rho_f \pi R^2 ((1-\phi) |\langle \mathbf{W} \rangle|)^2}, \\ C_f^{\text{loc}}(\theta) &= \frac{F_v^{\text{loc}}(\theta)}{3\pi \mu_f D (1-\phi) |\langle \mathbf{W} \rangle|}. \end{aligned} \quad (2.42)$$

The local profiles of pressure drag for different volume fractions at a mean flow Reynolds number of 100 are shown in figure 2.18(a). Although there appears to be a local minimum at  $\theta = 75^\circ$  for all the volume fractions we can see that there is no evident self-similarity in these profiles. The behavior of the local pressure profiles at the “trailing edge” is different for different volume fractions. In figure 2.18(c) we plot the local skin friction coefficient for different volume fractions at a Reynolds number of 100. As expected, maxima of the viscous drag are found at locations where the pressure drag has a minima.

In figure 2.18(b) we show the local pressure profiles for different mean flow Reynolds numbers at a volume fraction of 0.2 while the skin friction coefficients are plotted in figure 2.18(d). We can see that at  $\text{Re}_m = 20$  the pressure drag nearly follows a sinusoidal profile up to an angle of  $110^\circ$  and remains approximately constant beyond this angle. This behavior is similar to that observed for a single sphere in an unbounded fluid, where the pressure nearly obeys the

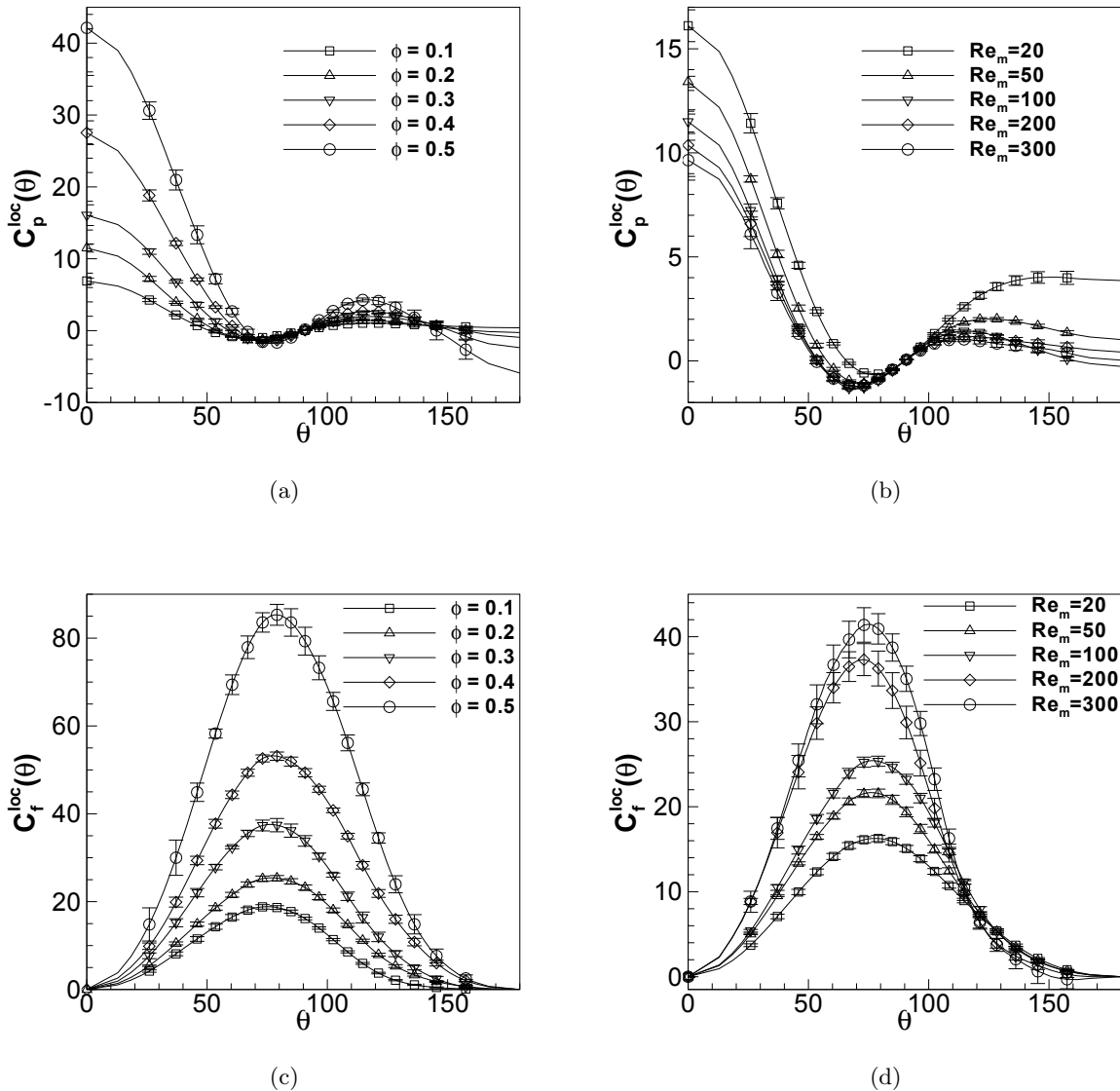


Figure 2.18 Profiles of local coefficient of pressure and coefficient of friction along the polar angle. Figure 2.18(a) shows the local pressure profiles for different volume fractions at a Reynolds number of 100 while figure 2.18(b) shows the local pressure profiles for various mean flow Reynolds numbers at a volume fraction of 0.2. Similarly figure 2.18(c) shows the local viscous drag profiles for different volume fractions at a Reynolds number of 100 while figure 2.18(d) shows the local viscous drag profiles for various mean flow Reynolds numbers at a volume fraction of 0.2.

potential flow solution up to the point of separation and remains constant beyond this point. Also, at this volume fraction, for  $\text{Re}_m > 100$  the profiles of  $C_p^{\text{loc}}$  nearly collapse onto a single curve again verifying the assumption that the pressure drag is quadratic in mean slip velocity.

The local profiles of pressure and viscous forces in random assemblies can be viewed as departures from those observed for an isolated sphere in an unbounded medium. These observations point to the fact that the drag law for random assemblies should be in the form of corrections to the single sphere drag law that reflect the dependence on  $\phi$  and  $\text{Re}_m$ . It is clear that there is no obvious self-similarity that collapses the local pressure and viscous drag profiles as simple functions of volume fraction and Reynolds number.

## 2.9 A new correlation for the average fluid-particle drag

Based on the normalized force values obtained from PReIBM simulations, the following function fits the data well with an average deviation of 2.5%:

$$F(\phi, \text{Re}_m) = \frac{F_{\text{isol}}(\text{Re}_m)}{(1-\phi)^3} + F_\phi(\phi) + F_{\phi, \text{Re}_m}(\phi, \text{Re}_m). \quad (2.43)$$

Here,  $F_{\text{isol}}$  is the drag force acting on an isolated sphere moving in an unbounded medium. We used the single sphere drag correlation proposed by Schiller and Naumann (1935) to get the drag on an isolated sphere. The remaining two terms in (3.24) are given by

$$\begin{aligned} F_\phi(\phi) &= \frac{5.81\phi}{(1-\phi)^3} + 0.48 \frac{\phi^{1/3}}{(1-\phi)^4}, \\ F_{\phi, \text{Re}_m}(\phi, \text{Re}_m) &= \phi^3 \text{Re}_m \left( 0.95 + \frac{0.61\phi^3}{(1-\phi)^2} \right). \end{aligned}$$

Figure 2.19 compares the PReIBM drag law given by (3.24) with the existing drag correlations. We used the drag correlations of HKL, BVK, Gidaspow (1986) and Syamlal and O'Brien (1987) (referred to as S&B in figure 2.19) for comparison. The drag values computed from PReIBM and HKL drag laws agree well upto  $\text{Re}_m = 100$ . By extending the HKL drag correlation beyond  $\text{Re}_m = 100$ , we noticed that the differences between PReIBM and HKL drag law increase with Reynolds number. However, since HKL drag correlation is valid only upto  $\text{Re}_m = 100$ , comparison is not made beyond this Reynolds number. Differences between the BVK and PReIBM drag law are more pronounced and increase significantly with increasing

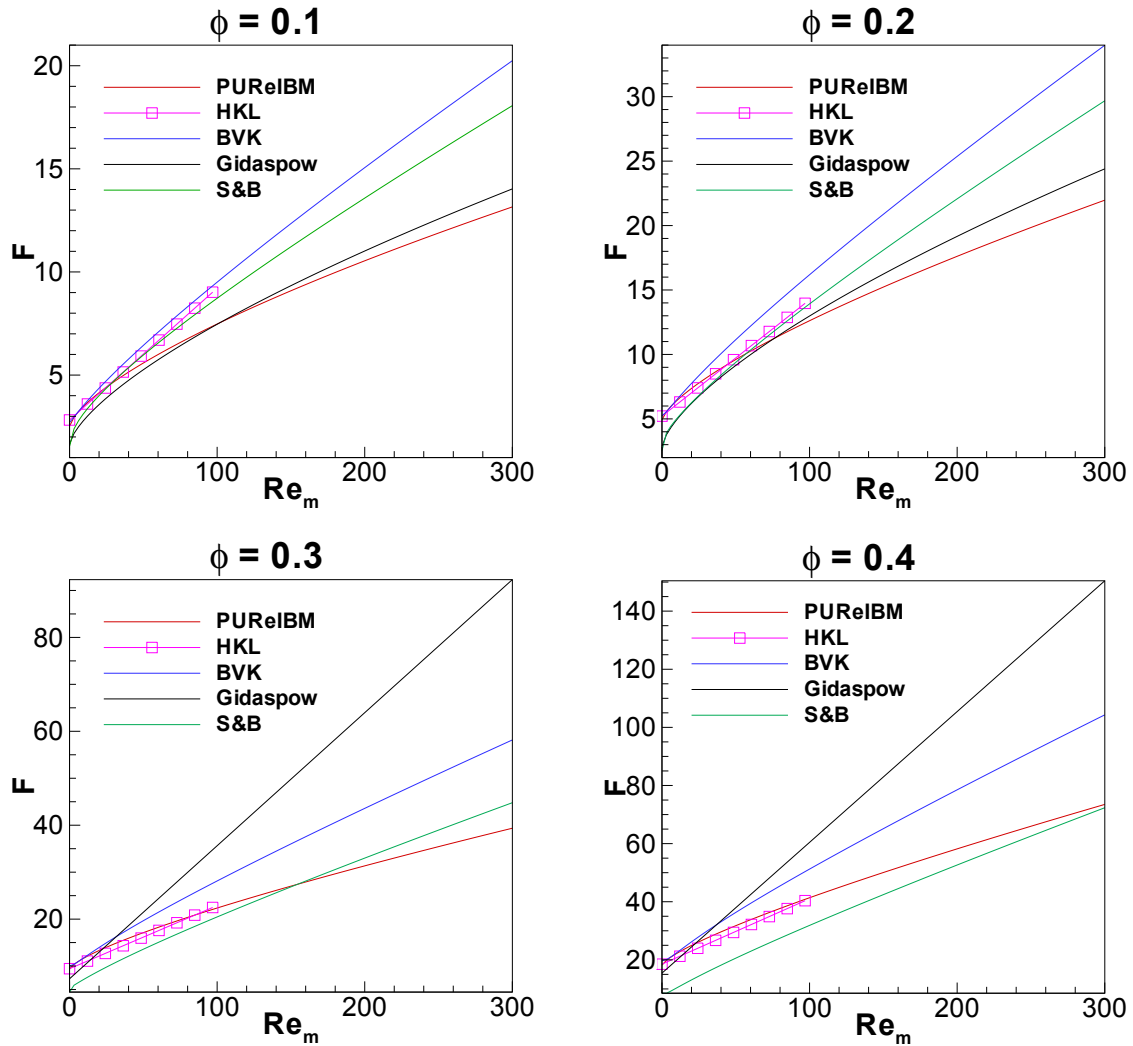


Figure 2.19 DingDong Plot comparing the normalized force values obtained from the PReIBM drag law (cf. 3.24) with those obtained from the drag laws of HKL, BVK, Gidaspow (1986) and Syamlal and O'Brien (1987) for four different solid volume fractions. The volume fraction at which the drag values are computed is shown at the top of each panel. For every volume fraction, the HKL drag law terminates at  $Re_m = 100$  since it is not valid beyond that Reynolds number.

Reynolds number. At the largest Reynolds number that we simulated ( $Re_m = 300$ ) PReIBM and BVK drag laws differ by about 38%. This difference is observed consistently at all volume fractions. The power law dependence of drag on Reynolds number predicted by each of these drag laws is also different.

Also shown in figure 2.19 is the comparison between PReIBM and the drag correlations of Gidaspow (1986) and Syamlal and O'Brien (1987), which are widely used in CFD simulations of gas–solid flow. Gidaspow's drag law reduces to the Wen–Yu drag law (Wen and Yu, 1966) when the solid volume fraction is less than 0.2 and for volume fractions greater than 0.2 it reduces to the Ergun equation (Ergun, 1952). Syamlal and O'Brien (1987) derived their drag law by converting terminal velocity correlations (Richardson and Zaki, 1954) to drag correlations. The behavior of these two drag laws with volume fraction and Reynolds number is very different from that of the PReIBM drag law. We estimate that numerical error and statistical variability due to finite number of configurations contribute to an uncertainty of about 5% in the estimate of mean drag from PReIBM simulations. So we conclude that differences of more than 30% observed in the values of drag obtained from PReIBM and the BVK drag law are significant and can play an important role in the predictive capability of two–fluid model.

## 2.10 Summary

In this work we studied the steady drag in gas–solids flow with finite fluid inertia using particle–resolved DNS of flow past fixed monodisperse particle assemblies. We employ the Particle–resolved Uncontaminated–fluid Reconcilable Immersed Boundary Method (PReIBM) to perform particle–resolved DNS of flow past fixed particle assemblies. In PReIBM, the continuum Navier–Stokes equations with no-slip and no-penetration boundary conditions on each particle's surface are solved using an immersed boundary (IB) forcing term that is added to the momentum equation. The IB forcing in PReIBM is solely restricted to those grid points that lie in the solid phase, and therefore the flow solution in the fluid phase is uncontaminated i.e., the unmodified Navier–Stokes equations are solved in the fluid phase. Through a comprehensive suite of tests it is demonstrated that PReIBM is an accurate and numerically convergent

particle-resolved DNS approach. We compared PReIBM for flow past fixed particles at solid volume fraction of 0.4 and mean flow Reynolds number of 100 with ANSYS-FLUENT, which uses a body-fitted solver. We observed that the difference in the value of drag obtained from both methods is about 1%, and we obtained an excellent match of the velocity and pressure fields. Thus we conclude that PReIBM computes solutions to the governing equations for gas-solids flow with an accuracy comparable to that of a body-fitted solver.

The normalized force values obtained from PReIBM agree reasonably well with HKL drag law over a fairly wide range of volume fractions and mean flow Reynolds numbers. PReIBM drag values differ by about 25% from the HKL drag law and by 38% from the BVK drag law at the largest Reynolds number that we simulated ( $Re_m = 300$ ), and this difference is observed consistently at all volume fractions. Our simulations reveal a weak power-law dependence of the viscous drag on  $Re_m$ , reaching an asymptote at  $Re_m > 200$  for all volume fractions. This replaces the prevailing notion that the viscous drag is independent of  $Re_m$  (Hill et al., 2001b). For pressure drag, we concur with HKL that at moderate Reynolds numbers the pressure drag can be approximated by a linear function in  $Re_m$ .

A new drag law for monodisperse suspensions is proposed using PReIBM simulations of flow past fixed particle assemblies. Since this drag law is inferred from fixed particle assemblies, the effect of the mobility of particles is not captured in the drag correlation. However, the fixed bed approximation is valid for high Stokes number particles that are characteristic of gas-solid flows. The differences between the PReIBM drag law and BVK drag law are more than 30% for  $Re_m > 200$ . The drag law is used to model the unclosed average interphase momentum transfer term in the mean momentum conservation equation of the two-fluid theory and determines the overall mean gas-solids flow structure. This improved PReIBM drag law can enhance the predictive capability of CFD simulations of gas-solids flow that are based on the two-fluid theory. The improved drag law can also be used to refine the stability limits for gas-solid suspensions since these limits are determined by the functional dependence of drag on volume fraction.

### CHAPTER 3. Quantification of gas–phase velocity fluctuations in statistically homogeneous gas–solid flow using particle–resolved direct numerical simulation

This chapter is a manuscript titled “Quantification of gas–phase velocity fluctuations in statistically homogeneous gas–solid flow using particle–resolved direct numerical simulation” that is currently in preparation. This manuscript is authored by S. Tenneti, R. Garg and S. Subramaniam.

#### Abstract

Gas–phase velocity fluctuations are quantified using particle–resolved direct numerical simulation (PR–DNS). The kinetic energy associated with the gas–phase velocity fluctuations  $k_f$  in steady flow past fixed random assemblies of monodisperse spheres is characterized as a function of solid volume fraction  $\phi$  and the Reynolds number based on the mean slip velocity  $Re_m$ . The PR–DNS approach is based on a formulation we refer to as the Particle–resolved Uncontaminated–fluid Reconcilable Immersed Boundary Method (PUREIBM). A simple scaling analysis is used to explain the dependence of  $k_f$  on  $\phi$  and  $Re_m$ . The steady value of  $k_f$  results from the balance between the source of  $k_f$  due to interphase transfer of kinetic energy, and the dissipation ( $\varepsilon_f$ ) of  $k_f$  in the gas–phase. It is found that it is appropriate to model the dissipation of  $k_f$  in gas–solid flows using a length scale that is analogous to the Taylor microscale used in single–phase turbulence. Using the PUREIBM PR–DNS data for  $k_f$  and  $\varepsilon_f$  we also infer an eddy viscosity for gas–solid flow.

### 3.1 Introduction

Gas-solid flows are encountered in industrial devices such as fluidized beds and in pneumatic conveying. It is generally agreed that gas-phase velocity fluctuations and particle-particle interactions play an important role in such gas-solid flows. For instance, the gas-solid flow in circulating fluidized bed risers is characterized by the tendency of the particles to segregate towards the pipe wall (Miller and Gidaspow, 1992). This can in turn affect the particle-wall heat transfer. Gas-phase velocity fluctuations also affect the heat transfer and mixing of chemical species inside the fluidized bed.

Device-scale calculations using computational fluid dynamics (CFD) simulations of multiphase flow are a promising route to inexpensive design and scale-up of industrial process equipment (Halvorsen et al., 2003; Kashiwa and Gaffney, 2003; Sun et al., 2007). CFD of multiphase flow involves solving the averaged equations for mass, momentum and energy in both the solid and fluid phases. Figure 4.1 shows a schematic of the computational domain in a typical CFD simulation of gas-solid flow. In every grid cell, conservation equations for averaged quantities such as volume fraction, and velocity are solved for both phases. These conservation equations are obtained using a statistical averaging procedure (Anderson and Jackson, 1967; Drew and Passman, 1998), and hence the solution to these average equations involves modeling the unclosed terms that represent interphase interactions. The conservation equation for mean momentum in the gas phase requires models for the average interphase momentum transfer and the transport of the second moments of the fluctuating velocity (Reynolds stress) in the gas phase. The average interphase momentum transfer has been extensively studied and there is a general consensus on drag models (Ergun, 1952; Wen and Yu, 1966; Syamlal and O'Brien, 1987; Gidaspow, 1994; Hill et al., 2001a,b; van der Hoef et al., 2005; Beetstra et al., 2007; Tenneti et al., 2011). However, the gas-phase Reynolds stress has not been comprehensively quantified in the parameter range corresponding to fluidized beds.

Nevertheless there is some evidence to indicate that gas-phase velocity fluctuations can be significant. Intrusive hot wire measurements by Moran and Glicksman (2003) indicate that the level of gas-phase velocity fluctuations can be significant in a circulating fluidized bed

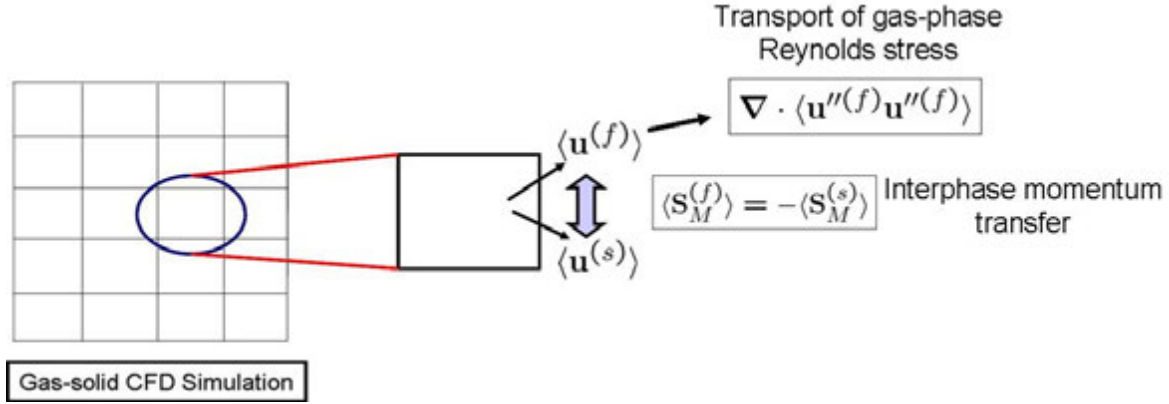


Figure 3.1 Schematic of a CFD simulation of gas–solid flow. In every computational grid cell, governing equations for the averaged quantities in both phases are solved. Here  $\langle \mathbf{u}^{(f)} \rangle$  is the average gas–phase velocity and  $\langle \mathbf{u}^{(s)} \rangle$  is the average solid–phase velocity. The average interphase momentum transfer  $\langle \mathbf{S}_M^{(f)} \rangle = -\langle \mathbf{S}_M^{(s)} \rangle$  that represents the coupling between the solid and the gas–phase appears as an unclosed term in both equations. Also, the transport of Reynolds stress in each phase is an unclosed term in the average momentum equation of that phase. Here  $\mathbf{u}''^{(f)}$  denotes the fluctuating velocity in the gas–phase.

riser at dilute solid volume fraction. In dense gas–solid flows non–intrusive measurements are difficult because of limited optical access, and the effect of intrusive instrumentation could alter the flow considerably. Although various numerical studies have been performed to understand the effect of particles on the flow turbulence, the vast majority of existing work (Squires and Eaton, 1991; Elghobashi and Truesdell, 1993; Boivin et al., 1998; Sundaram and Collins, 1999; Mashayek and Taulbee, 2002) addresses particle–turbulence interactions with particle diameter  $D$  smaller than the Kolmogorov scale of turbulence  $\eta$ . In industrial applications of gas–solids flow such as fluidized beds (Moran and Glicksman, 2003), the particle diameter  $D$  is usually larger than the Kolmogorov length scale  $\eta$ . There are relatively few studies (Uhlmann, 2008; Xu and Subramaniam, 2010; Lucci et al., 2011) for particles with  $D > \eta$ , and but for one study (Xu and Subramaniam, 2010) these focus on flows with nonzero mean slip velocity. Unlike in single–phase turbulence, the mean slip velocity is an important parameter in gas–solid flows with  $D > \eta$ . Therefore, there is a need to quantify the gas–phase Reynolds stress over a range of solids volume fraction and Reynolds number based on the mean slip velocity between the solid and gas–phase.

In the absence of such comprehensive quantification, the gas-phase Reynolds stress term is sometimes neglected in CFD simulations of dense gas-solid flow on the grounds that the dominant forces in the gas-phase momentum balance are the pressure drop and drag force (Hrenya and Sinclair, 1997). When models (Benyahia et al., 2005) for the transport of gas-phase Reynolds stress are used, such as in the widely used gas-solid flow CFD code MFIX (Syamlal et al., 1993), these models are simple extensions of single-phase turbulence models that have not been validated in canonical flows. Similarly, due to the lack of data for the gas-phase Reynolds stress at low volume fractions, this term is also neglected in some CFD simulations of dilute gas-solid flow (Agrawal et al., 2001). However, CFD simulations of gas-solid flow in circulating fluidized beds that incorporated a model for the transport of the gas-phase Reynolds stress generally showed good agreement for mean flow velocity profiles with experiments (Bolio et al., 1995; Bolio and Sinclair, 1995; Crowe, 2000; Zhang and Reese, 2003; Benyahia et al., 2005). These observations along with the measurements of Moran and Glicksman (2003) indicate that quantification and modeling of the gas-phase Reynolds stress is necessary.

In some studies (Ahmadi and Ma, 1990b; Bolio and Sinclair, 1995; Balzer et al., 1998; Benyahia et al., 2005) the gas-phase Reynolds stress term is modeled using an eddy viscosity in a fashion similar to single-phase turbulence. However, if the turbulent kinetic energy  $k_f$  and the dissipation rate  $\varepsilon_f$  were quantified in gas-solid flow, one could develop a validated eddy viscosity model. In other works (Ahmadi and Ma, 1990b,a; Bolio and Sinclair, 1995; Balzer et al., 1998; Benyahia et al., 2005) a two-equation approach with transport equations for  $k_f$  and  $\varepsilon_f$  that are modified to account for the presence of solid particles is used. There are also a few studies in which only a transport equation for  $k_f$  is solved (one-equation approach) and  $\varepsilon_f$  is modeled using a Kolmogorov scaling for dissipation (Ahmadi and Ma, 1990b,a; Kenning and Crowe, 1997; Crowe, 2000). A review of existing multiphase turbulence models can be found in Crowe et al. (1996).

Both the one-equation and two-equation approaches need accurate models for the generation and dissipation rate of  $k_f$ . The presence of particles and their changing configuration produces high levels of gas-phase velocity fluctuations, in addition to the turbulent motions already present in the gas phase. In order to account for the generation of gas-phase velocity

fluctuations by finite sized particles, Yuan and Michaelides (1992) proposed a model in which the velocity deficit in the wake of the particle is the source and the work done by the drag force is the dissipation of gas velocity fluctuations. Yarin and Hetsroni (1994) employed a similar idea but used a more detailed description of the wake. Although both models showed good agreement with experiments (Tsuji et al., 1984; Modarress et al., 1984), they are not derived by the application of detailed balance laws. Kenning and Crowe (1997) proposed a new turbulence model starting from the conservation equation of mechanical energy in gas–solid flow. In this model, work done by the particle drag force acts as a source for gas–phase velocity fluctuations. Dissipation of gas–phase velocity fluctuations is modeled along the lines of single–phase turbulence ( $\varepsilon_f \sim k_f^{3/2}/l_{\text{diss}}$ ). The length scale  $l_{\text{diss}}$  considered in their work corresponds to a hybrid length scale of inter–particle spacing and the dissipation length scale used in single–phase turbulence. This model was further improved and showed good agreement with experimental data obtained from particle–laden turbulent flow in pipes (Crowe, 2000).

Existing models for the gas–phase Reynolds stress in gas–solid flow that are widely used in CFD calculations are simple extensions of single–phase turbulence models. Most closure models do not distinguish between the velocity fluctuations generated by the presence of particles and inherent turbulence in the flow. This is because both these mechanisms essentially manifest themselves as a non–zero Reynolds stress in the gas–phase. However, because the physical mechanisms resulting in the generation and dissipation of these velocity fluctuations are different, one would expect that their scaling with nondimensional parameters could also be different. This would then imply that models for single–phase turbulence may not be adequate for modeling the pseudo–turbulent velocity fluctuations arising from the presence of particles. For instance, models used for the dissipation of turbulent kinetic energy are based on the Kolmogorov scaling ( $k_f^{3/2}/l_{\text{diss}}$ ) used in single–phase turbulence, but their validity in particle–laden flows is not verified. Furthermore, although two–equation  $k$ – $\varepsilon$  models are very widely used in CFD of gas–solid flows, the disadvantage of such models is that they cannot account for the anisotropy of the gas–phase Reynolds stress. Recent particle–resolved direct numerical simulation of flow past finite sized particles revealed that the Reynolds stress in the gas–phase is indeed highly anisotropic (Xu and Subramaniam, 2010). This anisotropic Reynolds stress

poses additional challenges in modeling gas–solid flows. Anisotropy in the Reynolds stress for the case of inherent turbulence in gas–solid flow with  $D < \eta$  has been accounted for in some recent models (Wang et al., 1998).

In this study we use direct numerical simulation to address these outstanding questions related to gas–phase velocity fluctuations in gas–solid flow. A popular numerical approach is the *point particle* direct numerical simulation methodology (Squires and Eaton, 1991; Elghobashi and Truesdell, 1993; Boivin et al., 1998; Sundaram and Collins, 1999; Mashayek and Taulbee, 2002) (DNS) in which the particles are treated as points and the effect of the particles on the gas–phase is represented by a force applied at the particle center. This approach is valid only when the particle size is much smaller compared to the Kolmogorov length scale. When the particle size is larger or comparable to the Kolmogorov length scale, the effects of the wake generated by the particles become important and hence it is important to resolve the boundary layers around the particle. For particles of size comparable to or larger than the Kolmogorov length scale, the appropriate numerical approach is the particle–resolved direct numerical simulation (PR–DNS) methodology in which all the scales of the inherent turbulence and the flow scales introduced by the presence of large particles are resolved. PR–DNS has been used to study the interaction of a single particle with decaying homogeneous isotropic turbulence (Bagchi and Balachandar, 2003; Burton and Eaton, 2005). PR–DNS has also been employed to study the effect of a collection of particles on decaying homogeneous isotropic turbulence (Lucci et al., 2011), particle–laden turbulent channel flow (Uhlmann, 2008) as well as gas–solid flow with upstream turbulence (Xu and Subramaniam, 2010). In fact, understanding the generation of gas–phase velocity fluctuations using PR–DNS has been identified as one of the future directions in the review article by Balachandar and Eaton (2010). Therefore, PR–DNS is appropriate to characterize the level of gas–phase velocity fluctuations in gas–solid suspensions of large, high Stokes number particles over a wide range of solid volume fraction and Reynolds number based on the mean gas–solid slip velocity.

We use PR–DNS to quantify the strength of gas–phase velocity fluctuations and the state of anisotropy of the gas–phase Reynolds stress tensor in steady flow through a statistically homogeneous fixed assembly of monodisperse spheres. To differentiate between the gas–phase

velocity fluctuations generated by the presence of particles and the inherent turbulence present in the flow field, we consider “laminar” gas–solids flow in this work. In the context of this work, “laminar” flow implies that there is no inherent turbulence in the flow field i.e. in the absence of particles, the flow field is not turbulent. In fixed–bed simulations the particles are held stationary and a steady flow is established by imposing a pressure gradient that corresponds to the desired flow rate. Use of the fixed–bed simulation methodology for gas–solid flows is justified if the configuration of the particles changes very slowly compared to the time it takes to attain mean momentum balance. The time scale over which the particle configuration changes depends on  $Re_T = DT^{1/2}/\nu_f$ , which is the Reynolds number based on the particle fluctuating velocity that is characterized by the particle granular temperature  $T$ . Particle–resolved simulations of freely evolving suspensions (Tenneti et al., 2010b) and recent high–speed imaging of particles (Cocco et al., 2010) show that this value of  $Re_T$  is low for high Stokes number suspensions. Moreover, using PR–DNS, Mehrabadi et al. (2012) observed that the level of gas–phase velocity fluctuations observed in freely evolving suspensions is close to that observed in fixed particle assemblies. The fixed–bed simulation setup has been used successfully to extract computational drag laws (Hill et al., 2001a,b; van der Hoef et al., 2005; Beetstra et al., 2007; Tenneti et al., 2011) as well as to understand the effect of particle clusters on gas–phase turbulence (Xu and Subramaniam, 2010). Using the data obtained from PR–DNS, we analyze the implications for modeling the dissipation rate of kinetic energy in the gas–phase by considering the energy balance equation similar to the work of Kenning and Crowe (1997). We also use the particle–resolved DNS data to propose an eddy viscosity for gas–solid flow in terms of solid volume fraction and mean flow Reynolds number.

The rest of the paper is organized as follows. In section 3.2 we define the ensemble–averaged quantities that are computed from PR–DNS. We briefly describe our PR–DNS approach and its validation in sections 3.3 and 3.4, respectively. The results quantifying the strength of gas–phase velocity fluctuations and anisotropy of gas–phase Reynolds stress in terms of solid volume fraction and mean flow Reynolds number are presented in section 3.6. The multiphase turbulence model derived using a simple scaling analysis is described in section 3.7. An eddy viscosity model for gas–solid flow is proposed in section 3.8, followed by the conclusions in

section 3.9.

### 3.2 Ensemble-averaged quantities

In the Eulerian two-fluid theory, the fluid-phase Reynolds stress is defined as a phasic average, which is an average conditional on the presence of the fluid phase Drew (1983); Drew and Passman (1998); Pai and Subramaniam (2009). If  $Q(\mathbf{x}, t)$  is any field, then its phasic average  $\langle Q^{(f)} \rangle(\mathbf{x}, t)$  referred to as its fluid-phase mean, is defined as:

$$\langle Q^{(f)} \rangle(\mathbf{x}, t) = \frac{\langle I_f(\mathbf{x}, t) Q(\mathbf{x}, t) \rangle}{\langle I_f(\mathbf{x}, t) \rangle}. \quad (3.1)$$

Here the fluid-phase indicator function  $I_f$  is unity if the point  $\mathbf{x}$  lies in the fluid-phase and zero otherwise.

Using this definition, the ensemble-averaged kinetic energy in the fluid phase  $\langle E^{(f)} \rangle$  is defined as

$$\langle E^{(f)} \rangle = \frac{1}{2} \frac{\langle I_f u_i u_i \rangle}{\langle I_f \rangle}, \quad (3.2)$$

where  $\mathbf{u}$  is the fluid velocity. It is easy to see that the average kinetic energy in the fluid phase is the sum of the kinetic energy in the mean fluid motion  $E_f$  and the average kinetic energy in the fluctuating motions  $k_f$ . The average kinetic energy in the mean fluid motion is given by  $E_f = \frac{1}{2} \langle u_i^{(f)} \rangle \langle u_i^{(f)} \rangle$ , where the quantity  $\langle u_i^{(f)} \rangle$  is the phase-averaged fluid velocity. The average kinetic energy in the fluctuating motion of the fluid is given by

$$k_f = \frac{1}{2} \frac{\langle I_f u_i''^{(f)} u_i''^{(f)} \rangle}{\langle I_f \rangle}, \quad (3.3)$$

where fluctuations in the fluid velocity field are defined with respect to the phase-averaged fluid velocity i.e.,  $u_i''^{(f)} = u_i - \langle u_i^{(f)} \rangle$ . We now describe how  $k_f$  is computed from solution of flow past statistically homogeneous suspensions using particle-resolved DNS.

#### 3.2.1 Quantifying gas-phase velocity variance from particle-resolved DNS

In PR-DNS a single realization from the ensemble of events that contribute to the phasic average in Eq. 3.3 is simulated (cf. Fig. 3.2). Here we describe how PR-DNS data from multiple

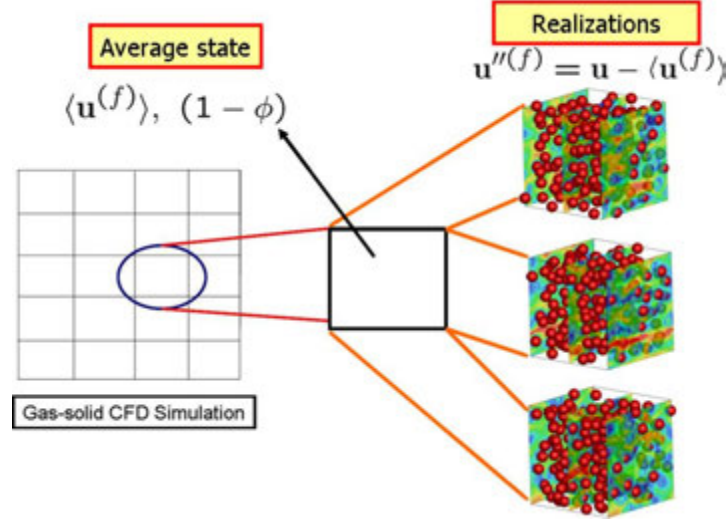


Figure 3.2 Schematic showing the concept of the average fluid-phase velocity. The average fluid-phase velocity that is solved in gas-solid CFD simulations is obtained by averaging over all possible realizations.

realizations is used to compute  $k_f$ . Let  $\mathbf{u}(\mathbf{x}, t; \omega)$  be the velocity field obtained from particle-resolved DNS of flow past a random configuration of particles represented by the positions and velocities  $\{\mathbf{X}^{(i)}, \mathbf{V}^{(i)}, i = 1, \dots, N_p\}$  of  $N_p$  particles. This configuration represents a realization  $\omega$  in the event space  $\Omega$ . The ensemble-averaged velocity field or the mathematical expectation is defined as (Subramaniam, 2000):

$$\langle \mathbf{u} \rangle(\mathbf{x}, t) = \int_{\Omega} \mathbf{u}(\mathbf{x}, t; \omega) dP_{\omega}, \quad (3.4)$$

where  $P_{\omega}$  is the probability measure that is defined on  $\Omega$ . This concept is explained schematically in Fig. 3.2. The average gas-phase velocity and volume fraction that are solved in the CFD calculations are obtained by averaging over all possible realizations. Fluctuations in the gas-phase velocity are defined as departures of the instantaneous velocity field from the average gas-phase velocity.

If the flow is statistically homogeneous, ensemble-averaged quantities can be approximated by taking the volumetric mean of the solution fields, e.g. the volumetric mean of the velocity field over the fluid region is defined as:

$$\langle \mathbf{u}^{(f)} \rangle_{\mathcal{V}}(t; \omega) = \frac{1}{V_f} \int_{\mathcal{V}} I_f(\mathbf{x}, t; \omega) \mathbf{u}(\mathbf{x}, t; \omega) dV, \quad (3.5)$$

where  $V_f$  is the volume of the region occupied by the fluid-phase. It has been shown elsewhere (Tenneti et al., 2011) that a statistically homogeneous gas–solid flow is well approximated by flow past a random configuration of particles in a periodically repeating unit cell. Therefore, volume averages can be used to estimate the true mathematical expectation. The volumetric mean approaches the ensemble average in the limit of infinite box size (i.e.,  $V \rightarrow \infty$ ). Periodic boundary conditions can be used in a computational domain with finite box size provided the two–point correlations in the particle and the fluid phases decay to zero within the box length<sup>1</sup>. In Section 3.5 we show that the Eulerian two–point correlation of fluid velocity does indeed decay to zero within 3 to 4 particle diameters for different grid resolutions, box sizes and Reynolds numbers. However, a finite box may not account for the statistical variability arising from different particle configurations, we require very large box sizes. In order to accurately estimate the ensemble–averaged quantities from finite box sizes, we can simulate fixed particle assemblies and average over different configurations. For fixed particle assemblies, the ensemble–average can be estimated by averaging over different configurations or realizations i.e.,

$$\left\{ \mathbf{u}^{(f)} \right\}_{V, \mathcal{M}}(t) = \frac{1}{\mathcal{M}} \sum_{\mu=1}^{\mathcal{M}} \left\langle \mathbf{u}^{(f)} \right\rangle_V(t; \omega_\mu). \quad (3.6)$$

In the above equation  $\left\{ \mathbf{u}^{(f)} \right\}_{V, \mathcal{M}}$  denotes an estimate to the true expectation  $\left\langle \mathbf{u}^{(f)} \right\rangle$  and  $\mathcal{M}$  denotes the number of independent realizations. Similarly, for each realization of the gas–solid flow we compute the kinetic energy in the fluctuating motions using volume averaging:

$$k_f^{(\mu)} = \frac{1}{V_f} \int_{V_f^{(\mu)}} \frac{1}{2} \left( \mathbf{u}(\mathbf{x}, t, \omega_\mu) - \left\{ \mathbf{u}^{(f)} \right\}_{V, \mathcal{M}} \right) \cdot \left( \mathbf{u}(\mathbf{x}, t, \omega_\mu) - \left\{ \mathbf{u}^{(f)} \right\}_{V, \mathcal{M}} \right) dV. \quad (3.7)$$

The  $k_f$  obtained from a single realization (cf. 3.7) is averaged over multiple independent realizations (MIS) to obtain an estimate for the ensemble-averaged kinetic energy:

$$k_f = \frac{1}{\mathcal{M}} \sum_{\mu=1}^{\mathcal{M}} k_f^{(\mu)}. \quad (3.8)$$

In the next section we describe the particle–resolved DNS approach that is used in this work to quantify  $k_f$  in steady flow past fixed assemblies of spheres.

<sup>1</sup>This is simply the two–phase extension of the criterion given by Pope (2000) for single–phase turbulent flows.

### 3.3 Numerical Method

The particle-resolved DNS methodology employed in this work is called Particle-resolved Uncontaminated-fluid Reconcilable Immersed Boundary Method (PUREIBM). In PUREIBM, we employ Cartesian grids and solve the mass and momentum conservation equations on all the grid points (including those lying inside the particles). A fictitious flow is generated inside the particles that does not affect the exterior flow solution. The mass and momentum conservation equations that are solved in PUREIBM are

$$\frac{\partial u_i}{\partial x_i} = 0, \quad (3.9)$$

and

$$\rho_f \frac{\partial u_i}{\partial t} + \rho_f \mathbf{S}_i = -g_{\text{IBM},i} + \mu_f \frac{\partial^2 u_i}{\partial x_j \partial x_j} + f_{\mathbf{u},i}, \quad (3.10)$$

respectively, where  $\mathbf{g}_{\text{IBM}}$  is the pressure gradient,  $\mathbf{S} = \nabla \cdot (\mathbf{u}\mathbf{u})$  is the convective term in conservative form, and  $\mathbf{u}$  is the instantaneous velocity field. In Eq. (3.10),  $\mathbf{f}_{\mathbf{u}}$  is the additional immersed boundary (IB) force term that accounts for the presence of solid particles by ensuring the no-slip and no-penetration boundary conditions at the particle-fluid interface.

The surface of the solid particle is represented by a discrete number of points called boundary points. For spherical particles, the boundary points are specified by discretizing the sphere in spherical coordinates. In Fig. 3.3, a schematic describing the computation of the IB forcing is shown for the equatorial plane passing through the spherical particle. Another set of points called exterior points are generated by projecting these boundary points onto a sphere of radius  $r + \Delta r$ , where  $r$  is the radius of the particle (see exterior point represented by an open circle on the dashed line in Fig. 3.3). Similarly, the boundary points are projected onto a smaller sphere of radius  $r - \Delta r$  and these points are called interior points. In our simulations  $\Delta r$  is taken to be same as the grid spacing. The IB force is computed at the interior points. At these points the fluid velocity is forced in a manner similar to the ghost cell approach used in standard finite-difference/finite-volume based methods (Patankar, 1980). Specifically for the case of zero solid particle velocity, the velocity at the interior points is forced to be equal in magnitude but opposite in direction of the fluid velocity at the corresponding exterior points. Velocities at the

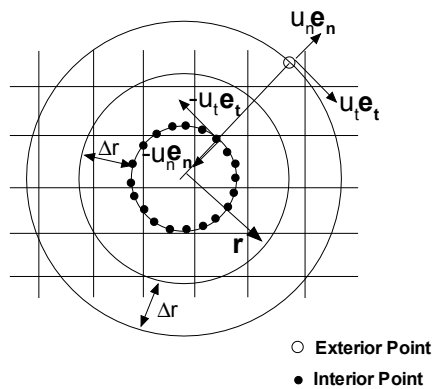


Figure 3.3 A schematic showing the computation of the immersed boundary forcing for a stationary particle. The solid circle represents the surface of the particle at  $r$ . Open dot shows the location of one exterior point at  $r + \Delta r$  (only one exterior point is shown for clarity, although there is one exterior point for each interior point) and filled dots show the location of interior points at  $r - \Delta r$  where the immersed boundary forcing is computed. For the special case of a stationary particle, the velocity at the interior points is forced to be the opposite of the velocity at the corresponding exterior points. In the schematic,  $u_n \mathbf{e}_n$  represents the normal velocity and  $u_t \mathbf{e}_t$  represents the tangential velocity at the exterior point.

exterior and interior points are obtained by interpolating the velocities from the neighboring grid nodes. The computation of IB forcing is similar to the direct forcing method proposed by Yusof (1996). The IB forcing at the  $(n + 1)^{\text{th}}$  time-step is specified to cancel the remaining terms in the momentum conservation, and to force the velocity to its desired value  $\mathbf{u}^d$  at the interior points:

$$f_{\mathbf{u},i}^{n+1} = \rho_f \frac{u_i^d - u_i^n}{\Delta t} + \rho_f S_i^n + g_{\text{IBM},i}^n - \mu_f \frac{\partial^2}{\partial x_j \partial x_j} u_i^n. \quad (3.11)$$

The IB forcing at the interior points is then interpolated to the neighboring grid nodes that do not include grid nodes in the fluid phase. It is noteworthy that the discretization of the sphere in spherical coordinates is independent of the grid resolution and hence to some extent, decouples the grid resolution from the accuracy with which the boundary condition is imposed.

The governing equations in PReIBM are solved by imposing periodic boundary conditions on fluctuating variables that are now defined. The velocity field is decomposed into a spatially uniform mean flow that is purely time-dependent and a fluctuating velocity field  $\mathbf{u}'$  that is periodic, i.e.,

$$\mathbf{u}(\mathbf{x}, t) = \langle \mathbf{u} \rangle_{\mathcal{V}}(t) + \mathbf{u}'(\mathbf{x}, t), \quad (3.12)$$

where the volumetric mean velocity

$$\langle \mathbf{u} \rangle_{\mathcal{V}}(t) = \frac{1}{V} \int_{\mathcal{V}} \mathbf{u}(\mathbf{x}, t) d\mathcal{V}, \quad (3.13)$$

is obtained by averaging the velocity field over the entire computational domain. Similar decompositions can be written for the non-linear term  $\mathbf{S}$ , pressure gradient  $\mathbf{g}$ , and immersed boundary forcing  $\mathbf{f}_u$  terms. Substituting the above decompositions in Eqs. (3.9) and (3.10), followed by averaging over the entire computational domain yields the volume averaged mass and momentum conservation equations. Since the volumetric means are independent of spatial location, mean mass conservation is trivially satisfied. The mean momentum balance in the whole domain is

$$\rho_f \frac{d \langle u_i \rangle_{\mathcal{V}}}{dt} = - \langle g_{\text{IBM},i} \rangle_{\mathcal{V}} + \langle f_{\mathbf{u},i} \rangle_{\mathcal{V}}, \quad (3.14)$$

where the volume integrals of convective and diffusive terms are zero because of periodic boundary conditions. The mean IB forcing term  $\langle \mathbf{f}_u \rangle_{\mathcal{V}}$  is computed by volume-averaging the IB force

specified by Eq. 3.11 over the region  $\mathcal{V}$ . The mean pressure gradient  $\langle \mathbf{g}_{\text{IBM}} \rangle_{\mathcal{V}}$  is computed such that we obtain the desired flow rate.

Evolution equations for the fluctuating variables are derived by subtracting Eq. (3.14) from Eq. (3.10). The resulting equations are solved using a pseudo-spectral method, with Crank-Nicolson scheme for the viscous terms, and an Adams-Bashforth scheme for the convective terms. A fractional time-stepping method that is based on Kim and Moin's approach (Kim and Moin, 1985) is used to advance the fluctuating velocity fields in time. The principal advantage of the PReIBM approach is that it enables the use of regular Cartesian grids to solve for flow past arbitrarily shaped moving bodies without the need for costly remeshing.

The salient features that distinguish PReIBM from other immersed boundary method approaches (including the original implementation of Yusof (1996)) are as follows:

1. Uncontaminated fluid: In PReIBM the immersed boundary (IB) forcing is solely restricted to those grid points that lie in the solid phase, and therefore the flow solution in the fluid phase is uncontaminated by the IB forcing. Consequently the velocity and pressure in the fluid phase is a solution to the unmodified Navier-Stokes equations (in contrast to IB implementations that smear the IB forcing on to grid points in the fluid phase adjoining solid boundaries, resulting in solution fields that do not correspond to unmodified Navier-Stokes equations).
2. Reconcilable: In PReIBM the hydrodynamic force experienced by a particle is computed directly from the stress tensor at the particle surface that is obtained from this uncontaminated fluid flow solution (in contrast to IB implementations that calculate the hydrodynamic force from the IB forcing field). This feature of PReIBM enables us to directly compare the DNS solution with any random-field theory of multiphase flow.

### 3.4 Validation

The PReIBM PR-DNS methodology has been extensively validated (Garg et al., 2011; Tenneti et al., 2011) by comparing the drag force obtained from PReIBM with available experimental and simulation data in the literature in a comprehensive suite of test cases:

1. Drag acting on a single sphere (Garg et al., 2011; Garg, 2009) with experimental correlation of Schiller and Naumann (1935)
2. Drag acting on simple cubic and face centered cubic arrangements (Tenneti et al., 2011) of particles in Stokes flow regime with those reported by Zick and Homsy (1982) using the Boundary Integral method (semi-analytic solution)
3. Drag acting on simple cubic (SC) and face centered cubic (FCC) arrangements (Tenneti et al., 2011) of particles at moderate Reynolds numbers with the results published by Hill et al. (2001b) using lattice Boltzmann method (LBM)
4. Mean drag acting on a random arrangement Tenneti et al. (2011) of particles in the Stokes flow regime with the results published by Hill et al. (2001a) and van der Hoef et al. (2005) using LBM
5. High Reynolds number flow past random arrays of monodisperse spheres with ANSYS-FLUENT CFD package

In addition to the comprehensive validation of the PReIBM method (Tenneti et al., 2011; Garg et al., 2011) , we present selected additional validation tests to establish the numerical convergence and accuracy of PReIBM near solid boundaries in Fig. 3.4. The first plot (see Fig. 3.4(a)) shows a comparison of the pressure coefficient along the surface of a sphere obtained from our PR-DNS with that reported in the book of Clift et al. (1978) (CGW) for an isolated sphere at a Reynolds number of 10. Figure 3.4(a) shows an excellent agreement of the pressure profile on the surface of the sphere with the data reported in CGW. The second plot (see Fig. 3.4(b)) shows a comparison of the velocity field in a square duct at a Reynolds number of 20 with the analytical solution given by Cornish (1928). We can see that the velocity profile obtained from PReIBM is numerically converged and accurate. These plots show that in addition to getting the total drag correct, our method computes the correct contributions of pressure and viscous drag forces. In the following section we describe the simulation setup used to compute the level of gas-phase velocity fluctuations and also discuss the choice of the numerical parameters needed to ensure numerically converged results.

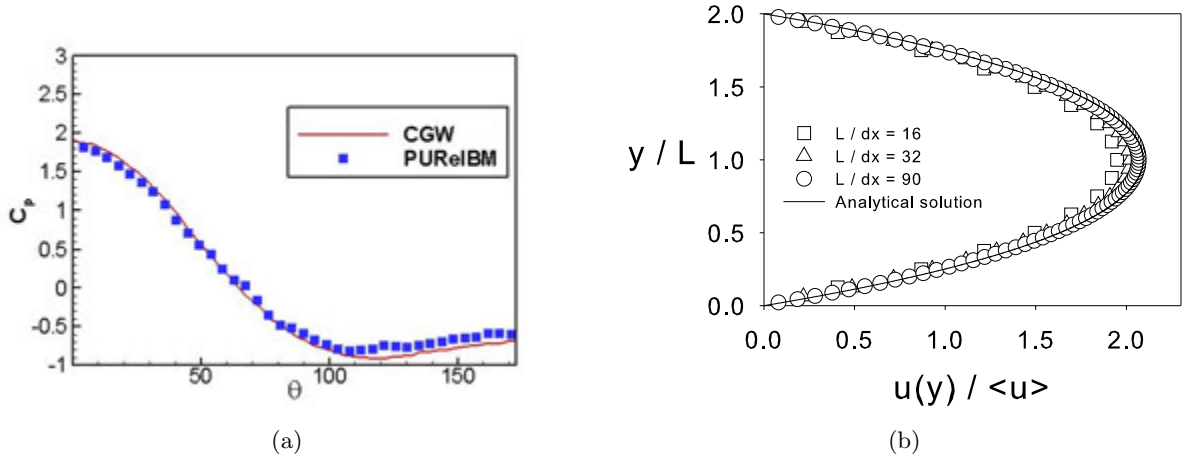


Figure 3.4 (a) Variation of the coefficient of pressure  $C_p$  along the surface of the sphere. Symbols are the data obtained from PReIBM simulations for a Reynolds number of 10, while the solid line is that reported in the book authored by Clift, Grace and Weber (CGW) Clift et al. (1978). (b) Comparison of the velocity profile in a square duct obtained from PReIBM simulations at a Reynolds number of 20 with analytical solution Cornish (1928). It is worthwhile to note that the walls are generated using the immersed boundary method.

### 3.5 Simulation Setup

In our simulation setup the particles are held stationary and a steady flow is established by imposing a pressure gradient that corresponds to the desired mean flow Reynolds number. A typical simulation of flow past random arrangement of particles with contours of local kinetic energy ( $k^{(f)} = \frac{1}{2}u_i''^{(f)}u_i''^{(f)}$ ) normalized by the mean energy are shown in Fig. 3.5. In all the simulations, mean flow is directed along the positive  $x$ -axis.

For flow past homogeneous particle assemblies, a Reynolds number based on the magnitude of mean slip velocity between the two phases is defined as

$$\text{Re}_m = \frac{|\langle \mathbf{W} \rangle| (1 - \phi) D}{\nu_f}, \quad (3.15)$$

where  $|\langle \mathbf{W} \rangle|$  is the magnitude of the mean slip velocity,  $D$  is the particle diameter and  $\phi$  is the solid volume fraction. The mean slip velocity  $\langle \mathbf{W} \rangle = \langle \mathbf{u}^{(s)} \rangle - \langle \mathbf{u}^{(f)} \rangle$  is defined as the difference between the average solid and gas-phase velocities. In the simulations, the mean flow Reynolds number (or the desired flow rate) is specified as an input and since for fixed

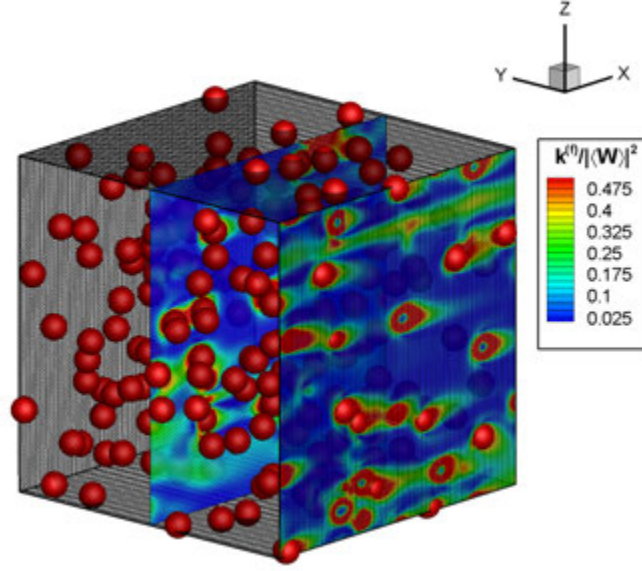


Figure 3.5 Contours of local kinetic energy ( $k^{(f)} = \frac{1}{2}u_i''^{(f)}u_i''^{(f)}$ ) in the gas-phase normalized by the mean energy for steady flow past random assembly of spheres at a solid volume fraction of 0.05 and mean flow Reynolds number of 50.

assemblies  $\langle \mathbf{u}^{(s)} \rangle = 0$ , the desired fluid-phase mean velocity  $\langle \mathbf{u}^{(f)} \rangle$  is known in terms of the input Reynolds number and other physical properties. The mean pressure gradient evolves in time until it attains the value required to drive the fluid at the desired flow rate.

Particles are initialized corresponding to a specified mean solid volume fraction  $\phi$ . The particles are fixed in a random equilibrium configuration they attain following elastic collisions (in the absence of ambient fluid) starting from a lattice arrangement with a Maxwellian velocity distribution. The elastic collisions are simulated using a soft-sphere discrete element model (Cundall and Strack, 1979; Garg et al., 2010a). The pair correlation function at equilibrium specifies the particle configuration for random assemblies.

The computational domain used is a cube with sides of length  $L$  which is discretized using a regular Cartesian grid with  $M$  grid cells in each direction so that  $\Delta x = L/M$  is the size of each grid cell. The spatial resolution is represented by the number of grid cells across the diameter of a particle, which is denoted  $D_m = D/\Delta x$ . For random arrangements of particles, the ratio  $L/D$  is an independent parameter. The minimum box length is determined by the criterion that the spatial autocorrelation of flow statistics must decay to zero within the box. This is to

$\phi$	$N_p$	$\mathcal{M}$	$D_m$	$L/D$
0.1	80/ 41	5	20/30	7.5/ 6
0.2	161/ 34	5	20/40	7.5/ 4.5
0.3	71/ 26	5	30/50	5/ 3.6
0.4	95/ 20	5	30/60	5/ 3
0.5	61/-	5	40/-	4/-

Table 3.1 Numerical parameters (number of particles  $N_p$ , number of MIS  $\mathcal{M}$ , particle diameter in grid units  $D_m$  and the ratio of the length of the box to the particle diameter  $L/D$ ) used for random arrays in PReIBM simulations. Different numerical parameters are used for  $Re_m \leq 100$  and  $Re_m > 100$ . These are separated by “/”. Numbers before the “/” correspond to  $Re_m \leq 100$  while numbers after the “/” correspond to  $Re_m > 100$ . At volume fraction 0.5 PReIBM simulations are performed only up to a Reynolds number of 100.

prevent the periodicity of the numerical solution from leading to unphysical flow fields. The numerical parameter  $L/D$  also determines the number of particles  $N_p$  in the box such that for a given volume fraction  $\phi$  it is given by

$$N_p = \frac{6\phi}{\pi} \left( \frac{L}{D} \right)^3. \quad (3.16)$$

The various numerical parameters used in the simulations are reported in Table 3.1.

All simulations start with the initial condition of uniform fluid velocity. We have verified that starting the simulations with a homogeneous isotropic turbulent velocity field does not affect the steady value of  $k_f$  attained by the system (Mehrabadi et al., 2012). Therefore the steady state value of  $k_f$  obtained in a fixed particle assembly depends only on the solids volume fraction and the mean flow Reynolds number. The grid resolutions used in the PReIBM simulations have been chosen such that they yield numerically converged solutions. For instance, the convergence characteristics of  $k_f/E_f$  with respect to the grid resolution  $D_m$  for a solid volume fraction of 0.3 and mean flow Reynolds number of 20 is shown in Fig. 3.6. The value of  $k_f/E_f$  averaged over 5 independent realizations clearly shows numerical convergence as the grid resolution is increased.

Besides convergence with grid resolution, it is also important to check whether the box size

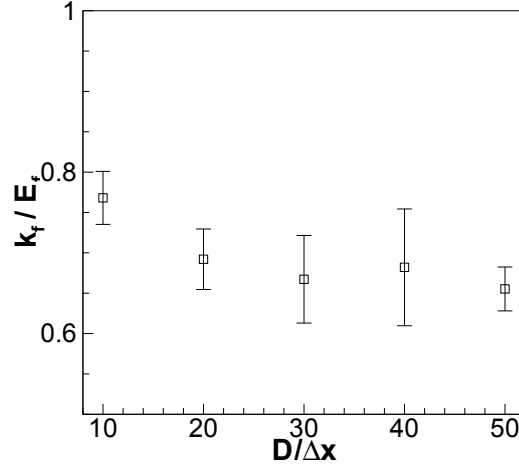


Figure 3.6 Convergence characteristics of  $k_f/E_f$  with grid resolution  $D/\Delta x$  for flow past random arrays of spheres at  $\phi = 0.3$  and  $Re_m = 20$ . The error bars denote 95% confidence intervals in the estimation of the average  $k_f$  from 5 independent realizations.

is adequate or not. The box size is deemed adequate if the two-point correlation functions in the fluid-phase decay to zero within the box length. To check this, the two-point velocity correlation function has been computed for the highest Reynolds number simulated. The fluid-phase velocity autocorrelation  $\rho_u(r)$  is defined as

$$\rho_u(r) = \frac{\langle I_f(\mathbf{x}) \mathbf{u}''^{(f)}(\mathbf{x}) \cdot I_f(\mathbf{x} + \mathbf{r}) \mathbf{u}''^{(f)}(\mathbf{x} + \mathbf{r}) \rangle}{\langle I_f \mathbf{u}''^{(f)} \cdot \mathbf{u}''^{(f)} \rangle}. \quad (3.17)$$

Figure 3.7(a) shows convergence of the fluid-phase velocity autocorrelation function with grid resolution as well as box size for a random configuration of particles at a solid volume fraction of 0.2 and Reynolds number of 20. The autocorrelation function has also been computed for the highest Reynolds number that we simulated and is shown in Fig. 3.7(b). These results clearly indicate that the numerical parameters used in our simulation are adequate to perform numerically converged simulations. We now present the results obtained from PURelBM simulations of flow past monodisperse fixed particle assemblies.

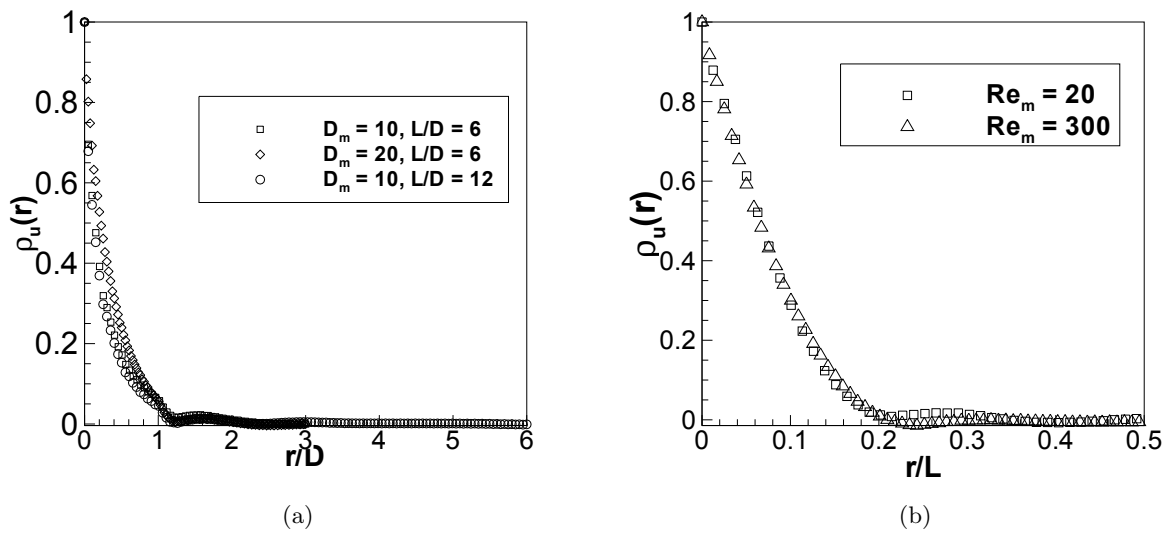


Figure 3.7 (a) Convergence of the fluid-phase velocity autocorrelation function with grid resolution as well as box size for a random configuration of particles at a solid volume fraction of 0.2 and Reynolds number of 20. (b) Decay of the fluid velocity autocorrelation function obtained from PUREIBM simulation of steady flow past a random configuration of spheres at a solid volume fraction of 0.2 and mean flow Reynolds numbers 20 (squares) and 300 (triangles). In these simulations  $L/D$  ratios of 6 and 4.5 are used for Reynolds numbers 20 and 300 respectively.

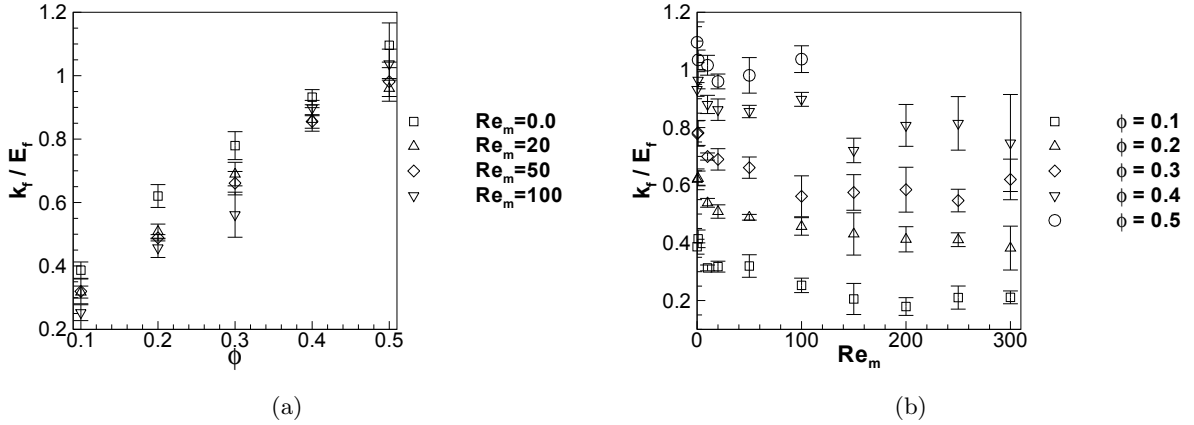


Figure 3.8 Variation of the turbulent kinetic energy normalized by  $E_f = \frac{1}{2} \langle \mathbf{u}^{(f)} \rangle \cdot \langle \mathbf{u}^{(f)} \rangle$  with  $Re_m$  and  $\phi$ . Figure 3.8(a) shows the behavior of  $k_f/E_f$  with  $\phi$  for different mean flow Reynolds numbers while Fig. 3.8(b) shows the behavior of  $k_f/E_f$  with  $Re_m$  for different solid volume fractions. For each volume fraction  $k_f$  obtained from PUnReIBM simulations is reported by averaging over 5 MIS and the error bars on the symbols in this figure represent 95% confidence intervals in the estimation of  $k_f$ .

### 3.6 Results

We performed PUnReIBM DNS of flow past fixed assemblies of monodisperse spheres over a wide range of solids volume fraction ( $0.1 \leq \phi \leq 0.5$ ) and mean flow Reynolds numbers ( $0.01 \leq Re_m \leq 300$ ). Using this data a new correlation for the average fluid–particle force in fixed beds has been proposed by Tenneti et al. (2011). Here we quantify the strength of gas–phase velocity fluctuations in terms of  $\phi$  and  $Re_m$ .

Figure 3.8(a) shows the variation of  $k_f/E_f$  with solids volume fraction for different mean flow Reynolds numbers while Fig. 3.8(b) shows the variation of  $k_f/E_f$  with mean flow Reynolds number for different solid volume fractions. As evident from Fig. 3.8(a), the kinetic energy in fluctuating motions normalized by the mean energy in the gas–phase increases dramatically with volume fraction. This behavior is expected because, as the volume fraction increases, the space available to the gas decreases. Owing to conservation of mass, the velocity of the gas increases thus causing  $k_f/E_f$  to increase with volume fraction. As shown in Fig. 3.8(b), at a given volume fraction  $k_f/E_f$  decreases rapidly with increasing mean flow Reynolds number up

to  $Re_m = 50$  and beyond  $Re_m = 50$  it has a weak power law dependence on  $Re_m$ . This behavior is a result of the normalization of  $k_f$  by  $E_f$ . It implies that the variance of gas velocity increases approximately as the square of the mean flow Reynolds number. Since the total kinetic energy of the gas increases with increasing mean flow Reynolds number, we expect the strength of gas-phase velocity fluctuations also to increase. Using the data obtained from PReIBM DNS we found that the following function fits the data with an average deviation of 5%:

$$\frac{k_f}{E_f}(\phi, Re_m) = 2\phi + 2.5\phi(1 - \phi)^3 \exp\left(-\phi Re_m^{1/2}\right), \quad 0.1 \leq \phi \leq 0.5, \\ 0.01 \leq Re_m \leq 300. \quad (3.18)$$

As shown in Eq. 3.18, the correlation is proposed from simulations in the range  $0.1 \leq \phi \leq 0.5$  and  $0.01 \leq Re_m \leq 300$ . The value of  $k_f/E_f$  from Eq. (3.18) tends to appropriate values in the limit of infinite dilution and creeping flow. In the limiting case of infinite dilution i.e.  $\phi \rightarrow 0$  the value of  $k_f/E_f$  is zero. This limiting value is consistent with the fact that in the absence of particles the flow field is uniform. In the Stokes flow regime ( $Re_m \rightarrow 0$ ) the value of  $k_f/E_f$  reaches an asymptote and depends only on the solid volume fraction. This behavior is consistent with the fact that the mean drag (which is shown to be the source of  $k_f$  in the next section) acting on the particles is linear in the Stokes flow regime and thus the normalized quantity  $k_f/E_f$  is independent of Reynolds number.

In addition to  $k_f$  we also quantified the state of anisotropy of the fluid phase Reynolds stress tensor. To quantify the state of anisotropy of the fluid phase Reynolds stress, the invariants  $\xi$  and  $\eta$  of the normalized Reynolds stress anisotropy tensor, which is defined as

$$b_{ij} = \frac{1}{2k_f} \left\langle I_f u_i^{(f)} u_j^{(f)} \right\rangle - \frac{1}{3} \delta_{ij},$$

are computed. The invariants are defined as  $6\xi^2 = b_{ij}b_{ij}$  and  $6\eta^3 = b_{ij}b_{jk}b_{ki}$  (Pope, 2000). The state of the anisotropy of the Reynolds stress tensor for various volume fractions and mean flow Reynolds number is plotted on the  $\xi$ - $\eta$  plane in Fig. 3.9. The key finding here is that at every Reynolds number the level of anisotropy decreases with increasing volume fraction. In other

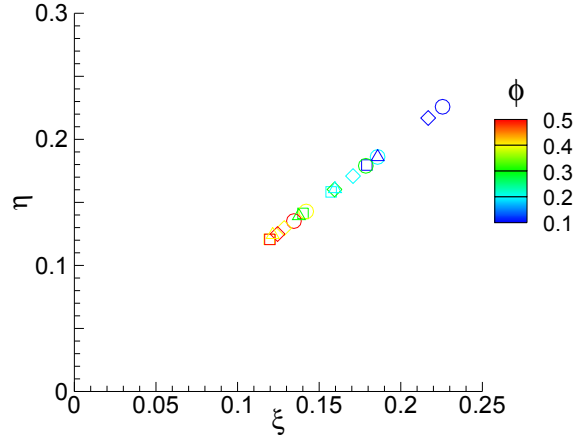


Figure 3.9 State of anisotropy of the gas-phase Reynolds stress tensor in the Lumley plane. Color of the symbol indicates the volume fraction going from  $\phi = 0.1$  (blue) to  $\phi = 0.5$  (red). For each volume fraction the invariants of the gas-phase Reynolds stress tensor are shown:  $Re_m = 0.01$  (squares),  $Re_m = 20$  (circles),  $Re_m = 100$  (diamonds) and  $Re_m = 200$  (triangles) are shown.

words, the gas-phase Reynolds stress tensor is more anisotropic at dilute volume fractions than at denser volume fractions.

Although our study is for homogeneous gas-solid suspensions, the dependence of  $k_f$  on the solid volume fraction and mean flow Reynolds number has implications for transport of the gas-phase Reynolds stress in inhomogeneous flows also. The strong dependence of  $k_f$  on  $\phi$  suggests that the transport of  $k_f$  could be significant in statistically inhomogeneous flows with spatial variation of  $\phi$ . Moreover, the dependence of  $k_f$  on  $\phi$  and  $Re_m$  (cf. Eq. (3.18)) obtained in this section has certain implications for modeling the dissipation of kinetic energy in the gas-phase, which are discussed in the following section by employing a scaling analysis.

### 3.7 Implications for modeling the dissipation of kinetic energy

In this simple flow the steady  $k_f$  results from a balance of interphase transfer of kinetic energy and dissipation of kinetic energy in the gas-phase. If we are able to obtain the correct scaling of each of these terms with  $\phi$  and  $Re_m$  then we can explain the dependence of  $k_f$  on  $\phi$  and  $Re_m$ . For statistically homogeneous flows the conservation law (Pai and Subramaniam,

2009; Ying and Subramaniam, 2007) for  $k_f$  is:

$$\frac{\partial}{\partial t} \{(1 - \phi) \rho_f k_f\} = - \left\langle u_i''(f) \tau_{ji} n_j^{(s)} \delta(\mathbf{x} - \mathbf{x}^{(I)}) \right\rangle + \left\langle u_i''(f) \frac{\partial (I_f \tau_{ji})}{\partial x_j} \right\rangle. \quad (3.19)$$

In this equation  $\tau_{ji}$  is the fluid phase stress tensor (cf. A),  $\delta(\mathbf{x} - \mathbf{x}^{(I)})$  is a generalized delta function at the fluid–particle interface  $\mathbf{x}^{(I)}$ , and  $\mathbf{n}^{(s)}$  is the unit normal vector pointing outward from the solid phase into the fluid phase. The second term on the right hand side is the covariance of the fluctuating fluid velocity field and the gradient of the stress tensor in the fluid phase. For statistically homogeneous flows this term simplifies (cf. Appendix A) to  $-2\mu_f \langle I_f s_{ij} s_{ij} \rangle$ , where  $2\mu_f \langle I_f s_{ij} s_{ij} \rangle$  can be identified as the dissipation that is strictly non negative. Thus the conservation equation for  $k_f$  simplifies to

$$\frac{\partial}{\partial t} \{(1 - \phi) \rho_f k_f\} = - \left\langle u_i''(f) \tau_{ji} n_j^{(s)} \delta(\mathbf{x} - \mathbf{x}^{(I)}) \right\rangle - 2\mu_f \langle I_f s_{ij} s_{ij} \rangle. \quad (3.20)$$

Here  $s_{ij} = \frac{1}{2} \left( \frac{\partial u_i''(f)}{\partial x_j} + \frac{\partial u_j''(f)}{\partial x_i} \right)$  is the strain rate of the fluctuating fluid velocity field and  $\mu_f$  is the dynamic viscosity of the fluid–phase.

The first term on the right hand side of Eq. (3.20) represents the interphase transfer of kinetic energy denoted  $\Pi_{k_f}$  so that

$$\Pi_{k_f} = - \left\langle u_i''(f) \tau_{ji} n_j^{(s)} \delta(\mathbf{x} - \mathbf{x}^{(I)}) \right\rangle, \quad (3.21)$$

which is non–zero at the fluid–solid interface owing to the Dirac delta function at  $\mathbf{x}^{(I)}$ . Ying and Subramaniam (2007) showed that for fixed particle assemblies the interphase kinetic energy transfer term simplifies to  $\langle \mathbf{W} \rangle \cdot \langle \mathbf{S}_M^{(f)} \rangle$ , where  $\langle \mathbf{W} \rangle = \langle \mathbf{u}^{(f)} \rangle - \langle \mathbf{u}^{(s)} \rangle$  is the mean slip velocity between the solid and the fluid phases, and  $\langle \mathbf{S}_M^{(f)} \rangle = - \left\langle \tau_{ji} n_j^{(s)} \delta(\mathbf{x} - \mathbf{x}^{(I)}) \right\rangle$  is the average momentum transfer between the fluid and the solid phase. This simplification is possible because particles in a fixed bed are stationary and the fluid velocity field satisfies the no–slip condition at the particle surfaces, as a consequence of which  $\mathbf{u}''(f) = - \langle \mathbf{u}^{(f)} \rangle$  at every point on the fluid–particle interface in Eq. 3.21. For random assemblies, since the mean slip velocity is aligned with the mean interphase momentum transfer (Hill et al., 2001b; Tenneti et al., 2011),  $\Pi_{k_f}$  is positive and represents a source of gas–phase velocity fluctuations. The second term ( $2\mu_f \langle I_f s_{ij} s_{ij} \rangle$ ) on the right hand side of Eq. (3.20) is usually expressed as  $\rho_f (1 - \phi) \varepsilon_f$  where  $\varepsilon_f$  is the dissipation of  $k_f$ . Since  $s_{ij} s_{ij}$  is always positive,  $\varepsilon_f$  represents a sink of  $k_f$ .

An expression for the interphase transfer of kinetic energy  $\Pi_{k_f}$  can be derived by expressing the interphase momentum transfer in terms of the average drag force acting per particle:

$$\Pi_{k_f} = \langle \mathbf{W} \rangle \cdot \langle \mathbf{S}_M^{(f)} \rangle = \frac{18\phi(1-\phi)^2\mu_f}{D^2} F(\phi, \text{Re}_m) |\langle \mathbf{W} \rangle|^2. \quad (3.22)$$

In the above expression,  $F(\phi, \text{Re}_m)$  is the normalized average drag force per particle given by

$$F = \frac{|\langle \mathbf{F} \rangle|}{F_{\text{Stokes}}}, \quad (3.23)$$

where  $\langle \mathbf{F} \rangle$  is the average hydrodynamic force per particle and  $F_{\text{Stokes}} = 3\pi\mu_f D(1-\phi)|\langle \mathbf{W} \rangle|$  is the Stokes drag acting on an isolated sphere moving with a slip velocity of  $(1-\phi)|\langle \mathbf{W} \rangle|$ . The expression for the source of  $k_f$  due to interface transfer of kinetic energy, derived in Eq. (3.22) is similar to the one derived by Crowe (2000). While Crowe (2000) used the single sphere drag correlation for  $F(\phi, \text{Re}_m)$ , here we obtain this value directly from the particle-resolved DNS. An accurate correlation for  $F(\phi, \text{Re}_m)$  has been developed using the data obtained from PUnReIBM simulations (Tenneti et al., 2011). The drag correlation is summarized below for the sake of completeness. The average normalized drag force acting per particle in flow past a random assembly of monodisperse spheres is given by

$$F(\phi, \text{Re}_m) = \frac{F_{\text{isol}}(\text{Re}_m)}{(1-\phi)^3} + F_\phi(\phi) + F_{\phi, \text{Re}_m}(\phi, \text{Re}_m) \quad (3.24)$$

where,  $F_{\text{isol}}$  is the drag force acting on an isolated sphere moving in an unbounded medium. We used the drag correlation proposed by Schiller and Naumann (1935) to get the drag on an isolated sphere. The remaining two terms in Eq. 3.24 are given by

$$F_\phi(\phi) = \frac{5.81\phi}{(1-\phi)^3} + 0.48 \frac{\phi^{1/3}}{(1-\phi)^4},$$

$$F_{\phi, \text{Re}_m}(\phi, \text{Re}_m) = \phi^3 \text{Re}_m \left( 0.95 + \frac{0.61\phi^3}{(1-\phi)^2} \right).$$

At steady state the source and sink of kinetic energy must balance each other i.e.,

$$\Pi_{k_f} = \rho_f(1-\phi)\varepsilon_f. \quad (3.25)$$

To our knowledge, all the turbulence models for multiphase flows use a Kolmogorov scaling for the dissipation term in a manner similar to single phase turbulence models i.e.,  $\varepsilon_f \sim k_f^{3/2}/l_K$ .

An alternative expression for the dissipation rate in single-phase turbulence is  $\varepsilon_f \sim 2\nu_f k_f / l_T^2$ , where  $l_T$  is the Taylor microscale and  $\nu_f$  is the kinematic viscosity of the fluid-phase. This expression can be generalized to any random velocity field with a finite spatial autocorrelation length. In the following we show that the Kolmogorov scaling does not yield a plausible behavior for  $l_K$  with  $\text{Re}_m$  for gas-solid flows with finite sized particles, whereas the behavior of  $l_T$  is reasonable.

Using the Kolmogorov scaling for the dissipation term and substituting  $\varepsilon_f = k_f^{3/2} / l_K$  in Eqs. (3.25) and (3.22) implies the following expression for  $l_K / D$ :

$$\frac{l_K}{D} = \left( \frac{k_f}{E_f} \right)^{3/2} \left( 36\sqrt{2}\phi(1-\phi)^2 \frac{F(\phi, \text{Re}_m)}{\text{Re}_m} \right)^{-1}. \quad (3.26)$$

Similarly, using the Taylor microscale scaling for the dissipation term and substituting  $\varepsilon_f = 2\nu_f k_f / l_T^2$  in Eqs. (3.25) and (3.22) results in the following expression for  $l_T / D$ :

$$\frac{l_T}{D} = \left( \frac{k_f}{E_f} \right)^{1/2} (18\phi(1-\phi)F(\phi, \text{Re}_m))^{-1/2}. \quad (3.27)$$

The behavior of the length scales  $l_K$  and  $l_T$  with solids volume fraction and mean flow Reynolds number can be inferred by substituting Eqs. (3.18) and (3.23) in Eqs. (3.26) and (3.27) respectively. The variation of  $l_K$  and  $l_T$  with solid volume fraction and Reynolds number are compared in Fig. 3.10. The behavior of length scale  $l_K$  obtained by modeling the dissipation term by Kolmogorov scaling ( $\varepsilon_f \sim k_f^{3/2} / l_K$ ) is shown by dashed lines. This length scale increases with mean flow Reynolds number and decreases with volume fraction. The behavior of the length scale  $l_T$  obtained using a Taylor microscale scaling ( $\varepsilon_f \sim 2\nu_f k_f / l_T^2$ ) is shown in Fig. 3.10 using solid lines. This length scale decreases with both mean flow Reynolds number and solids volume fraction.

For laminar flow past a single sphere, the length scale on which the velocity gradients vary is of the order of the boundary layer thickness  $\delta / D$  which varies inversely with  $\sqrt{\text{Re}_m}$ . We expect this length scale to decrease with increasing solids volume fraction. Since the hypothesis of energy cascade may not hold in gas-solid flow with finite-sized particles, the applicability of the Kolmogorov scaling is questionable, as also evidenced by the behavior of  $l_K$  with  $\text{Re}_m$ . On the other hand, the scaling of  $l_T$  indicates that the Taylor microscale is a better choice to

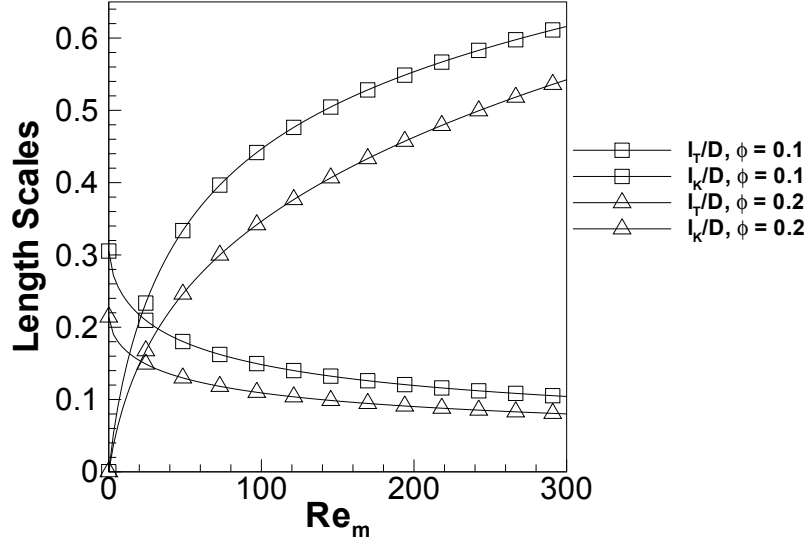


Figure 3.10 Variation of dissipation length scales with Reynolds number for solid volume fractions 0.1 and 0.2. Dashed lines are obtained by modeling the dissipation term as  $k_f^{3/2}/l_K$  while the solid lines are obtained by modeling the dissipation as  $2\nu_f k_f/l_T^2$ .

model the dissipation term in gas–solid flows with finite sized particles. However, it must be noted that neither  $l_K$  nor  $l_T$  may correspond to the exact length scales of dissipative motions in gas–solids flow.

### 3.8 Eddy viscosity for gas–solid flow

In several studies the gas–phase Reynolds stress term is modeled in a fashion similar to single–phase turbulence i.e.,

$$\langle u_i''^{(f)} u_j''^{(f)} \rangle = \frac{2}{3} \delta_{ij} \left( k_f + \nu_t \frac{\partial \langle u_k^{(f)} \rangle}{\partial x_k} \right) - \nu_t \left( \frac{\partial \langle u_i^{(f)} \rangle}{\partial x_j} + \frac{\partial \langle u_j^{(f)} \rangle}{\partial x_i} \right).$$

In this model  $\nu_t$  is the eddy viscosity for gas–solid flow and it depends on the turbulent kinetic energy ( $k_f$ ) and dissipation rate ( $\varepsilon_f$ ) through the relation  $\nu_t = C_\mu k_f^2/\varepsilon_f$ . In this relation  $C_\mu$  is a model constant and usually the value for the constant associated with the  $k - \varepsilon$  models of single–phase turbulence are used in gas–solid flows as well. Since we have quantified both  $k_f$  (cf. Eq. (3.18)) and  $\varepsilon_f$  (cf. Eq. (3.25)) using particle–resolved DNS, we can infer an eddy viscosity

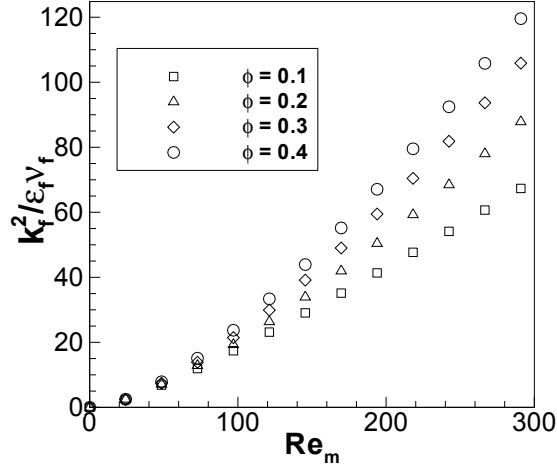


Figure 3.11 Behavior of the ratio  $k_f^2 / (\varepsilon_f \nu_f)$  with mean flow Reynolds number for different solid volume fractions.

for gas–solid flow as a function of solid volume fraction and mean flow Reynolds number. From Eqs. (3.18) and (3.25), it is clear that the ratio  $k_f^2 / (\varepsilon_f \nu_f)$  can be expressed as

$$\frac{k_f^2}{\varepsilon_f \nu_f} = \frac{1}{18\phi(1-\phi)^3} \left( \frac{k_f}{E_f} \right)^2 \frac{\text{Re}_m^2}{F(\phi, \text{Re}_m)}. \quad (3.28)$$

This ratio is shown as a function of  $\text{Re}_m$  for different  $\phi$  in Fig. 3.11. We see that the ratio  $k_f^2 / (\varepsilon_f \nu_f)$  increases with both solid volume fraction and mean flow Reynolds number. This dependence on the mean flow Reynolds number indicates that the transport of gas–phase Reynolds stress can become important if there are large gradients in the mean flow and solid volume fraction, as found in many multiphase flow applications. Further, the PR–DNS of Mehrabadi et al. (2012) shows that the value of  $k_f$  in freely evolving gas–solid suspensions is very close to that observed in fixed–beds. This observation confirms the applicability of the proposed eddy viscosity model in device–scale CFD simulations of gas–solid flow applications.

### 3.9 Conclusions

In this work we quantified the strength of gas–phase velocity fluctuations in gas–solid flows as a function of solids volume fraction and Reynolds number based on mean slip velocity using particle–resolved DNS of steady flow past fixed particle assemblies. We employ the Particle–

resolved Uncontaminated–fluid Reconcilable Immersed Boundary Method (PReIBM) to perform particle–resolved DNS of flow past fixed particle assemblies. We observe that the presence of particles generates high level of fluctuations in the gas velocity. The kinetic energy in the fluctuating motions ( $k_f$ ) can be as high as the kinetic energy in the mean motion ( $E_f$ ), especially for systems with higher solid volume fraction greater than 0.4. The ratio  $k_f/E_f$  increases with the solids volume fraction and decreases with mean flow Reynolds number. We observe that the gas–phase Reynolds stress in the bed is anisotropic at all Reynolds numbers and volume fractions. Based on the PReIBM DNS data, we propose a correlation for  $k_f/E_f$  in terms of solid volume fraction and mean flow Reynolds number. Our results indicate that the use of a length scale analogous to Taylor microscale is appropriate to model the dissipation term in gas–solid flows.

## CHAPTER 4. Heat transfer in dense gas–solid flow as revealed by particle–resolved direct numerical simulation

This chapter is a manuscript titled “Role of fluid heating in dense gas–solid flow as revealed by particle–resolved direct numerical simulation” that has been accepted for publication in the International Journal of Heat and Mass Transfer. This paper is authored by S. Tenneti, B. Sun, R. Garg and S. Subramaniam.

### Abstract

Heat transfer is important in gas–solid flows that are encountered in many industrial applications such as energy generation. Computational fluid dynamics (CFD) simulations of heat transfer in gas–solid flow are based on statistical theories that result in averaged equations (eg., Eulerian–Eulerian two–fluid model). These averaged equations require accurate models for unclosed terms such as the average gas–solid heat flux. The average gas–solid or interphase heat flux is closed in terms of the Nusselt number  $Nu$ , which is specified as a function of the solid volume fraction  $\phi$ , mean flow Reynolds number  $Re_m$  and Prandtl number  $Pr$ . In developing closure models for the average interphase heat flux it is assumed that the gas–solid flow is locally homogeneous i.e., the effect of fluid heating (or cooling) on the average fluid temperature is neglected. However, continuous heating (or cooling) of the fluid along the flow direction causes the average fluid temperature to become inhomogeneous. In this work we develop a particle–resolved direct numerical simulation (PR–DNS) methodology to study heat transfer in steady flow past statistically homogeneous random assemblies of stationary particles. By using an analogy with thermally fully developed flow in pipes, we develop a thermal similarity condition that ensures a statistically homogeneous Nusselt number, even though the average

fluid temperature field is inhomogeneous. From PR–DNS results we find that the effect of fluid heating cannot be neglected for gas–solid systems with high solid volume fractions and low mean flow Reynolds numbers. These results indicate that the assumption of scale separation implicit in two–fluid models is not always valid.

## 4.1 Introduction

Gas–solid flows occur in many industrial applications such as energy generation, food, chemical, and pharmaceutical processing. Carbon–neutral energy generation using biomass (Azar et al., 2006) or chemical looping combustion (Shen et al., 2008) (CLC), and CO<sub>2</sub> capture from flue gases using dry sorbents (Yi et al., 2007; Abanades et al., 2004) are examples of emerging technologies (Wall, 2007) where an improved understanding of gas–solid heat transfer is crucial for process and component design. For instance, accurate prediction of the fluid–phase temperature field is very important for the CLC application because the reaction rates in combustion chemistry are highly temperature dependent. Similarly, the CO<sub>2</sub> capture process using dry sorbents involves both exothermic and endothermic reactions and hence gas–solid heat transfer is crucial for the efficient performance of the process. Both CLC and CO<sub>2</sub> capture technologies can be implemented using fluidized beds, where the particle diameter  $D$  can vary from 50–150  $\mu\text{m}$ . The particles are typically larger than the Kolmogorov length scale of turbulent dissipation  $\eta$ . Moreover, gas–solid flow in fluidized beds can have a solid volume fraction ranging from near close packed (64% for random configurations of monodisperse spheres) to as low as 5% in the riser region. A fundamental understanding of heat transfer in fluid flow past finite sized particles ( $D > \eta$ ) over a wide range of physical parameters like solid volume fraction and flow Reynolds number is therefore important for process design.

Computational fluid dynamics (CFD) simulations (Syamlal et al., 1993; Kashiwa and Gaffney, 2003; Sun et al., 2007) of gas–solid flow are increasingly being used as an efficient approach for design optimization because experiments are often costly and time-consuming. In CFD simulations of gas–solid flow, averaged equations governing mass, momentum, and energy are solved. Figure 4.1 shows a schematic of the computational domain in a CFD simulation of gas–solid flow. In every grid cell, governing equations for averaged quantities such as volume fraction,

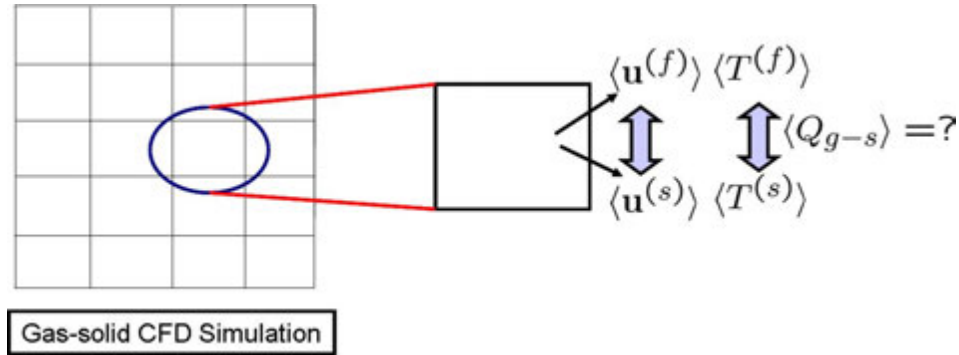


Figure 4.1 Schematic of a CFD simulation of gas–solid flow. In every computational grid cell, governing equations for the averaged quantities in both phases are solved. Here,  $\langle \mathbf{u}^{(f)} \rangle$  is the average fluid–phase velocity,  $\langle T^{(f)} \rangle$  is the average fluid–phase temperature,  $\langle \mathbf{u}^{(s)} \rangle$  is the average solid–phase velocity and  $\langle T^{(s)} \rangle$  is the average solid–phase temperature. In this schematic,  $\langle Q_{g-s} \rangle$  denotes the average gas–solid interphase heat transfer.

velocity and temperature are solved for both phases. Since these equations are obtained using a statistical averaging procedure (Anderson and Jackson, 1967; Drew and Passman, 1998), the average interaction terms corresponding to mass, momentum, and energy exchange between different phases need to be modeled. For example, two–fluid CFD formulations for heat transfer in gas–solid flow require closure of the average gas–solid heat transfer rate per unit volume  $\langle Q_{g-s} \rangle$ . The average interphase heat transfer rate  $\langle Q_{g-s} \rangle$  is modeled in terms of an average Nusselt number and the difference between the average fluid and solid–phase temperature ( $\langle T^{(f)} \rangle - \langle T^{(s)} \rangle$ ). This Nusselt number is usually given by a correlation that depends on solid volume fraction  $\phi$ , mean slip Reynolds number  $Re_m$  and the Prandtl number  $Pr$ .

Correlations for the Nusselt number corresponding to gas–solid heat transfer are typically obtained from a combination of experimental and theoretical studies. However, the experimental data from which these empirical correlations are deduced vary by orders of magnitude (Wakao and Kaguei, 1982; Breault and Guenther, 2009). Most experimental measurements of heat transfer in gas–solid flow are intrusive. Theoretical studies of heat transfer in gas–solid systems are limited to creeping flow past ordered (Pfeffer and Happel, 1964; Sorensen and Stewart, 1974b) and random assemblies of spheres (Gunn, 1978; Acrivos et al., 1980). The

randomness in particle positions and velocities together with the nonlinearity of the governing equations make the analytical treatment intractable at finite Reynolds numbers. Particle-resolved direct numerical simulation (PR–DNS) of heat transfer in gas–solid flow is a first-principles, model-free simulation method that can be used to gain better understanding of heat transfer in gas–solid flow. Furthermore, PR–DNS can be used to specify closure models for the unclosed average interphase interaction terms that arise in CFD simulations of gas–solid flow.

In applying closure models for the average interphase interaction terms such as the average interphase momentum transfer and interphase heat flux, it is assumed that the gas–solid flow is locally homogeneous. In other words, the average fluid and solid–phase velocities and temperatures are assumed to be uniform in the grid cell. Therefore, in order to specify closure models for the unclosed terms it is natural to simulate a statistically homogeneous gas–solid suspension using PR–DNS. Indeed, PR–DNS has been used successfully to solve the hydrodynamic problem and to provide a closure model for the average gas–solid momentum transfer. The closure for the average interphase momentum transfer is popularly known as a “drag law” and several researchers have extracted computational drag correlations for gas–solid flow by simulating steady flow past statistically homogeneous random assemblies of stationary spherical particles (Hill et al., 2001a,b; van der Hoef et al., 2005; Beetstra et al., 2007; Yin and Sundaresan, 2009a,b; Holloway et al., 2010; Tenneti et al., 2011) in periodic domains. Tenneti et al. (2011) have rigorously shown that the evolution equation for the volume averaged fluid–phase momentum obtained from this setup is consistent with statistically homogeneous ensemble–averaged equations. This problem setup ensures that the flow field is statistically homogeneous and statistics such as the average interphase momentum transfer can be easily obtained by volume averaging.

In the heat transfer problem, the assumption of a statistically homogeneous average fluid temperature implies that the effect of heating (or cooling) by the particles does not change the average fluid temperature significantly. However, continuous heating (or cooling) of the fluid by the particles along the flow direction can cause the average fluid temperature to vary in that direction. The extent of this variation of the average fluid temperature depends on the solid volume fraction and mean flow Reynolds number. Although the hydrodynamic problem

is *statistically homogeneous*, for some regimes of gas–solid flow it is conceivable that anisotropy in the fluid velocity results in a *statistically inhomogeneous* fluid temperature field. Therefore, PR–DNS methodologies that are used to specify a closure model for the average Nusselt number in terms of the average solid volume fraction and mean flow Reynolds number must account for this inhomogeneity in the fluid temperature field. In this work we present a PR–DNS methodology to study heat transfer in statistically homogeneous gas–solid flow in periodic domains that accounts for the inhomogeneity in the temperature field. We use the analogy of flow in a fixed bed of particles with thermally fully developed flow in internal pipes to develop a thermal similarity condition that guarantees a statistically homogeneous Nusselt number. Using this new formulation we examine the regime of validity of the assumption of statistical homogeneity in the average fluid temperature field that is implicit in two–fluid CFD models.

We use the Particle–resolved Uncontaminated–fluid Reconcilable Immersed Boundary Method (PUREIBM) (Garg et al., 2011; Tenneti et al., 2010b, 2011) to solve for heat transfer in gas–solid flow. We employ three–dimensional Cartesian grids to solve for the velocity, pressure, as well as the temperature fields. Dirichlet boundary conditions for both velocity and temperature at the surface of the particle are imposed via an immersed boundary (IB) forcing that is added to the momentum and temperature equations, respectively. The idea behind the extension of the IB method to the temperature equation is similar to the one used by Feng and Michaelides (2008) to study heat transfer in particle–laden flow with solid to fluid density ratio in the range 1.001–1.1.

The rest of the paper is organized as follows. The problem description and the assumptions made to simplify the problem are described in section 4.2. The formulation of the heat transfer problem that is simulated in the particle–resolved DNS methodology is discussed in section 4.3. The governing equations are developed in section 4.4 and the numerical method used in our PR–DNS approach is described in section 4.5. The results obtained from PR–DNS of heat transfer in gas–solid flow are discussed in section 4.6 and finally the principal conclusions of this work are summarized in section 4.7.

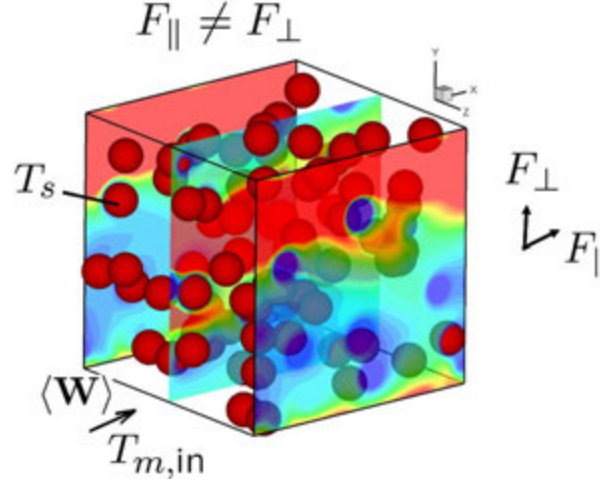


Figure 4.2 Schematic showing contours of steady temperature field in a flow through fixed bed of particles (solid volume fraction 0.1 and Reynolds number 20). In this schematic,  $\langle \mathbf{W} \rangle$  is the mean slip velocity between the solid and the fluid-phase. The fluid enters the domain at a bulk temperature of  $T_{m,in}$  and all the particles are held at a uniform constant temperature  $T_s$ .

## 4.2 Problem description

A schematic of the problem setup that is used in this work to study gas–solid heat transfer in a homogeneous suspension of randomly distributed spherical particles is shown in Fig. 4.2. The figure shows a random assembly of spherical particles in a unit cell, which repeats infinitely in all three directions. A steady flow is established by imposing a mean pressure gradient that corresponds to a mean flow Reynolds number that is defined based on the magnitude of mean slip velocity between the two phases as follows:

$$\text{Re}_m = \frac{|\langle \mathbf{W} \rangle| (1 - \phi) D}{\nu_f}. \quad (4.1)$$

Here  $|\langle \mathbf{W} \rangle|$  is the magnitude of the mean slip velocity between the solid and fluid phases, which is in the direction shown in Fig. 4.2,  $D$  is the particle diameter and  $\nu_f$  is the kinematic viscosity of the fluid. The bulk temperature of the fluid at the “inlet” of this unit cell is  $T_{m,in}$  and all the particles are held at a uniform constant temperature of  $T_s$ . The bulk temperature of the fluid is the flux-weighted average temperature in a plane perpendicular to the direction of the mean slip velocity (see section 4.3 for a detailed definition). The difference in the bulk fluid temperature and the surface temperature of the particle drives gas–solid heat transfer. Here

we consider only gas–solid flow so the Prandtl number is chosen to be 0.72. We neglect viscous heating, radiation and the effect of temperature change on the momentum equation due to density variation (free convection effects). The simplifying assumptions used in our problem setup are justified in B. We now develop a formulation that can be used to study the gas–solid flow heat transfer problem described in this section.

### 4.3 Formulation of the heat transfer problem

In order to use the problem setup shown in Fig. 4.2 to quantify the average Nusselt number, we must ensure that the heat transfer problem admits a statistically homogeneous Nusselt number. In other words, a thermally fully developed flow must be established in the fixed bed. Flow through a fixed bed of spheres is anisotropic due to finite mean slip velocity  $\langle \mathbf{W} \rangle$  between the solid and fluid phases. This directionality in the flow implies that fluid downstream of a particle is heated up (or cooled down) by interphase heat transfer. This continuous heating of the fluid by the particles results in a mean fluid temperature that is inhomogeneous (Acrivos et al., 1980) in the coordinate directed along the mean flow. However, since Nusselt number is a nondimensional interphase heat flux, if the driving force (temperature difference between bulk fluid and particles) has the same variation as that of the interphase heat flux along the flow coordinate, it is possible to obtain a statistically homogeneous Nusselt number. In this section we develop a formulation that renders the Nusselt number statistically homogeneous, although the interphase heat flux and the mean fluid temperature are inhomogeneous.

In order to understand the heat transfer problem in statistically homogeneous suspensions we draw analogy from forced convection heat transfer in internal pipe flow. Statistically homogeneous gas–solid flow is analogous to fully developed pipe flow in two respects. Firstly, the flow field is statistically axisymmetric (Tenneti et al., 2012), similar to the fully developed flow field in a pipe. Secondly, the *average* area occupied by the fluid (or the area fraction) in any plane perpendicular to the streamwise direction is constant in a statistically homogeneous suspension, and hence can be compared to a pipe with a constant area of cross section. Therefore, in an *average* sense we expect the heat transfer problem in statistically homogeneous gas–solid suspensions with isothermal particles to be similar to thermally fully developed flow in pipes

with isothermal walls. For internal pipe flow, the flow is said to be thermally fully developed when the scaled temperature is not varying in the streamwise direction (Incropera et al., 2006), i.e.,

$$\frac{\partial}{\partial x} \left( \frac{T(\mathbf{x}, t) - T_w}{T_m(x, t) - T_w} \right) = 0. \quad (4.2)$$

Without loss of generality we will assume that the flow direction is along the  $x$ -axis. In the definition of the scaled temperature given above,  $T_w$  is the temperature of the isothermal pipe wall and  $T_m$  is called the “mixing-cup” or “bulk” temperature, which is defined as follows:

$$T_m(x) = \frac{\int_{A_f} (\mathbf{u}T) \cdot \mathbf{e}_{\parallel} dA_f}{\int_{A_f} \mathbf{u} \cdot \mathbf{e}_{\parallel} dA_f} \quad (4.3)$$

where  $\mathbf{e}_{\parallel}$  is the unit vector along the streamwise direction and  $A_f$  is the area occupied by the fluid in a plane perpendicular to the streamwise direction. The thermally fully developed condition implies that for a pipe with constant cross-sectional area and isothermal walls, the local heat transfer coefficient at the wall (or Nusselt number) is independent of axial location (Incropera et al., 2006). In other words, the local wall heat flux scaled by the temperature difference ( $T_m(x) - T_w$ ) is a constant. By using an analogy with pipe flow, the average Nusselt number in gas–solid flow will be statistically homogeneous if we ensure that the scaled temperature field  $\theta$ , which is defined below is statistically homogeneous:

$$\theta(\mathbf{x}, t) = \frac{T(\mathbf{x}, t) - T_s}{\langle T_m \rangle(x, t) - T_s}. \quad (4.4)$$

In this definition,  $\langle T_m \rangle(x, t)$  is the ensemble-averaged bulk temperature and  $T_s$  is the uniform temperature at which all the particles are maintained. In the next section we discuss the governing equations and boundary conditions for the problem of heat transfer past stationary isothermal particles in periodic domains that ensure that the normalized interphase heat flux is statistically homogeneous.

#### 4.4 Governing Equations

The fluid temperature field  $T(\mathbf{x}, t)$ , in the absence of viscous heating, radiation and free convection effects, obeys the following convection–diffusion equation:

$$\frac{\partial T}{\partial t} + \frac{\partial (u_j T)}{\partial x_j} = \alpha_f \frac{\partial^2 T}{\partial x_j \partial x_j}, \quad (4.5)$$

where  $\alpha_f = k_f / (\rho_f C_{pf})$ . Here  $k_f$  is the thermal conductivity,  $\rho_f$  is the thermodynamic density, and  $C_{pf}$  is the heat capacity of the fluid respectively. Equation (4.5) needs to be solved in the fluid together with the Dirichlet boundary condition of  $T = T_s$  at the surface of the particles. At the boundaries of the computational domain, periodic boundary conditions are applied on the *scaled temperature*  $\theta$  (cf. Eq. 4.4). In the definition of  $\theta$  for a random particle assembly, Eq. (4.3) gives an area-averaged estimate for the bulk temperature  $\langle T_m \rangle$ .

Since the boundary conditions at the domain boundaries are in terms of  $\theta$ , it would appear to be easier to rewrite Eq. 4.5 in terms of  $\theta$  and solve directly for  $\theta$ . However, the evolution equation for  $\theta$  contains additional terms that represent the evolution of the bulk temperature  $T_m$ . Therefore, in order to solve for  $\theta$  we need to solve an additional equation for  $T_m$ . Moreover, solving for the evolution equation for  $T_m$  requires the computation of heat flux from every particle that intersects the plane perpendicular to the mean flow at each  $x$  location in the direction of the mean flow. Since there is a finite number of particles in the computational domain, the solution may suffer from statistical error. Therefore, it turns out to be easier to transform the periodic boundary conditions on  $\theta$  to obtain similarity conditions on the temperature field  $T(\mathbf{x}, t)$  and solve Eq. (4.5) for  $T(\mathbf{x}, t)$ .

In order to simplify the thermal similarity conditions and also to homogenize the boundary conditions on the particle surfaces we define a non dimensional temperature field  $\phi(\mathbf{x}, t)$  as follows:

$$\phi(\mathbf{x}, t) = \frac{T(\mathbf{x}, t) - T_s}{T_{m,\text{in}} - T_s} \quad (4.6)$$

where,  $T_{m,\text{in}}$  is the bulk temperature at  $x = 0$ . Using this definition of the non dimensional temperature, it is easy to see that the non dimensional bulk temperature  $\phi_m(x)$  has a similar definition:

$$\phi_m(x, t) = \frac{T_m(x, t) - T_s}{T_{m,\text{in}} - T_s}. \quad (4.7)$$

Substituting Eq. (4.6) in Eq. (4.5) gives the governing equation for the non dimensional temperature:

$$\frac{\partial \phi}{\partial t} + \frac{\partial (u_j \phi)}{\partial x_j} = \alpha_f \frac{\partial^2 \phi}{\partial x_j \partial x_j}. \quad (4.8)$$

The isothermal boundary conditions on the particle surface reduce to  $\phi = 0$ .

In order to understand the periodicity conditions and also for ease of implementation we introduce a quantity called the heat ratio  $r_h$  which is defined as:

$$r_h = \frac{T_{m,\text{in}} - T_s}{T_{m,\text{out}} - T_s}, \quad (4.9)$$

where  $T_{m,\text{out}}$  is the bulk temperature at  $x = L$  and  $L$  is the length of the box. The heat ratio is the ratio of the bulk temperature at the inlet ( $x = 0$ ) to the bulk temperature at the outlet ( $x = L$ ). In other words the heat ratio is simply the inverse of the non dimensional bulk temperature at  $x = L$  i.e.,

$$r_h = \frac{1}{\phi_{m,\text{out}}}. \quad (4.10)$$

The heat ratio quantifies by how much a *fluid* particle heats up when it leaves the box and so this quantity depends solely on the flow structure and the interphase heat transfer in the domain. A control volume analysis of the governing equation for  $\phi$  reveals the following relation for the heat ratio:

$$r_h = \frac{T_m(x) - T_s}{T_m(x+L) - T_s} = \frac{T_m(x \pm a) - T_s}{T_m(x+L \pm a) - T_s}, \quad (4.11)$$

where  $a$  is any displacement in the streamwise direction. The periodic boundary conditions on  $\phi$  now appear in a very simple form:

$$\begin{aligned} \phi(0, y, z) &= r_h \phi(L, y, z), \\ \phi(x, 0, z) &= \phi(x, L, z), \\ \phi(x, y, 0) &= \phi(x, y, L). \end{aligned} \quad (4.12)$$

An important point to be noted is that the heat ratio, or the amount by which the fluid gets heated up (or cooled down) when it reaches the end of the box, is an unknown quantity and it is part of the solution. In this formulation the thermal similarity conditions (cf. Eq. (4.12)) are defined in terms of the heat ratio. So the heat transfer problem has to be solved iteratively until the heat ratio converges. In the next section we describe the immersed boundary methodology that is used to solve the heat transfer problem in statistically homogeneous suspensions.

## 4.5 Solution Approach

The complete details of the hydrodynamic PReIBM solver are discussed elsewhere (Garg et al., 2011; Tenneti et al., 2011). Here the discussion is limited to the solution of the heat transfer problem in statistically homogeneous suspensions using PReIBM. In PReIBM, we employ Cartesian grids and solve the mass and momentum conservation equations at all the grid points (including those lying inside the particles). Similarly the nondimensional temperature field is also solved at all grid points. The governing equation for  $\phi$  that is solved in PReIBM is

$$\frac{\partial \phi}{\partial t} + \frac{\partial (u_j \phi)}{\partial x_j} = \frac{\partial q_j^\phi}{\partial x_j} + I_s f_\phi, \quad (4.13)$$

where  $\mathbf{q}^\phi = \alpha_f \nabla \phi$  is the heat flux, and  $f_\phi$  is the additional immersed boundary (IB) forcing term that is nonzero only in the solid phase. The immersed boundary forcing  $f_\phi$  accounts for the presence of the solid particles in the domain by ensuring that the isothermal boundary condition  $\phi = 0$  is satisfied on the surface of the solid particles.

The surface of the solid particle is represented by a discrete number of points called boundary points. For spherical particles, the boundary points are specified by discretizing the sphere in spherical coordinates. In figure 4.3, a schematic describing the computation of the IB forcing is shown for the equatorial plane passing through the spherical particle. Another set of points called exterior points are generated by projecting these boundary points onto a sphere of radius  $r + \Delta r$ , where  $r$  is the radius of the particle (see exterior point represented by an open circle on the dashed line in figure 4.3). Similarly, the boundary points are projected onto a smaller sphere of radius  $r - \Delta r$  and these points are called interior points. In our simulations  $\Delta r$  is taken to be same as the grid spacing. The IB forcing is computed only at the interior points. At these points the fluid temperature is forced in a manner similar to the ghost cell approach used in standard finite-difference/finite-volume based methods (Patankar, 1980). For the boundary condition  $\phi = 0$  used in this work, the value of  $\phi$  at the interior points is forced to be opposite in magnitude to the value of  $\phi$  at the corresponding exterior points.

The distinctive feature of PReIBM is that the forcing  $f_\phi$  is computed only at points lying inside the solid particles. This ensures that the fluid-phase temperature field is not contami-

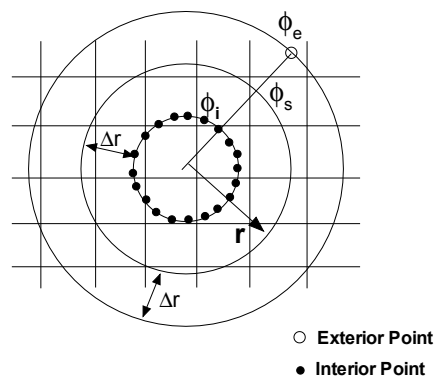


Figure 4.3 A schematic showing the computation of the immersed boundary forcing  $f_\phi$  for an isothermal particle. The solid circle represents the surface of the particle at  $r$ . Open dot shows the location of one exterior point at  $r + \Delta r$  (only one exterior point is shown for clarity, although there is one exterior point for each interior point) and filled dots show the location of interior points at  $r - \Delta r$  where the immersed boundary forcing is computed. In the schematic,  $\phi_e$  represents the temperature at the exterior point,  $\phi_s$  is the surface temperature while  $\phi_i$  is the temperature at the interior point.

nated by the scalar IB forcing term  $f_\phi$ , just as the fluid-phase velocity field is not contaminated by the hydrodynamic IB forcing. The consequences of fluid velocity contamination by IB forcing are discussed in detail by Tenneti et al. (2011). The computation of  $f_\phi$  is similar to the computation of the IB forcing for the velocity field. The IB forcing term  $f_\phi^{n+1}$  at the  $(n + 1)^{\text{th}}$  time-step is specified to cancel the remaining terms in the governing equation for  $\phi$  and force the nondimensional temperature to its desired value  $\phi^d$  at the interior points:

$$f_\phi^{n+1} = \frac{\phi^d - \phi^n}{\Delta t} + C_\phi^n - \left( \frac{\partial q_j^\phi}{\partial x_j} \right)^n \quad (4.14)$$

where  $C_\phi^n$  is the convective term at the  $n^{\text{th}}$  time step.

The heat transfer equation (cf. Eq. 4.13) in PUReIBM is solved using a pseudo-spectral method, with a Crank–Nicolson scheme for the viscous terms, and an Adams-Bashforth scheme for the convective terms. The use of Fourier transforms in the cross stream directions and the Crank–Nicolson scheme in the streamwise direction results in an independent set of cyclic tridiagonal systems that are solved using the Sherman–Morrison formula (Sherman and Morrison, 1950). The coefficient matrices in the tridiagonal systems depend on the heat ratio  $r_h$  which is not known *a priori*. The temperature field is initialized with  $r_h = 1$  and the simulation is performed iteratively till the value of the heat ratio converges. It must be noted that in this work we use the steady velocity field that is obtained from the hydrodynamic solver and the velocity field is not advanced during the solution of the heat transfer problem.

## 4.6 Results and Discussion

The hydrodynamic solver in the PUReIBM methodology has been extensively validated using a comprehensive suite of test cases (Tenneti et al., 2011). In order to check the accuracy of the IB methodology for temperature and also to verify the thermal similarity boundary condition, we simulate convective heat transfer in a square duct. The no slip walls of the duct for the velocity field as well as the isothermal condition at the walls for the temperature field are generated using the IB methodology described in the previous section.

Using an analytical calculation, Shah and London (1978) found that the Nusselt number for a thermally fully developed laminar flow in a square duct is 2.976. We compare the Nusselt

Reynolds number	PUReIBM	Analytical
20	3.013	2.976
50	3.029	2.976
100	3.033	2.976

Table 4.1 Comparison of Nusselt number obtained from PUReIBM simulation of duct flow for three different Reynolds numbers with the Nusselt number derived from an analytical calculation.

number obtained from PUReIBM simulations for three different Reynolds numbers with the analytical solution in table 4.1. We see that the results obtained from PUReIBM simulations agree very well with the analytical solution. The numerical convergence of Nusselt number with grid resolution for a Reynolds number of 100 is shown in Fig. 4.4(a). In this figure we plot the relative error between the analytical and numerical solution. We see that the Nusselt number obtained from PUReIBM simulations converge to the analytical value given by Shah and London (1978). In figure 4.4(b) we plot the contours of the scaled temperature  $\theta$  (cf. Eq. 4.4) along the flow direction. This plot verifies that the thermal similarity condition applied at the ends of the domain generates a thermally fully developed flow. These tests confirm the accuracy and numerical convergence of the PUReIBM temperature solver and also the correctness of the application of the thermal similarity condition.

We now study heat transfer in statistically homogeneous gas–solid flow using PUReIBM DNS of steady flow and heat transfer past stationary, isothermal particles in periodic domains. Particle centers are initialized corresponding to a specified mean solid volume fraction  $\phi$ . The particles are fixed in a random equilibrium configuration they attain following elastic collisions (in the absence of ambient fluid) starting from a lattice arrangement with a Maxwellian velocity distribution. The elastic collisions are simulated using a soft–sphere discrete element model (Cundall and Strack, 1979; Garg et al., 2010a). The pair correlation function at equilibrium specifies the particle configuration for random assemblies. Steady flow is established in the fixed bed by imposing a mean pressure gradient that corresponds to a mean flow Reynolds number. The hydrodynamic solver has been extensively validated in a comprehensive suite of

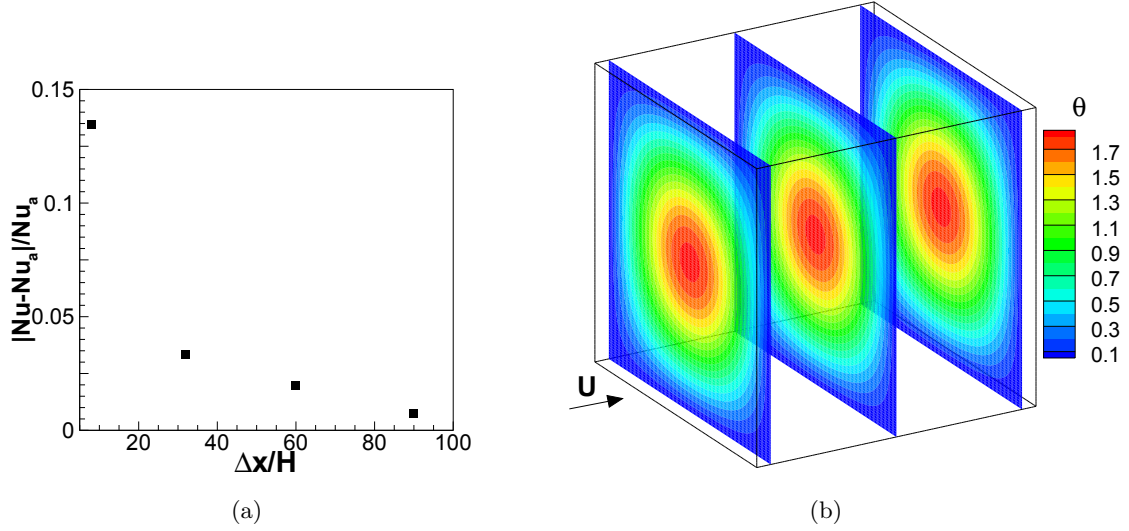


Figure 4.4 (a) Convergence characteristics of Nusselt number with grid resolution for internal duct flow at a Reynolds number of 100 are shown in. In this plot  $Nu_a$  refers to the analytical value of the Nusselt number obtained by Shah and London (1978),  $\Delta x$  is the size of the grid cell and  $H$  is the channel height. (b) Contours of the scaled temperature  $\theta$  are shown in three planes along the direction of the flow shown by the arrow.

tests (Tenneti et al., 2011). The steady velocity field that is established in the fixed bed is used to evolve the temperature in pseudo-time until the heat ratio reaches a steady state.

The heat transfer problem is statistically inhomogeneous only in the direction of the mean flow and hence all statistics are estimated using area averages in planes perpendicular to the mean flow. Each random particle configuration is termed a realization of the gas–solid flow corresponding to a specified volume fraction and pair correlation function. The streamwise variation of Nusselt number for the  $\omega^{\text{th}}$  realization is defined as

$$Nu(x; \omega) = \frac{q''(x; \omega) D}{k_f P (\phi_m(x) - \phi_s)}. \quad (4.15)$$

In this definition,  $q''(x; \omega)$  is the interphase heat flux from the particles to the fluid that is averaged in the cross plane at the location  $x$ , and  $P$  is the perimeter formed by cutting the particles with the plane. The streamwise variation of Nusselt number obtained from a single realization is prone to statistical uncertainty due to finite number of particles in the computational domain. Therefore, the streamwise variation of Nusselt number from a single realization

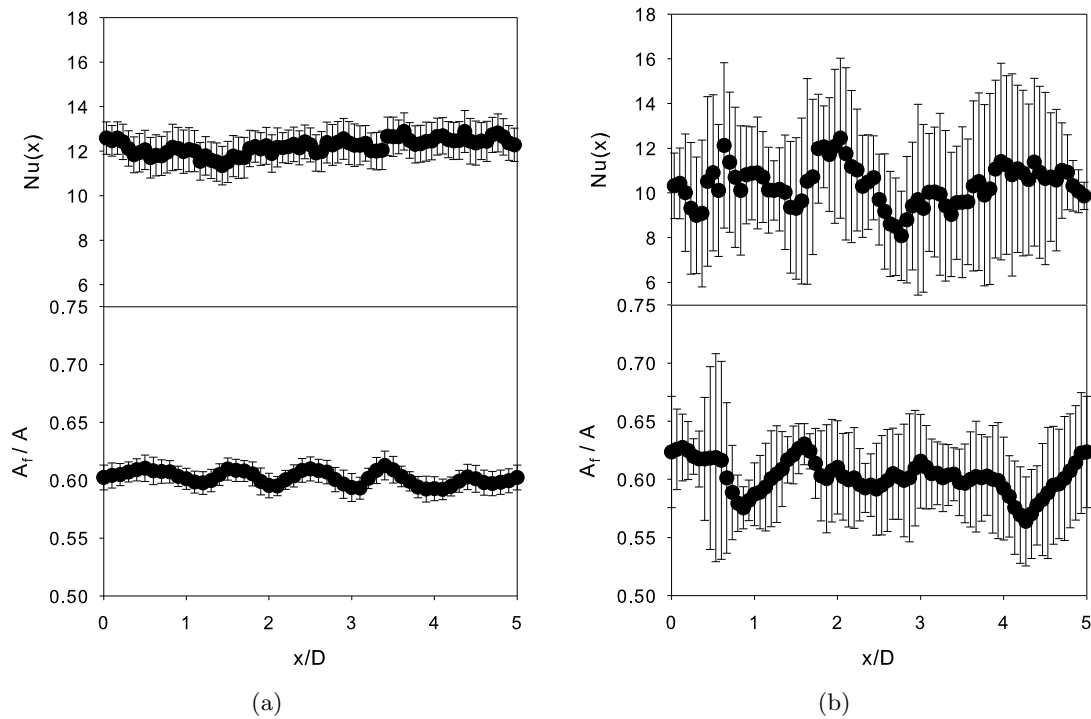


Figure 4.5 Variation of Nusselt number and the area occupied by the fluid-phase along the direction of the mean flow, obtained from PReIBM simulations of heat transfer in a fixed bed at a volume fraction of 0.4 and mean flow Reynolds number of 100. The local Nusselt number is reported by averaging over (a) 50 and (b) 5 MIS.

must be averaged over multiple independent simulations (MIS), each corresponding to a different realization of the particle configuration, to get a better estimate for the ensemble-averaged streamwise Nusselt number. If the streamwise Nusselt number obtained from averaging over several realizations is independent of the spatial location, we can say that the Nusselt number is statistically homogeneous. In that case volume averaging can also be used to improve this estimate.

From the PReIBM heat transfer simulations we verify that the thermal similarity boundary condition produces a statistically homogeneous streamwise Nusselt number. Figure 4.5 shows the streamwise variation of Nusselt number (top panels) for a fixed bed with a solid volume fraction of 0.4 and mean flow Reynolds number of 100. In Fig. 4.5 we compare the local Nusselt number obtained from averaging over 50 MIS (figure 4.5(a)) with that obtained from averaging over 5 independent realizations (figure 4.5(b)). We see that the Nusselt number ob-

tained from 50 MIS is constant along the flow direction. The Nusselt number from 5 MIS shows some variation along the axial direction. The finite size of the computational domain in the cross stream direction and also the small number of independent realizations are responsible for this streamwise variation in the Nusselt number. To see this more clearly, the variation of the area occupied by the fluid  $A_f$  along the flow direction is also shown in Fig. 4.5 (bottom panels). Recall that one of the conditions for statistical homogeneity of Nusselt number is that the area occupied by the fluid should be constant along the flow direction. The figures indicate that the estimate for the average area occupied by the fluid can vary along the flow direction and also at any given axial location there are fluctuations in the area across realizations (indicated by error bars). The amplitude of the fluctuation in the area is found to be about 7% when the averaging is performed over 5 MIS. From convergence studies, we found that 50 realizations are required to reduce the amplitude in the fluctuation of the area to 2%. Similar requirements on the number of independent realizations were reported by Xu and Subramaniam (2010) in their study of particles in upstream turbulence. Figure 4.5(a) shows that the variation as well as the level of fluctuations in the Nusselt number and the area fraction are reduced when the averaging is performed over 50 MIS. We conclude that for statistically homogeneous assemblies, the formulation developed for the heat transfer problem ensures that the local Nusselt number is statistically homogeneous.

Due to the statistical homogeneity of the Nusselt number in the streamwise direction, we can compute the average Nusselt number  $\langle Nu \rangle$  by averaging  $Nu(x)$  along the axial direction. Figure 4.6 compares the average Nusselt number obtained from PReIBM simulations with the Nusselt number predicted by Gunn's correlation (Gunn, 1978). From the figure we see that the average Nusselt number increases with both solid volume fraction and mean flow Reynolds number and this behavior is consistent with the trend predicted by the correlation. It must be noted that the Nusselt number correlation given by Gunn (1978) is a fit to experimental data obtained by several researchers for packed beds ( $\phi = 0.6$ ). Given that the experimental data itself has a wide variation, the agreement between the PReIBM DNS and the correlation is excellent.

In addition to the average Nusselt number, the nature of inhomogeneity of the fluid tem-

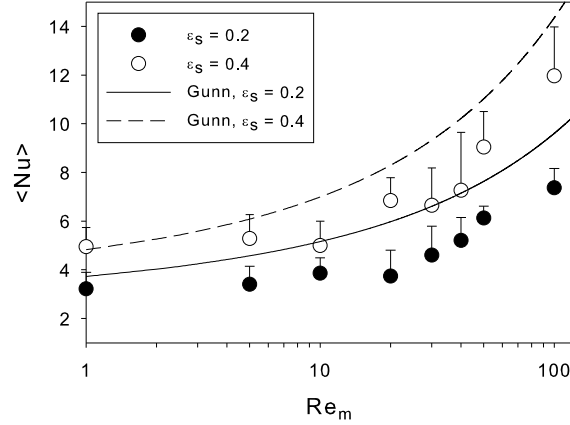


Figure 4.6 Behavior of the average Nusselt number  $\langle \text{Nu} \rangle$  with mean flow Reynolds number for two solid volume fractions. Symbols indicate data obtained from PReIBM simulations while the solid lines are obtained from Gunn's correlation (Gunn, 1978). The average Nusselt number from PReIBM simulations is reported by averaging over 5 MIS and the error bars on the symbols in this figure represent 95% confidence intervals in the estimation of Nusselt number.

perature field or fluid heating is important in modeling the average interphase heat transfer  $\langle Q_{g-s} \rangle$ . We plot the non-dimensional bulk temperature  $\phi_m$  along the flow direction for two mean flow Reynolds numbers (1 and 100) and two solid volume fractions (0.2 and 0.4) in figure 4.7(a). In this setup the particles are cooler than the incoming fluid and so the effect of the particles is to reduce the bulk fluid temperature. The results confirm the fact that the temperature field is not homogeneous in the flow direction. We see that the inhomogeneity in the nondimensional bulk temperature is especially apparent at high solid volume fraction and low Reynolds number. This spatial inhomogeneity is found to arise from the effect of fluid cooling, which is more pronounced at high solid volume fraction and low Reynolds number. This result is more easily evident when we consider the behavior of heat ratio  $r_h$ . Recall that the heat ratio gives a measure of the fluid cooling because  $(1 - r_h) / r_h = (T_{m,\text{out}} - T_{m,\text{in}}) / (T_{m,\text{in}} - T_s)$ . Two limiting cases are of interest. If there is negligible fluid cooling, then  $T_{m,\text{out}} \approx T_{m,\text{in}}$ , and  $r_h \approx 1$ , in which case  $(1 - r_h) / r_h \approx 0$ . The other limiting case is of extreme cooling such that  $T_{m,\text{out}} \approx T_s$ , in which case  $(1 - r_h) / r_h \approx -1$ . Figure 4.7(b) shows a plot of this measure of

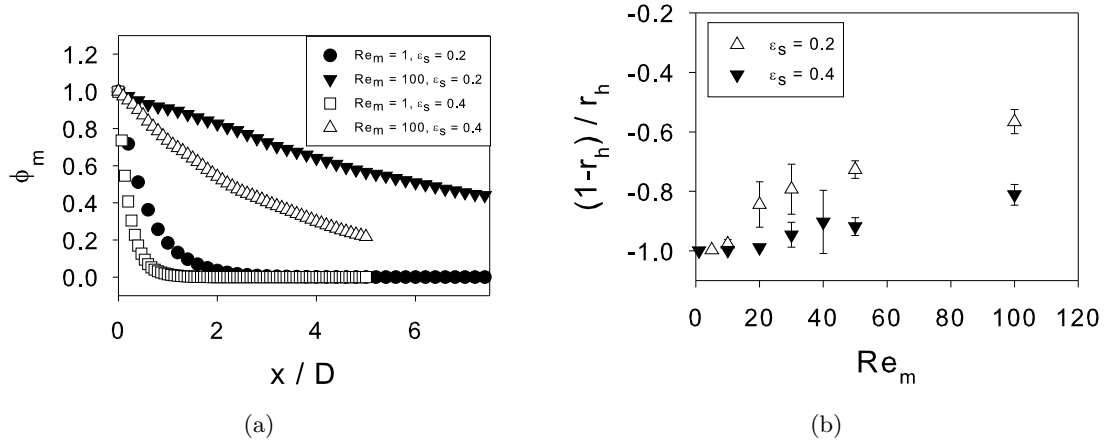


Figure 4.7 (a) Variation of the nondimensional bulk fluid temperature along the axial direction for two mean flow Reynolds numbers (1 and 100) and two solid volume fractions (0.2 and 0.4). (b) Behavior of heat ratio with Reynolds number for two solid volume fractions (0.2 and 0.4).

fluid cooling, and we see that  $(1 - r_h)/r_h$  is close to -1 at low mean slip Reynolds numbers and this corresponds to near maximal cooling. As the Reynolds number increases the amount of cooling reduces and  $(1 - r_h)/r_h$  departs from -1 towards zero.

The inhomogeneity in the mean fluid temperature has certain implications on modeling the average gas–solid heat transfer in two–fluid models. In treating the solid phase as a continuum in the two–fluid models there is an implicit assumption of separation of scales. It is assumed that the mean solid phase velocity and temperature vary on length scales that are much larger than the length scales over which the microstructure varies. And in turn, it requires the mean fluid temperature also to vary on similar length scales. However, the scale of variation of  $\phi_m$  in Fig. 4.7(a) indicates that the mean fluid temperature can be inhomogeneous on the scale of the particle diameter. Therefore, the inhomogeneity of the average fluid–phase temperature cannot be neglected for all values of the solid volume fraction and mean slip Reynolds number in the CFD implementations of models for average gas–solid heat transfer. Consequently, these results indicate that in general a more sophisticated multiphase large-eddy simulation (LES) approach is necessary to properly account for the effects of fluid cooling (or heating) over all values of the solid volume fraction and mean slip Reynolds number.

## 4.7 Conclusions

In this work we present a particle-resolved direct numerical simulation methodology to study heat transfer in statistically homogeneous gas-solid flow. The Particle-resolved Uncontaminated-fluid Reconcilable Immersed Boundary Method (Tenneti et al., 2011) (PUReIBM) has been extended to investigate heat transfer in fixed periodic assemblies of monodisperse spherical particles held at a constant uniform temperature. Periodic arrangement of particles induces a velocity field that is periodic in all three directions. Since the mean fluid velocity has a direction and all the particles are held at the same temperature, the resulting temperature field will not be periodic. In order to be consistent with the periodic arrangement of the particles, a thermal similarity boundary condition is applied on the temperature field by drawing analogy from thermally fully developed flow in pipes. The extension of PUReIBM to solve for the temperature field is validated by solving the heat transfer problem in a square duct. Numerical convergence and the validity of the thermal similarity condition in flow past random assemblies of spheres is verified. From PUReIBM PR-DNS of heat transfer in fixed particle assemblies, we establish that the formulation developed for heat transfer results in a statistically homogeneous average Nusselt number. We conclude that fluid heating (cooling) in gas-solid systems results in an inhomogeneous bulk fluid temperature. However, two-fluid CFD models that are used to solve for heat transfer in gas-solid systems employ the assumption of local homogeneity of the bulk fluid temperature. Based on the PR-DNS results presented here, we conclude that for  $\phi < 0.4$  and  $Re_m > 10$ , the bulk fluid temperature decays over a few particle diameters. The inhomogeneity of the bulk fluid temperature in these gas-solid flow systems can be accounted for in two-fluid CFD models by an appropriate choice of the grid size. However, for gas-solid flow systems with  $\phi > 0.4$  and  $Re_m < 10$  the bulk fluid temperature decays over a length scale that is on the order of a particle diameter. In such regimes, the assumption of separation of scales that is implicit in the underlying continuum formulation itself breaks down. Hence, more sophisticated subgrid models for the bulk fluid temperature are required for CFD of heat transfer in gas-solid systems of high solid volume fraction and low mean flow Reynolds number.

## CHAPTER 5. Particle-resolved direct numerical simulation of freely evolving gas-solid suspensions at moderate Reynolds number

This chapter is an article (Tenneti et al., 2010b) titled “Direct numerical simulation of gas-solid suspensions at moderate Reynolds number: quantifying the coupling between hydrodynamic forces and particle velocity fluctuations” published in Powder Technology journal. This is authored by S. Tenneti, R. Garg, C. M. Hrenya, R. O. Fox and S. Subramaniam.

### Abstract

Predictive device-level computation fluid dynamics (CFD) simulation of gas-solid flow is dependent on accurate models for unclosed terms that appear in the averaged equations for mass, momentum and energy conservation. In the multifluid theory, the second moment of particle velocity represents the strength of particle velocity fluctuations and is known to play an important role in the prediction of core-annular flow structure in risers (Hrenya and Sinclair, 1997). In homogeneous suspensions the evolution of the second velocity moment is governed by the particle acceleration-velocity covariance. Therefore, fluctuations in the hydrodynamic force experienced by particles in a gas-solid flow affect the evolution of particle velocity fluctuations, which in turn can affect the mean and variance of the hydrodynamic force. This coupling has been studied in the limit of Stokes flow by Koch and co-workers using a combination of kinetic theory and multipole expansion simulations. For Reynolds numbers beyond the Stokes limit, direct numerical simulation is a promising approach to quantify this coupling. Here we present direct numerical simulation (DNS) results for the evolution of particle granular temperature and particle acceleration variance in freely evolving homogeneous gas-solid suspensions. It is found that simple extension of a class of mean particle acceleration models to their corresponding

instantaneous versions does not recover the correlation of particle acceleration with particle velocity. This study motivates the development of better instantaneous particle acceleration models that are able to accurately capture the coupling between particle acceleration and velocity.

## 5.1 Introduction

Gas–solid flows are commonly encountered in energy generation and chemical processing. The design and scale-up of industrial devices motivates a better understanding of gas-solid flow characteristics and transport phenomena. A fundamental understanding of gas-solid flow is increasingly relevant with renewed interest in zero-carbon and carbon-negative energy generation technology such as chemical looping combustion.

Computational fluid dynamics (CFD) simulations that solve for averaged equations of multiphase flow are being increasingly used in the design process because they provide detailed information about the solid volume fraction and phasic mean velocity fields in gas-solid flow (Halvorsen et al., 2003). Most CFD codes for device-level simulations of gas-solid flow are based on the Eulerian-Eulerian (EE) multifluid approach because these are computationally less expensive than Lagrangian-Eulerian (LE) simulations. In the EE multifluid approach both the solid and fluid phases are treated as interpenetrating continua, and averaging techniques (Anderson and Jackson, 1967; Drew, 1983; Drew and Passman, 1998) are used to derive the equations governing the conservation of average mass and momentum in the fluid and particle phases. This results in a closure problem similar to that encountered in the statistical theory of single-phase turbulence because the averaging procedure results in unclosed terms that need to be modeled. For instance, the mean momentum conservation equation in the particle phase requires closure of the average fluid–particle interaction force (mean drag force) and the average stress in the solid particle phase. Accurate models for these unclosed terms are needed for predictive CFD simulation of gas-solid flow.

As with all statistical closures, an important modeling question is the adequacy of the mathematical representation to capture physical phenomena of engineering relevance. For instance, it is now established that the prediction of core-annular structure in riser flows requires

solving the transport equation for the particle granular temperature or pseudo-thermal energy (Hrenya and Sinclair, 1997). This informs us that a closure at the level of mean quantities is not adequate to predict important flow characteristics such as core-annular structure, but a closure at the level of second moments is necessary. However, it is not clear that closure at the level of the second moments is sufficient for predictive CFD simulation that will facilitate design and scale-up. Closure at the level of third-order moments has been attempted by some researchers (Simonin, 1995; Peirano and Leckner, 1998).

An alternative approach to the closure of moment transport equations is to consider the evolution of the one-particle distribution function. Just as closure at the level of the transport equation for the probability density function (PDF) in single-phase turbulent reactive flow implies a closure for all moment equations, similarly a kinetic equation that achieves a closure for the one-particle distribution function in kinetic theory implies a closure for all moment equations. In particular, a closure at the one-particle distribution level automatically implies closure of the mean momentum and particle velocity second moment equations. Furthermore, closures at the one-particle distribution level are guaranteed to satisfy realizability criteria, whereas special care is needed to ensure the same in the case of moment closures. These considerations motivate the development of models for the unclosed terms in the transport equation for the one-particle distribution function corresponding to gas-solid flow.

While there is considerable work on kinetic theory of granular flows where the interaction with ambient fluid is neglected, the kinetic theory of gas-solid flow is still being developed. For low Reynolds number flow in the Stokes regime, Koch and co-workers (Koch, 1990; Koch and Sangani, 1999) developed a kinetic theory closure with a model for the conditional particle acceleration that accounts for the presence of ambient fluid in the term transporting the distribution function in velocity space. This theoretical framework allows us to consider two coupled effects: (i) the effect of particle velocity fluctuations on the mean drag, and (ii) the effect of fluctuating particle acceleration on particle velocity fluctuations or granular temperature. Wylie et al. (2003) studied the effect of particle velocity variance on the mean drag for the limiting case of high Stokes number where the particles move under elastic collisions but are unaffected by the hydrodynamic forces. They showed that particle velocity fluctuations

do not affect the mean drag in Stokes flow. This result is not surprising because in Stokes flow the particle acceleration is a linear function of instantaneous particle velocity. However, at moderate mean slip Reynolds numbers the drag law is nonlinear and Wylie et al. (2003) showed that particle velocity fluctuations do affect the mean particle acceleration. They proposed a modified drag law in terms of volume fraction,  $Re_m$  and  $Re_T$ . The focus of this paper is on the second effect: the effect of fluctuating hydrodynamic forces on granular temperature.

For statistically homogeneous gas-solid flows, the correlation between the particle fluctuating velocity and its acceleration fluctuation determines the evolution of the particle velocity second moment. In the limiting case of Stokes flow, Koch (Koch, 1990; Koch and Sangani, 1999) analyzed the granular temperature, which is the trace of the particle velocity second moment, and decomposed the particle acceleration–velocity covariance as the sum of source and sink contributions. Particle granular temperature decreases due to inelastic collisions and viscous interactions with the ambient fluid, and these effects are represented by the sink term. If particle collisions are elastic or flow past fixed particle assemblies is considered, then the granular temperature decreases only due to viscous interactions with the ambient fluid. In the Stokes flow regime the sink term simply relaxes the granular temperature to zero on the viscous relaxation time scale. In Koch’s decomposition of the acceleration-velocity covariance into source and sink terms (Koch and Sangani, 1999), the source term due to hydrodynamic interactions with neighboring particles can balance the sink term leading to a steady state granular temperature in stable homogeneous suspensions. For moderate Reynolds number, there is no unique decomposition of the particle acceleration–velocity covariance as the sum of source and sink contributions.

The source term in the granular temperature equation plays an important role in sustaining a nonzero value of the granular temperature. In its absence the granular temperature in a homogeneous suspensions would simply decay to zero, leading to an infinite Mach number in the particle phase. Not only is this problematic from a numerical standpoint for CFD simulations, but it is also unphysical over a wide range of mean flow Reynolds number and volume fraction. The origin of the source term lies in the hydrodynamic interactions that each particle experiences with its neighbors, and the range of this interaction depends on the mean

flow Reynolds number and the solid volume fraction. It is well known that a sphere sedimenting in a fluid can have a “drafting” effect on its neighbors and draw them into its wake. The draft, kiss and tumble phenomena are well documented in Glowinski et al. (2001). These physical mechanisms can manifest as a source in particle velocity fluctuations by changing each particle’s velocity. This effect is quantified through DNS of freely evolving suspensions in this work.

Although Koch’s analysis is useful in the Stokes flow regime, it is difficult to extend the analysis to moderate Reynolds number cases. At moderate Reynolds number, DNS offers a promising approach to quantify unclosed terms in the transport equations for particle velocity moments, or the transport equation for the one-particle distribution function. This naturally leads to an evaluation of existing models. We use DNS of gas-solid flow at moderate Reynolds number to evaluate a class of acceleration models. The results indicate the need for improved instantaneous particle acceleration models that are capable of capturing the coupling between particle velocity fluctuations and hydrodynamic forces in gas-solid flow.

The next section describes pertinent details of the statistical modeling approach that motivate this study. This is followed by a description of the Particle-resolved Uncontaminated-fluid Reconcilable Immersed Boundary Method (PUREIBM) that is used to perform DNS of gas-solid flow. Then the simulation details for fixed particle assemblies and freely moving suspensions are presented. Results that quantify the coupling are reported, and a class of particle acceleration models is evaluated. Finally, the conclusions of this study are summarized.

## 5.2 Statistical models

The averaged equations for mean momentum conservation and transport of the second moment of particle velocity in the multifluid theory can be derived using an Eulerian-Eulerian or Lagrangian-Eulerian approach. A comprehensive summary of the relations between the moment equations obtained from these statistical approaches can be found in Pai and Subramaniam (2009). Here we choose the Lagrangian-Eulerian approach with the one-particle distribution function as our starting point because it naturally leads to an explicit connection with the moment equations.

### 5.2.1 One-particle distribution function

The one-particle distribution function, which is the number density of particles in an appropriately defined phase space, is the fundamental quantity of interest in the kinetic theory of granular and multiphase flow (Liboff, 2003; Koch, 1990; Subramaniam, 2000, 2001; Garzo et al., 2007a). It is also referred to as the droplet distribution function in spray theory (Williams, 1958). For monodisperse particles the distribution function  $f(\mathbf{x}, \mathbf{v}, t)$  is defined in a position-velocity space, and evolves by the following transport equation:

$$\frac{\partial f}{\partial t} + \nabla_{\mathbf{x}} \cdot (\mathbf{v}f) + \nabla_{\mathbf{v}} \cdot (\langle \mathbf{A} | \mathbf{x}, \mathbf{v}; t \rangle f) = \dot{f}_{\text{coll}}, \quad (5.1)$$

where  $\nabla_{\mathbf{x}}$  and  $\nabla_{\mathbf{v}}$  denote the gradient operators in the position and velocity space, respectively, and  $\dot{f}_{\text{coll}}$  is the collisional term that can depend on higher order statistics. A closure model for the collisional term results in a kinetic equation. This well-known equation has been extensively studied in the context of granular flows where collisions are inelastic. Extensions to non-dilute cases that follow the Enskog approach have also been pursued. The focus in the kinetic theory of granular flow is on obtaining closed-form solutions (Ernst, 1981), or constitutive relations (Jenkins and Savage, 1983; Lun et al., 1984; Sela and Goldhirsch, 1998; Garzo et al., 2007a,b), starting from a kinetic equation. Most of these studies rely on the Chapman-Enskog expansion about a normal solution in terms of a nonuniformity parameter that is essentially the Knudsen number.

The principal difference between the kinetic theory of gases and the kinetic theory of gas-solid flow is that in the latter, the conditional particle acceleration term  $\langle \mathbf{A} | \mathbf{x}, \mathbf{v}; t \rangle$  appears inside the velocity derivative in the velocity transport term because particle drag depends on particle velocity through slip with respect to the fluid. This dependence of particle acceleration on particle velocity in Eq. 6.1 results in the correlation of  $\mathbf{A}$  and  $\mathbf{v}$  that determines the evolution of the second moment of particle velocity, and its trace, the particle granular temperature. In the transport equation for the distribution function (cf. Eq. 6.1),  $\langle \mathbf{A} | \mathbf{x}, \mathbf{v}; t \rangle$  represents the average particle acceleration conditional on position  $\mathbf{x}$  and velocity  $\mathbf{v}$ . For the spatially homogeneous case with monodisperse particles it can be interpreted as the average acceleration experienced by a particle with velocity  $\mathbf{v}$ . The averaging operator  $\langle \cdot \rangle$  represents

integration over all higher-order multiparticle distribution functions (Koch, 1990; Subramaniam, 2000) that can be defined on the basis of the ensemble of particles with position and velocity  $\{\mathbf{X}^{(n)}(t), \mathbf{V}^{(n)}(t), n = 1, \dots, N\}$ . In particular, the conditional acceleration  $\langle \mathbf{A} | \mathbf{x}, \mathbf{v}; t \rangle$  is obtained by integrating out its dependence on the two-particle density (pair correlation function). In other words, the conditional acceleration  $\langle \mathbf{A} | \mathbf{x}, \mathbf{v}; t \rangle$  is not completely determined by the particle velocity, but may be affected by the presence of neighbor particles. The statistical description of multiparticle interactions is not contained in the one-particle distribution function.

Subramaniam (2001) notes that when the gas phase is represented by Reynolds-averaged fields, a class of models for the unclosed conditional acceleration term  $\mathbf{A}^*$  can be written as:

$$\langle \mathbf{A} | \mathbf{x}, \mathbf{v}; t \rangle = \mathbf{A}^*(\{\langle Q_g(\mathbf{x}, t) \rangle\}, q(f(\mathbf{x}, \mathbf{v}, t)), \mathbf{x}, \mathbf{v}, \dots; t), \quad (5.2)$$

where  $\{\langle Q_g(\mathbf{x}, t) \rangle\}$  represents a set of averaged fields from the gas-phase solution (such as the mean gas velocity and turbulent kinetic energy), and  $q(f)$  is any simply computed function of the distribution function. The ellipsis denotes the dependence on statistical quantities that are not represented in the distribution function, e.g., dependence on higher order multiparticle statistics, or fluid phase statistics not represented in  $\{\langle Q_g(\mathbf{x}, t) \rangle\}$ . Recall that the physical origins of the source term in the granular temperature equation lie in the hydrodynamic interactions with neighbor particles and fluid-phase velocity fluctuations. The statistics of neighbor particles are not contained in  $f(\mathbf{x}, \mathbf{v}, t)$ . If the implementation of the multifluid theory accounts for fluid-phase velocity fluctuations, then this dependence can be incorporated in the acceleration model of Eq. 5.2. However, many implementations of the multifluid theory do not account for fluid-phase velocity fluctuations.

As noted earlier, closure of the transport equation for the distribution function (cf. Eq. 6.1) implies closure for all moment equations. In the following, the implied closure for the mean and second moment of particle velocity is examined.

## 5.2.2 Moment equations

The averaged equations for mean momentum conservation and transport of the second moment of particle velocity implied by Eq. 6.1 are derived using the usual procedure to derive hydrodynamic equations in kinetic theory, except for the fact that the velocity dependence in the conditional acceleration results in an additional term in the second moment equation (Koch, 1990; Pai and Subramaniam, 2009). Here these equations are discussed in the context of modeling the conditional acceleration  $\langle \mathbf{A} | \mathbf{x}, \mathbf{v}; t \rangle$  to capture the coupling between particle velocity fluctuations and hydrodynamic force. Since the DNS results we present in this study are for fixed particles or for those undergoing elastic collisions, the moment equations are presented for the case of elastic collisions only.

*Mean particle velocity* The mean momentum conservation equation written in index notation is

$$\frac{\partial}{\partial t} (\rho_p \phi \langle v_j \rangle) + \frac{\partial}{\partial x_k} (\rho_p \phi \langle v_j \rangle \langle v_k \rangle) = \rho_p \phi \langle A_j \rangle - \frac{\partial}{\partial x_k} (\rho_p \phi \langle v_j'' v_k'' \rangle), \quad (5.3)$$

where  $\rho_p$  is the particle density,  $\phi$  is the solid volume fraction given by  $\phi = n\pi d_p^3/6$ , where  $n$  is the number density of the particles and  $d_p$  is the particle diameter. For gas-solid flow, the mean particle acceleration  $\langle \mathbf{A} \rangle$  due to the fluid-particle drag force is an unclosed term in Eq. 5.3. In EE multifluid theory, the mean particle acceleration  $\langle \mathbf{A} \rangle$  is modeled using a drag law as

$$\langle \mathbf{A} \rangle = -\beta \langle \mathbf{W} \rangle, \quad (5.4)$$

where  $\langle \mathbf{W} \rangle = \langle \mathbf{v} \rangle - \langle \mathbf{u}^{(f)} \rangle$  is the mean slip velocity between the solid and fluid phases. In this definition,  $\langle \mathbf{u}^{(f)} \rangle$  and  $\langle \mathbf{v} \rangle$  are the fluid and solid phase-averaged velocities, respectively. For an isolated particle in Stokes flow,  $\beta$  is a constant equal to  $3\pi\mu_f d_p$ , where  $\mu_f$  is the dynamic viscosity of the fluid. The Reynolds number based on the mean slip velocity between the fluid and particulate phase quantifies the relative importance of fluid inertia, and is defined as

$$\text{Re}_m = (1 - \phi) \frac{\rho_f |\langle \mathbf{v} \rangle - \langle \mathbf{u}^{(f)} \rangle| d_p}{\mu_f}, \quad (5.5)$$

where  $\rho_f$  is the density of the fluid. When the Reynolds number based on the mean slip  $\text{Re}_m$  is moderate ( $\text{Re}_m > 1$ ),  $\beta$  is a function of the mean slip velocity between the particle and the

fluid phase, i.e.  $\beta = \beta(|\langle \mathbf{W} \rangle|)$ , and the drag is no longer linearly dependent on the mean slip velocity.

Typical drag laws for gas-solid flow (Wen and Yu, 1966; Syamlal and O'Brien, 1987; Gidaspow, 1994) characterize the dependence of fluid-particle drag force on the mean slip Reynolds number and solid volume fraction  $\phi$ . These are obtained by a combination of fitting experimental data and using semi-analytical approaches in limiting cases. More recently, direct numerical simulation of flow past homogeneous fixed particle assemblies have been used to deduce drag laws (Hill et al., 2001a; Beetstra et al., 2007; Garg et al., 2009) describing the dependence on mean slip Reynolds number and solid volume fraction.

In the mean particle velocity evolution equation, the last term on the right hand side of Eq. 5.3 is the transport of particle Reynolds stress arising from correlation of particle velocity fluctuations. Particle velocity fluctuations are defined about the mean velocity as

$$\mathbf{v}'' = \mathbf{v} - \langle \mathbf{v} \rangle, \quad (5.6)$$

and the particle granular temperature <sup>1</sup> that characterizes the strength of these fluctuations is

$$T = \frac{1}{3} \langle \mathbf{v}'' \cdot \mathbf{v}'' \rangle. \quad (5.7)$$

This term is calculated by solving a transport equation for the particle velocity covariance.

*Transport of particle velocity covariance* The evolution equation for the second moment of velocity written in index notation is (Koch, 1990; Koch and Sangani, 1999; Pai and Subramaniam, 2009)

$$\begin{aligned} \frac{\partial}{\partial t} (\rho_p \phi \langle v_i'' v_j'' \rangle) + \frac{\partial}{\partial x_k} (\rho_p \phi \langle v_i'' v_j'' \rangle \langle v_k \rangle) = \\ - \frac{\partial}{\partial x_k} (\rho_p \phi \langle v_i'' v_j'' v_k'' \rangle) - \rho_p \phi \left( \langle v_i'' v_k'' \rangle \frac{\partial \langle v_j \rangle}{\partial x_k} + \langle v_j'' v_k'' \rangle \frac{\partial \langle v_i \rangle}{\partial x_k} \right) \\ + \rho_p \phi (\langle A_i'' v_j'' \rangle + \langle A_j'' v_i'' \rangle). \end{aligned} \quad (5.8)$$

<sup>1</sup>Note that we do not distinguish between particle velocity fluctuations arising from collisions and other sources, as suggested by Breault et al. (2008). Our definition is consistent with the standard definition in kinetic theory of granular and gas-solid flow, and it is also the definition adopted in the two-fluid theory.

For statistically homogeneous gas-solid flow with no mean velocity gradients the transport, production, and triple-velocity correlation terms drop out and Eq. 5.8 reduces to

$$\frac{\partial}{\partial t} (\rho_p \phi \langle v_i'' v_j'' \rangle) = \rho_p \phi (\langle A_i'' v_j'' \rangle + \langle A_j'' v_i'' \rangle), \quad (5.9)$$

showing that the particle velocity covariance evolves according to the particle acceleration-velocity covariance (fluctuations in the acceleration are defined about the mean acceleration, i.e.  $A_j'' = A_j - \langle A_j \rangle$ .) This equation shows how fluctuations in the hydrodynamic forces affect the particle velocity covariance. Contracting the indices in Eq. 5.9 results in the evolution of particle granular temperature for a statistically homogeneous gas-solid flow:

$$\frac{dT}{dt} = \frac{2}{3} \langle A_i'' v_i'' \rangle. \quad (5.10)$$

In the above equation, the trace of the particle acceleration-velocity covariance  $\langle A_i'' v_i'' \rangle$  can be either a positive or negative quantity, and hence it can act as a source or a sink of granular temperature.

### 5.2.2.1 Mean and fluctuating particle acceleration

From this discussion of moment equations we see that the mean acceleration affects mean momentum, and fluctuations in acceleration correlate with fluctuating velocity to act as a source or sink term in the granular temperature equation. In the following, we relate the mean acceleration and acceleration fluctuations to the one-particle distribution function.

The mean acceleration  $\langle \mathbf{A} \rangle$  is obtained as the integral of the conditional expectation of particle acceleration over velocity space:

$$\langle \mathbf{A} \rangle(\mathbf{x}, t) = \frac{1}{n(\mathbf{x}, t)} \int_{[\mathbf{v}]} \langle \mathbf{A} | \mathbf{x}, \mathbf{v}; t \rangle f(\mathbf{x}, \mathbf{v}, t) d\mathbf{v}, \quad (5.11)$$

and this leads to the expression  $\langle \mathbf{F}^{fp} \rangle = \rho_p \phi \langle \mathbf{A} \rangle$  for the fluid-particle drag (per unit volume) in the mean particle momentum equation. The expression for the mean acceleration is useful because it tells us how the velocity dependence in the conditional acceleration can affect the mean drag through the distribution function. The one-particle distribution function can be decomposed (Subramaniam, 2001) into the product of a number density  $n(\mathbf{x}, t)$  and a velocity

probability density function  $f_{\mathbf{V}}^c(\mathbf{v}; \mathbf{x}, t)$ :

$$f(\mathbf{x}, \mathbf{v}, t) = n(\mathbf{x}, t) f_{\mathbf{V}}^c(\mathbf{v}; \mathbf{x}, t). \quad (5.12)$$

Therefore, changes in the distribution and level of particle velocity fluctuations are characterized by the particle velocity probability density function  $f_{\mathbf{V}}^c(\mathbf{v}; \mathbf{x}, t)$ , and these affect the mean drag through Eq. 5.11.

In the kinetic theory description of gas–solid flow using the one–particle distribution function, the fluctuating acceleration is simply the difference between the conditional and unconditional mean:  $A_j'' = \langle A_i | \mathbf{v} \rangle - \langle A_i \rangle$ . Using this definition, the particle acceleration–velocity covariance can be written in terms of the one-particle distribution function as

$$\langle A_i'' v_j'' \rangle = \frac{1}{n} \int_{[\mathbf{v}]} \{ \langle A_i | \mathbf{v} \rangle - \langle A_i \rangle \} v_j'' f(\mathbf{v}, t) d\mathbf{v}. \quad (5.13)$$

As noted earlier, fluctuations in particle acceleration can arise from particle velocity fluctuations, hydrodynamic interactions with neighbor particles, and fluid–phase velocity fluctuations. While Eq. 5.13 explicitly accounts for the effect of particle velocity fluctuations, the other effects must be incorporated in the model for the conditional particle acceleration.

### 5.2.2.2 Modeling the conditional particle acceleration

A straightforward extension of the mean particle acceleration model given by Eq. 5.4 to its conditional counterpart is

$$\mathbf{A}^* = -\beta \mathbf{W} = -\beta \left( \mathbf{v} - \langle \mathbf{u}^{(f)} \rangle \right), \quad (5.14)$$

where  $\mathbf{A}^*$  represents a model (cf. Eq. 5.2) for the conditional particle acceleration  $\langle \mathbf{A} | \mathbf{v} \rangle$ , and  $\mathbf{W}$  is the instantaneous slip velocity. Here we have written the instantaneous slip velocity as the difference between the instantaneous particle velocity and the mean fluid velocity, rather than as the difference between the instantaneous velocities in each phase, i.e.  $\mathbf{W} = \mathbf{v} - \mathbf{u}$ . This is because in CFD models based on the multifluid theory there is no representation of the instantaneous gas phase velocity and the gas–phase motions are represented only by the mean gas velocity. Although this simple model results in the same mean drag as in Eq. 5.4, its implied closure for the acceleration–velocity covariance in the granular temperature equation results in

only a sink of granular temperature. This is because the simple extension in Eq. 5.14 does not represent the effects of neighboring particles or fluctuations in the fluid velocity relative to its mean.

For Stokes flow, Koch (1990) derived an analytical closure for the source term in the granular temperature equation (cf. Eq. 5.10) using a kinetic equation applicable to a dilute monodisperse gas–solid suspension with high particle inertia. He defined the instantaneous slip velocity as  $\mathbf{W} = \mathbf{v} - \mathbf{u}^{(i)}$ , where  $\mathbf{u}^{(i)}$  is the fluid velocity excluding the direct effect of the  $i$ th particle (but including the disturbance effects of all the other particles). This definition of the slip velocity gives rise to a source term in the granular temperature equation. Linearity of the governing equations in the Stokes flow limit and the assumption of a dilute suspension allowed the derivation of an explicit expression for  $\mathbf{u}^{(i)}$  and the source term. For moderately dense suspensions, the assumptions made by Koch (1990) in the kinetic theory approach are not valid and hence Koch and Sangani (1999) used a semi-analytical approach that used multipole expansion simulations to derive an expression for the source of granular temperature in the Stokes flow limit.

In section 5.2.3, we review the closures for the source term given by Koch (1990) and Koch and Sangani (1999) in the Stokes flow limit. Developing similar closures for  $\langle \mathbf{A} | \mathbf{x}, \mathbf{v}; t \rangle$  and the source term at moderate Reynolds numbers is difficult because the governing Navier–Stokes equations are nonlinear. In section 5.3, we present a direct numerical simulation methodology based on PReIBM as a promising approach to develop closures for the source and sink terms in the granular temperature equation at moderate Reynolds numbers.

### 5.2.3 Closure for high Stokes number particles undergoing elastic collisions in Stokes flow

In a high Stokes number suspension the particle velocities are not significantly affected by hydrodynamic forces. For a dilute suspension of very massive particles (high Stokes number) undergoing perfectly elastic collisions in Stokes flow, Koch (1990) showed that the steady state

particle velocity distribution in the kinetic theory description is Maxwellian<sup>2</sup>. Therefore, in this limit the particle velocity covariance tensor is isotropic and its evolution can be simply described by the granular temperature evolution equation.

### 5.2.3.1 Dilute suspensions of perfectly elastic particles

For a dilute homogeneous suspension of highly massive and perfectly elastic monodisperse particles in Stokes flow, the evolution equation of the granular temperature derived by Koch (1990) is

$$\frac{dT}{dt} = -\frac{2R}{\tau}T + \frac{2S_I}{3}. \quad (5.15)$$

The first term on the right hand side of Eq. 5.15 is the sink of particle granular temperature due to viscous dissipation. In this term,  $R = 1 + 3\phi^{1/2}/\sqrt{2}$  is the dimensionless particle momentum relaxation rate and  $\tau = m/(6\pi\mu_f a)$  is the characteristic time scale over which the velocity of a particle of mass  $m$  and radius  $a$  relaxes due to viscous forces. The second term on the right hand side of Eq. 5.15 is the source due to hydrodynamic interactions. In the dilute limit, the expression for this source term is

$$S_I = \left( a |\langle \mathbf{W} \rangle|^2 \right) / \left( 2\pi^{1/2} \tau^2 T^{1/2} \right). \quad (5.16)$$

The source term in the dilute limit is denoted  $S_I$  to distinguish it from the source term  $S_{II}$  at higher volume fractions that is discussed in the following subsection.

### 5.2.3.2 Moderately dense to dense suspensions of perfectly elastic particles

Koch and Sangani (1999) used the multipole expansion method to evaluate the source term due to hydrodynamic forces for dense homogeneous suspensions of massive elastic particles in Stokes flow. In their simulation the particles move as a granular gas and their motion is not affected by the interstitial fluid. The evolution equation for the granular temperature is written as

$$\frac{dT}{dt} = -\frac{2R_{\text{diss}}(\phi)}{\tau}T + \frac{2S_{II}}{3}. \quad (5.17)$$

<sup>2</sup>Later Koch and Sangani (1999) used an approximate multipole method to show that even for dense suspensions of elastic particles in Stokes flow, the velocity distribution is Maxwellian.

For the sink term due to viscous dissipation (first term on the right hand side of Eq. 5.17), the expression for the dimensionless dissipation rate  $R_{\text{diss}}(\phi)$  as a function of volume fraction given by Sangani et al. (1996) is used. The source term in granular temperature (second term on the right hand side of Eq. 5.17) is expressed as an integral of the temporal autocorrelation of the force experienced by the particles. The final expression for the source term given by Koch and Sangani (1999) is

$$S_{II} = \frac{a}{\tau^2} \frac{|\langle \mathbf{W} \rangle|^2}{T^{1/2}} S^*(\phi) \quad (5.18)$$

where  $S^*(\phi)$  is the dimensionless source term. Expressions for the dimensionless dissipation rate and the dimensionless source as a function of the volume fraction can be found in Koch and Sangani (1999).

### 5.3 Direct numerical simulation approach

Here we describe a DNS approach based on the Particle-resolved Uncontaminated-fluid Reconcilable Immersed Boundary Method (PUREIBM) that is used to solve for flow past arbitrary arrangements of solid spherical particles. Two types of simulation results are presented: (i) for fixed particle assemblies, and (ii) for freely moving suspensions. The hydrodynamic solver that is common to both types of simulations is first described. Then the solution approach for fixed particle assemblies is outlined. This is followed by a description of the simulations of freely evolving suspensions where the positions and velocities of the particles evolve under the action of hydrodynamic and collisional forces.

#### 5.3.1 Hydrodynamic solver

PUREIBM is a particle-resolved direct numerical simulation approach for gas-solid flow where the continuum Navier-Stokes equations with no-slip and no-penetration boundary conditions on each particle's surface are solved using a forcing term that is added to the momentum equation. The salient features that distinguish PUREIBM from other immersed boundary method approaches are as follows:

1. Uncontaminated fluid: In PReIBM the immersed boundary (IB) forcing is solely restricted to those grid points that lie in the solid phase, and therefore the flow solution in the fluid phase is uncontaminated by the IB forcing. Consequently the velocity and pressure in the fluid phase is a solution to the unmodified Navier-Stokes equations (in contrast to IB implementations that smear the IB forcing on to grid points in the fluid phase adjoining solid boundaries, resulting in solution fields that do not correspond to unmodified Navier–Stokes equations).
2. Reconcilable: In PReIBM the hydrodynamic force experienced by a particle is computed directly from the stress tensor at the particle surface that is obtained from this uncontaminated fluid flow solution (in contrast to IB implementations that calculate the hydrodynamic force from the IB forcing field). This feature of PReIBM enables us to directly compare the DNS solution with any random-field theory of multiphase flow. In particular, for statistically homogeneous suspensions it is shown in Garg et al. (2009) that if the volume-averaged hydrodynamic force exerted on the particles by the fluid is computed from a PReIBM simulation, it is a consistent numerical calculation of the average interphase momentum transfer term  $\langle \tau'_{ji} n_j^{(s)} \delta(\mathbf{x} - \mathbf{x}^{(I)}) \rangle$  in the two-fluid theory (Drew, 1983). This reconciles DNS results with multiphase flow theory.

Owing to these specific advantages, it is shown elsewhere (Garg et al., 2009; Garg, 2009) that PReIBM is a numerically convergent and accurate particle-resolved DNS method for gas-solids flow. Its performance has been validated in a comprehensive suite of tests: (i) Stokes flow past simple cubic (SC) and face centered cubic (FCC) arrangements (ranging from dilute to close-packed limit) with the boundary–integral method of Zick and Homsy (1982), (ii) Stokes flow past random arrays of monodisperse spheres with LBM simulations of van der Hoef et al. (2005) (iii) moderate to high Reynolds numbers ( $Re_m \leq 300$ ) in SC and FCC arrangements with LBM simulations of Hill et al. (2001b) and (iv) high Reynolds number flow past random arrays of monodisperse spheres with ANSYS–FLUENT CFD package. It has also been extended to study passive scalar transport, and validated for heat transfer from a single isolated sphere (Garg, 2009; Garg et al., 2010b).

The numerical scheme used in PReIBM is a primitive-variable, pseudo-spectral method, using a Crank-Nicolson scheme for the viscous terms, and an Adams-Bashforth scheme for the convective terms. A fractional time-stepping method that is based on Kim and Moin's approach (Kim and Moin, 1985) is used to advance the velocity fields in time. The principal advantage of the PReIBM approach is that it enables the use of regular Cartesian grids to solve for flow past arbitrarily shaped moving bodies without the need for costly remeshing. It also considerably simplifies parallelization of the flow solver as compared to unstructured body-fitted grids.

### 5.3.2 Fixed particle assemblies

The particle configuration for DNS of flow past fixed assemblies is generated by first allowing particles to attain a random spatial arrangement through elastic collisions. A homogeneous configuration of non-overlapping spheres corresponding to the specified solid volume fraction is generated with particle centers on a lattice, and particles are assigned a Maxwellian velocity distribution. Particles are allowed to equilibrate under purely elastic collisions (in the absence of any interstitial fluid) to generate a homogeneous particle configuration for the DNS flow solver. Ensemble-averaged flow statistics are obtained by averaging over multiple independent simulations (MIS) performed with several such configurations. Each statistically identical configuration corresponds to the same average solid volume fraction and pair-correlation (macrostate), but differs in the specific arrangement of particles (microstates). The PReIBM simulation methodology and details of the computation of the mean acceleration (or mean drag) for a fixed particle assembly are described in Garg et al. (2009).

### 5.3.3 Freely evolving suspensions

Numerical simulations (Yin and Koch, 2007) of freely evolving suspensions have been performed to study the sedimentation of monodisperse particles under gravity in the presence of a fluid. Simulations of freely sedimenting suspensions are carried out in periodic domains such that the imposed pressure gradient in the fluid balances the weight of the particles. In sedimentation calculations the steady mean flow Reynolds number attains a unique value that

depends on the problem parameters (fluid and particle densities, solid volume fraction and the value of acceleration due to gravity), and this value is not known *a priori*. In the present study we seek to simulate freely evolving particle suspensions at arbitrary mean slip Reynolds numbers while maintaining the solid/fluid density ratio and solid volume fraction at fixed values. We also want to specify the mean flow Reynolds number as input to the simulation. This can be accomplished by specifying a mean pressure gradient that does not exactly balance the weight of the particles, but exerts the requisite body force to maintain the desired slip velocity between the particles and fluid. However, now both the mean particle velocity and the mean fluid velocity change in time because there is no steady solution in the laboratory frame to the mean momentum balance in each phase. Note that even though the mean phasic velocities are evolving in time, their difference—the mean slip velocity—attains a steady value.

The difficulty in simulating this flow setup in the laboratory frame with periodic boundary conditions is that the continuous increase in fluid and particle velocities places unnecessary restrictions on the time step through the Courant condition. To circumvent this problem we developed a different simulation setup that performs the DNS in an accelerating reference frame such that the particles have a zero mean velocity with respect to the computational grid. The equations of motion are solved in an accelerating frame of reference that moves with the mean velocity of the particles. In this frame, the particles execute only fluctuating motion. In our setup, particles *on average* do not flow in or out of the computational domain, thereby maintaining a reasonable time step that is based on the mean slip velocity. Particles do flow in and out of the domain because of their fluctuating velocity. The advantage of our setup is that the desired mean flow Reynolds number is specified as an input parameter, and we are able to solve the problem with reasonable time steps that resolve the flow. Details of the equations solved in the accelerating reference frame are given in Appendix C.

In the freely evolving DNS, each particle moves with an acceleration that arises from hydrodynamic and collisional forces. The particles are represented in a Lagrangian frame of reference at time  $t$  by  $\{\mathbf{X}^{(i)}(t), \mathbf{V}^{(i)}(t) \mid i = 1, \dots, N_p\}$ , where  $\mathbf{X}^{(i)}(t)$  denotes the  $i^{\text{th}}$  particle's position and  $\mathbf{V}^{(i)}(t)$  denotes its translational velocity. The position and translational velocity of the  $i^{\text{th}}$

particle evolve according to Newton's laws as:

$$\frac{d\mathbf{X}^{(i)}(t)}{dt} = \mathbf{V}^{(i)}(t), \quad (5.19)$$

$$m \frac{d\mathbf{V}^{(i)}(t)}{dt} = \mathbf{B} + \mathbf{F}_d^{(i)}(t) + \sum_{\substack{j=1 \\ j \neq i}}^{N_p} \mathbf{F}_{ij}^c(t), \quad (5.20)$$

where  $\mathbf{B}$  is any external body force (zero in the simulations shown here),  $\mathbf{F}_d^{(i)}$  is the hydrodynamic force (from pressure and viscous stress that is calculated from the velocity and pressure fields at the particle surface) and  $\mathbf{F}_{ij}^c$  is the contact force on the  $i^{\text{th}}$  particle as a result of collision with  $j^{\text{th}}$  particle. Particle–particle interactions are treated using soft–sphere collisions based on a spring–dashpot contact mechanics model that was originally proposed by Cundall and Strack (1979). The advantage of using soft–sphere collisions is that the simulations can be extended to higher volume fractions because enduring multi–particle contacts are taken into account. In the soft–sphere approach, the contact mechanics between two overlapping particles is modeled by a system of springs and dashpots in both normal and tangential directions. The spring causes colliding particles to rebound, and the dashpot mimics the dissipation of kinetic energy due to inelastic collisions. The spring stiffness coefficients in the tangential and normal directions are  $k_t$  and  $k_n$ , respectively. Similarly, the dashpot damping coefficients in the tangential and normal directions are  $\eta_t$  and  $\eta_n$ , respectively. The spring stiffness and dashpot damping coefficients are related to the coefficient of restitution and the coefficient of friction (see Garg et al. (2010a) for details of the implementation).

The particles considered in this study are assumed to be perfectly elastic and frictionless. Since the particles are perfectly elastic, the damping force arising from the dashpot is zero. The tangential component of the contact force is zero for frictionless particles. Therefore, only the normal component of the spring force  $\mathbf{F}_{nij}^S$  contributes to the contact force  $\mathbf{F}_{ij}^c$  at time  $t$ :

$$\mathbf{F}_{ij}^c(t) = \mathbf{F}_{nij}^S(t). \quad (5.21)$$

At the initiation of contact, the normal spring force  $\mathbf{F}_{nij}^S$  is equal to  $-k_n \delta_{ij}$ , where  $\delta_{ij}$  is the overlap between the particles computed using the relation

$$\delta_{ij} = d_p - \left| \mathbf{X}^{(i)} - \mathbf{X}^{(j)} \right|. \quad (5.22)$$

A time history of the spring forces is maintained once the contact initiates. At any time during the contact, the normal spring force is given by

$$\mathbf{F}_{nij}^S(t + \Delta t) = \mathbf{F}_{nij}^S(t) - k_n \mathbf{V}_{nij} \Delta t, \quad (5.23)$$

where  $\mathbf{V}_{nij}$  is the relative velocity in the normal direction (defined below) that is computed using

$$\mathbf{V}_{nij} = \left[ \left( \mathbf{V}^{(i)} - \mathbf{V}^{(j)} \right) \cdot \hat{\mathbf{r}}_{ij} \right] \hat{\mathbf{r}}_{ij}. \quad (5.24)$$

The normal vector  $\hat{\mathbf{r}}_{ij}$  is the unit vector along the line of contact pointing from particle  $i$  to particle  $j$ . The governing equations of motion that are solved in the fluid, and the details of the computation of the hydrodynamic force acting on the particles are discussed in Appendix C.

A homogeneous particle configuration is generated in the same way as for the fixed particle assemblies by equilibrating an ensemble of particles undergoing elastic collisions in the absence of interstitial fluid. Following the simulation methodology of Garg et al. (2009), a steady flow at the desired mean flow Reynolds number is first established for this fixed particle assembly. Once the mean fluid–particle drag experienced by this fixed particle assembly reaches a steady state, the particles are released at time  $t = 0$  for the freely evolving DNS simulation.

The particles are advanced on a time step  $\Delta t_{\text{coll}}$  that is determined by the spring stiffness and the dashpot coefficients. The flow fields are updated on a time step  $\Delta t_{\text{fluid}}$ , which ensures that both the convective and viscous time scales are well resolved. At the start of a flow time step the forces acting on the particles are computed based on the flow fields obtained at the end of the previous flow time step. If  $\Delta t_{\text{coll}}$  is smaller than  $\Delta t_{\text{fluid}}$  the particles are stepped by  $\Delta t_{\text{coll}}$  until the end of the flow time step, otherwise both the particles and the fluid are stepped by  $\Delta t_{\text{coll}}$ . The simulation is continued until the granular temperature reaches a steady state.

## 5.4 Results

We first present results from a validation test for fixed particle assemblies. We then quantify particle acceleration and its coupling to fluctuations in the particle velocity in flow past fixed particle assemblies as well as freely moving suspensions.

### 5.4.1 Fixed particle assemblies

Simulations with fixed particle positions and velocities are representative of physical fluid-particle systems in which the particle velocities do not change significantly over characteristic fluid time scales (the relevant scale here being the time to transit a characteristic length scale such as the particle diameter at the mean slip velocity). This is true for high Stokes number (gas-solid) suspensions. Simulations of flow past fixed particle assemblies are less computationally demanding than freely evolving suspensions, and are useful for parametric studies (variation of mean flow Reynolds number and mean solid volume fraction). This approach has been extensively used to deduce computational drag laws for homogeneous gas-solid (high Stokes number) suspensions by many researchers (Hill et al., 2001a,b; van der Hoef et al., 2005; Beetstra et al., 2007; Yin and Sundaresan, 2009b). Here we use this test to compare PReIBM DNS results with existing LBM-based drag correlations.

The mean drag obtained from PReIBM DNS is compared with the LBM-based drag correlation of Hill et al. (2001b) in Figure 5.1. The normalized mean fluid-particle force  $F$  is

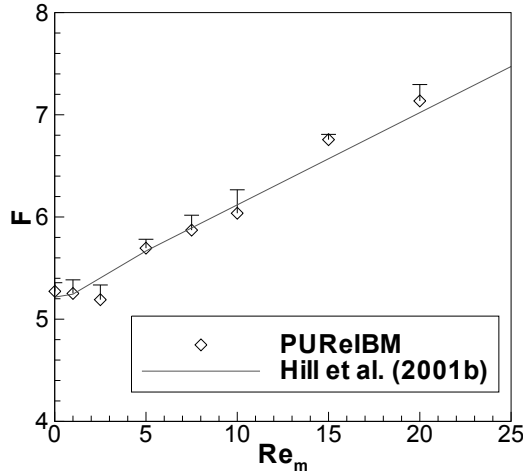


Figure 5.1 Figure shows the comparison of the mean drag obtained from PReIBM simulations with the drag correlation reported by Hill et al. (2001b) at a solid volume fraction of 0.2 for the baseline case of zero particle velocity fluctuations.

defined as

$$F = \frac{|\langle \mathbf{f} \rangle|}{3\pi\mu_f d_p |\langle \mathbf{W} \rangle|} \quad (5.25)$$

where  $\langle \mathbf{f} \rangle$  is the average fluid–particle force per particle. The PReIBM DNS results show an excellent match with the drag correlation of Hill et al. (2001b).

The validation test shown here is performed with all the particles at rest, so the fluctuations in particle velocity are zero. If a random velocity is assigned to each particle in the fixed bed according to a Maxwellian distribution corresponding to a specified value of the particle granular temperature, then the fixed bed simulation can be considered an instantaneous snapshot of a freely evolving suspension. Of course in a freely evolving suspension the dynamic response of the particles to the hydrodynamic forces will affect the particle velocity fluctuations, and this is not captured by the fixed bed simulation. Nevertheless, this still allows us to consider the effect of particle velocity fluctuations on the hydrodynamic forces, albeit in a limited sense.

The magnitude of particle velocity fluctuations is characterized by defining a Reynolds number based on the granular temperature  $Re_T$  as:

$$Re_T = \frac{\rho_f d_p T^{1/2}}{\mu_f}. \quad (5.26)$$

In Fig. 5.2 we plot the streamwise component of fluctuating acceleration  $A'_x$  for each particle versus its fluctuation in the streamwise velocity component  $v'_x$  for  $Re_m = 20$  and  $Re_T = 16$  at a solid volume fraction of 0.2. The first observation is that  $A'_x$  and  $v'_x$  are negatively correlated. This is to be expected because as seen from the schematic of the flow setup in Fig. 5.3, a positive fluctuation in particle velocity results in a lower slip velocity that corresponds to a lower drag value because of the relation  $\mathbf{A} \propto -\mathbf{W}$  for isolated particles. This manifests as a negative fluctuation in particle acceleration. However, the second interesting observation from the scatter plot in Fig. 5.2 is that some positive fluctuations in velocity actually result in positive fluctuations in the acceleration. In other words, the presence of neighbor particles and the resulting hydrodynamic interactions can occasionally violate the  $\mathbf{A} \propto -\mathbf{W}$  relation for isolated particles. Also the fluid velocity in the proximity of the particle can be significantly different from the mean fluid velocity, and the definition of the instantaneous slip as  $\mathbf{W} = \mathbf{v} - \langle \mathbf{u}^{(f)} \rangle$  may not accurately represent the instantaneous slip velocity. The joint statistics of particle acceleration and particle velocity represent the coupling between hydrodynamic forces and particle velocity fluctuations. In particular, the acceleration-velocity covariance is important

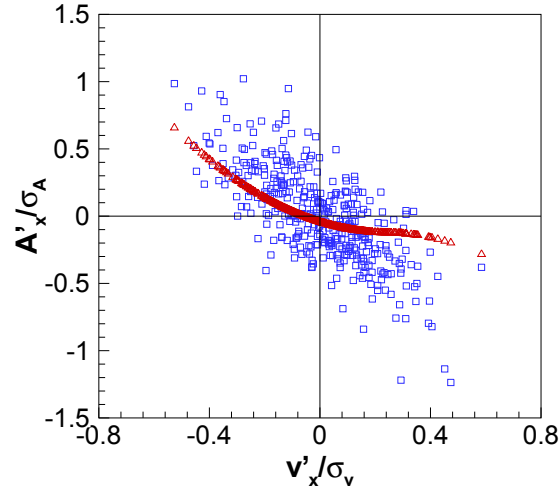


Figure 5.2 Scatter plot of streamwise component of fluctuating acceleration versus the streamwise component of fluctuating velocity. Square symbols ( $\square$ ) show fluctuations in the particle acceleration obtained from DNS using PReIBM simulations, while upper triangles ( $\triangle$ ) show fluctuations in the particle acceleration predicted by simple extension of a mean drag law to its instantaneous counterpart.

for accurate prediction of the particle granular temperature evolution.

We now investigate the predictions for joint particle acceleration-velocity statistics using a simple model (this model is used in other works such as Wylie et al. (2003) to predict the effect of particle velocity fluctuations on mean drag). The instantaneous counterpart of the acceleration model described in Eq. 5.14,

$$\mathbf{A} = -\beta\mathbf{W},$$

is used to compute the instantaneous particle acceleration for each particle velocity value in the DNS. In this model  $\beta$  is taken from the drag correlation proposed by Hill et al. (2001b). The acceleration-velocity scatter plot obtained from this model is also shown in Fig. 5.2 (upper triangles). One can see that this simple extension of the mean acceleration model does not recover the scatter obtained in the DNS, but instead it predicts a significantly different joint statistical behavior. The data points in quadrants Q1 and Q3 that are found in the scatter plot from DNS are totally absent in the model. Clearly this comparison points to the need for an

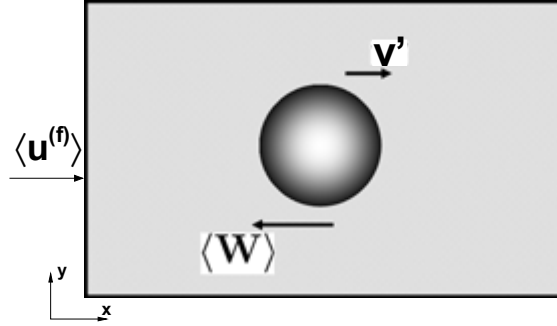


Figure 5.3 Schematic of the flow setup. The mean velocity of the fluid phase  $\langle \mathbf{u}^{(f)} \rangle$  is directed along the positive  $x$  axis as shown. The mean velocity  $\langle \mathbf{v} \rangle$  of the particles is zero and so the mean slip velocity  $\langle \mathbf{W} \rangle = \langle \mathbf{v} \rangle - \langle \mathbf{u}^{(f)} \rangle$  is along the negative  $x$  axis. The solid particle shown in this figure has a positive velocity fluctuation  $\mathbf{v}'$  along the positive  $x$  axis. The schematic illustrates that a positive fluctuation about the mean velocity of the particles implies a reduced instantaneous slip velocity,  $\mathbf{v}' - \langle \mathbf{u}^{(f)} \rangle$  between the particle and the fluid.

improved model for the conditional particle acceleration in the velocity transport term in the evolution equation for the one-particle distribution function in the kinetic theory of multiphase flow.

While useful information regarding instantaneous particle acceleration-velocity joint statistics can be extracted from fixed particle simulations, they are inadequate to characterize the temporal evolution of the particle granular temperature. For this purpose we perform DNS of freely evolving suspensions.

#### 5.4.2 Freely moving suspensions

DNS of a freely evolving suspension in periodic domain is performed for a volume fraction of  $\phi = 0.2$ . Unlike sedimentation studies where the mean slip velocity is limited by the settling velocity of the particles in suspension, here we solve the equations of motion in an accelerating frame of reference so that arbitrary mean flow Reynolds numbers  $Re_m$  can be simulated. A value of  $Re_m = 20$  is chosen for the simulations reported here, which is well outside the Stokes

regime. Three different particle to fluid density ratios ( $\rho_p/\rho_f = 10, 100$  and  $1000$ ) are used to analyze the dynamics of the system.

First we examine the mean fluid–particle drag in the freely evolving suspension for different values of the particle to fluid density ratio. The time evolution of the normalized drag  $F$  (cf. Eq. 5.25) is shown in Fig. 5.4(a). Figure 5.4(a) shows that the mean drag in the suspension

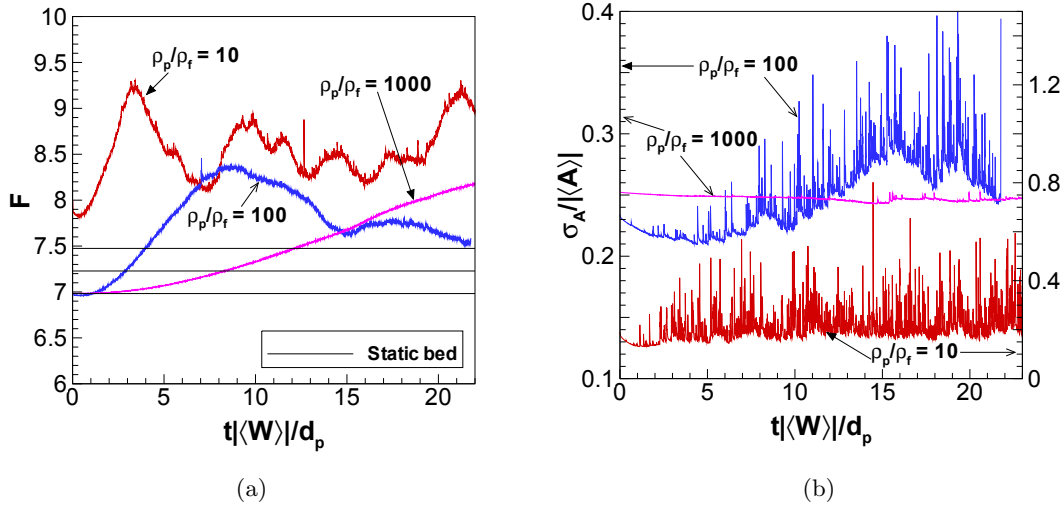


Figure 5.4 Figure 5.4(a) shows the evolution of the normalized mean drag at a volume fraction of 0.2 and a mean flow Reynolds number of 20 for three different particle to fluid density ratios:  $\rho_p/\rho_f = 10$  (red), 100 (blue), and 1000 (purple). The black solid line indicates the drag in a static bed at the same mean flow Reynolds number and volume fraction. The dashed lines represent 95% confidence limits on the mean drag for the static bed. Figure 5.4(b) shows the evolution of the standard deviation of fluctuations in the particle acceleration relative to the mean drag at a volume fraction of 0.2 and a mean flow Reynolds number of 20 for different density ratios. In this plot, data for  $\rho_p/\rho_f = 10$  are shown on the right hand side  $y$ -axis. The standard deviation in the acceleration obtained for a fixed bed is 0.22

for a particle to fluid density ratio of 1000 varies slowly in time when compared to the other two cases. This is because the particle configuration changes very slowly due to high inertia of the particles. Thus, when compared to the other two density ratios, the behavior of this system is expected to be much closer to that of a fixed bed. However, even the case with density ratio of 1000 is not identical to a fixed bed with zero particle velocity fluctuations because of the changing particle configuration, nonzero particle velocity fluctuations and the effect of added mass in the hydrodynamic force. Nevertheless, it is clear that as the density ratio increases the

mean drag experienced by the particles in a freely evolving suspension is better approximated by the corresponding fixed bed simulation.

The fluctuations in the particle acceleration play a very important role in the dynamics of the suspension as discussed earlier. In Figure 5.4(b), the level of acceleration fluctuations  $\sigma_A$  relative to the mean acceleration is plotted with time for the three density ratios. It can be seen that the particle acceleration fluctuations are almost constant for the suspension with the highest density ratio of 1000. The steady value of  $\sigma_A/|\langle \mathbf{A} \rangle|$  for the case with highest density ratio is very close to that obtained from a fixed assembly of particles at the same volume fraction of 0.2 and mean flow Reynolds number of 20.

The plot of acceleration fluctuations in Fig. 5.4(b) has several significant implications. First of all, it tells us that the steady state value of  $\sigma_A/|\langle \mathbf{A} \rangle|$  in freely evolving suspensions is not negligible. Therefore, fluctuating hydrodynamic forces (relative to the mean drag) are important not just in the Stokes regime, but at moderate Reynolds numbers also. Secondly, it informs us that the level of acceleration fluctuations in freely evolving suspensions is not very different from that in fixed particle assemblies. This partially justifies the calculation of joint acceleration-velocity statistics from fixed particle assemblies and their comparison with a simple model that was presented earlier. The third inference we draw from Fig. 5.4(b) is that the instantaneous particle acceleration model must represent the increasing level of temporal variations in fluctuating hydrodynamic force that accompany a decrease in particle to fluid density ratio.

We now quantify the effect of the fluctuations in the hydrodynamic force on particle velocity fluctuations in freely evolving suspensions. The evolution of granular temperature for the three different particle to fluid density ratio values that are considered is shown in Figure 5.5. Details of the estimation of granular temperature from DNS of freely evolving suspensions are given in Appendix C.

As expected, the lower density ratio cases attain a higher steady granular temperature, and the rate at which the steady value is reached is inversely proportional to the particle to fluid density ratio. The value of the scaled granular temperature is relatively low when compared with the turbulence intensity in single-phase turbulence. It indicates a high Mach number

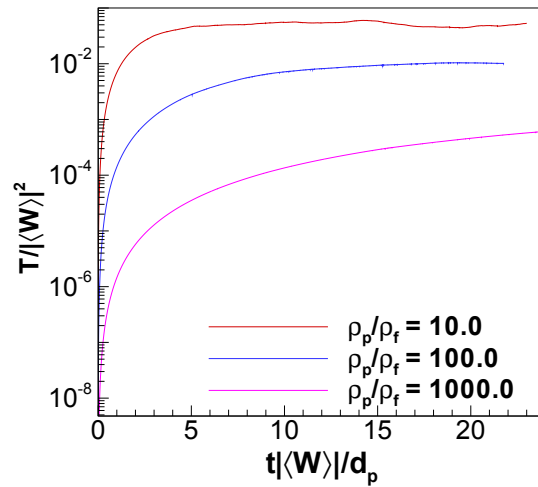


Figure 5.5 Evolution of the particle granular temperature at a volume fraction of 0.2 and a mean flow Reynolds number of 20 for different density ratios.

in the particle phase (on the order of 100 for a scaled granular temperature of  $10^{-4}$ ). This indicates that the particles in the gas-solid suspension are not dominated by collisions like molecular gases at STP, but rather they are closer to a super-cooled state. For comparison, the values of granular temperature in Stokes flow as estimated by the theory of Koch and Sangani (1999) are 2 to 3 orders of magnitude smaller than the DNS results shown here for a mean flow Reynolds number of 20.

## 5.5 Conclusions

The coupling between hydrodynamic forces and particle velocity fluctuations in gas-solid suspensions at moderate Reynolds number is studied using direct numerical simulation of freely evolving suspensions that imposes no-slip and no-penetration boundary conditions on the surface of each particle. The DNS results show that fluctuations in particle acceleration are significant at moderate Reynolds numbers. The standard deviation in acceleration relative to the mean acceleration ranges from 0.2 to 0.4 depending on the particle to fluid density ratio. This extends current understanding of this coupling that has been extensively studied by

Koch and co-workers in the limit of Stokes flow. Another key finding that emerges from this work is that the steady state granular temperature from DNS of freely evolving suspensions at  $Re_m = 20$  is two to three orders of magnitude larger than that predicted by the theory of Koch and Sangani (1999) for Stokes flow. A simple extension of drag laws for mean particle acceleration (based on the mean slip velocity) to model the instantaneous particle acceleration does not recover the correct acceleration–velocity covariance that is obtained from DNS. This work motivates the development of better models for instantaneous particle acceleration that are capable of accurately representing the coupling between hydrodynamic forces and particle velocity fluctuations.

### Acknowledgment

This work was supported by a Department of Energy grant DE-FC26-07NT43098 through the National Energy Technology Laboratory.

## Nomenclature

$f$	One-particle distribution function ( $s^3/m^6$ )
$\dot{f}_{\text{coll}}$	Source of the one-particle distribution function due to particle collisions ( $s^2/m^6$ )
$\mathbf{v}$	Sample space variable for velocity of the particle (m/s)
$\mathbf{x}$	Position vector (m)
$x, y, z$	Components of the position vector $\mathbf{x}$ (m)
$v_x, v_y, v_z$	Components of the velocity vector $\mathbf{v}$ (m/s)
$\nabla_{\mathbf{x}}$	Gradient operator in position space given by $\mathbf{i}\frac{\partial}{\partial x} + \mathbf{j}\frac{\partial}{\partial y} + \mathbf{k}\frac{\partial}{\partial z}$
$\nabla_{\mathbf{v}}$	Gradient operator in velocity space given by $\mathbf{i}\frac{\partial}{\partial v_x} + \mathbf{j}\frac{\partial}{\partial v_y} + \mathbf{k}\frac{\partial}{\partial v_z}$
$t$	Time (s)
$\mathbf{i}, \mathbf{j}, \mathbf{k}$	Unit vectors in the $x, y$ and $z$ directions respectively
$\langle \mathbf{A}   \mathbf{x}, \mathbf{v}; t \rangle$	Conditional expectation of particle acceleration ( $m/s^2$ )
$p(\mathbf{x}, t)$	Fluid pressure field ( $N/m^2$ )
$\langle \mathbf{A} \rangle$	Unconditional expectation of particle acceleration ( $m/s^2$ )
$\langle \mathbf{f} \rangle$	Average fluid-particle force per particle (N)
$\langle \mathbf{v} \rangle$	Average particle velocity (m/s)
$\langle \mathbf{F}^{fp} \rangle$	Mean fluid-particle drag (N)
$\langle \bar{\mathbf{g}} \rangle_{\mathbf{v}}$	Mean pressure gradient in the accelerating frame ( $N/m^3$ )

$\langle \mathbf{u}^{(f)} \rangle$	Phasic averaged fluid velocity (m/s)
$\langle \mathbf{u}^{(s)} \rangle$	Phasic averaged solid velocity (m/s)
$\langle \mathbf{W} \rangle$	Mean slip velocity between the solid and the fluid phases (m/s)
$\beta$	Interphase momentum transfer coefficient ( $s^{-1}$ )
$\bar{\mathbf{x}}$	Position vector in the accelerating frame (m)
$\mathbf{B}$	External body force (N)
$\mathbf{W}$	Instantaneous particle slip velocity (m/s)
$\mathbf{V}^{(i)}$	Velocity vector of the $i^{th}$ particle (m/s)
$\mathbf{X}^{(i)}$	Position vector of the $i^{th}$ particle (m)
$\{T\}$	Granular temperature estimated from DNS ( $m^2/s^2$ )
$\{\mathbf{u}^{(s)}\}$	Mean solids velocity estimated from DNS (m/s)
$\Delta \bar{t}$	Time step in the accelerating frame (s)
$\Delta t_{coll}$	Time step used to resolve particle–particle collisions (s)
$\Delta t_{fluid}$	Time step used to resolve flow field (s)
$\delta_{ij}$	Overlap between the particles $i$ and $j$ (m)
$\langle \bar{\mathbf{g}} \rangle^{n+1}$	Mean pressure gradient at $(n + 1)^{th}$ time step in the accelerating frame ( $N/m^3$ )
$\langle \bar{\mathbf{u}}^{(f)} \rangle^d$	Desired mean fluid velocity in the accelerating frame (m/s)
$\langle \bar{\mathbf{u}}^{(f)} \rangle^{n+1}$	Mean fluid velocity at $(n + 1)^{th}$ time step in the accelerating frame (m/s)
$\langle \bar{\mathbf{u}}^{(s)} \rangle^{n+1}$	Mean solid velocity at $(n + 1)^{th}$ time step in the accelerating frame (m/s)
$\langle \bar{\mathbf{u}}^{(f)} \rangle^n$	Mean fluid velocity at $n^{th}$ time step in the accelerating frame (m/s)
$\langle \bar{\mathbf{u}}^{(s)} \rangle^n$	Mean solid velocity at $n^{th}$ time step in the accelerating frame (m/s)

$\overline{\mathbf{F}}_D^n$	Total drag force acting on the solid particles at $n^{\text{th}}$ time step in the accelerating frame (N)
$\mathbf{A}_f^{n+1}$	Frame acceleration at $(n + 1)^{\text{th}}$ time step ( $\text{m/s}^2$ )
$\eta_n$	Dashpot damping coefficient in the normal direction used in the soft–sphere collision model (Ns/m)
$\eta_t$	Dashpot damping coefficient in the tangential direction used in the soft–sphere collision model (Ns/m)
$\mathbf{F}_{nij}^S$	Normal component of the spring force between particles $i$ and $j$ that arises in the soft–sphere collision model (N)
$\mathbf{F}_d^{(i)}$	Total drag force acting on the $i^{\text{th}}$ particle (N)
$\hat{\mathbf{r}}_{ij}$	Unit vector along the line of contact pointing from particle $i$ to particle $j$
$\mathcal{V}_s^{(n)}$	Region occupied by the $n^{\text{th}}$ particle
$\mathbf{F}_{ij}^c$	Contact force on the $i^{\text{th}}$ particle due to collision with $j^{\text{th}}$ particle (N)
$\mathcal{V}$	Region of the physical domain
$\mathcal{V}_f$	Region occupied by the fluid phase
$\mathcal{V}_s$	Region occupied by the solid phase
$Re_T$	Reynolds number based on the particle granular temperature
$\mu_f$	Dynamic viscosity of the fluid ( $\text{Ns/m}^{-2}$ )
$\nu_f$	Kinematic viscosity of the fluid ( $\text{m}^2/\text{s}$ )
$\overline{\mathbf{F}}_D$	Total drag force acting on the solid particles (N)
$\overline{\mathbf{g}}$	Pressure gradient in the accelerating frame ( $\text{N/m}^3$ )
$\overline{\mathbf{g}}'$	Fluctuating pressure gradient in the accelerating frame ( $\text{N/m}^3$ )

$\bar{\mathbf{S}}$	Convective term of the Navier–Stokes equations in the accelerating frame (m/s <sup>2</sup> )
$\bar{t}$	Time in the accelerating frame (s)
$\partial\mathcal{V}$	Boundary of the periodic box
$\partial\mathcal{V}_s$	Interface between the solid and the fluid phases
$\partial\mathcal{V}_s^{(n)}$	Surface of the $n^{\text{th}}$ particle
$\phi$	Solid volume fraction
$\text{Re}_m$	Reynolds number based on the mean slip velocity
$\rho_f$	Thermodynamic density of the fluid (kg/m <sup>3</sup> )
$\rho_p$	Thermodynamic density of the particles (kg/m <sup>3</sup> )
$\sigma_A$	Standard deviation in the particle accelerations (m/s <sup>2</sup> )
$\tau$	Viscous relaxation time scale (s)
$\mathbf{V}_{nij}$	Relative velocity between the particles $i$ and $j$ in the normal direction (m/s)
$d_p$	Particle diameter (m)
$dA$	Infinitesimal area element on the surface of the sphere (m <sup>2</sup> )
$F$	Normalized mean fluid–particle force per particle
$f_{\mathbf{V}}^c$	Velocity probability density function (s <sup>3</sup> /m <sup>3</sup> )
$k_n$	Spring stiffness coefficient in the normal direction used in the soft–sphere collision model (N/m)
$k_t$	Spring stiffness coefficient in the tangential direction used in the soft–sphere collision model (N/m)
$m$	Mass of the particle (kg)

$n$	Number density ( $1/\text{m}^3$ )
$N_p$	Number of particles in the domain
$R$	Dimensionless particle momentum relaxation rate used by Koch (1990)
$R_{\text{diss}}$	Dimensionless dissipation rate used by Sangani et al. (1996)
$S^*$	Dimensionless source of granular temperature used by Koch (1990) and Sangani et al. (1996)
$S_I$	Source of granular energy in the dilute volume fraction limit derived by Koch (1990) ( $\text{m}^2/\text{s}^3$ )
$S_{II}$	Source of granular temperature in the moderate volume fraction limit given by Sangani et al. (1996) ( $\text{m}^2/\text{s}^3$ )
$T$	Particle granular temperature ( $\text{m}^2/\text{s}^2$ )
$V$	Volume of the physical domain ( $\text{m}^3$ )
$V_f$	Volume of the region occupied by fluid ( $\text{m}^3$ )
$V_s$	Volume of the region occupied by the solid phase ( $\text{m}^3$ )
$\bar{\mathbf{u}}(\bar{\mathbf{x}}, \bar{t})$	Fluid velocity field in the accelerating frame ( $\text{m}/\text{s}$ )
$\mathbf{A}''$	Particle acceleration fluctuations ( $\text{m}/\text{s}^2$ )
$\mathbf{A}^*$	Modeled instantaneous particle acceleration ( $\text{m}/\text{s}^2$ )
$\mathbf{A}_f$	Frame acceleration ( $\text{m}/\text{s}^2$ )
$\mathbf{n}^{(n)}$	Unit normal vector pointing outward from the surface of the $n^{\text{th}}$ particle
$\mathbf{n}^{(s)}$	Unit normal vector pointing outward from the surface of the solid
$\mathbf{u}(\mathbf{x}, t)$	Fluid velocity field in the laboratory frame ( $\text{m}/\text{s}$ )

$\mathbf{u}^{(i)}$	Fluid velocity excluding the direct effect of the $i$ th particle used by Koch (1990) (m/s)
$\mathbf{v}''$	Particle velocity fluctuations (m/s)
$\mathbf{v}'^{(n)}$	Fluctuating velocity of the $n^{\text{th}}$ particle (m/s)
$\mathbf{V}_f$	Frame velocity (m/s)
$\psi'$	Fluctuating pressure (N/m <sup>2</sup> )
CFD	Computational Fluid Dynamics
DNS	Direct Numerical Simulation
EE	Eulerian–Eulerian
IB	Immersed Boundary
IBM	Immersed Boundary Method
LE	Lagrangian–Eulerian
MIS	Multiple Independent Simulations
PDF	Probability Density Function
PUReIBM	Particle–resolved Uncontaminated–fluid Reconcilable Immersed Boundary Method

## CHAPTER 6. Stochastic acceleration model for inertial particles in gas–solid suspensions

This chapter is a manuscript titled “Stochastic acceleration model for inertial particles in gas–solid suspension” that is under preparation. A part of this chapter is also published as an article (Tenneti et al., 2010a) in the conference proceedings of International Conference of Multiphase Flow. The title of the conference paper is “Instantaneous particle acceleration model for gas-solid suspensions at moderate Reynolds numbers Particle-Laden Flows” and is authored by S. Tenneti, R. O. Fox and S. Subramaniam. Some of the results shown in this chapter have been included a manuscript titled “Enskog kinetic theory for monodisperse gas–solid suspensions” that is accepted for publication in the Journal of Fluid Mechanics.

### Abstract

Device–scale computational fluid dynamics (CFD) simulations of gas–solid flow that solve for average quantities such as solid volume fraction and phasic mean velocity fields are being extensively used in the industrial design process. The capability of these simulations to accurately predict the characteristics of gas–solid flow depends upon the accuracy of the models for unclosed terms that appear in the equations for mass, momentum and energy conservation. Hrenya and Sinclair (1997) show that the particle granular temperature (particle velocity variance) plays an important role in the prediction of the core annular structure in riser flows. In statistically homogeneous gas–solid suspensions undergoing elastic collisions, the particle acceleration–velocity covariance alone governs the evolution of granular temperature. This acceleration–velocity covariance can be decomposed into a source and dissipation of granular temperature due to hydrodynamic forces. Koch and co-workers (Koch, 1990; Koch

and Sangani, 1999) quantified the hydrodynamic source and dissipation terms in the granular temperature evolution using a combination of kinetic theory closure and multipole expansion simulations at very low Reynolds numbers (Stokes flow regime). At moderate Reynolds numbers, particle-resolved direct numerical simulation (PR-DNS) is as a viable tool to quantify the hydrodynamic source and dissipation. In this study, PR-DNS of freely evolving gas-solid suspensions are performed using the Particle-resolved Uncontaminated-fluid Reconcilable Immersed Boundary Method (PReIBM) that has been developed. Analysis of PR-DNS results shows that the fluctuations in the particle acceleration that are aligned with the fluctuations in the particle velocity give rise to source in the granular temperature. It is found that simple extension of a class of mean particle acceleration models to their corresponding instantaneous versions does not predict the correct joint acceleration-velocity statistics that are obtained from DNS. Also such models do not give rise to any source in the granular temperature due to hydrodynamic effects. This motivates the development of better instantaneous particle acceleration models. It is found that a Langevin equation for the increment in the particle velocity reproduces the PR-DNS results for particle velocity autocorrelation in freely evolving suspensions. Particle-resolved simulations of freely evolving gas-solid suspensions are performed over a wide range of solid volume fraction ( $0.1 \leq \phi \leq 0.4$ ), Reynolds number based on the slip velocity between the solid and the fluid-phase ( $10 \leq Re_m \leq 100$ ) and solid to fluid density ratio ( $100 \leq \frac{\rho_p}{\rho_f} \leq 2000$ ). Based on the data obtained from the simulations, functional dependence of the model coefficients on solid volume fraction, Reynolds number and solid to fluid density ratio is obtained.

## 6.1 Introduction

Gas-solid flows are common in many industrial applications such as fluidized bed combustors, coal gasification, and pneumatic transport lines. A fundamental understanding of gas-solid flow is relevant due to increasing interest in carbon-neutral energy generation technologies such as chemical looping combustion. applications, gas-solid flows are also encountered in many naturally occurring phenomena such as [dispersion of volcanic ash, pollen?]

Computational fluid dynamics (CFD) simulations that solve for the averaged equations

of multiphase flow are a cost-effective solution for rapid evaluation of design and scale up of industrial devices like fluidized beds. Device-scale CFD simulations are usually based on the Eulerian-Eulerian two-fluid approach in which averaged equations for conservation of mass, momentum and energy are written for each phase, with coupling terms representing the interphase interactions. These equations contain unclosed terms that need to be modeled. For example, the mean momentum conservation equation in the particle phase requires closure of the average fluid-particle interaction force (mean drag force) and the average stress in the solid particle phase. Accurate models for the unclosed terms are therefore needed for predictive device-scale CFD simulations of gas-solid flow.

In any statistical closure problem, an important modeling question is the adequacy of the mathematical representation to capture physical phenomena. Hrenya and Sinclair (1997) show that it is necessary to solve the transport equation for the particle granular temperature (particle velocity variance) to predict the core-anular structure observed in riser flows. This shows that closure only at the level of the mean momentum is not adequate, but a closure at the level of second moment of particle velocities is necessary.

An alternative approach to the closure of moment transport equations is to consider the evolution of the one-particle distribution function. Just as closure at the level of the transport equation for the probability density function (PDF) in single-phase turbulent reactive flow implies a closure for all moment equations, similarly a kinetic equation that achieves a closure for the one-particle distribution function in kinetic theory implies a closure for all moment equations. In particular, a closure at the one-particle distribution level automatically implies closure of the mean momentum and particle velocity second moment equations. Furthermore, closures at the one-particle distribution level are guaranteed to satisfy realizability criteria, whereas special care is needed to ensure the same in the case of moment closures. These considerations motivate the development of models for the unclosed terms in the transport equation for the one-particle distribution function corresponding to gas-solid flow.

For monodisperse particles the one-particle distribution function  $f(\mathbf{x}, \mathbf{v}, t)$  is defined in a position-velocity space (Williams, 1958; Koch, 1990; Subramaniam, 2000, 2001; Liboff, 2003;

Garzo et al., 2007a), and evolves by the following transport equation:

$$\frac{\partial f}{\partial t} + \nabla_{\mathbf{x}} \cdot (\mathbf{v}f) + \nabla_{\mathbf{v}} \cdot (\langle \mathbf{A} | \mathbf{x}, \mathbf{v}; t \rangle f) = \dot{f}_{\text{coll}}, \quad (6.1)$$

where  $\nabla_{\mathbf{x}}$  and  $\nabla_{\mathbf{v}}$  denote the gradient operators in the position and velocity space, respectively, and  $\dot{f}_{\text{coll}}$  is the collisional term that can depend on higher order statistics. A closure model for the collisional term results in a kinetic equation. This well-known equation has been extensively studied in the context of granular flows where collisions are inelastic. Extensions to non-dilute cases that follow the Enskog approach have also been pursued. The averaged equations for mean momentum conservation and transport of the second moment of particle velocity implied by Eq. 6.1 are derived using the usual procedure to derive hydrodynamic equations in kinetic theory (Koch, 1990; Pai and Subramaniam, 2009).

The principal difference between the kinetic theory of gases and the kinetic theory of gas-solid flow is that in the latter, the conditional particle acceleration term  $\langle \mathbf{A} | \mathbf{x}, \mathbf{v}; t \rangle$  appears inside the velocity derivative in the velocity transport term and it depends on particle velocity through slip with respect to the fluid. This conditional particle acceleration is caused by the hydrodynamic force  $\mathbf{F}_{\text{fluid}} = m \langle \mathbf{A} | \mathbf{x}, \mathbf{v}; t \rangle$  experienced by the particle due to the pressure and velocity gradient fields at the particle surface. As an illustration of the former, the pressure field is given in figure 6.1(b), which shows a single motionless particle suspended in mean fluid flow or, equivalently, a sphere moving in the same direction as that of the mean fluid flow. For this simple case, the hydrodynamic force acting on the particle is typically expressed as  $\mathbf{F}_{\text{fluid}} = m\beta(\langle \mathbf{u}^{(f)} \rangle - \langle \mathbf{v} \rangle)$ , where  $m$  is the mass of a single particle and  $\beta$  is a drag coefficient that depends on the particle Reynolds number,  $\langle \mathbf{u}^{(f)} \rangle$  is the mean fluid velocity and  $\langle \mathbf{v} \rangle$  is the (mean) particle velocity. A slightly more complex situation is depicted in figure 6.1(c), where the particle is now moving in a different direction than the mean fluid flow, as indicated by the arrow, but still unaffected by neighbor particle effects. The presence of such particle motion leads to a change in the pressure field (and velocity-gradient field, not shown) at the particle surface, thereby causing a change in  $\mathbf{F}_{\text{fluid}}$ . An even more complex scenario is shown in figure 6.1(d), where the presence of surrounding, moving particles causes a continual change in the pressure (and velocity) field around the particle of interest, resulting in a dynamic gas-solid

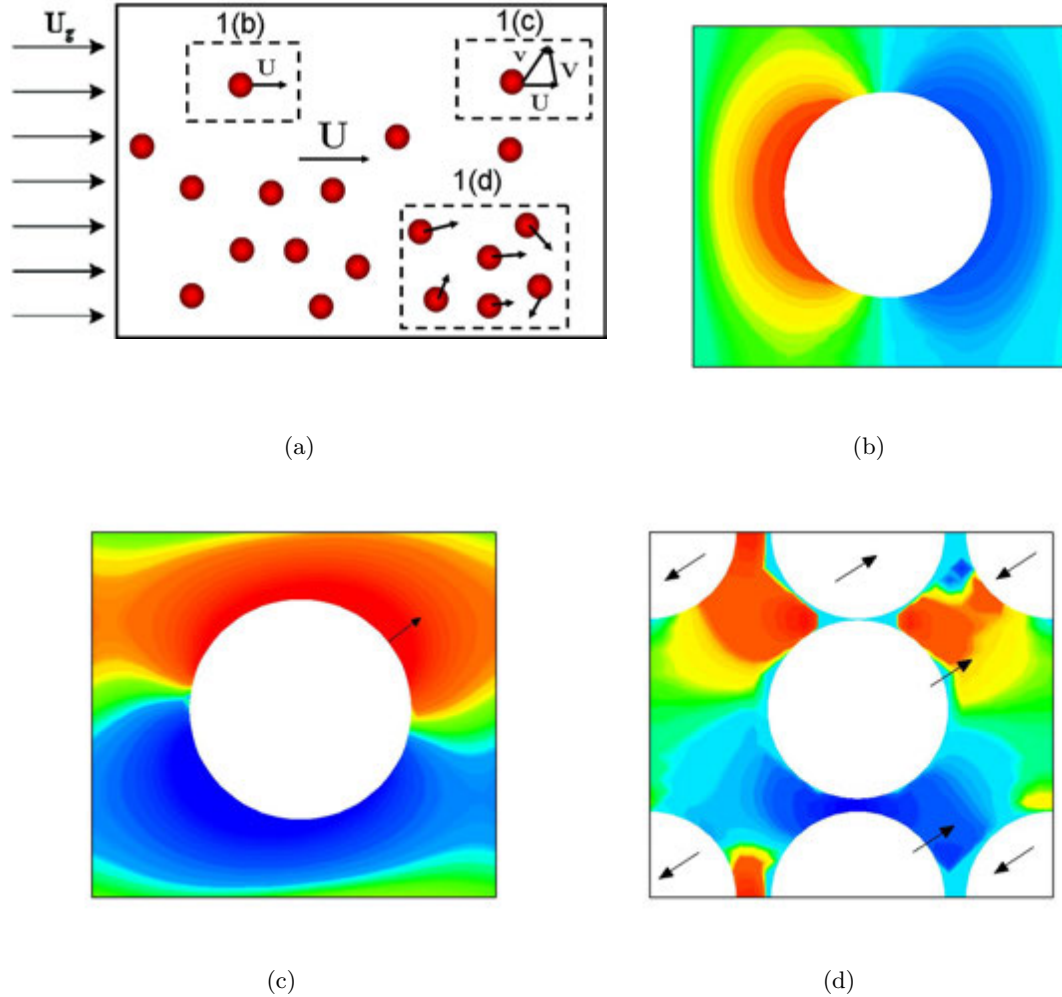


Figure 6.1 Illustration of different contributions to the instantaneous gas-solid force in a suspension with a mean fluid velocity  $\langle \mathbf{u}^f \rangle$  and a mean particle velocity  $\langle \mathbf{v} \rangle$  is shown in top left panel (a). Pressure contours are shown for (b) a single particle far away from its neighbors and moving with a velocity equal to the mean particle velocity (top right panel), (c) a particle moving in a different direction than the mean fluid flow and far from its neighbors (bottom left panel), and (d) a collection of particles moving in different directions (bottom right panel). The pressure contours are obtained from particle-resolved direct numerical simulations (PR-DNS) for a gas-solid suspension that corresponds to a solid volume fraction of 0.2 and mean flow Reynolds number 0.01.

interaction force. Accordingly, the hydrodynamic force experienced by a single particle can be decomposed into the contributions arising from mean slip velocity between the solid and the gas-phase (figure 6.1(b)), instantaneous particle velocity fluctuations with respect to mean velocity of the particles (figure 6.1(c)) and the contribution due to neighbor particle effects (figure 6.1(d)). It is worthwhile to note that this last system (figure 6.1(d)) best captures the interactions occurring in practical gas-solid systems such as fluidized beds.

In the transport equation for the distribution function (cf. Eq. 6.1),  $\langle \mathbf{A} | \mathbf{x}, \mathbf{v}; t \rangle$  depends on the instantaneous particle velocity  $\mathbf{v}$  and can vary in both space and time. For the spatially homogeneous case with monodisperse particles it can be interpreted as the average acceleration experienced by a particle with velocity  $\mathbf{v}$ . The averaging operator  $\langle \cdot \rangle$  represents integration over all higher-order multiparticle distribution functions (Koch, 1990; Subramaniam, 2000) that can be defined on the basis of the ensemble of particles with position and velocity  $\{\mathbf{X}^{(n)}(t), \mathbf{V}^{(n)}(t), n = 1, \dots, N\}$ . In particular, the conditional acceleration  $\langle \mathbf{A} | \mathbf{x}, \mathbf{v}; t \rangle$  is obtained by integrating out its dependence on the two-particle density (pair correlation function). In other words, the conditional acceleration  $\langle \mathbf{A} | \mathbf{x}, \mathbf{v}; t \rangle$  is not completely determined by the particle velocity, but may be affected by the presence of neighbor particles. Following from the earlier discussion surrounding figure 6.1, different approximations for the conditional particle acceleration have been made, leading to differences in the moment equations appearing in the literature.

Consider first the simplest case, where the instantaneous particle acceleration is modeled as a mean acceleration, namely  $\langle \mathbf{A} | \mathbf{x}, \mathbf{v}; t \rangle = \beta(\langle \mathbf{u}^{(f)} \rangle - \langle \mathbf{v} \rangle)$ , where  $\beta$  is a function of the solid volume fraction and Reynolds number based on the mean slip velocity ( $\langle \mathbf{u}^{(f)} \rangle - \langle \mathbf{v} \rangle$ ) between the gas and the solid-phase (cf. figure 6.1(b)). For this model, a mean particle acceleration term appears in the mean momentum equation of the solid-phase, but no terms appear in the granular temperature equation. Next, consider an approximation which accounts for the fluctuation in the particle velocity (cf. figure 6.1(c)) in the following manner:  $\langle \mathbf{A} | \mathbf{x}, \mathbf{v}; t \rangle = \beta(\langle \mathbf{u}^{(f)} \rangle - \mathbf{v})$  and thus is a function of the instantaneous particle velocity  $\mathbf{v}$ , though  $\beta$  still remains a function of the solid volume fraction and slip Reynolds number. In this case, an additional sink term (which is proportional to  $\beta$ ) arises in the equation for the granular temperature due to viscous drag (for

example, see Koch (1990)). In a third and improved approximation, fluctuations in both phases are considered in the fluid-force relation (cf. figure 6.1(d)), namely  $\langle \mathbf{A} | \mathbf{x}, \mathbf{v}; t \rangle = \beta(\mathbf{u}^{(f)} - \mathbf{v})$ , where  $\mathbf{u}^{(f)}$  is the instantaneous gas velocity and with  $\beta$  again typically treated as a function of the mean quantities. This treatment leads to an additional source term in the granular energy balance arising from fluid-dynamic interactions (for example, see Gidaspow (1994)). However, this approximation leads to a single point fluid-particle velocity covariance that Xu and Subramaniam (2006) have shown to be inconsistent for finite particle size.

As discussed above, the closure model for the conditional particle acceleration affects both the mean momentum and the particle granular temperature, as these are derived from the kinetic equation 6.1. In a typical gas–solid flow system (cf. figure 6.1(d)), the presence of numerous particles moving in different directions will lead to continually-changing hydrodynamic interactions between particles (i.e., fluctuations in the fluid velocity and pressure fields). Finally, and perhaps more importantly, a common assumption in works that incorporate gas- and/or solid-phase fluctuations is that the basic form of the mean particle acceleration  $\langle \mathbf{A} | \mathbf{x}, \mathbf{v}; t \rangle = \beta(\langle \mathbf{u}^{(f)} \rangle - \langle \mathbf{v} \rangle)$  also holds for its instantaneous counterpart by simply replacing the mean quantities with instantaneous ones i.e.,  $\langle \mathbf{A} | \mathbf{x}, \mathbf{v}; t \rangle = \beta(\mathbf{u}^{(f)} - \mathbf{v})$ . Recent findings by Tenneti et al. (2010b), however, indicate that such treatments are not appropriate. Figure 6.2 shows a plot of the streamwise component of fluctuations in particle acceleration  $\mathbf{A}''$  versus the streamwise component of fluctuations in particle velocity  $\mathbf{v}''$ . The fluctuations in the particle acceleration and velocity are defined with respect to their corresponding mean values. The particle acceleration fluctuations are normalized by the standard deviation in the particle acceleration distribution  $\sigma_A$ , while the fluctuations in the particle velocity are normalized by the standard deviation in the particle velocity distribution  $\sigma_v$ . Square symbols are the particle acceleration fluctuations obtained from particle–resolved direct numerical simulation (PR–DNS) of a freely evolving gas–solid suspension. Triangles are the fluctuations in the particle acceleration predicted by using a model for the fluid–particle acceleration of the form  $\langle \mathbf{A} | \mathbf{x}, \mathbf{v}; t \rangle = \beta(\mathbf{u}^{(f)} - \mathbf{v})$ . It is clear that the joint statistics of the particle acceleration and particle velocity that are crucial for the accurate prediction of the evolution of granular temperature are not well captured by this simplified class of instantaneous particle acceleration

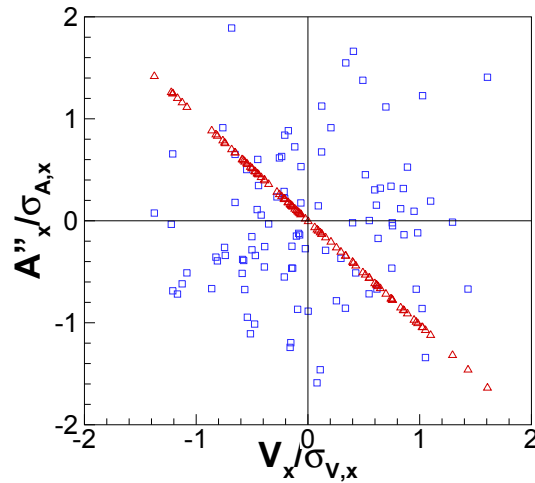


Figure 6.2 Scatter plot of streamwise component of particle acceleration fluctuations  $\mathbf{A}''$  (normalized by the standard deviation in the particle acceleration distribution  $\sigma_A$ ) versus the streamwise component of particle velocity fluctuations  $\mathbf{v}''$  (normalized by the standard deviation in the particle acceleration distribution  $\sigma_v$ ). Square symbols ( $\square$ ) denote the fluctuations in the particle acceleration obtained from PR-DNS of a freely evolving gas–solid suspension corresponding to a solid volume fraction of 0.2, mean flow Reynolds number of 1.0 and solid to fluid density ratio of 1000. Upper triangles ( $\triangle$ ) denote the fluctuations in the particle acceleration predicted by using a model for the fluid–particle acceleration of the form  $\langle \mathbf{A} | \mathbf{x}, \mathbf{v}; t \rangle = \beta(\mathbf{u}^{(f)} - \mathbf{v})$ .

models. Although such models result in a sink of particle granular temperature, it does not account for the source in granular temperature that is responsible for points in quadrants I and III of the fluctuating particle acceleration–velocity scatter plot. Moreover, the scatter observed in the particle acceleration fluctuations suggests a stochastic contribution to the fluid–particle force that arises due to the effect of the neighbor particles.

For the limiting case of a statistically homogeneous gas–solid flow in the Stokes flow regime, Koch and co-workers (Koch, 1990; Koch and Sangani, 1999) developed a kinetic theory closure with a model for the conditional particle acceleration that accounts for the presence of ambient fluid in the term transporting the distribution function in velocity space via analytical means (Koch, 1990) and through the use of multipole expansions (Koch and Sangani, 1999). For statistically homogeneous gas–solid flows, the correlation between the particle fluctuating velocity and its acceleration fluctuation determines the evolution of the particle velocity second moment. In the limiting case of Stokes flow, Koch (Koch, 1990; Koch and Sangani, 1999) decomposed the particle acceleration–velocity covariance as the sum of source and sink contributions. If particle collisions are elastic then the granular temperature decreases only due to viscous interactions with the ambient fluid. In the Stokes flow regime the sink term simply relaxes the granular temperature to zero on the viscous relaxation time scale. In Koch’s decomposition of the acceleration–velocity covariance into source and sink terms (Koch and Sangani, 1999), the source term due to hydrodynamic interactions with neighboring particles can balance the sink term leading to a steady state granular temperature in stable homogeneous suspensions.

The source term in the granular temperature equation plays an important role in sustaining a nonzero value of the granular temperature. In its absence the granular temperature in a homogeneous suspensions would simply decay to zero, leading to an infinite Mach number in the particle phase. Not only is this problematic from a numerical standpoint for CFD simulations, but it is also unphysical over a wide range of mean flow Reynolds number and volume fraction. Although Koch’s analysis is useful in the Stokes flow regime, it is difficult to extend the analysis to moderate Reynolds number cases. At moderate Reynolds number, particle–resolved direct numerical simulation (PR–DNS) offers a promising approach to quantify unclosed terms in

the transport equations for particle velocity moments, or the transport equation for the one-particle distribution function. We use PR–DNS of gas–solid flow at moderate Reynolds number to develop a class of particle acceleration models that are capable of capturing the coupling between particle velocity fluctuations and hydrodynamic forces in gas–solid flow.

The rest of the paper is organized as follows. First the numerical method is briefly described followed by the details of the instantaneous particle acceleration model. Results from PR–DNS of freely evolving suspensions are discussed next. The procedure used for determining the coefficients of the acceleration model is described followed by the specification of these coefficients in terms of solid volume fraction, mean flow Reynolds number, solid to fluid density ratio and particle granular temperature.

## 6.2 Numerical Method

In this study, PR–DNS of freely evolving gas–solid suspensions are performed using the Particle–resolved Uncontaminated–fluid Reconcilable Immersed Boundary Method (PUREIBM) that has been developed at Iowa State University to simulate flow past fixed particle assemblies (Garg et al., 2011) and freely evolving suspensions (Tenneti et al., 2010b). PUREIBM is a particle–resolved direct numerical simulation approach for gas–solid flow with the following features that distinguish it from other immersed boundary method approaches:

1. Uncontaminated fluid: In PUREIBM the immersed boundary (IB) forcing is solely restricted to those grid points that lie in the solid phase, and therefore the flow solution in the fluid phase is uncontaminated by the IB forcing. Consequently the velocity and pressure in the fluid phase is a solution to the unmodified Navier–Stokes equations (in contrast to IB implementations that smear the IB forcing on to grid points in the fluid phase adjoining solid boundaries, resulting in solution fields that do not correspond to unmodified Navier–Stokes equations).
2. Reconcilable: In PUREIBM the hydrodynamic force experienced by a particle is computed directly from the stress tensor at the particle surface that is obtained from this uncontaminated fluid flow solution (in contrast to IB implementations that calculate the

hydrodynamic force from the IB forcing field). This feature of PReIBM enables us to directly compare the DNS solution with any random-field theory of multiphase flow. In particular, for statistically homogeneous suspensions it is shown that (Garg et al., 2011) if the volume-averaged hydrodynamic force exerted on the particles by the fluid is computed from a PReIBM simulation, it is a consistent numerical calculation of the average interphase momentum transfer term  $\langle \tau'_{ji} n_j^{(\beta)} \delta(\mathbf{x} - \mathbf{x}^{(I)}) \rangle$  in the two-fluid theory (Drew, 1983). This reconciles DNS results with multiphase flow theory.

Owing to these specific advantages, it is shown elsewhere (Garg et al., 2011; Garg, 2009) that PReIBM is a numerically convergent and accurate particle-resolved DNS method for gas-solids flow. Its performance has been validated in a comprehensive suite of tests: (i) Stokes flow past simple cubic (SC) and face centered cubic (FCC) arrangements (ranging from dilute to close-packed limit) with the boundary-integral method of Zick and Homsy (1982), (ii) Stokes flow past random arrays of monodisperse spheres with LBM simulations of van der Hoef et al. (2005) (iii) moderate to high Reynolds numbers ( $Re_m \leq 300$ ) in SC and FCC arrangements with LBM simulations of Hill et al. (2001b) and (iv) high Reynolds number flow past random arrays of monodisperse spheres with ANSYS-FLUENT CFD package. It has also been extended to study passive scalar transport, and validated for heat transfer from a single isolated sphere (Garg, 2009; Garg et al., 2010b). In this work, the DNS methodology based on PReIBM developed by Tenneti et al. (2010b) to simulate freely evolving suspensions is used to propose an instantaneous particle acceleration model that incorporates the effect of particle velocity fluctuations and hydrodynamic effects of neighboring particles.

### 6.3 Instantaneous particle acceleration model

We propose the following stochastic model for the increment in the particle velocity:

$$dv_i = -\beta \langle W_i \rangle dt - \gamma v_i'' dt + B dW_i. \quad (6.2)$$

The above equation is an isotropic form of the general Langevin model. In the above equation  $dv_i$  is the increment in the particle velocity,  $v_i''$  is the fluctuation in the particle velocity and  $dW_i$  is a Wiener process increment. Fluctuations in the particle velocity are defined about the mean

particle velocity, i.e.  $v_j'' = v_j - \langle v_j \rangle$ . The first term on the right hand side of Eq. 1 accounts for the effect of the mean slip velocity. The mean slip velocity, defined as  $\langle \mathbf{W} \rangle = \langle \mathbf{v} \rangle - \langle \mathbf{u}^{(f)} \rangle$ , is the relative velocity between the solid phase mean velocity and the fluid phase mean velocity. The second term accounts for the fluctuation in the particle velocity and the last term models the effect of the hydrodynamic interaction of the neighboring particles. The coefficient  $\gamma$  is the inverse of the Lagrangian particle velocity autocorrelation time. It quantifies how long a particle retains memory of its initial velocity. These coefficients are functions of volume fraction ( $\phi$ ), mean flow Reynolds number ( $\text{Re}_m$ ) and particle to fluid density ratio ( $\rho_p/\rho_f$ ). To extract a functional form for the Langevin model coefficients, simulations of freely evolving suspensions where, the motion of the particles is affected by the surrounding fluid, are performed using the DNS methodology developed by Tenneti et al. (2010b). Results from the simulations freely evolving suspensions are presented in the following section.

## 6.4 Results

PUReIBM simulations of freely evolving suspensions are performed for solid volume fractions between 0.1 and 0.4 and for mean flow Reynolds numbers between 10 and 100. The Reynolds number based on the mean slip velocity between the fluid and particulate phase is defined as

$$\text{Re}_m = (1 - \phi) \frac{\rho_f |\langle \mathbf{v} \rangle - \langle \mathbf{u}^{(f)} \rangle| d_p}{\mu_f}, \quad (6.3)$$

where  $\phi$  is the solid volume fraction,  $\rho_f$  and  $\mu_f$  are the density and dynamic viscosity of the fluid phase respectively, and  $d$  is the particle diameter. When characterizing the effect of particle velocity fluctuations it is useful to define a Reynolds number based on the granular temperature  $\text{Re}_T$  as:

$$\text{Re}_T = \frac{\rho_f d T^{1/2}}{\mu_f} \quad (6.4)$$

where  $T$  is the granular temperature which is given by  $T = \frac{1}{3} \langle v_i'' v_i'' \rangle$ . Estimation of granular temperature from DNS of freely evolving suspensions is discussed in detail by Tenneti et al. (2010b). The evolution of  $\text{Re}_T$  for a freely evolving suspension at a volume fraction of 0.1 and solid to fluid density ratio of 100 is shown in Fig. 6.3. Firstly, we observe that for

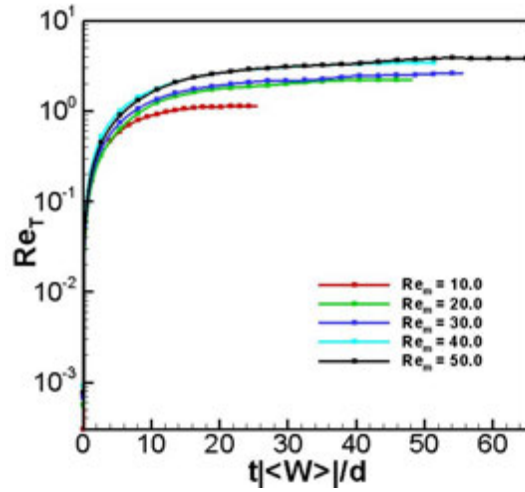


Figure 6.3 Plot showing the evolution of the Reynolds number based on granular temperature ( $Re_T$ ) for a freely evolving suspension of elastic particles at a volume fraction of 0.1 and solid to fluid density ratio of 100.

all mean flow Reynolds numbers, the granular temperature attains a statistical steady state. From the figure we can also see that at a given solid to fluid density ratio, the steady state granular temperature increases with increasing mean flow Reynolds number. This result can be explained based on the fact that the particles pick up energy from the fluid and the energy in the system increases with increasing  $Re_m$ . To the authors' knowledge, this is the first report of the effect of mean flow Reynolds number on granular temperature. Similar behavior of the steady granular temperature with  $Re_m$  is observed for all the volume fractions studied ( $\phi = 0.1, 0.2, 0.3$  and  $0.4$ ). The Langevin model for the particle acceleration is verified by computing the particle velocity autocorrelation function after the granular temperature reaches a steady state.

### 6.5 Verification of Langevin model

In this section, verification of the Langevin model for the instantaneous particle acceleration is presented. For this purpose we consider the increment in the particle velocity fluctuations:

$$dv_i'' = -\gamma v_i'' dt + BdW_i. \quad (6.5)$$

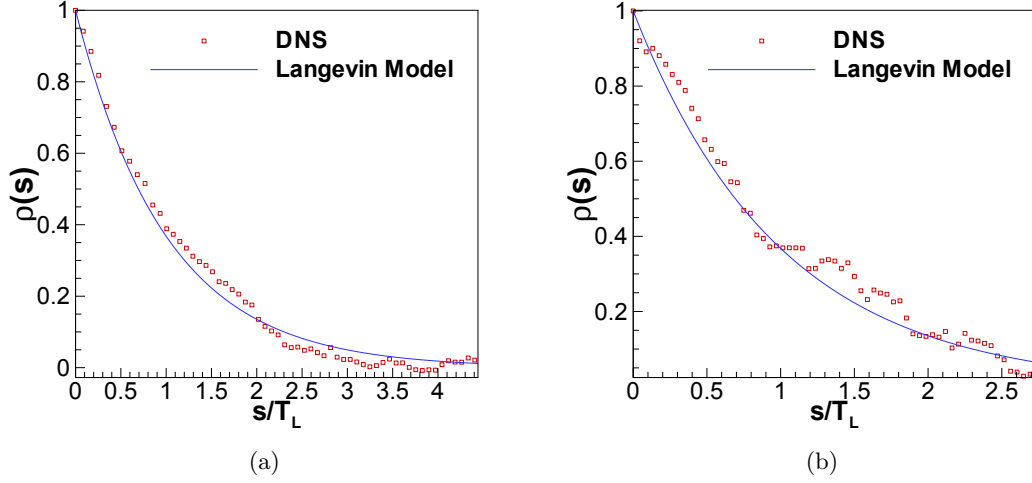


Figure 6.4 (a) Comparison of the particle velocity autocorrelation function extracted from the DNS of freely evolving suspension (solid volume fraction of 0.2, mean slip Reynolds number 20 and solid to fluid density ratio of 10) with the exponential decay predicted by the Langevin model. (b) Same as Fig. 6.4(a) for a suspension with solid to fluid density of 100.

As described earlier, in the above equation the model coefficient  $\gamma$  is the inverse of the integral time scale of the particle velocity autocorrelation. The particle velocity autocorrelation function  $\rho(s)$  is defined as follows:

$$\rho(s) = \frac{\langle v_i''(t_0) v_i''(t_0 + s) \rangle}{\langle v_k''(t_0) v_k''(t_0) \rangle}$$

where  $s$  is the separation in time. The integral time scale for the autocorrelation function is defined as  $T_L = \int_0^\infty \rho(s) ds$ . Using this definition, we computed the integral time scale from DNS after the granular temperature reached a steady state. If a stochastic process obeys the Langevin equation with an integral time scale of  $T_L$ , then its autocorrelation function should decay exponentially, i.e.,  $\rho(s) = e^{-s/T_L}$ . We extracted the autocorrelation function from the DNS and compared it with the exponential function predicted by the Langevin model. This comparison is shown in Fig. 6.4. We can see that for both density ratios considered, the evolution of the autocorrelation function obtained from DNS matches with the exponential decay predicted by the Langevin model. We established that Langevin model predicts the dynamics of a freely evolving suspension very well after the granular temperature reaches steady state. However, at a given volume fraction, mean flow Reynolds number and solid to

fluid density ratio, we need to specify the coefficients as a function of the granular temperature so that we can predict the evolution of the suspension using the Langevin model. In order to do this, we have to identify the source and dissipation of granular temperature from the PR–DNS data. In the next section, the procedure to specify the model coefficients from PR–DNS is presented.

## 6.6 Specification of the model coefficients

The objective of the particle acceleration model is to predict the evolution of the granular temperature correctly. In order to achieve this we have to match the source  $S$  and dissipation  $\Gamma$  obtained from PR–DNS. The procedure to uniquely identify source and dissipation of granular temperature from PR–DNS is outlined in Appendix D. The model coefficients  $\gamma$  and  $B$  can be written as follows:

$$\gamma = \frac{\Gamma(\phi, \text{Re}_m, \rho_p/\rho_f)}{2T}$$

$$B^2 = \frac{S(\phi, \text{Re}_m, \rho_p/\rho_f)}{2T}.$$

Clearly, source and dissipation and in turn the model coefficients are functions of a large number of parameters. It is desirable to find a scaling for source (and dissipation) such that there is a reduction in some of the parameters. From the phase space plots (cf. Fig. D.2) and the evolution of the granular temperature (cf. Fig. 6.3), we see that the evolution of granular temperature for different volume fractions and Reynolds numbers is self similar. Thus, it is natural to analyze the dynamics of the suspension as departures from the steady state values. We introduce the following scaling for temperature, source and dissipation respectively:

$$\theta = \frac{T - T_{SS}}{T_{SS}}$$

$$\hat{S} = \frac{S - S_{SS}}{S_{SS}}$$

$$\hat{\Gamma} = \frac{\Gamma - \Gamma_{SS}}{\Gamma_{SS}}.$$

In the above equation  $T_{SS}$ ,  $S_{SS}$  and  $\Gamma_{SS}$  are the temperature, source and dissipation at steady state. At steady state, source and dissipation are equal and hence  $\Gamma_{SS} = S_{SS}$ . The model

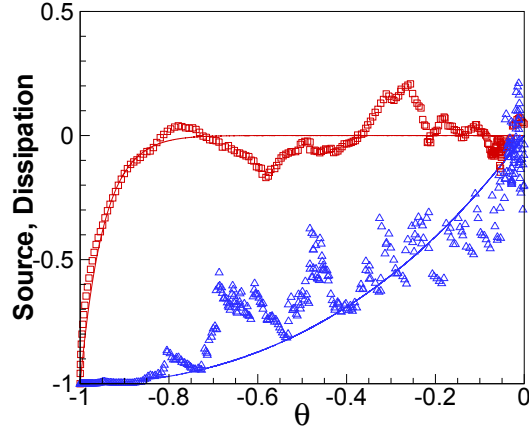


Figure 6.5 Plot showing the scaling of source and dissipation with granular temperature in nondimensional phase space. Red squares denote the source and blue triangles denote dissipation. The solid lines are the curve fits for source and dissipation given by Eqs. 6.6 and 6.7 respectively.

coefficients can now be cast in the following form:

$$\gamma = \frac{1}{2} \frac{\hat{\Gamma}(\theta) + 1}{\theta + 1} \frac{S_{SS}(\phi, \text{Re}_m, \rho_p/\rho_f)}{T_{SS}}$$

$$B^2 = (\hat{S}(\theta) + 1) S_{SS}(\phi, \text{Re}_m, \rho_p/\rho_f).$$

Figure 6.5 shows the functional dependence of  $\hat{S}$  and  $\hat{\Gamma}$  on the non dimensional temperature. We propose the following functional forms to model the non dimensional source and dissipation:

$$\hat{S} = -\frac{e^{\theta^4} - \theta^4 - e}{e - 2}, \quad (6.6)$$

$$\hat{\Gamma} = \frac{e^{\theta+1} - \theta - 2}{e - 2}. \quad (6.7)$$

In order to complete the specification of the model coefficients we need a functional form for the dependence of steady granular temperature and source on the solid volume fraction, mean flow Reynolds number and the solid to fluid density ratio. Figure 6.6(a) shows the variation of  $\frac{T_{SS}}{|\langle \mathbf{w} \rangle|^2}$  with solid volume fraction and mean flow Reynolds number for a solid to fluid density ratio of 100. The steady granular temperature decreases with both volume fraction and mean flow Reynolds number. Figure 6.6(b) shows the behavior of the steady granular temperature

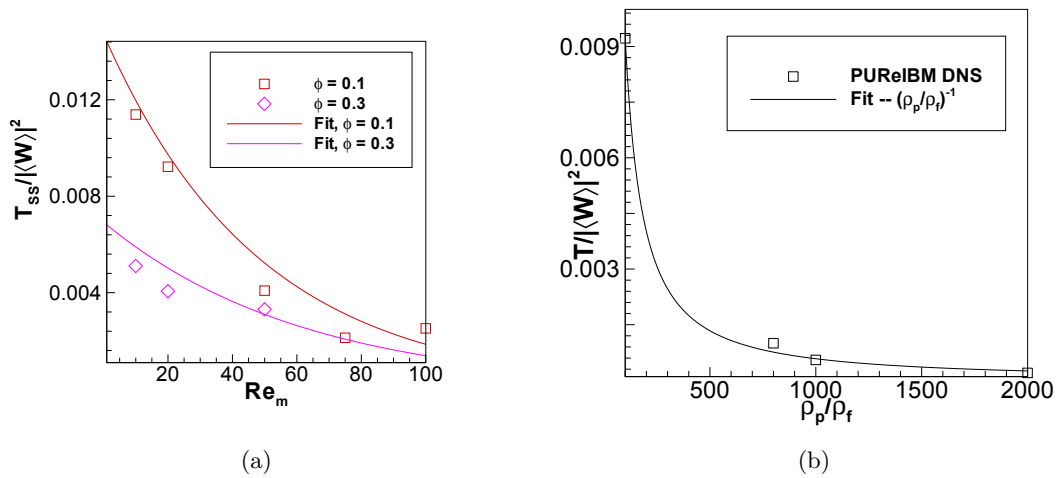


Figure 6.6 Plot in 6.6(a) shows the variation of steady granular temperature with volume fraction and mean flow Reynolds number for a density ratio of 100. Symbols are data obtained from PReIBM DNS and the solid lines indicate the fit given by Eq. 6.8. Plot in 6.6(b) shows the variation of steady granular temperature with solid to fluid density ratio for a solid volume fraction of 0.1 and mean flow Reynolds number 20. Symbols denote the data obtained from PReIBM DNS and the solid line indicates the function  $\left(\frac{\rho_p}{\rho_f}\right)^{-1}$ .

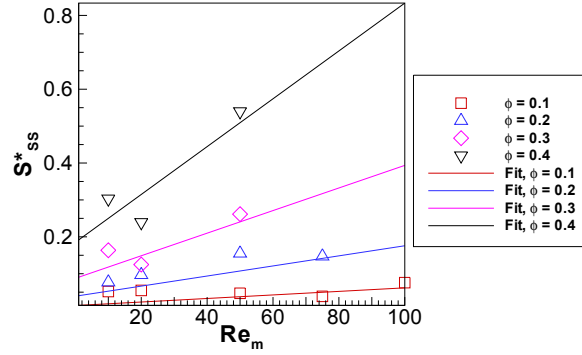


Figure 6.7 Plot showing the behavior of steady source with volume fraction and Reynolds number for a solid to fluid density ratio of 100. Symbols indicate PUREIBM DNS data and solid lines indicate the fit given by Eq. 6.11

with solid to fluid density ratio for a solid volume fraction of 0.2 and mean flow Reynolds number of 20. As expected, the steady temperature decreases with increasing inertia of the particles. Based on the data obtained from PUREIBM DNS, the following functional form is proposed for the steady value of granular temperature:

$$\frac{T_{SS}}{|\langle \mathbf{W} \rangle|^2} \left( \phi, \text{Re}_m, \frac{\rho_p}{\rho_f} \right) = 2(1 - \phi)^3 \exp -0.02(1 - \phi) \text{Re}_m \left( \frac{\rho_p}{\rho_f} \right)^{-1}. \quad (6.8)$$

In order to specify the steady state source in terms of  $\phi$ ,  $\text{Re}_m$  and  $\frac{\rho_p}{\rho_f}$ , we use the following normalization:

$$S_{SS}^* = \frac{S_{SS} m}{3\pi\mu_f D (1 - \phi)^2 |\langle \mathbf{W} \rangle|^2}, \quad (6.9)$$

where  $m$  is the mass of the particle and  $\mu_f$  is the dynamic viscosity of the fluid. Figure 6.7 shows the behavior of the normalized steady source with volume fraction and mean flow Reynolds number for a solid to fluid density ratio of 100. The normalized source increases with both volume fraction and Reynolds number. This behavior can be explained by employing a simple scaling analysis. Since the source of granular temperature is caused due to the correlation of particle acceleration fluctuations and particle velocity fluctuations, the source scales as  $S_{SS} \sim \sigma_A T_{SS}^{1/2}$ , where  $\sigma_A$  is the standard deviation in the particle acceleration. This

scaling implies that the normalized source scales as

$$S_{SS}^* = \frac{S_{SS}m}{3\pi\mu_f D (1-\phi)^2 |\langle \mathbf{W} \rangle|^2} \sim \frac{\sigma_A}{|\langle \mathbf{A} \rangle|} \frac{F(\phi, \text{Re}_m)}{(1-\phi)} \frac{T_{SS}}{|\langle \mathbf{W} \rangle|^2}, \quad (6.10)$$

where  $F(\phi, \text{Re}_m)$  is the normalized mean drag per particle which increases with both solid volume fraction and mean flow Reynolds number. Although the steady granular temperature decreases with both solid volume fraction and Reynolds number, the strong dependence of the mean drag on determines the overall behavior of normalized source. The dependence of the normalized source on the solid to fluid density ratio is determined by the dependence of steady granular temperature on  $\frac{\rho_p}{\rho_f}$ . In fact, the PReIBM DNS data indicates that  $S_{SS}^*$  varies inversely with  $\left(\frac{\rho_p}{\rho_f}\right)^{1/2}$ . Based on the DNS data the following functional form is proposed for the normalized steady source:

$$S_{SS}^* \left( \phi, \text{Re}_m, \frac{\rho_p}{\rho_f} \right) = (1 + 0.035\text{Re}_m) \frac{\phi}{(1-\phi)^3} \left( \frac{\rho_p}{\rho_f} \right)^{-1/2}. \quad (6.11)$$

The functional forms for steady temperature and source given by Eqs. 6.8 and 6.11 respectively complete the specification of the stochastic acceleration model for inertial particles in gas–solid suspensions.

## 6.7 Conclusions

Evolution of the particle granular temperature in gas–solid suspensions at moderate Reynolds numbers is studied by DNS of freely evolving suspensions using PReIBM. DNS results show that the steady granular temperature increases with the mean flow Reynolds number. This steady granular temperature is independent of the initial granular temperature of the suspension. A key finding that emerges from this work is that at steady state the particle velocity autocorrelation function decays exponentially thus motivating the use of a Langevin–like model to describe the increment in particle velocity. A Langevin equation is proposed to model the instantaneous particle acceleration in gas–solid suspensions at moderate Reynolds numbers. Expressions to compute the source and sink of granular temperature from DNS are derived. Previous work by Tenneti et al. (2010b) shows that simple extension of mean particle acceleration models does not recover the joint acceleration–velocity statistics that are obtained from

DNS. Using the expressions for source and dissipation derived in this work it is also shown that such models do not produce any source for the particle granular temperature which justifies the use of Langevin-like models to model the instantaneous particle acceleration. PReIBM simulations of freely evolving suspensions are performed over a wide range of relevant fluid and particle properties. We considered four values of volume fraction ( $\phi = 0.1, 0.2, 0.3$  and  $0.4$ ), five values of mean flow Reynolds number ( $Re_m = 10, 20, 50, 75$  and  $100$ ) and four values of solid to fluid density ratio ( $\frac{\rho_p}{\rho_f} = 100, 800, 1000$  and  $2000$ ). By defining similarity variables as departures from the steady state values, we reduce the model specification to determining the functional dependence of only three functions. We determined the functional dependence of the non dimensional source and dissipation on the non dimensional granular temperature. We developed the functional dependence of steady state source and granular temperature on solid volume fraction, mean flow Reynolds number and solid to fluid density ratio. This stochastic acceleration model can be used in discrete element simulations of gas–solid flow as well as in direct quadrature method of moments. The expressions for source and dissipation of granular temperature at moderate Reynolds numbers determined in this work can be applied in the Eulerian two–fluid simulations and also in deriving kinetic theory closures for gas–solid flow.

### Acknowledgments

This work was supported by a Department of Energy grant DE-FC26-07NT43098 through the National Energy Technology Laboratory.

## CHAPTER 7. Interphase momentum transfer and the level of gas-phase velocity fluctuations in polydisperse gas-solid suspensions

This chapter describes the quantification of interphase momentum transfer and the level of gas-phase velocity fluctuations (gas-phase TKE) in polydisperse gas-solid suspensions using PR-DNS. The objective here is to formulate a general drag law for polydisperse suspensions that can be implemented in moment closures that arise in EE continuum models. In order to investigate the effect of particle size distribution, we start with a bidisperse suspension. A statistical approach based on the one-particle distribution function is used to describe the binary mixture.

PURIBM simulations are performed for flow past bi-disperse suspensions with no relative velocity between the size classes at moderate Reynolds numbers for various volume fractions, volume fraction ratios and diameter ratios. In these simulations, the particles are held fixed and equal velocities are assigned to the particles belonging to both size classes. Beetstra et al. (2007) expressed the drag on each size class in the bidisperse suspension as the product of a quadratic function in  $y_\alpha$  (the particle diameter of the size class  $\alpha$  normalized by the Sauter mean diameter of the bidisperse suspension) and the drag experienced by an equivalent monodisperse suspension. Our drag results from IBM simulations of bi-disperse suspensions indicate that the quadratic dependence on  $y_\alpha$  seems to hold. However, the actual values of the drag do not agree well with the correlation of Beetstra et al. (2007). The reason is the difference between the monodisperse drag correlation proposed using PURIBM DNS (Tenneti et al., 2011) and that of Beetstra et al. (2007). These bidisperse simulations are also used to quantify the level of gas-phase velocity fluctuations and are compared with the level of gas-phase TKE observed in equivalent monodisperse suspensions.

When we consider bi-disperse systems with a finite slip velocity between the size classes, the

fixed bed simulation approach is no longer valid at moderate Reynolds numbers. So we have to perform simulations of freely evolving suspensions. The PReIBM PR–DNS methodology has been successfully extended by Tenneti et al. (2010b) to simulate freely evolving suspensions of monodisperse particles. This method is further extended to account for polydispersity. For polydisperse suspensions, the equations of motion are solved in an accelerating frame of reference that moves with the mixture mean solid velocity. Simulations of freely evolving bi-disperse suspensions show that the slip velocity between the two size classes has a steady state and this steady value depends on the physical parameters of the problem. This shows that for a given mean volume fraction, Reynolds number, diameter ratio, volume fraction ratio and solid to fluid density ratio, one cannot fix the slip velocity between the size classes arbitrarily.

### 7.1 Discrete representation of a polydisperse suspension

A Lagrangian-Eulerian (LE) description is employed to describe the multiphase flow. The starting point for the LE description is the one–particle distribution function which evolves as:

$$\frac{\partial f}{\partial t} + \frac{\partial}{\partial x_i} (v_i f) + \frac{\partial}{\partial v_i} (\langle \mathbf{A} | \mathbf{x} \mathbf{v}, r; t \rangle f) = \dot{f}_{\text{coll}} \quad , \quad (7.1)$$

where,  $\dot{f}_{\text{coll}}$  is the collisional term that depends on higher order statistics. The one–particle distribution function  $f(\mathbf{x}, \mathbf{v}, r, t)$  is a function of particle position, velocity and radius. It can be expressed in terms of the number density  $n(\mathbf{x}, t)$  and a joint probability distribution function  $f_{\mathbf{V}R}^c(\mathbf{v}, r | \mathbf{x}; t)$  as

$$f(\mathbf{x}, \mathbf{v}, r, t) = n(\mathbf{x}, t) f_{\mathbf{V}R}^c(\mathbf{v}, r | \mathbf{x}; t). \quad (7.2)$$

This joint pdf can in turn be expressed in terms of a velocity distribution conditional on particle size and a particle size distribution as follows:

$$f_{\mathbf{V}R}^c(\mathbf{v}, r | \mathbf{x}; t) = f_{\mathbf{V}|R}^c(\mathbf{v} | r, \mathbf{x}; t) f_R^c(r; \mathbf{x}, t). \quad (7.3)$$

In a polydisperse suspension,  $f_R^c$  is specified and a size–class can be thought of as an integral of  $f_R^c$  over the interval  $(r, r + \Delta r)$  size classes. Using the description in Eq. (7.3), we can express  $f(\mathbf{x}, \mathbf{v}, r, t)$  as,

$$f(\mathbf{x}, \mathbf{v}, r, t) = n(\mathbf{x}, r; t) f_{\mathbf{V}|R}^c(\mathbf{v} | r; \mathbf{x}, t), \quad (7.4)$$

where  $n(\mathbf{x}, r; t) = n(\mathbf{x}, t) f_R^c(r|\mathbf{x}; t)$  is the number density conditional on particle size. For a bi-disperse suspension with radii  $R_1$  and  $R_2$ , the distribution function  $f_R^c(r|\mathbf{x}; t)$  can be written as:

$$f_R^c(r|\mathbf{x}; t) = p_1 \delta(r - R_1) + p_2 \delta(r - R_2) \quad (7.5)$$

and hence

$$n = n_1 + n_2 \quad (7.6)$$

where  $n_1 = np_1$  and  $n_2 = np_2$  are the number densities of the size classes 1 and 2 respectively. Therefore any polydisperse suspension can be represented in terms of a discrete number of size classes and conservation equations can be derived for each size class as shown in the next section.

## 7.2 Interphase momentum transfer in a polydisperse suspension

Conservation equations for the mean mass and mean momentum of each size class can be derived by taking the moments of Eq. (7.1). For a statistically homogeneous system, the mean momentum conservation equation for the size class  $\alpha$  with radius  $R_\alpha$  is:

$$\begin{aligned} \frac{\partial}{\partial t} (\rho_\alpha \phi_\alpha \langle v_j | r = R_\alpha; t \rangle) + \frac{\partial}{\partial x_k} (\rho_\alpha \phi_\alpha \langle v_j | r = R_\alpha; t \rangle \langle v_k | r = R_\alpha; t \rangle) \\ = - \frac{\partial}{\partial x_k} (\rho_\alpha \phi_\alpha \langle v_j'' v_k'' | r = R_\alpha; t \rangle) + \mathcal{S}_j \\ + \rho_\alpha \phi_\alpha \langle A_j | r = R_\alpha; t \rangle, \quad \alpha = 1, 2. \end{aligned} \quad (7.7)$$

$$(7.8)$$

In the above equation  $\rho_\alpha$  and  $\phi_\alpha$  are the density and volume fraction of the size class  $\alpha$  respectively. The first term on the right hand side of Eq. (7.8) is the Reynolds stress due to fluctuations in the particle velocity and the second term is the momentum source/sink due to collisions with particles belonging to other size classes. The particle velocity fluctuations are defined about the mean velocity conditional on particle size, i.e.,  $v_j'' = v_j - \langle v_j | r = R_\alpha; t \rangle$ . The last term on the left hand side denoted by  $\mathbf{f}_{g-\alpha}$  is the total force per unit volume of the suspension acting on the size class  $\alpha$ . It is related to the average force acting per particle through the expression  $f_{g-\alpha, j} = n_\alpha \langle F_j | r = R_\alpha; t \rangle$ . The total force  $f_{g-\alpha, j}$  experienced by the

particles belonging to a particular size class arises due to the mean pressure gradient acting on the suspension, the viscous stresses and the fluctuating pressure acting on the particles:

$$f_{g-\alpha,j} = n_\alpha \langle F_j | r = R_\alpha; t \rangle = -\phi_\alpha \frac{\partial P}{\partial x_j} + n_\alpha \langle F_{D,j} | r = R_\alpha; t \rangle \quad (7.9)$$

Here the second term on the right hand side denotes the contributions of viscous stress and fluctuating pressure to the total force. Drag laws for polydisperse suspensions in the Stokes flow regime that are proposed by van der Hoef et al. (2005) and Yin and Sundaresan (2009b) report  $\langle F_{D,j} | r = R_\alpha; t \rangle$  as the drag force where as Hill et al. (2001b) and Tenneti et al. (2011) reported  $\langle F_j | r = R_\alpha; t \rangle$  that includes the mean pressure gradient term.

In a polydisperse suspension, drag laws are written for each size class and the existing polydisperse drag laws are based on the drag correlations proposed for an equivalent monodisperse suspension. The equivalent monodisperse suspension is defined as a suspension of equi-sized particles at a volume fraction  $\phi$  (equal to the total volume fraction of the polydisperse suspension) and diameter  $\langle D \rangle$ , where

$$\langle D \rangle = \frac{\sum_{\alpha=1}^2 N_\alpha D_\alpha^3}{\sum_{\alpha=1}^2 N_\alpha D_\alpha^2} \quad (7.10)$$

is called the Sauter mean diameter. In general, the drag force is a function of the volume fraction and the mixture mean Reynolds number,  $\text{Re}_m = \left| \langle \tilde{\mathbf{V}} \rangle - \langle \mathbf{u}^{(f)} \rangle \right| \langle D \rangle / \nu_f$ , where  $\langle \tilde{\mathbf{V}} \rangle$  is the mixture mass-weighted mean velocity. In this work, we report the total fluid-particle force acting on each size class. The normalized drag force per particle acting on the size class  $\alpha$  is defined as

$$F_\alpha(\phi, \text{Re}_m) = \frac{|\langle \mathbf{F} | r = R_\alpha; t \rangle|}{3\pi\mu D_\alpha(1-\phi) |\langle \mathbf{W} | r = R_\alpha; t \rangle|} \quad (7.11)$$

where  $\langle \mathbf{W} | r = R_\alpha; t \rangle$  is the mean slip velocity experienced by that size class. It must be noted that only fixed beds are used for the purpose of studying the drag force. Hence, the all size classes have the same slip velocity with respect to the fluid. For suspensions with slip velocity between size classes, Yin and Sundaresan (2009b) used a viscous scaling to normalize the drag force in the Stokes flow regime. Although we performed Pr-DNS of freely evolving suspensions in this study, we did not study the drag acting on the size classes in these simulations.

At moderate Reynolds numbers Beetstra et al. (2007) used LBM simulations to conclude

that the drag force on a bi-disperse suspension can be written as:

$$F_{\alpha}(\phi, \text{Re}_m) = [y_{\alpha}(1 - \phi) + \phi y_{\alpha}^2] F(\phi, \text{Re}_m) \quad (7.12)$$

where  $F(\phi, \text{Re}_m)$  is the average fluid-particle force per particle acting on an equivalent monodisperse suspension and  $y_{\alpha} = D_{\alpha}/\langle D \rangle$  is a normalized particle diameter. Using PReIBM simulations we verify whether the dependence of the ratio  $F_{\alpha}(\phi, \text{Re}_m)/F(\phi, \text{Re}_m)$  holds at moderate Reynolds numbers.

### 7.3 Drag and gas-phase velocity fluctuations from PReIBM simulations

PReIBM simulations of flow past bi-disperse suspensions (with no relative velocity between the size classes) are performed for  $\text{Re}_m$  values of 50, 65, 75, and 100 at total volume fractions equal to 0.1, 0.2, 0.3 and 0.4. At each volume fraction, the volume fraction ratio ( $\phi_2/\phi_1$ ) is varied from 1 to 6 and the diameter ratio ( $D_2/D_1$ ) from 1.5 to 4. The results of PReIBM simulations of flow past bi-disperse suspensions are shown in figure 7.1 for a total volume fraction of 0.3 and 0.4 and two mean flow Reynolds numbers (50 and 75). The simulation data is compared with the drag predicted by equation 7.12. The solid lines are obtained by substituting the PReIBM drag correlation (Tenneti et al., 2011) for  $F(\phi, \text{Re}_m)$  in Eq. (7.12). The dashed lines are obtained by substituting the monodisperse drag correlation given by Beetstra et al. (2007) for  $F(\phi, \text{Re}_m)$  in Eq. (7.12). We can see clearly that the values of  $F_{\alpha}(\phi, \text{Re}_m)$  from the simulations do not agree with the values predicted by the drag correlation of Beetstra et al (2007). The reason for this is the difference between the PReIBM drag correlation and the correlation of Beetstra et al. (2007) for monodisperse suspensions. However, it is interesting to see that the functional form for  $F_{\alpha}(\phi, \text{Re}_m)/F(\phi, \text{Re}_m)$  proposed by Beetstra et al. (2007) seems to hold from PReIBM simulations also.

The level of gas-phase velocity fluctuations have also been quantified from the PReIBM simulations of bidisperse suspensions. The behavior of the gas-phase TKE (normalized by the kinetic energy in the mean motions) with diameter ratio is shown for two different total solid volume fractions (0.3 and 0.4) at a mean flow Reynolds number of 50 in figure 7.2. The level of gas-phase TKE in monodisperse suspensions that have been quantified in chapter 3

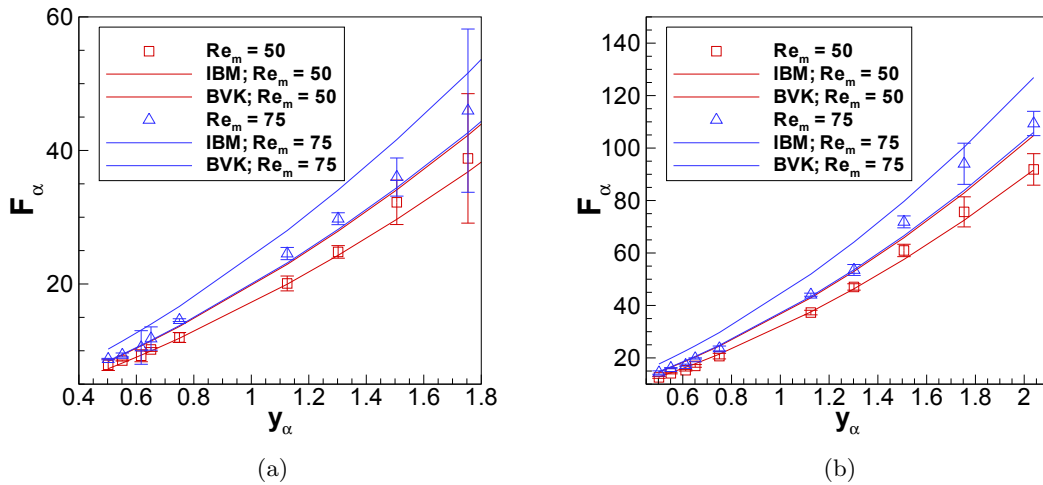


Figure 7.1 Plot showing the normalized force obtained from PUREIBM simulations of flow past bi-disperse particle assemblies at a total volume fraction of (a) 0.3 and (b) 0.4 for two mean flow Reynolds numbers ( $Re_m = 50$  and 75). Solid lines are obtained by substituting the monodisperse drag correlation obtained from PUREIBM simulations performed by Tenneti et al. (2011) for  $F(\phi, Re_m)$  in Eq. (7.12). Dashed lines are obtained by substituting the monodisperse drag correlation given by Beetstra et al. (2007) for  $F(\phi, Re_m)$  in Eq. (7.12). The normalized force is reported by averaging over 5 MIS and the error bars show 95% confidence intervals in the estimation of the normalized force.

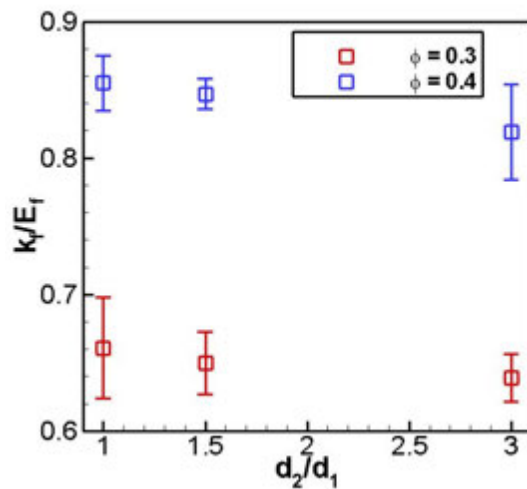


Figure 7.2 Behavior of  $k_f/E_f$  for bidisperse suspension with diameter ratio for two solid volume fractions (0.3 and 0.4) at a mean flow Reynolds number of 50.

is also shown for reference. It is clear that  $k_f/E_f$  strongly depends on the total solid volume fraction and it is not very sensitive to the diameter ratio. Therefore, we conclude that  $k_f/E_f$  in a polydisperse suspension is the same as the  $k_f/E_f$  observed in an equivalent monodisperse gas–solid suspension.

To summarize, interphase momentum transfer and gas–phase TKE have been quantified from PUReIBM DNS of flow past fixed random assemblies of bidisperse particles. It is observed that the correlations for drag and gas–phase TKE developed for monodisperse suspensions (chapters 2 and 3) can be extended seamlessly to polydisperse suspensions also. We now discuss the dynamics of bi–disperse suspensions with relative velocity between size classes.

#### 7.4 Bi-disperse suspensions with relative velocity between size classes

When all the particles move with the same velocity (zero relative velocity between size classes), we can make a Galilean-invariant (GI) frame transformation such that the particles are at rest in the new frame. Thus, performing fixed bed simulations is justified in the case of zero relative velocity between the size classes. However, fixed bed simulations for finite relative velocity between size classes are valid only in the limit of very low Reynolds number (Stokes flow regime). At moderate Reynolds numbers, we need to perform simulations of freely evolving suspensions to account for the finite slip between size classes. An important point to be noted is that the slip velocity between size classes is not an independent parameter.

The PUReIBM PR–DNS methodology has been used to simulate freely evolving monodisperse suspensions by solving the governing equations of motion in an accelerating frame of reference. This reference frame moves with the average velocity of the solid particles so that the particles do not travel in and out of the computational on an average. The frame acceleration appears as an additional force that sets the average velocity of the solids to be zero. Viewed from the laboratory frame, the force due to the frame acceleration can be thought of as an additional time dependent body force that acts on the system to keep the average solid velocity to be zero. Tenneti et al. (2010b) successfully applied this simulation methodology to perform simulations of freely evolving mono-disperse suspensions. This methodology has been extended to simulate freely evolving bi-disperse suspensions with the assumption that the density of the

size classes is the same.

The governing equations of motion solved in the freely evolving bi-disperse suspensions are given in Appendix E. The average solid velocity for each size class evolves because of the force exerted by the mean pressure gradient, the fluid-particle drag force, contact force due to collisions with particles belonging to other size classes and the pseudo force due to the frame acceleration. For a mono-disperse suspension, the mean solid velocity is not influenced by the collisional forces because the total force due to collisions is zero (Newton's third law). However, for poly-disperse suspensions collisions with particles belonging to other size classes affect the average velocity. In the simulations of poly-disperse suspensions, the accelerating frame of reference moves with the mixture mean velocity such that the mean mixture momentum is zero. The slip velocity between size classes 1 and 2 denoted  $\langle \mathbf{W}^{(2,1)} \rangle$  evolves according to the following equation:

$$\frac{d}{dt} \langle \mathbf{W}^{(2,1)} \rangle = \frac{1}{\rho_p V} \left[ \frac{1}{\phi_2} \mathbf{F}_{D-2} - \frac{1}{\phi_1} \mathbf{F}_{D-1} \right] + \frac{1}{\rho_p V} \left[ \frac{1}{\phi_1} + \frac{1}{\phi_2} \right] \mathbf{F}_{2-1}^C. \quad (7.13)$$

Here  $\mathbf{F}_{D-1}$  is the sum of the pressure and viscous forces acting on all the particles belonging to size class 1 and  $\mathbf{F}_{2-1}^C$  is the total contact force between particles of size classes 1 and 2. This equation says that the slip velocity between the two size classes will reach a steady state because of the balance between the drag and contact forces due to collisions between the size classes. It is not known *a priori* if such a balance exists or not. Besides the slip velocity another important quantity to observe is the granular temperature for each size class.

To answer these questions we performed PUReIBM simulations of a bi-disperse suspension at a nominal volume fraction of 0.2 and mean slip Reynolds number of 20. We considered equal volume fractions and a diameter ratio of 2. Both size classes have the same density and the solid to fluid density ratio is taken to be 100. Figure 7.3 shows the evolution of the slip velocity between the size classes. The slip velocity between size classes is defined as  $\langle \mathbf{u}^{(s,2)} \rangle - \langle \mathbf{u}^{(s,1)} \rangle$ . We can see that the magnitude of the slip velocity increases in time. During this time there are no collisions between the particles because the particles slowly gain energy from the fluid. When the collisions start the slip velocity appears to reach a dynamic steady state. We can also see from the figure that the granular temperature in each size class reaches a steady state.

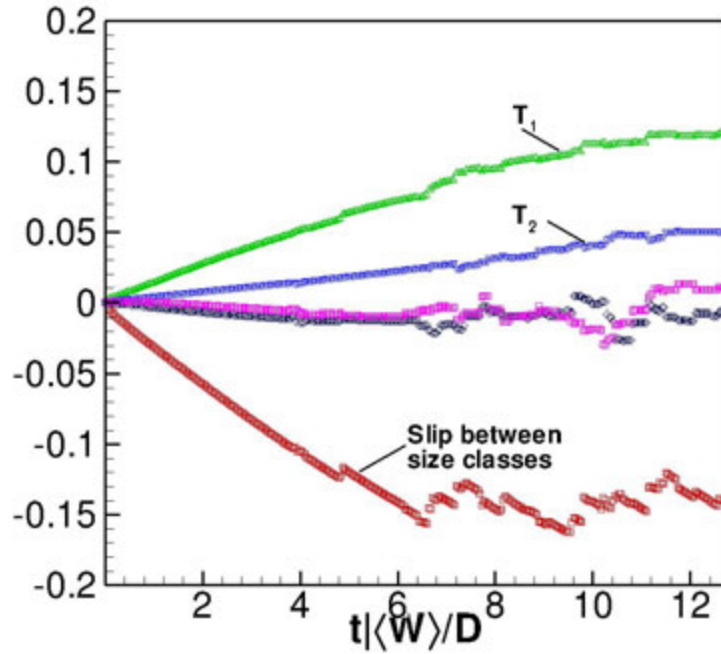


Figure 7.3 Evolution of slip velocity between size classes and granular temperature of each size class for a bi-disperse freely evolving suspension at a total solid volume fraction of 0.2, mean flow Reynolds number 20 and solid to fluid density ratio 100. In this simulation the volume fractions of the size classes are taken to be equal. Red symbols denote the streamwise component of the slip velocity while purple and black represent the cross-stream components of the slip velocity between the size classes.

The granular temperature for each size class is defined as

$$T_{\alpha} = \frac{1}{N_{\alpha}} \sum_{n=1}^{N_{\alpha}} \left( \mathbf{v}^{(n,\alpha)} - \langle \mathbf{u}^{(s,\alpha)} \rangle \right) \cdot \left( \mathbf{v}^{(n,\alpha)} - \langle \mathbf{u}^{(s,\alpha)} \rangle \right). \quad (7.14)$$

Thus, for a bi-disperse suspension once we fix the physical parameters of the problem, the slip velocity cannot be arbitrary and also one cannot provide a drag law by performing fixed bed simulations. Understanding the implications of the steady slip velocity attained between the size classes on modeling polydisperse gas–solid suspensions is a potential future work that has come out of this study.

## CHAPTER 8. Parallelization and scale-up of PReIBM (Particle-resolved Uncontaminated–fluid Reconcilable Immersed Boundary Method) for direct numerical simulation of gas–solid flows on petascale computers

This chapter describes the strategy used for the parallelization of the Particle–resolved Uncontaminated–fluid Reconcilable Immersed Boundary Method (PReIBM) approach for performing DNS of gas–solid flows in periodic domains on peta–scale computers. For performing particle–resolved simulations of gas–solid flow at high Reynolds numbers, the number of grid points across the diameter of the sphere has to be large enough so as to accurately resolve the thin boundary layers around the particles. Moreover large computational domain sizes are needed to understand to study multi–scale phenomena such as particle clustering. The amount of memory needed to perform such highly resolved simulations in large computational domains dictates the use of parallel computers. Designing a good parallel algorithm is also essential so as to obtain the solution in a reasonable amount of time.

The parallel PReIBM code has been successfully ported to the petascale computer Jaguarpf at Oak Ridge Leadership Computing Facility (OLCF). Several test cases are presented that confirm the accuracy of the parallel solver. An idealized riser with a solid volume fraction of 1% has been chosen to assess the weak scaling behavior of the solver. The parallel PReIBM solver shows an excellent scaling with increasing number of processors. The time taken to complete a time step increases only by 20% as the number of processors increases from 64 to 1024. We are able to successfully scale the PReIBM code to 12288 processors and it takes about 7.5 seconds to complete one time step. This performance implies that it takes only about 3 days to simulate physical times that correspond to the time taken by the flow to pass the entire length of the box (flow through time).

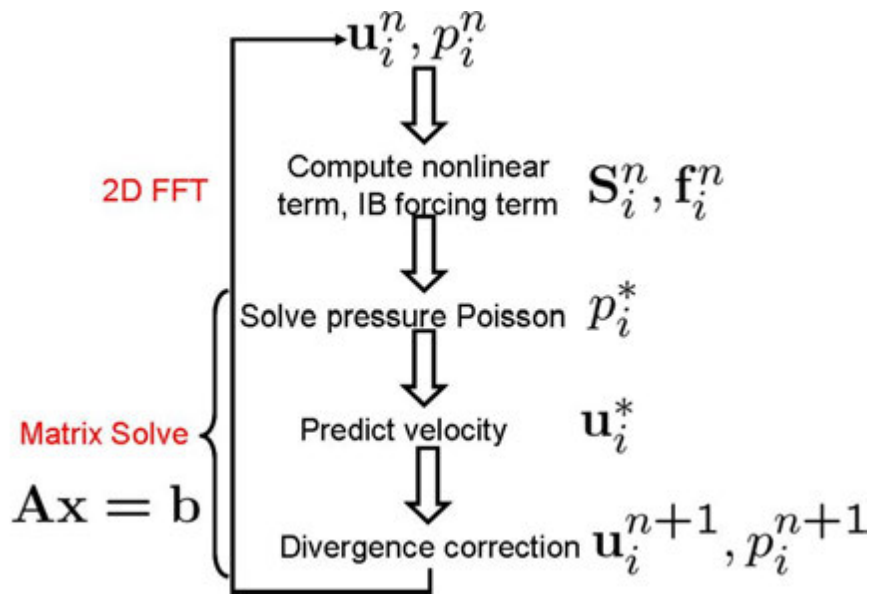


Figure 8.1 Schematic showing the serial algorithm of the PReIBM solver

### 8.1 Serial algorithm

The starting point of any parallelization effort is to understand the serial algorithm and identify the steps that can be performed in parallel. The numerical scheme used in PReIBM is a primitive-variable pseudo-spectral method. For temporal discretization we use Crank-Nicholson scheme for the viscous terms, and an Adams-Bashforth scheme for the convective terms. A predictor-corrector algorithm is employed to advance the velocity and pressure fields in time. Spatial discretization is performed using two dimensional Fourier transforms in the  $y$  and  $z$  directions, while finite differencing is used in the  $x$  direction. The steps involved in the serial algorithm are outlined in figure 8.1.

As shown in the figure, the velocity and pressure fields at a time level  $n$  are used to compute the convective and the immersed boundary forcing term. These terms are then used to predict the pressure and velocity. Since we are considering only incompressible flows, the condition for a divergence free velocity field is imposed to obtain the solution at the time level  $n+1$ . The use of Fast Fourier Transforms (FFT) in the  $y$  and  $z$  directions generates an independent system of linear equations for every point in the  $yz$  plane. These linear equations form a tridiagonal

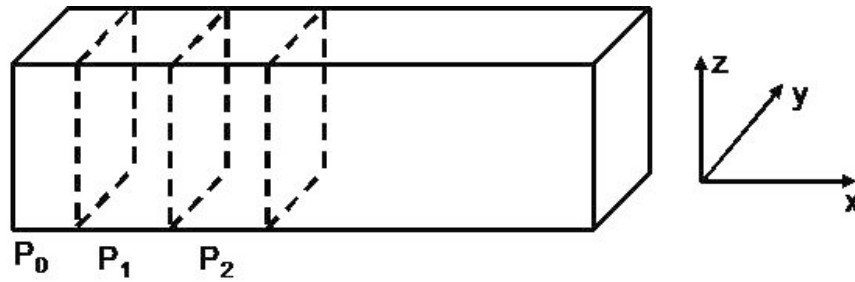


Figure 8.2 Schematic showing the partition of the domain in the PUREIBM solver.

system that needs to be solved for every point in the  $yz$  plane.

### Parallelization strategy

The first step in parallelization is domain decomposition. A major advantage of the PUREIBM code is the ability to solve for flow over complex geometries on a uniform Cartesian grid. The use of Cartesian meshes can be exploited to develop very efficient parallelization strategies. Since Fourier transforms are used in two directions, the simplest parallelization strategy is to decompose the domain in the direction in which finite differencing is used. Decomposition of Cartesian topologies is very straightforward and efficient subroutines are provided in any standard MPI implementation. A schematic describing the partition of the domain is shown in figure 8.2. At every  $x$  location the points in the  $yz$  plane lie completely on a single processor and so the steps involving FFTs behave exactly as the serial code. The two dimensional FFTs in PUREIBM are performed using the FFTW package. The multi-core architecture of peta scale machines can be exploited to achieve a better performance for the FFT step in the parallel code over its serial version. The FFTW package provides an option to perform the FFTs on more than one core in parallel. The strategy to perform the 2D FFTs using multiple threads in parallel has been implemented and tested in the PUREIBM code.

The present parallel implementation of PUREIBM is limited to stationary particles uniformly distributed in space. As a result load balancing of particles is not required and particles are allocated to a processor if their centres belong to it. A particle that cuts across two or more

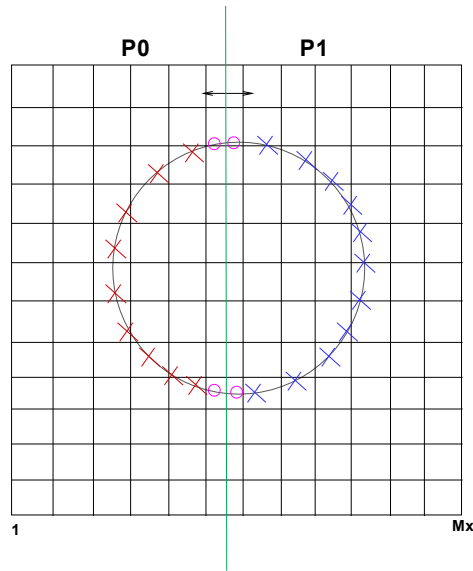


Figure 8.3 Figure shows the parallelization strategy for the immersed boundary method with two processors. The domain is partitioned in the  $x$ - direction. The partition boundary is shown by the green dashed line. A particle that cuts across two processors is handled by the processors in parallel. In IBM, the particle surface is represented by a finite number of points. These are shown by the crosses. The red crosses are the points which are handled by the processor  $P0$  and the blue crosses are handled by the processor  $P1$ . The points which belong to the grid cell that contains the partition boundary (shown by pink circles) are processed by both the processors.

processors is partitioned as shown in figure 8.3. Velocity and pressure fields computed on the grid nodes shown by dashed lines must be exchanged between the processors after every time step. These are enough for the computation of the forcing term on the particle surface. The immersed boundary forcing field is also exchanged in every time step.

The most important step in the parallelization that needs careful consideration is the parallel solution of the tridiagonal system. For every grid point in the  $yz$  plane the tridiagonal matrix that is generated is shown in figure 8.4. We also show how this matrix is distributed over the processors. The idea behind the parallelization strategy is that once the solution for the unknowns shown in the red boxes in figure 8.4 is known, the solution for the remaining unknowns can be computed locally on each processor. It can be seen that the unknowns shown

$$\mathbf{A} = \begin{bmatrix} b & a & 0 & . & . & . & . & . & a \\ a & b & a & . & . & . & . & . & 0 \\ 0 & a & b & a & . & . & . & . & 0 \\ \hline 0 & 0 & a & b & a & . & . & . & 0 \\ 0 & . & . & a & b & a & . & . & 0 \\ 0 & . & . & . & a & b & a & . & 0 \\ \hline 0 & . & . & . & . & a & b & a & 0 \\ 0 & . & . & . & . & . & a & b & a \\ a & 0 & . & . & . & . & 0 & a & b \end{bmatrix}$$

Figure 8.4 Form of the tridiagonal matrix that is inverted in the PUREIBM solver. The horizontal blue lines show the partition boundaries.

in red boxes lie on the boundary or interface between the processors. In order to solve for the unknowns that lie on the interface, we generate a system of equations that we refer to as the interface system. This interface system is generated by performing row operations on the part of the matrix that is available locally on a processor. It can be shown that this global interface system also is tridiagonal and diagonally dominant. So this procedure is numerically stable. The part of the interface system from each processor can be gathered on all processors and the resulting system can be solved sequentially on every processor. However, this process has to be repeated for every grid point in the  $yz$  plane and so the number of communication calls becomes very large and this might degrade the performance drastically. So we need to employ a different strategy to obtain the solution of the interface system.

We show the strategy that is used to solve the interface system in figure 8.5. Note that for every grid point in the  $yz$  plane, each processor generates two rows of the interface matrix. There are a total of  $N_y^2$  elements in the  $yz$  plane and these are arranged as rows in figure 8.5. Each column in the matrix shown in this figure denotes a processor. On every processor the elements in the  $yz$  plane are divided into a block of  $N_y^2/N$  elements, where  $N$  is the total number of processors. In order to solve the system for each of these elements in the block we need information from all the other processors. In other words, if we perform a transpose of the matrix shown in figure 8.5, we end up with a new matrix where the entire interface system

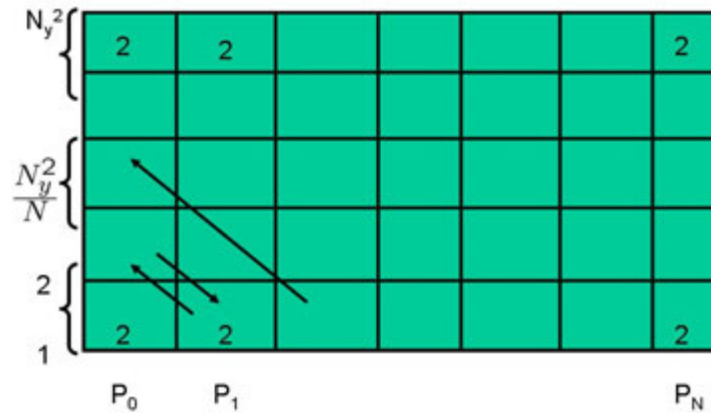


Figure 8.5 Schematic showing the transpose strategy used to solve the interface system. In this figure  $N_y^2$  denotes the number of grid points in the  $yz$  plane and  $N$  denotes the total number of processors.

for every element in the block is available completely on a single processor. For every element or point in the block, the interface system can be solved sequentially on every processor. In this way we achieve some parallelism even in the  $yz$  directions.

In the PReIBM code, the transpose of the matrix is performed using the ALLTOALL operation. Once the interface system is solved, the solution on each processor is arranged similarly in a matrix and a transpose of this matrix sends the solution elements to the corresponding processors. Once the solution to the interface elements is known, the remaining system of equations can be solved locally. In addition to the global communication calls described above, point-to-point communications are also needed between neighbor processors. Because of the use of space centered finite differences, every processor requires the solution on the first layer of grid nodes that lie adjacent to the partition boundaries on the neighboring processors and thus the solution after every time step must be exchanged with the neighboring processors. This point-to-point communication has been implemented using the asynchronous send/receive calls thus allowing for overlap of communication and computation.

Configuration	$\frac{D}{\Delta x}$	$\epsilon_1$	$\epsilon_2$	$\epsilon_3$	$\epsilon_4$
Simple	46.4	0.63271616E-14	0.86949156E-16	0.88190940E-16	0.41440159E-14
FCC	29.24	0.23248653E-14	0.62514764E-15	0.62624656E-15	0.13055491E-14
Random	15	0.30301074E-15	0.89068307E-16	0.11269121E-15	0.65079639E-16

Table 8.1 Error in the velocity and pressure fields between the serial and parallel versions of the PReIBM code for different configurations.

## 8.2 Validation

Validation of the parallel PReIBM code is performed by comparing the velocity and pressure fields with those obtained from the serial version for simple cubic (SC), face centered cubic (FCC) and random configurations at a Reynolds number (based on the mean slip velocity) of 20. In order to perform a quantitative comparison,  $L_1$  norm of the error between the serial and parallel solutions is extracted. Let the solution vector at any grid point be denoted  $\mathbf{Q} = (u, v, w, p)^T$ . If the solution from the serial version is denoted  $\mathbf{Q}^{(s)}$  and that from the parallel version is denoted  $\mathbf{Q}^{(p)}$ , then the error is defined as

$$\epsilon_l = \frac{1}{M_x N_y^2} \sum_{i=1}^{M_x} \sum_{j=1}^{N_y} \sum_{k=1}^{N_y} \left| Q_l^{(p)}(i, j, k) - Q_l^{(s)}(i, j, k) \right| \quad (8.1)$$

where  $M_x$  is the total number of grid points in the  $x$  direction. The values of the error are given in table 8.1

## 8.3 Performance

The test case that has been chosen to assess the performance of the PReIBM code is shown in figure 8.6. As shown in the figure, the test case used is an idealized riser with periodic boundaries in all three directions. The width of the box in the cross stream direction is denoted  $W$  and the length of the box in the stream wise direction is denoted  $L$ . The ratio of the width of the box to the particle diameter  $D$  is chosen to be 20.5. The solid volume

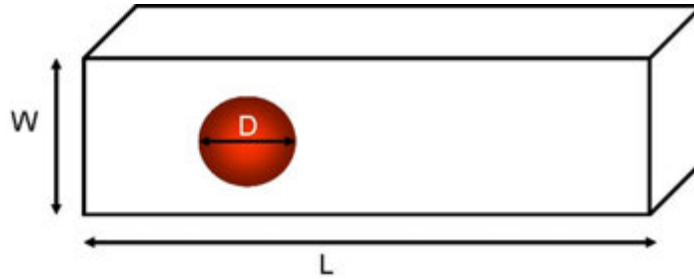


Figure 8.6 Schematic of the test case chosen to assess the performance of the parallel PReIBM code

fraction is 1% and the mean flow Reynolds number is 20. The number of grid points across the diameter of the particle is 25 and this grid resolution corresponds to 512 grid points in the cross stream direction. The challenge in particle-resolved DNS of gas-solid flow is to perform a highly accurate simulation of the largest possible problem in the shortest possible time. In this work we have chosen to report the weak scaling of the parallel PReIBM code. This is because in weak scaling, the problem size per processor is fixed and by increasing the number of processors, the total problem size increases. So we will use the timing tests to determine the time taken for the largest problem that can be solved using the PReIBM code.

The number of grid points in the stream wise direction per processor  $N_x$  is a variable parameter that should be chosen depending on the amount of memory available on the processor. For the problem chosen here, the maximum number of grid points that can be used per a processor of Jaguarpf is 8. This parameter determines the problem size that can be solved with a given number of processors. For  $N_x = 8$  the variation of the problem size and number of particles with the number of processors is shown in table 8.2. The test cases shown in table 8.2 are simulated with the PReIBM code and the maximum time taken to complete a time step among all the processors is averaged 10 time steps. This average value is reported as the time taken for the parallel code to complete one flow time step. As we can see from table 8.2, the minimum number of processors required to simulate a cubic box is 64. The time taken to simulate a single time step on 64 processors denoted  $T_{64}$  is taken as the reference. The performance of the parallel PReIBM code is reported in terms of  $T_N/T_{64}$ , where  $T_N$  is

No. of processors	$L/W$	No. of particles	$M_x$
64	1	164	512
128	2	328	1024
256	4	656	2048
512	8	1312	4096
1024	16	2624	8192

Table 8.2 Variation of the problem size and number of particles with increasing the number of processors with  $N_x = 8$ .

$L/W$	$N_x = 8(N)$	$N_x = 4(N)$
1	22.22 (64)	11.87 (128)
2	22.49 (128)	12.26 (256)
4	23.03 (256)	12.85 (512)
8	24.18 (512)	14.86 (1024)
16	26.19 (1024)	16.95 (2048)

Table 8.3 Comparison of the performance of PReIBM with  $N_x = 8$  and  $N_x = 4$ . The numbers in the paranthesis denote the number of processors.

the time taken to complete one time step using processors. The weak scaling performance of the parallel PReIBM code is shown in figure 8.7. It can be seen from the figure that the performance of the PReIBM solver is excellent with increasing number of processors. The time taken per time step increases only by 20% as the number of processors increases from 64 to 1024. In order to obtain the strong scaling of PReIBM, we also simulated the same test cases using  $N_x = 4$ . Table 8.3 compares the performance of the PReIBM code with  $N_x = 8$  and  $N_x = 4$ . The performance of the code is excellent up to a problem size of  $L/W = 4$  and drops slightly for the largest problem size of  $L/W = 16$ .

The performance tests shown so far are simulated using only MPI processes. The multi-core architecture of the petascale machines can be exploited to achieve a better performance by performing the Fourier transform that is used in PReIBM using multiple cores. The two dimensional FFTs in PReIBM are performed using the FFTW package. The FFTW package provides an option to perform the FFTs on more than one core in parallel. The strategy to

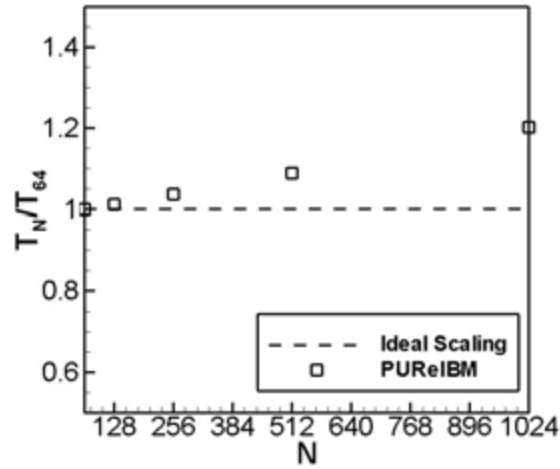


Figure 8.7 Weak scaling of the parallel PReIBM code with number of processors for the case of  $N_x = 8$ . Symbols show the time obtained from the PReIBM code while the dashed line shows the ideal behavior with no communication.

perform the 2D FFTs using multiple threads in parallel has been implemented in the PReIBM code. The largest problem with  $L/W = 16$  has been simulated using a total of 12288 processors. Out of the 12288 processors, 2048 are used (with  $N_x = 4$ ) for MPI tasks and the remaining processors are used for multi-threaded FFT. The time taken to complete one time step using this processor configuration is 7.5 seconds, which is a 60% improvement of the same problem solved using only MPI processes.

To summarize, the parallel PReIBM code has been ported successfully to the petascale computer Jaguarpf at Oak Ridge Leadership Computing Facility (OLCF). Several test cases were simulated to assess the weak scaling behavior of the solver. The parallel PReIBM solver shows an excellent scaling with increasing number of processors. We are able to successfully scale the PReIBM code to 12288 processors and it takes about 7.5 seconds to complete one time step. This performance implies that it takes only about 3 days to simulate physical times that correspond to the time taken by the flow to pass the entire length of the box (flow through time).

## CHAPTER 9. Future work

The long term objective of this work is to develop a fundamental understanding of the wide variety of complex phenomena observed in gas–solid flows and subsequently improve the theoretical description of gas–solid flows based on high fidelity numerical simulations. The PR–DNS methodology developed in this work has far–reaching implications in terms of the variety of problems that can be solved. In this thesis, the application of PR–DNS to study the flow past fixed and freely evolving statistically homogeneous polydisperse gas–solid suspensions is described. A more fundamental understanding of the properties of bi–disperse suspensions and implications on modeling polydisperse gas–solid flows is currently being pursued in our research group by Mohammad Mehrabadi. The framework developed to model interphase momentum transfer in homogeneous gas–solid flows is being applied to model the interphase momentum transfer in flows with particle clusters. Insights obtained from PR–DNS of heat transfer in gas–solid flows show the lack of separation of length scales. This motivates the development of more sophisticated large eddy simulation (LES) type approaches to simulate gas–solid flows. The required sub–grid scale closures for LES type calculations can be obtained from PR–DNS. Study of heat transfer in freely evolving and clustered gas–solid suspensions is another important direction that can be pursued with the approaches developed in this work. The heat transfer formulation described in this thesis is currently being extended by Bo Sun to study reactions and chemistry–pseudo–turbulent interactions in the gas–phase. Granular filtration of micron sized particles is being studied using the PR–DNS solution fields by Ravi Kolakaluri. Another important problem that is currently being pursued is the understanding of instabilities arising in gas–solid flows. The lack of separation of length scales that is inherent in gas–solid flows needs to be examined carefully in the development of a stability theory. This chapter lays the foundation for the development of metrics that are useful in analyzing

stability of systems that may not exhibit a separation of scales.

### 9.1 Stability of gas–solid suspensions with finite fluid inertia

It is well known that particles in gas–solid flow applications exhibit meso-scale structures such as clusters, streamers etc. The formation of such structures affects the average gas–solid drag, heat and mass transfer. For instance, particles that are in close proximity experience lesser fluid drag and hence travel faster when compared to isolated particles. This in turn affects the local fluid flow, and this coupling between the gas and the solid phase results in multiscale phenomena such as particle clustering. The theoretical foundations to describe the formation of meso-scale structures and accurate modeling of the effect of such structures on interphase interactions are important for predictive device-scale computational fluid dynamics (CFD) simulations.

The stability of the homogeneous base state of a fluidized bed has been studied by several researchers using a linear stability analysis. In this approach, the governing equations of motion that describe the gas and particulate phase are derived using either a volume–averaging (Anderson and Jackson, 1967) or ensemble–averaging procedure (Drew, 1983). The averaging procedure results in unclosed terms for interphase interactions such as average drag, particle phase pressure, source and dissipation of particle phase granular temperature, which are modeled. The models used for these unclosed terms determine a base state to which a sinusoidal perturbation is introduced. The perturbed equations are linearized and the response of the homogeneous base state to sinusoidal perturbations is studied.

Depending on the models used for the unclosed terms, different stability limits have been obtained. For instance Jackson (1963) neglected the particle pressure and obtained the result that a uniform fluidized bed is always unstable to particle concentration waves. Later, particle pressure was introduced (Anderson and Jackson, 1967; Batchelor, 1988) into the momentum equation of the particle phase and it was found to have a stabilizing effect.

Koch (1990) derived a kinetic theory for a dilute sedimenting monodisperse gas–solid suspension with negligible fluid inertia. From his stability analysis he found that a gas–solid suspension of highly inertial particles was unstable to all wavelengths of volume fraction per-

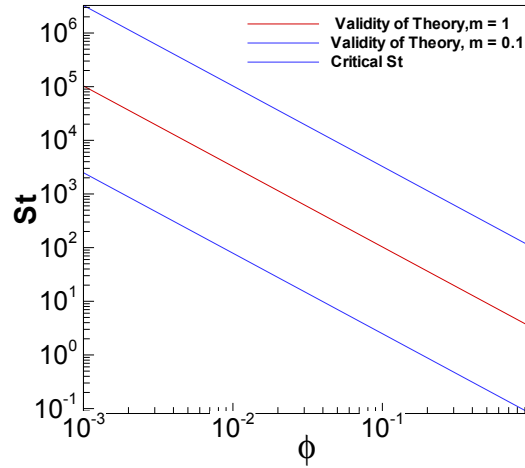


Figure 9.1 Plot showing the various regions of validity of Koch's analysis.

turbations. Stability limits have been derived for different regimes of Stokes numbers. These regimes are distinguished based on the ratio of the time between collisions  $\tau_{\text{coll}}$  to the viscous relaxation time  $\tau_{\text{vis}}$ . Suspensions of high Stokes number particles are dominated by collisions and the ratio  $m = \tau_{\text{coll}}/\tau_{\text{vis}}$  is less than unity. Depending on the value of  $m$  one can obtain different regimes where the theory for high Stokes number particles is valid. The regions of validity of the theory for different values of  $m$  (1 and 0.1) and the stability criterion are plotted together in figure 9.1. From the figure we can say that the highly massive suspension is always unstable. However, at a given volume fraction the critical Stokes number predicted by the theory (dashed line) is much less than the Stokes number above which the theory is valid. Koch and Sangani (1999) provided marginal stability limits for dense gas-solid suspensions in the Stokes flow regime. For particles with high inertia the uniform state is unstable to particle volume fraction waves with wavenumbers ranging between 0 and a maximum value.

Gas-solid flows are characterized by an intrinsic statistical variability in quantities such as the number of particles, or the volume occupied by the particles in any given region. Due to the inherent statistical variability in gas-solid flows we do not expect that the boundary of stability to be sharp as obtained from the linear stability analysis of averaged equations. Moreover, due to the linear stability analysis, the amplitude of the volume fraction waves does not affect the

stability limits. We now briefly describe the governing equations that are used in the linear stability analysis of gas–solid flows.

## 9.2 Instabilities in the averaged equations

As explained earlier, stability analysis is carried out on the averaged equations of motion. The generation of instabilities in the averaged state can be understood by analyzing the governing equations. In the analysis of Koch (1990) the conservation equations of mean mass, momentum and kinetic energy for the solid phase undergoing elastic collision in the Stokes flow regime are written along the direction of gravity as follows:

$$\begin{aligned}\frac{\partial \phi}{\partial t} + \frac{\partial}{\partial z} (\phi U) &= 0, \\ \frac{\partial U}{\partial t} + U \frac{\partial}{\partial z} (U) &= -\frac{\partial p_s}{\partial z} - \frac{R(\phi)U}{\tau} - g, \\ \frac{\partial T}{\partial t} + U \frac{\partial}{\partial z} (T) &= S(\phi) - \Gamma(\phi).\end{aligned}\tag{9.1}$$

In the above equations  $\phi$  is the solid volume fraction,  $U$  is the component of velocity along the direction of the acceleration due to gravity  $g$  and  $T$  is the granular temperature. The term  $R(\phi)$  appearing in the conservation of mean momentum is the drag coefficient that is only a function of the solid volume fraction in the Stokes flow regime. the hydrodynamic source and dissipation of granular temperature denoted by  $S$  and  $\Gamma$  also depend only on the solid volume fraction.

Instabilities in the volume fraction field that obeys Eq. (9.1) arise from a variety of coupled physical mechanisms, including: (a) the dependence of mean drag on volume fraction, (b) reduction of particle granular temperature due to viscous dissipation in the fluid, (c) reduction of particle granular temperature due to particle-particle interactions, and (d) production of granular temperature due to particle-neighbor interactions, which might have a stabilizing effect. The preceding discussion gives rise to several open questions, some of which are discussed here. Each question is followed by a discussion of the working hypothesis.

1. Q1. What are the stability limits for suspensions with finite fluid inertia from average equations?

*Hypothesis:* Stability limits for suspensions with finite fluid inertia can be inferred from average equations along the lines of the theory by Koch (1990) for Stokes flow regime. However, stability limits for suspensions at moderate Reynolds numbers depend on the dependence of the mean drag on the solid volume fraction as well as mean flow Reynolds number. The closure models for the interphase momentum transfer and the source and dissipation of granular temperature obtained from PR–DNS of gas–solid suspensions at moderate Reynolds numbers in this work can be used to infer stability limits in the regime of finite fluid inertia. Although linear stability analysis can be applied in principle, one has to verify the assumptions involved in applying the average equations and the stability analysis.

2. Q2. What is the mechanism of generation of instabilities in initially homogeneous gas–solid suspensions in periodic domains?

*Hypothesis:* It is important to see from PR–DNS if initially homogeneous gas–solid suspensions demonstrate large scale inhomogeneity in the volume fraction field in sufficiently large periodic domains. Firstly, periodic domains are useful since the natural inhomogeneity present in wall bounded flows is eliminated. In such situation the origin of instabilities is purely from the microscale (see section 9.3 for an elaboration of this hypothesis). The stabilization or destabilization of the suspension purely depends on the dependence of the mean drag force on the local volume fraction fluctuations. The hypothesis is that local rearrangements of the particles perturbs the pair correlation function and in turn changes the level of volume fraction fluctuations (see section 9.4 for details). The dependence of the mean drag on the intensity of local volume fraction fluctuations in a measurement volume determines the stability properties of the gas–solid flow. This question then leads to the following two questions that are discussed next.

3. Q3. What is the dependence of the mean drag force on the pair correlation function?

*Hypothesis:* From the preceding discussion, we hypothesize that the mean drag force depends on the local arrangements of the particles. The pair correlation function  $g(r)$  is a measure of the local arrangement of the particles. It is important to determine the

dependence of the mean gas–solid force on the pair correlation function. As a first step to study this dependence, frozen particle configurations corresponding to different pair correlation functions will be generated and the mean drag will be computed by simulating flow past such fixed configurations using PR–DNS.

4. Q4. What is the role of amplitude of perturbations of the solid volume fraction?

*Hypothesis:* In linear stability analysis the amplitude of perturbation of the solid volume fraction does not play any role in determining the stability properties of the flow. The hypothesis is that if the amplitude of perturbations of the solid volume fraction is small compared to the natural level of volume fraction fluctuations, such perturbations might not lead to development of instabilities. This question can be answered by performing carefully designed simulations in which the initial configurations are such that the local volume fraction fluctuations exceed the base state. If such perturbations to the volume fraction field generates instabilities then it warrants a nonlinear theory for stability. It is clear that in order to answer these questions, we need a measure or a metric to quantify the local volume fraction fluctuations. The origin of fluctuations in the volume fraction, and a metric for these fluctuations that accounts for the multiscale nature of gas–solid flow are discussed in detail in section 9.4.

5. Q5. What is the appropriate continuum formulation for non scale separated gas–solid flow systems?

*Hypothesis:* The existing conituum theories for gas–solid flow employ a differential or strong formulation that relies on the continuum hypothesis or the assumption of a separation of length scales. Given that there is considerable evidence to indicate that there is no separation of scales in clustering gas–solid suspensions, an alternative approach is warranted. We hypothesize that an integral or weak formulation is the appropriate approach for non scale separated gas–solid systems. The integral formulation of balance laws always holds, even if there is no separation of scales. The basis for the weak formulation is the formulation of conservation laws of mass, momentum and energy in a control volume (or a measurement volume). In such formulation the strength of volume

fraction fluctuations in a measurement volume becomes important. The analysis on the local volume fraction fluctuations lays the foundation for exploring the development of a continuum theory for non scale separated gas–solid flows based on the weak formulation.

In the following sections we describe the progress made in answering the questions that are formulated above. In particular we elaborate on hypothesis for the generation of instabilities, the development of a multiscale metric to characterize the level of volume fraction fluctuations and a discussion on the formulation of a continuum theory based on the weak formulation.

### 9.3 Mechanism of generation of instabilities

Instabilities in a gas–solid flow can be induced from the microscale or due to gradients in the volume fraction at the macroscale. Instabilities at the microscale can arise from a variety of mechanisms that induce particle clustering. These mechanisms include both particle–particle interactions such as inelastic collisions, cohesive forces and electrostatic interactions, and particle–fluid hydrodynamic interactions such as neighbor particle interactions including particle shielding, and enhanced local energy dissipation in the fluid due to viscous effects. Since many of these microscale interactions are averaged out in EE formulations, it is not clear if a stability analysis of the averaged equations reflects the instabilities observed in individual realizations of the flow through experiment, PR–DNS or an LE simulation with a model for the particle drag and collisions. Large scale gradients in the volume fraction field such as those found in wall bounded flows can also give rise to instabilities. The source of instability in this case is from the macroscopic scales. It is therefore important to distinguish between statistically homogeneous and inhomogeneous gas–solid flows.

*Statistically homogeneous suspensions:* As explained in the preceding section, the basic approach of a linear stability analysis of the averaged equations is to perturb the homogeneous base state of the governing equations. There are a few subtle points here that need to be examined carefully. Firstly, the set of equations on which the stability analysis is performed is derived by averaging and implicitly assumes scale separation. It is assumed that the macroscopic quantities such as the solid volume fraction vary on length scales that are much larger

than the length scales over which the underlying microstructure of the particles varies. Therefore, when the system is perturbed the perturbations also should vary on macroscopic length scales in order for the continuum description to be valid. A natural question that arises in this context is regarding the origin of these large scale perturbations in a homogeneous suspension. If no perturbations are imposed, a homogeneous suspension cannot exhibit volume fraction instabilities. This has been confirmed in the recent device-scale simulations performed using both the Quadrature Based Moment Methods (QBMM) and the Eulerian–Eulerian two-fluid model by Passalacqua et al. (2010). A homogeneous gas-solid suspension with no imposed perturbations can become unstable if the fluctuations in the number and volume occupied by the particles at the microscale affect the meso and macroscale quantities. These fluctuations would manifest in the pair–correlation or structure factor, but the average number density (or volume fraction) of the suspension is spatially uniform.

*Wall bounded flows:* In a real experiment, the gas-solid flow is bounded by walls. When particles undergo inelastic collisions with walls, they lose their energy and start to form aggregates near the wall. The formation of large particle clusters near the walls has been observed in recent high speed images of gas-solid flow in fluidized bed risers. For the purpose of stability analysis, wall bounded flows are in a naturally perturbed state. In this scenario, the linear stability analysis needs to be performed by applying the right boundary conditions on the perturbed variables and this might lead to different stability limits.

As a first step we restrict our focus to the stability of homogeneous gas–solid suspensions. PR–DNS captures particle-fluid, particle-particle and neighbor interactions accurately and the flow is completely characterized and hence the stability of gas–solid flows at the microscale can be investigated rigorously. We first study the effect of the state of microstructure on the stability of homogeneous gas-solid suspensions.

### 9.3.1 PR–DNS of freely evolving suspensions with finite fluid inertia

To investigate the evolution of the microstructure we performed PR–DNS of freely evolving gas-solid suspensions with finite fluid inertia. We performed two types of simulations. In simulations of the first type, particles are initialized according to an equilibrium hard-sphere

microstructure. Initially the particles are fixed and a steady flow is established through the fixed assembly by imposing a pressure gradient. After the flow reaches a steady state, the particles were allowed to move according to the force acting on them due to the fluid. This hydrodynamic force is computed by integrating the fluid stress tensor over the particle surface. Inter-particle collisions are handled through a soft-sphere approach.

After the particle–phase granular temperature reaches a statistically stationary state, the pair correlation function  $g(r)$  is computed by averaging over different snapshots of the simulation. The  $g(r)$  for three different coefficients of restitution is shown in Fig. 9.2(a). There is no significant change in the equilibrium microstructure. We have verified that this is very close to the equilibrium pair correlation function of a hard sphere system. This result is consistent with the observation of Koch and Sangani (1999) that at higher particle inertia, the effect of the fluid on the particles is not very significant and hence the system behaves like a granular gas. Moreover, in this situation there is a source of particle granular energy due to hydrodynamic interactions. Therefore, this gas-solid system is less likely to exhibit clustering than an inelastic granular gas, where the continuous dissipation of granular energy due to inelastic collisions causes the particles to cluster in regions of low granular temperature. However, in the presence of a fluid, the granular temperature reaches a statistically stationary state where the source and dissipation of energy due to hydrodynamic effects nearly balance each other. We have verified that the collisional dissipation is very small compared to the viscous dissipation, and hence there is no significant change in the pair correlation function even for inelastic particles. Hence, local particle clustering is not observed in these simulations.

Note that the simulation times for these cases are small compared to those of inelastic granular gases in which significant clustering is observed. While it is easy to perform event-driven simulations of inelastic granular gases for fairly long physical times ( $O(10^4)$  collision times), it is computationally very expensive to perform PR–DNS of freely evolving suspensions for similar lengths of time. This is because, in event driven simulations, only the collision events are tracked and hence it is inexpensive to track about  $10^4$  collisions. However, in PR–DNS, the time between the collisions is also resolved in order to resolve the fluid flow accurately and therefore simulating such long physical times is computationally prohibitive.

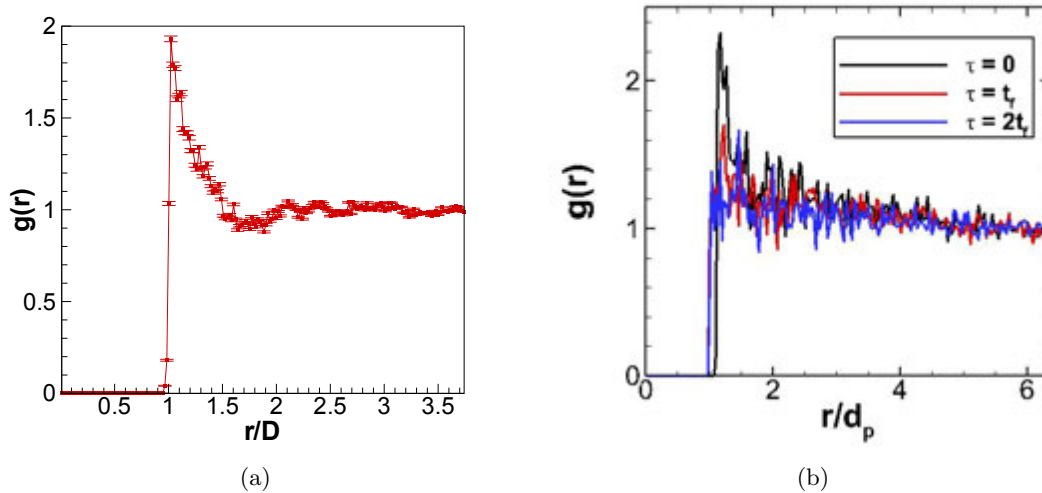


Figure 9.2 (a) Pair correlation function obtained from PR-DNS of freely evolving gas-solid suspensions corresponding to a solid volume fraction of 0.2, mean flow Reynolds number of 20 and solid to fluid density ratio of 100. These parameters correspond to a Stokes number of 278. These simulations have been performed for three different coefficients of restitution. ((b))Pair correlation function at three different times obtained from PR-DNS of gas-solid suspension at a solid volume fraction of 0.05, mean flow Reynolds number of 50 and solid to fluid density ratio of 100. The Stokes number of the suspension is 694. Initial configuration is taken from an inelastic granular gas simulation and the later times are one and two flow through times of the periodic box respectively.

Since it is difficult to perform PR–DNS of freely evolving suspensions for physical times comparable to the time required for the formation of clusters in an inelastic granular gas, we designed the second type of simulations such that we could investigate the evolution from an initially clustered microstructure. We used four different particle configurations from an inelastic granular gas simulation that is deep in the clustering regime. The evolution of the microstructure is tracked in time. Figure 9.2(b) shows the pair correlation function at three different time snapshots. The value of the pair correlation function at contact for the initial time is quite high indicating a clustered configuration. However, as the particles evolve, we see that the microstructure evolves to a non-clustered configuration. Further investigation into the generation of instabilities from the microscale is needed and this hypothesis is dented H2.

#### **9.4 Multiscale metrics for characterizing statistically homogeneous gas–solid flows**

Gas–solid flows are characterized by an intrinsic statistical variability in quantities such as the number of particles, or the volume occupied by the particles in any given region. Furthermore, phenomenon such as particle clustering lead the breakdown of the separation of length scales. Therefore, there is a need to develop metrics that characterize the level of clustering as well as the shape and size of clusters that are valid even in systems that do not exhibit scale separation. Given the inherent statistical variability in gas–solid flows it is natural to use statistical metrics to characterize particle clustering, and these can then be incorporated into statistical theories. In order to connect the physical mechanisms to cluster metrics, there is a need for a unifying framework in which any clustering mechanism and its outcome can be described. In the following section we develop a multiscale statistical metric and connect it to the two–particle distribution function.

##### **9.4.1 Local volume fraction fluctuations in statistically homogeneous gas–solid flows**

Gas–solid flows are characterized by an intrinsic statistical variability in quantities such as the number of particles, or the volume occupied by the particles in any given region. Moreover,

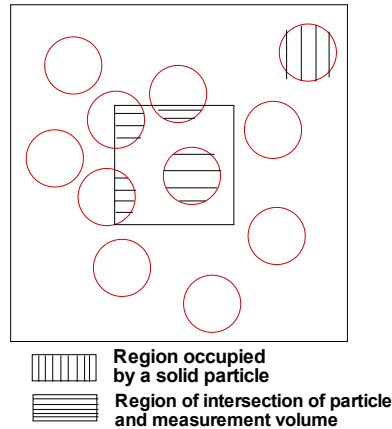


Figure 9.3 Schematic showing the intersection of solid particles with the measurement region. The region of space occupied by the solids is hatched with vertical lines. The region of intersection of the solid particles with the measurement region is hatched with horizontal lines.

formation of clusters leads to a lack of separation of length scales. Therefore, the inherent statistical variability present in the volume occupied the particles in any region or “measurement region” needs to be characterized in a statistically homogeneous suspension.

In this context we introduce the concept of “measurement region”. A measurement region is a region of arbitrary shape and fixed size in the gas-solid flow domain. It can be thought of as an observation window or frame in an experiment. The size of the measurement region sets the length scale of investigation. Hence the length scale information is contained in the size of the measurement region. We define statistical measures to characterize level of local volume fraction fluctuations in a measurement region. A schematic with the measurement region in the flow domain is shown in Fig. 9.3. The solid phase is represented by the indicator function  $I_s(\mathbf{x})$  which is unity if the point  $\mathbf{x}$  lies in the solid phase and zero otherwise. The solid phase volume fraction fluctuations in any measurement volume  $\mathcal{V}_m$  depend on the microstructure or the particle configuration. It is useful to define the one-point and two-point probability

functions  $S_1(\mathbf{x}_1)$  and  $S_2(\mathbf{x}_1, \mathbf{x}_2)$  as follows:

$$\begin{aligned} S_1(\mathbf{x}_1) &= \langle I_s(\mathbf{x}_1) \rangle \\ S_2(\mathbf{x}_1, \mathbf{x}_2) &= \langle I_s(\mathbf{x}_1) I_s(\mathbf{x}_2) \rangle. \end{aligned} \quad (9.2)$$

Here  $S_1$  is the probability of finding a point in the solid phase. For statistically homogeneous gas–solid suspensions this quantity is equal to the volume fraction of the solid phase  $\phi$ . The quantity  $S_2(\mathbf{x}_1, \mathbf{x}_2)$  is the probability of finding two points  $\mathbf{x}_1$  and  $\mathbf{x}_2$  simultaneously in the solid phase (Torquato and Stell, 1982; Sundaram and Collins, 1994). For statistically homogeneous and isotropic gas–solid suspensions,  $S_2$  is only a function of the magnitude of the separation between the points i.e.,  $S_2(\mathbf{x}_1, \mathbf{x}_2) = S_2(|\mathbf{x}_1 - \mathbf{x}_2|)$ . Two limits of this function are of interest. When the separation between the points is very small,  $S_2 \rightarrow \phi$  and when the separation becomes very large  $S_2 \rightarrow \phi^2$ .

The inherent statistical variability in the volume fraction of the solid phase can be characterized in terms of the variance of the local volume fraction in a given measurement volume. In order to perform this calculation, the local volume fraction (Quintanilla and Torquato, 1997) in a measurement volume centered at location  $\mathbf{x}$  is defined as

$$\varepsilon(\mathbf{x}) = \frac{1}{V_m} \int_{\mathcal{V}_m^{\mathbf{x}}} I_s(\mathbf{x}) d\mathbf{x}. \quad (9.3)$$

When the measurement volume is large i.e.,  $V_m \rightarrow \infty$  the local volume fraction tends to the volume fraction of the solid phase. At the other extreme when the measurement volume becomes very small, the local volume fraction becomes the indicator function of the solid phase at the point  $\mathbf{x}$ .

It is useful to express the local volume fraction in terms of volume integrals over the entire domain. The physical domain is deterministic and so the expectation operator and the integral operator commute. In order to define the local volume fraction as an integral over the whole domain, we define an indicator function for the measurement region as follows:

$$I_{\mathcal{V}^{\mathbf{x}}}(\mathbf{y}) = \begin{cases} 1 & \text{if } \mathbf{y} \in \mathcal{V}_m^{\mathbf{x}} \\ 0 & \text{otherwise.} \end{cases} \quad (9.4)$$

From the definition it is clear that  $I_{V^x}(\mathbf{y}) = I_{V^0}(\mathbf{y} - \mathbf{x})$ . Therefore, the indicator function of a measurement region centered at any point  $\mathbf{x}$  is written in terms of the indicator function of the measurement region centered at origin. With this definition, the local volume fraction in a measurement region centered at a point  $\mathbf{x}$  can be written as

$$\varepsilon(\mathbf{x}) = \frac{1}{V_m} \int_V I_s(\mathbf{y}) I_{V^0}(\mathbf{y} - \mathbf{x}) d\mathbf{y}. \quad (9.5)$$

It is clear that the expected value of the local volume fraction is nothing but the volume fraction of the solid phase. A measure of the local volume fraction fluctuations can be obtained by examining the ratio of the standard deviation of the local volume fraction and the solid phase volume fraction. This ratio  $k_\phi = \sigma_\varepsilon/\phi$  gives a measure of the nonuniformity of the local volume fraction. Here, the standard deviation of the local volume fraction is defined as  $\sigma_\varepsilon^2 = \langle \varepsilon^2 \rangle - \phi^2$ . It is instructive to examine the limits of the intensity of volume fraction fluctuations  $k_\phi$ . For large measurement volumes,  $k_\phi \rightarrow 0$ . For very small measurement volumes  $\sigma_\varepsilon^2 \rightarrow \phi - \phi^2$  and hence  $k_\phi \rightarrow \sqrt{\frac{1-\phi}{\phi}}$ .

We now derive the relationship between the standard deviation of the local volume fraction and the two-point correlation function  $S_2$ . The expected value of the square of the local volume fraction fluctuations is given by:

$$\begin{aligned} \langle \varepsilon^2 \rangle &= \frac{1}{V_m^2} \left\langle \int_V I_s(\mathbf{y}) I_{V^0}(\mathbf{y} - \mathbf{x}) d\mathbf{y} \int_V I_s(\mathbf{z}) I_{V^0}(\mathbf{z} - \mathbf{x}) d\mathbf{z} \right\rangle \\ &= \frac{1}{V_m^2} \int_V \int_V \langle I_s(\mathbf{y}) I_s(\mathbf{z}) \rangle I_{V^0}(\mathbf{y} - \mathbf{x}) I_{V^0}(\mathbf{z} - \mathbf{x}) d\mathbf{y} d\mathbf{z} \\ &= \frac{1}{V_m^2} \int_V \int_V S_2(\mathbf{y}, \mathbf{z}) I_{V^0}(\mathbf{y} - \mathbf{x}) I_{V^0}(\mathbf{z} - \mathbf{x}) d\mathbf{y} d\mathbf{z}. \end{aligned} \quad (9.6)$$

Since the gas–solid flow is homogeneous,  $S_2(\mathbf{y}, \mathbf{z}) = S_2(\mathbf{y} - \mathbf{z})$ . Now invoking a transformation  $\mathbf{r} = \mathbf{y} - \mathbf{z}$ , we see that

$$\begin{aligned} \langle \varepsilon^2 \rangle &= \frac{1}{V_m^2} \int_{V_r} S_2(\mathbf{r}) \int_V I_{V^0}(\mathbf{y} - \mathbf{x}) I_{V^0}(\mathbf{y} - (\mathbf{x} + \mathbf{r})) d\mathbf{y} d\mathbf{r} \\ &= \frac{1}{V_m^2} \int_{V_r} S_2(\mathbf{r}) V_2^{\text{int}}(\mathbf{r}) d\mathbf{r}. \end{aligned} \quad (9.7)$$

In the above expression,  $V_2^{\text{int}}(\mathbf{r})$  is the volume of intersection of two measurement regions separated by  $\mathbf{r}$ . This is because,  $I_{V^0}(\mathbf{y} - \mathbf{x})$  is the indicator function of a measurement volume

centered at  $\mathbf{x}$ . Similarly,  $I_{\mathcal{V}^0}(\mathbf{y} - (\mathbf{x} + \mathbf{r}))$  is the indicator function of a measurement region centered at the point  $\mathbf{x} + \mathbf{r}$ . Hence the volume integral

$$V_2^{\text{int}}(\mathbf{r}) = \int_{\mathcal{V}} I_{\mathcal{V}^0}(\mathbf{y} - \mathbf{x}) I_{\mathcal{V}^0}(\mathbf{y} - (\mathbf{x} + \mathbf{r})) d\mathbf{y} \quad (9.8)$$

gives the volume of intersection of these two measurement regions. This volume of intersection depends on the shape and size of the measurement regions. From the definition of the intersection volume, it is clear that  $\int_{\mathcal{V}_r} V_2^{\text{int}}(\mathbf{r}) d\mathbf{r} = V_m^2$ . Therefore, the variance of volume fraction fluctuations can now be written as

$$\begin{aligned} \sigma_\varepsilon^2 &= \frac{1}{V_m^2} \int_{\mathcal{V}_r} S_2(\mathbf{r}) V_2^{\text{int}}(\mathbf{r}) d\mathbf{r} - \phi^2 \\ &= \frac{1}{V_m^2} \int_{\mathcal{V}_r} S_2(\mathbf{r}) V_2^{\text{int}}(\mathbf{r}) d\mathbf{r} - \phi^2 \frac{1}{V_m^2} \int_{\mathcal{V}_r} V_2^{\text{int}}(\mathbf{r}) d\mathbf{r} \\ &= \frac{1}{V_m^2} \int_{\mathcal{V}_r} [S_2(\mathbf{r}) - \phi^2] V_2^{\text{int}}(\mathbf{r}) d\mathbf{r}. \end{aligned} \quad (9.9)$$

Therefore, the final expression for the intensity of volume fraction fluctuations becomes

$$k_\phi = \frac{1}{\phi V_m} \left[ \int_{\mathcal{V}_r} [S_2(\mathbf{r}) - \phi^2] V_2^{\text{int}}(\mathbf{r}) d\mathbf{r} \right]^{1/2}. \quad (9.10)$$

We can connect the intensity of local volume fractions to the pair correlation function by relating  $S_2(\mathbf{r})$  to  $g(\mathbf{r})$ . This relationship has been derived rigorously by several researchers (Torquato and Stell, 1982; Sundaram and Collins, 1994). For a system of non overlapping spheres that are distributed corresponding to a homogeneous number density  $n$  and a pair correlation function  $g(\mathbf{r})$ , the function it can be shown that

$$S_2(\mathbf{r}) - \phi^2 = nI(\mathbf{r}) + n^2 \int h(\mathbf{z}) I(\mathbf{r} - \mathbf{z}) d\mathbf{z}. \quad (9.11)$$

In this expression  $h(\mathbf{z}) = g(\mathbf{z}) - 1$  is the total correlation function and  $I(\mathbf{r})$  is the volume of intersection of two spheres whose centers are separated by a vector  $\mathbf{r}$ .

From the results of PR-DNS it is found that the microstructure of a stable homogeneous gas-solid suspensions corresponds to that of an equilibrium hard sphere configuration. By computing the strength of volume fraction fluctuations for an equilibrium hard sphere configuration we can determine the base value of the volume fraction fluctuations.

## 9.5 Correct governing equations for stability analysis

When considering the stability of suspensions it is customary to analyze the stability of the averaged equations that are written in a differential or strong form. This differential or strong formulation relies on the continuum hypothesis, or in other words it assumes separation of scales. Given that there is considerable evidence to indicate that there is no separation of scales in clustering gas-solid suspensions, an alternative approach is warranted. Note that the integral or weak formulation of balance laws always holds, even if there is no separation of scales. For instance the conservation of mass can be written in weak form as:

$$\frac{\partial}{\partial t} \int_{V_m} \langle \phi \rangle dV = - \oint_{A_m} \langle \mathbf{J}_\phi \rangle \cdot \mathbf{n} dA \quad (9.12)$$

where  $\langle \mathbf{J}_\phi \rangle = \langle \phi \mathbf{v} \rangle$ . This average flux can be decomposed as  $\langle \mathbf{J}_\phi \rangle = \langle \mathbf{v} \rangle \langle \phi \rangle + \langle \mathbf{v}' \phi' \rangle$ . In the absence of scale separation, the correlation between the velocity fluctuations and volume fraction fluctuations is not statistical error in the estimation of the mean flux, but is a physically meaningful quantity. However, it is neglected in existing stability theories. The instabilities in the strong form of the mean mass conservation equation have their origin in the dependence of the average drag on the average solid volume fraction. The importance of fluctuations in volume fraction in clustering particle suspensions raises an important question regarding the dependence of drag statistics on volume fraction fluctuations. The weak formulation poses new challenges in modeling and PR-DNS can play a pivotal role in the development of models that are relevant to this formulation.

## CHAPTER 10. Conclusions

Gas–solid flows are an important class of multiphase flows that are frequently encountered in engineering applications. Understanding the physical mechanisms of momentum, kinetic energy and heat transfer between the gas–phase and the solid particles is a crucial step in the design process. Furthermore, since CFD simulations of gas–solid flow are increasingly being used in the design process, development of accurate mathematical models for these interphase transfer phenomena that can be used in gas–solid CFD simulations is very important. In this work we studied the interphase momentum, kinetic energy and heat transfer by accounting for the key characteristics of gas–solid flows such as polydispersity, gas–phase velocity fluctuations, and particle velocity fluctuations, using particle–resolved direct numerical simulation (PR–DNS) approach.

We developed the Particle–resolved Uncontaminated–fluid Reconcilable Immersed Boundary Method (PUREIBM) and demonstrated that it is a viable method for understanding gas–solid flow physics as well as for model development. The salient features of this method that make it appropriate for PR–DNS of gas–solid flow are: (i) the unmodified NSE are solved in the fluid phase, (ii) it is reconcilable with statistical theories, (iii) numerically convergent and (iv) gives Galilean–invariant numerical solutions to the underlying physical problem. We have rigorously established the connection between the PUREIBM solution and the unclosed terms that need to be modeled in the statistical approaches of gas–solid flows.

We studied interphase momentum transfer in both mono and bi–disperse gas–solid suspensions using PUREIBM PR–DNS of flow past fixed particle assemblies. We developed a new high resolution monodisperse drag correlation based on the insights into the scaling of pressure and viscous contributions to drag from PR–DNS. In bi–disperse suspensions we found that the polydispersity correction for the drag force proposed by Beetstra et al. (2007) is valid, but a

high resolution monodisperse drag correlation such as the one developed in this work is needed in order to obtain an accurate polydisperse drag law.

Gas-phase velocity fluctuations arising from the interaction between particles and mean slip velocity in laminar gas-solid flows have been investigated using PR-DNS. We quantified the kinetic energy associated with the fluctuating motions in the gas-phase and found that it is a significant fraction of energy associated with the mean slip velocity. We developed an eddy viscosity that can be used for modeling the gas-phase Reynolds stress in gas-solid CFD calculations.

The effect of the fluid-dynamic forces on particle velocity fluctuations and vice versa has been studied by performing PR-DNS of freely evolving gas-solid suspensions. PR-DNS data indicate that a stochastic model is necessary for the particle acceleration in order to capture the correct evolution of particle granular temperature. A Langevin model is proposed for the increment in the particle velocity and the model parameters have been related to the source and dissipation of particle granular temperature. We have developed a method to uniquely identify the source and dissipation of granular temperature from PR-DNS, and specified the model parameters as functions of solid volume fraction, mean slip Reynolds number and solid-to-fluid-density ratio.

A novel PR-DNS methodology has been developed to study forced convective heat transfer in fixed assemblies of isothermal particles in periodic domains. This formulation accounts for the fluid heating (or cooling) by particles. It is found that fluid heating is important and can occur on scales of a particle diameter in certain parameter ranges thereby precluding scale separation necessary for averaged models.

A parallel implementation of PReIBM has been designed and implemented as a part of this work. This parallelization strategy allows PR-DNS of large problems on peta scale supercomputers. The PR-DNS methodology developed in this work has far-reaching implications in terms of the variety of problems that can be solved and paves the way for the long term objective of developing a fundamental understanding of the wide variety of complex phenomena observed in gas-solid flows and subsequently improve the theoretical description of gas-solid flows based on high fidelity numerical simulations.

**APPENDIX A. Simplification of the covariance of fluctuating velocity and gradient of stress tensor to dissipation in statistically homogeneous gas–solid flow**

the conservation equation for  $k_f$  in statistically homogeneous flows is written as

$$\frac{\partial}{\partial t}\{(1 - \phi)\rho_f k_f\} = -\left\langle u_i''(f)\tau_{ji}n_j^{(s)}\delta(\mathbf{x} - \mathbf{x}^{(I)})\right\rangle + \left\langle u_i''(f)\frac{\partial(I_f\tau_{ji})}{\partial x_j}\right\rangle. \quad (\text{A.1})$$

In this equation  $\tau_{ji}$  is the fluid phase stress tensor given by

$$\tau_{ji} = -p\delta_{ji} + \mu_f\left(\frac{\partial u_i}{\partial x_j} + \frac{\partial u_j}{\partial x_i}\right),$$

where  $p$  and  $\mathbf{u}$  are the instantaneous pressure and velocity fields respectively. The second term on the right hand side is the covariance of the fluctuating fluid velocity field and the gradient of the stress tensor in the fluid phase. Using the product rule this term can be written as

$$\left\langle u_i''(f)\frac{\partial(I_f\tau_{ji})}{\partial x_j}\right\rangle = \left\langle \frac{\partial}{\partial x_j}(I_f u_i''(f)\tau_{ji})\right\rangle - \left\langle I_f\tau_{ji}\frac{\partial u_i''(f)}{\partial x_j}\right\rangle. \quad (\text{A.2})$$

Commuting the gradient and averaging operators and invoking the assumption of statistical homogeneity, the first term on the right hand side of the above equation simplifies to zero. The second term on the right hand side can be further simplified by considering the definition of the stress tensor:

$$\tau_{ji}\frac{\partial u_i''(f)}{\partial x_j} = \left(-p\delta_{ji} + \mu_f\left(\frac{\partial u_i''(f)}{\partial x_j} + \frac{\partial u_j''(f)}{\partial x_i}\right)\right)\frac{\partial u_j''(f)}{\partial x_i} \quad (\text{A.3})$$

Since the fluctuating velocity field is divergence free, the pressure term is zero. So the above equation reduces to:

$$\tau_{ji}\frac{\partial u_i''(f)}{\partial x_j} = \mu_f\left[\frac{\partial u_i''(f)}{\partial x_j}\frac{\partial u_i''(f)}{\partial x_j} + \frac{\partial^2}{\partial x_i\partial x_j}(u_i''(f)u_j''(f))\right] = 2\mu_f s_{ij}s_{ij}, \quad (\text{A.4})$$

where,  $s_{ij} = \frac{1}{2} \left( \frac{\partial u_i^{''(f)}}{\partial x_j} + \frac{\partial u_j^{''(f)}}{\partial x_i} \right)$ . Therefore, the second term on the right hand side of Eqs. (A.1) and (3.19) simplifies to

$$\left\langle u_i^{''(f)} \frac{\partial (I_f \tau_{ji})}{\partial x_j} \right\rangle = -2\mu_f \langle I_f s_{ij} s_{ij} \rangle, \quad (\text{A.5})$$

which is strictly negative and can be identified as the dissipation rate of  $k_f$  in statistically homogeneous gas–solid flow.

## APPENDIX B. Regime of applicability of the assumptions in PR–DNS of gas–solid heat transfer

The assumptions employed in this work and their regime of validity are discussed in this section. The use of a fixed bed setup for gas–solid flows is justified if the configuration of the particles changes very slowly compared to the time it takes to attain mean momentum balance. The time scale over which the particle configuration changes depends on  $\text{Re}_T = D\Theta^{1/2}/\nu_f$ , which is the Reynolds number based on the particle fluctuating velocity that is characterized by the particle granular temperature  $\Theta$ . The particle granular temperature  $\Theta$  is a measure of the variance in the particle velocities and is defined as  $\Theta = 1/3 \langle \mathbf{v}'' \cdot \mathbf{v}'' \rangle$ , where  $\mathbf{v}''$  is the fluctuation in the particle velocity defined with respect to the mean particle velocity. Particle–resolved simulations of freely evolving suspensions (Tenneti et al., 2010b) and recent high–speed imaging of particles (Cocco et al., 2010) show that this value of  $\text{Re}_T$  is  $O(1)$  for high Stokes number particles that are characteristic of gas–solid flows (e.g., coal particles in air). This indicates that the particle configuration changes slowly relative to fluid time scales.

An important simplification made in this work is the use of a uniform temperature for the particles. The extent of variation of the temperature inside a particle is governed by the Biot number ( $\text{Bi}$ ), which is defined as  $\text{Bi} = hD/k_s$ . In this definition  $h$  is the convection heat transfer coefficient between the particle and the fluid, and  $k_s$  is the thermal conductivity of the solid. For many gas–solid systems the thermal conductivity of the solid is greater than that of the gas by more than an order of magnitude (e.g. air–coal, air–Ferrous oxide, air–fused silica) and results in a Biot number that is less than 0.1. The small Biot number encountered in many practical gas–solid systems suggests a lumped capacitance model for the particle temperature, where the spatial variation of temperature inside the particle can be neglected.

In addition to the assumption of uniform temperature of the particle, we also assume that

this uniform temperature is constant in time i.e., we assume the particles are isothermal. This simplification follows from the observation that the thermal response time of the particles is large compared to the time it takes for the fluid to travel a distance equal to the particle diameter. The thermal response time of the particle  $\tau_{tp} \sim hA_s / (mC_{ps})$ , where  $A_s$  is the surface area,  $m$  is the mass and  $C_{ps}$  is the specific heat of the particle, respectively. The time taken by the fluid to travel over a particle  $\tau_f \sim D / |\langle \mathbf{W} \rangle|$ , where  $\langle \mathbf{W} \rangle$  is the mean slip velocity between the particle and the fluid. The ratio of these time scales

$$\frac{\tau_{tp}}{\tau_f} \sim \left( \frac{\rho_p C_{ps}}{\rho_f C_{pf}} \right) \left( \frac{\text{Re}_m \text{Pr}}{\text{Nu}} \right),$$

where  $\rho_p$  is the density of the particle,  $\rho_f$  is the density of the fluid,  $C_{pf}$  is the specific heat of the fluid and Nu is the Nusselt number. Experimental studies (Gunn, 1978) of heat transfer in gas–solid systems reveal that the ratio  $\frac{\text{Re}_m \text{Pr}}{\text{Nu}} \sim O(1)$ . For gas–solid flows the ratio of the density of the particles to the density of the fluid density is very high ( $\sim O(10^3)$ ). Due to the high thermal inertia of the particles the thermal response time of the particles is about three orders of magnitude larger than the convective time scale of the fluid. Hence, the uniform temperature of a particle can be assumed to be constant in time. In addition to the assumption of a uniform and constant particle temperature, we also assume that all particles in the bed are maintained at the same temperature. The assumption that the particles equilibrate to the same surface temperature is consistent with earlier works (Gunn, 1978; Acrivos et al., 1980).

Neglecting viscous dissipation, radiation and free convection effects limits the gas–solid systems to which our simulation methodology applies. Viscous heating becomes important in flows with Mach numbers comparable or greater than unity and since we are concerned with subsonic flows, viscous dissipation is neglected in this work. Free convection is quantified by the Grashof number, which is defined as

$$Gr = \frac{g\beta(T_f - T_s)D^3}{\nu_f^2}, \quad (\text{B.1})$$

where  $T_f$  is the free stream temperature,  $T_s$  is the temperature of the solid surface, and  $\beta$  is the volumetric thermal expansion coefficient ( $\beta = 1/T_f$  for gases). Free convection effects can be neglected if  $Gr/\text{Re}_m^2 < 1$ . For each Reynolds number, this constraint imposes an upper

limit on the particle diameter above which free convection effects cannot be neglected. For a given value of  $T_f/T_s$ , the upper limit on the particle diameter  $D$  increases with increasing Reynolds number. If a typical value of 100 is taken for the fluid to solid temperature ratio (i.e.  $T_f/T_s = 100$ ), and air is assumed to be the fluid under terrestrial conditions ( $g = 9.81 \text{ m/s}^2$ ), then for a Reynolds number  $Re_m = 1$  the particle diameter has to be less than  $350 \mu\text{m}$  for negligible free convection. This restriction on the particle diameter becomes less severe as the Reynolds number increases.

For an isolated particle at  $T_s$  with emissivity equal to one, and surrounded by fluid at  $T_f$ , the ratio of radiation to forced convection heat transfer can be expressed as

$$\hat{q}_{rc} = \frac{q_{\text{rad}}}{q_{\text{conv}}} = \frac{\sigma(T_s + T_f)(T_s^2 + T_f^2)}{h_{fs}} = \frac{\sigma D(T_s + T_f)(T_s^2 + T_f^2)}{\text{Nu } k_f},$$

where  $\sigma = 5.67 \times 10^{-8} \text{ W/m}^2 \cdot \text{K}^4$  is the Stefan–Boltzmann constant. Assuming air to be the surrounding fluid at  $T_f = 1000\text{K}$  ( $k_f = 0.060 \text{ W/m}\cdot\text{K}$ ) and the particle temperature  $T_s = 300\text{K}$ , for Stokes flow (i.e.  $\text{Nu} \approx 2$ ) the ratio of radiation to forced convection heat transfer increases linearly with particle diameter from  $0.66 \times 10^{-4}$  to  $0.66 \times 10^{-2}$ , for particle diameter in the range 1 to 100 microns. While this estimate is valid in the Stokes flow regime, with increasing Reynolds number the higher value of average Nusselt number reduces the ratio of radiation to forced convection heat transfer, thus relaxing the restriction on particle diameter. These estimates of the relative importance of forced convection to free convection and radiation heat transfer show that the restriction on particle diameter is most severe in the Stokes flow regime, and is progressively less restrictive with increasing Reynolds number. Therefore, the assumptions used in this work are indeed applicable and relevant to practical gas–solid systems.

## APPENDIX C. Equations of motion in an accelerating frame of reference

Consider a two-phase flow in a finite flow volume  $\mathcal{V}$  in physical space as an ensemble of spherical particles as shown in figure C.1. At time  $t$ , the  $n^{\text{th}}$  particle is characterized by its position vector  $\mathbf{X}^{(n)}(t)$  and its velocity vector  $\mathbf{V}^{(n)}(t)$ . A Lagrangian description is used for the particles and an Eulerian description is used for describing the motion of the fluid.

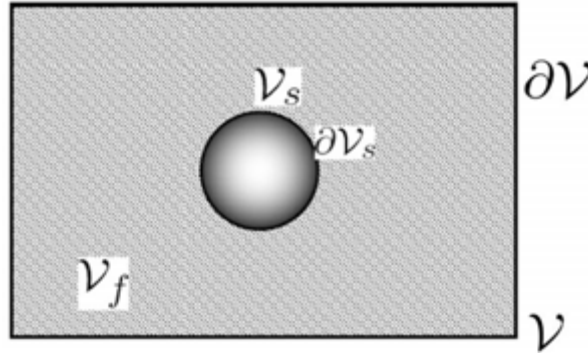


Figure C.1 Schematic of the physical domain. Hatched lines represent the volume  $\mathcal{V}_f$  occupied by the fluid phase, solid fill represents the volume  $\mathcal{V}_s$  occupied by the solid particle, and  $\mathcal{V} = \mathcal{V}_f + \mathcal{V}_s$  is the total volume.  $\partial\mathcal{V}$  and  $\partial\mathcal{V}_s$  represent, respectively, the areas of the computational box and the solid particle.

Denoting the velocity and pressure fields of the fluid by  $\mathbf{u}(\mathbf{x}, t)$ ,  $p(\mathbf{x}, t)$  respectively, the governing equations of motion for the fluid phase in a reference frame fixed in space (laboratory frame) are:

$$\frac{\partial u_i}{\partial x_i} = 0, \quad (\text{C.1})$$

$$\frac{\partial u_i}{\partial t} + u_j \frac{\partial u_i}{\partial x_j} = -\frac{1}{\rho_f} \frac{\partial p}{\partial x_i} + \nu_f \frac{\partial^2 u_i}{\partial x_j \partial x_j}. \quad (\text{C.2})$$

In the above equation,  $\rho_f$ ,  $\nu_f$  are the density and kinematic viscosity of the fluid respectively.

These equations are to be solved with the boundary conditions  $\mathbf{u} = \mathbf{V}^{(n)}(t)$  on  $\partial\mathcal{V}_s^{(n)}(t)$ . Here,

$\partial\mathcal{V}_s^{(n)}(t)$  is the surface of the  $n^{\text{th}}$  particle whose spatial location changes with time because of the motion of the particle. The governing equations of motion for the particles in the laboratory frame are:

$$m \frac{dV_i^{(n)}}{dt} = - \int_{\partial\mathcal{V}_s^{(n)}(t)} p n_i^{(n)} dA + \mu_f \int_{\partial\mathcal{V}_s^{(n)}(t)} \frac{\partial u_i}{\partial x_j} n_j^{(n)} dA \quad (\text{C.3})$$

where  $\mu_f = \rho_f \nu_f$  is the dynamic viscosity of the fluid. In the above equation,  $n_j^{(n)}$  denotes the component of the normal pointing outward from the surface of the  $n^{\text{th}}$  particle.

The objective here is to solve the equations of motion of both the phases in a reference frame that moves with the mean velocity of the particles. Since the particles will be accelerating in the laboratory frame, the new reference frame denoted  $\bar{E}$  will be a non-inertial frame of reference. Let the velocity and acceleration of  $\bar{E}$  with respect to the laboratory frame  $E$  be  $\mathbf{V}_f(t)$  and  $\mathbf{A}_f(t)$  respectively. The transformation rules between the two frames are :

$$\begin{aligned} \bar{\mathbf{u}} &= \mathbf{u} - \mathbf{V}_f, \\ \bar{\mathbf{x}} &= \mathbf{x} - \int_0^t \mathbf{V}_f(t') dt' \\ \bar{t} &= t. \end{aligned} \quad (\text{C.4})$$

Effecting the transformation rules defined above into Eq. E.2 the governing equations of motion for the fluid phase in  $\bar{E}$  are (see Pope (2000) for details of the derivation)

$$\frac{\partial \bar{u}_i}{\partial \bar{x}_i} = 0, \quad (\text{C.5})$$

$$\frac{\partial \bar{u}_i}{\partial \bar{t}} + \bar{u}_j \frac{\partial \bar{u}_i}{\partial \bar{x}_j} = - \frac{1}{\rho_f} \frac{\partial p}{\partial \bar{x}_i} + \nu_f \frac{\partial^2 \bar{u}_i}{\partial \bar{x}_j \partial \bar{x}_j} - A_{f,i}. \quad (\text{C.6})$$

It should be noted that the pressure being a scalar remains the same in both the frames. Following the notation of Garg et al. (2009), the momentum equation in Eq. C.6 can be rewritten as

$$\frac{\partial \bar{u}_i}{\partial \bar{t}} + \bar{S}_i = - \frac{1}{\rho_f} \bar{g}_i + \nu_f \frac{\partial^2 \bar{u}_i}{\partial \bar{x}_j \partial \bar{x}_j} - A_{f,i} \quad (\text{C.7})$$

where  $\bar{\mathbf{S}}$  and  $\bar{\mathbf{g}}$  respectively are the convective and pressure gradient terms in  $\bar{E}$ . It is assumed that the particle assemblies are homogeneous at all times. If the particle configuration is

homogeneous then the ensemble averaged quantities can be estimated by volume averaging. The flow quantities can be decomposed as a sum of the volumetric mean and a fluctuating part. For instance, the pressure gradient can be decomposed as  $\bar{\mathbf{g}} = \langle \bar{\mathbf{g}} \rangle_{\mathcal{V}} + \bar{\mathbf{g}}'$  where, the volumetric mean pressure gradient  $\langle \bar{\mathbf{g}} \rangle_{\mathcal{V}}$  is defined as

$$\langle \bar{\mathbf{g}} \rangle_{\mathcal{V}} = \frac{1}{V} \int_{\mathcal{V}} \bar{\mathbf{g}} d\mathcal{V}. \quad (\text{C.8})$$

In the above equation,  $V$  is the volume of the physical domain. Thus, E.5 can be rewritten as:

$$\frac{\partial \bar{u}_i}{\partial t} + \bar{S}_i = -\frac{1}{\rho_f} \langle \bar{g}_i \rangle_{\mathcal{V}} - \frac{1}{\rho_f} \frac{\partial \psi'}{\partial \bar{x}_i} + \nu_f \frac{\partial^2 \bar{u}_i}{\partial \bar{x}_j \partial \bar{x}_j} - A_{f,i}. \quad (\text{C.9})$$

In the above equation,  $\bar{\mathbf{g}}'$  is written as the gradient of a fluctuating pressure  $\psi'$ . In a similar fashion averaged fluid velocity can be estimated by averaging the fluid velocity fields over the fluid volume i.e,

$$\langle \bar{u}_i^{(f)} \rangle = \frac{1}{V_f} \int_{\mathcal{V}_f} \bar{u}_i d\mathcal{V}_f. \quad (\text{C.10})$$

where  $V_f$  is the volume of the region occupied by the fluid. The evolution equation for the phasic averaged fluid velocity can be obtained by integrating Eq. E.7 over the fluid volume.

The resulting equation is:

$$V_f \frac{d}{dt} \langle \bar{u}_i^{(f)} \rangle = -\frac{1}{\rho_f} \langle \bar{g}_i \rangle_{\mathcal{V}} V_f + \frac{1}{\rho_f} \int_{\partial \mathcal{V}_s} \psi' n_i^{(s)} dA - \nu_f \int_{\partial \mathcal{V}_s} \frac{\partial \bar{u}_i}{\partial \bar{x}_j} n_j^{(s)} dA - A_{f,i} V_f \quad (\text{C.11})$$

In the above equation  $\partial \mathcal{V}_s$  denotes the solid surface bounding the fluid volume and  $n_j^{(s)}$  denotes the component of normal vector pointing outward from the surface of the solid particles.

Dividing the entire equation by the fluid volume  $V_f$  and rearranging the terms gives:

$$-\frac{1}{\rho_f} \langle \bar{g}_i \rangle_{\mathcal{V}} = \frac{d}{dt} \langle \bar{u}_i^{(f)} \rangle + \frac{1}{(1-\phi)V} \left[ -\frac{1}{\rho_f} \int_{\partial \mathcal{V}_s} \psi' n_i^{(s)} dA + \nu_f \int_{\partial \mathcal{V}_s} \frac{\partial \bar{u}_i}{\partial \bar{x}_j} n_j^{(s)} dA \right] + A_{f,i} \quad (\text{C.12})$$

Now, the equations of motion for the particles in the reference frame  $\bar{E}$  will be derived. The velocity of the  $n^{\text{th}}$  particle transforms as  $\bar{\mathbf{V}}^{(n)}(t) = \mathbf{V}^{(n)}(t) - \mathbf{V}_f(t)$ . Substituting the transformation rules in Eq. C.3, the equation of motion for the  $n^{\text{th}}$  particle is obtained as:

$$m \frac{d\bar{V}_i^{(n)}}{dt} = -\langle \bar{g}_i \rangle_{\mathcal{V}} V^{(n)} + \rho_f \left[ -\frac{1}{\rho_f} \int_{\partial \mathcal{V}_s^{(n)}(t)} \psi' n_i^{(n)} dA + \nu_f \int_{\partial \mathcal{V}_s^{(n)}(t)} \frac{\partial \bar{u}_i}{\partial \bar{x}_j} n_j^{(n)} dA \right] - m A_{f,i} \quad (\text{C.13})$$

The phasic mean solid velocity can be estimated as  $\langle \bar{\mathbf{u}}^{(s)} \rangle = (1/N_p) \sum_{n=1}^{N_p} \bar{\mathbf{V}}^{(n)}$  where  $N_p$  is the total number of particles in the domain. The evolution equation for the mean solid velocity can be derived by summing Eq. E.11 over all the particles. The resulting equation is:

$$\begin{aligned} \rho_p V_s \frac{d}{dt} \langle \bar{u}_i^{(s)} \rangle = & - \langle \bar{g}_i \rangle_{\mathcal{V}} V_s + \rho_f \left[ -\frac{1}{\rho_f} \int_{\partial \mathcal{V}_s} \psi' n_i^{(s)} dA + \nu_f \int_{\partial \mathcal{V}_s} \frac{\partial \bar{u}_i}{\partial \bar{x}_j} n_j^{(s)} dA \right] \\ & - \rho_p V_s A_{f,i} \end{aligned} \quad (\text{C.14})$$

where  $\rho_p$  is the density of the particles and  $V_s$  is the total volume occupied by the solid phase. It should be noted that the surface integrals in Eq. E.11 are taken over the surface of the  $n^{\text{th}}$  particle and in Eq. C.14, the surface integration is over all the solid surfaces. This is because,

$$\int_{\partial \mathcal{V}_s} = \sum_{n=1}^{N_p} \int_{\partial \mathcal{V}_s^{(n)}}.$$

Eq. C.14 can be rewritten as

$$\begin{aligned} \frac{d}{dt} \langle \bar{u}_i^{(s)} \rangle = & -\frac{1}{\rho_p} \langle \bar{g}_i \rangle_{\mathcal{V}} + \frac{1}{\phi V} \frac{\rho_f}{\rho_p} \left[ -\frac{1}{\rho_f} \int_{\partial \mathcal{V}_s} \psi' n_i^{(s)} dA + \nu_f \int_{\partial \mathcal{V}_s} \frac{\partial \bar{u}_i}{\partial \bar{x}_j} n_j^{(s)} dA \right] \\ & - A_{f,i} \end{aligned} \quad (\text{C.15})$$

Rearranging the above equation, an equation for the mean pressure gradient can be obtained as

$$\begin{aligned} -\frac{1}{\rho_p} \langle \bar{g}_i \rangle_{\mathcal{V}} = & \frac{d}{dt} \langle \bar{u}_i^{(s)} \rangle - \frac{1}{\phi V} \frac{\rho_f}{\rho_p} \left[ -\frac{1}{\rho_f} \int_{\partial \mathcal{V}_s} \psi' n_i^{(s)} dA + \nu_f \int_{\partial \mathcal{V}_s} \frac{\partial \bar{u}_i}{\partial \bar{x}_j} n_j^{(s)} dA \right] \\ & + A_{f,i} \end{aligned} \quad (\text{C.16})$$

The total drag force on the particles denoted  $\bar{\mathbf{F}}_D$  is given by

$$\bar{F}_{D,i} = \rho_f \left[ -\frac{1}{\rho_f} \int_{\partial \mathcal{V}_s} \psi' n_i^{(s)} dA + \nu_f \int_{\partial \mathcal{V}_s} \frac{\partial \bar{u}_i}{\partial \bar{x}_j} n_j^{(s)} dA \right].$$

Using the above notation, Eq. C.12 and C.16 can be simplified and summarized as follows:

$$-\frac{1}{\rho_f} \langle \bar{g}_i \rangle_{\mathcal{V}} = \frac{d}{dt} \langle \bar{u}_i^{(f)} \rangle + \frac{1}{(1-\phi)V} \frac{\bar{F}_{D,i}}{\rho_f} + A_{f,i} \quad (\text{C.17})$$

$$-\frac{1}{\rho_p} \langle \bar{g}_i \rangle_{\mathcal{V}} = \frac{d}{dt} \langle \bar{u}_i^{(s)} \rangle - \frac{1}{\phi V} \frac{\bar{F}_{D,i}}{\rho_p} + A_{f,i} \quad (\text{C.18})$$

The above two systems of equations contain two unknowns namely the mean pressure gradient  $\langle \bar{g}_i \rangle_{\mathcal{V}}$  and the frame acceleration  $A_{f,i}$ . The frame acceleration can be eliminated from the above equations to give a general expression for the mean pressure gradient:

$$\left( \frac{1}{\rho_f} - \frac{1}{\rho_p} \right) \langle \bar{g}_i \rangle_{\mathcal{V}} = \frac{d}{dt} \langle \bar{u}_i^{(s)} \rangle - \frac{d}{dt} \langle \bar{u}_i^{(f)} \rangle - \frac{\bar{F}_{D,i}}{V} \left[ \frac{1}{\phi \rho_p} + \frac{1}{(1-\phi)\rho_f} \right] \quad (\text{C.19})$$

The fixed particle simulations described in the paper are a special case where the particles are so massive that they do not move i.e,  $\rho_p \rightarrow \infty$  and the rate of change of the mean solid velocity is zero. So taking the limit  $\rho_p \rightarrow \infty$  in Eq. E.16, we get

$$\frac{1}{\rho_f} \langle \bar{g}_i \rangle_{\mathcal{V}} = -\frac{d}{dt} \langle \bar{u}_i^{(f)} \rangle - \frac{\bar{F}_{D,i}}{V} \frac{1}{(1-\phi)\rho_f} \quad (\text{C.20})$$

which is the same as the one derived by Garg et al. (2009).

The frame acceleration can be obtained from C.18 as:

$$A_{f,i} = -\frac{1}{\rho_p} \langle \bar{g}_i \rangle_{\mathcal{V}} - \frac{d}{dt} \langle \bar{u}_i^{(s)} \rangle + \frac{1}{\phi V} \frac{\bar{F}_{D,i}}{\rho_p} \quad (\text{C.21})$$

It can be seen that the mean pressure gradient depends upon the rate of change of the fluid and solids velocity. Equations E.16 and E.17 can be discretized in time as follows:

$$\left( \frac{1}{\rho_f} - \frac{1}{\rho_p} \right) \langle \bar{g}_i \rangle_{\mathcal{V}}^{n+1} = -\frac{\langle \bar{u}_i^{(f)} \rangle^{n+1} - \langle \bar{u}_i^{(f)} \rangle^n}{\Delta \bar{t}} - \frac{\langle \bar{u}_i^{(s)} \rangle^{n+1} - \langle \bar{u}_i^{(s)} \rangle^n}{\Delta \bar{t}} \quad (\text{C.22})$$

$$- \frac{\bar{F}_{D,i}^n}{V} \left[ \frac{1}{\phi \rho_p} + \frac{1}{(1-\phi)\rho_f} \right] \quad (\text{C.23})$$

$$A_{f,i}^{n+1} = -\frac{1}{\rho_p} \langle \bar{g}_i \rangle_{\mathcal{V}}^{n+1} - \frac{\langle \bar{u}_i^{(s)} \rangle^{n+1} - \langle \bar{u}_i^{(s)} \rangle^n}{\Delta \bar{t}} + \frac{1}{\phi V} \frac{\bar{F}_{D,i}^n}{\rho_p} \quad (\text{C.24})$$

It is desired that the mean solids velocity be zero and that the mean fluid velocity be driven to a desired value  $\langle \bar{\mathbf{u}}^{(f)} \rangle^d$  which is set by the Reynolds number. Substituting  $\langle \bar{\mathbf{u}}^{(f)} \rangle^{n+1} = \langle \bar{\mathbf{u}}^{(f)} \rangle^d$  and  $\langle \bar{\mathbf{u}}^{(s)} \rangle^{n+1} = 0$  in the above two equations and noting that the initial mean solids velocity is zero, the resulting numerical equations are:

$$\left( \frac{1}{\rho_f} - \frac{1}{\rho_p} \right) \langle \bar{g}_i \rangle_{\mathcal{V}}^{n+1} = -\frac{\langle \bar{u}_i^{(f)} \rangle^d - \langle \bar{u}_i^{(f)} \rangle^n}{\Delta \bar{t}} - \frac{\bar{F}_{D,i}^n}{V} \left[ \frac{1}{\phi \rho_p} + \frac{1}{(1-\phi)\rho_f} \right] \quad (\text{C.25})$$

and

$$A_{f,i}^{n+1} = -\frac{1}{\rho_p} \langle \bar{g}_i \rangle_V^{n+1} + \frac{1}{\phi V} \frac{\bar{F}_{D,i}^n}{\rho_p}. \quad (\text{C.26})$$

From the above analysis it can be seen that there are two free parameters in this problem namely the mean pressure gradient and the frame acceleration. The mean pressure gradient can be thought of as a means to set the desired average fluid velocity and the frame acceleration can be seen as a time varying body force which will be tuned at every instant to give the desired mean solids velocity.

### Estimation of granular temperature from the DNS of freely evolving suspensions

Solving the equations of motion in an accelerating frame of reference using equations C.25 and C.26 ensures that: (i) the mean solids velocity is zero and (ii) the mean fluid velocity is such that the desired Reynolds number (based on slip velocity) is attained. At every time instant, the mean solids velocity is estimated from the DNS as

$$\{\mathbf{u}^{(s)}\}(t) = \frac{1}{N_p} \sum_{n=1}^{N_p} \mathbf{v}^{(n)}. \quad (\text{C.27})$$

The mean velocity of the solids is denoted  $\{\mathbf{u}^{(s)}\}$  to point out the fact that it is only an estimate to the true mean which is denoted  $\langle \mathbf{u}^{(s)} \rangle$ . The fluctuating velocity of the  $n^{\text{th}}$  particle  $\mathbf{v}'^{(n)}$  is computed from DNS as

$$\mathbf{v}'^{(n)}(t) = \mathbf{V}^{(n)}(t) - \{\mathbf{u}^{(s)}\}(t). \quad (\text{C.28})$$

At every time instant, the granular temperature is estimated using the formula

$$\{T\}(t) = \frac{1}{3N_p} \sum_{n=1}^{N_p} \left( \mathbf{v}'^{(n)}(t) \cdot \mathbf{v}'^{(n)}(t) \right). \quad (\text{C.29})$$

It is important to note that in C.28 particle velocity fluctuations are defined about the mean solids velocity which is estimated as a number average and not as a time average. Figures C.2(a) and C.2(b) show the evolution of mean solids velocity and mean fluid velocity in the

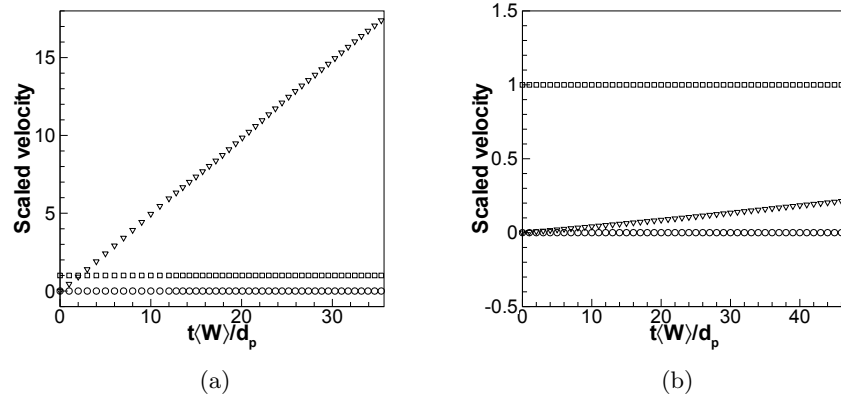


Figure C.2 Evolution of the mean solids velocity and mean fluid velocity in the moving frame and the frame velocity with respect to the laboratory frame obtained from the DNS of a freely evolving suspension of volume fraction 0.2,  $Re_m = 20$ . Figure C.2(a) shows the results for a solid to fluid density ratio of 10 while Figure C.2(b) shows the results for a solid to fluid density ratio of 1000. In both figures, the mean solids velocity (open circles), the mean fluid velocity ( $\square$ ) and the frame velocity ( $\nabla$ ) are scaled by the desired mean slip velocity.

moving frame and the frame velocity with respect to the laboratory frame for solid to fluid density ratios of 10 and 1000 respectively. The volume fraction and the mean flow Reynolds number for both suspensions are 0.2 and 20 respectively. From these figures we observe that the frame velocity (shown by  $\nabla$ ) varies linearly with time. Imbalance between the mean pressure gradient and the drag force acting on the particles causes the particles to accelerate in the laboratory frame. Acceleration of the moving frame accounts for this imbalance and ensures that the mean solids velocity is zero in the moving frame. We can clearly see from Figures C.2(a) and C.2(b) that the mean solids velocity (shown by  $\square$ ) is indeed zero and that the mean fluid velocity (shown by open circles) is such that the desired slip velocity is attained. Thus, we can conclude that the granular temperature we estimate from DNS is indeed a measure of the strength of the particle velocity fluctuations.

## APPENDIX D. Identification of source and dissipation of granular temperature from PR–DNS

Using the Langevin model for the increment in the particle velocity fluctuations (cf. Eq. (6.2)), we can derive the evolution equation for the modeled granular temperature  $T^*$  as:

$$\frac{dT^*}{dt} = -2\gamma T^* + B^2. \quad (\text{D.1})$$

In the above equation, we can clearly identify that the source for the granular temperature is  $B^2$  and that the dissipation is  $2\gamma T^*$ . For a statistically homogeneous suspension, the evolution equation for the granular temperature can be written as:

$$\frac{dT}{dt} = \frac{2}{3} \langle A''_i v''_i \rangle.$$

In the above equation, the fluctuations in the acceleration are defined about the mean particle acceleration, i.e.  $A''_j = A_j - \langle A_j \rangle$ . The instantaneous particle acceleration model should model evolution of the granular temperature correctly. In order to do this, we have to match the source and dissipation implied by the Langevin model to the source and dissipation obtained from DNS. However, given the correlation  $\langle A''_i v''_i \rangle$ , it is non-trivial to uniquely decompose it into source and dissipation. Koch (1990) derived analytical expressions for the source and dissipation in the limit of low volume fractions and low Reynolds numbers. Later Koch and Sangani (1999) used approximate multipole expansions approach to determine the source and dissipation for dense suspensions but limited to the Stokes flow regime. Here we present a method to extract the same from the DNS at moderate Reynolds numbers.

The fluctuation in the acceleration experienced by the  $n^{\text{th}}$  particle is denoted  $A''^{(n)}$  and similarly, the fluctuation in the velocity is denoted  $v''^{(n)}$ . The fluctuating acceleration can be written as:

$$A''_i^{(n)} = -\zeta^{(n)} v''_i^{(n)} + A''_{R,i}^{(n)} \quad (\text{D.2})$$

In the above equation, we decomposed the fluctuating acceleration vector along a direction parallel to the particle fluctuating velocity and along a direction perpendicular to it. The component of the acceleration perpendicular to the fluctuating velocity is denoted  $A''_{R,i}^{(n)}$  to represent the remainder term. It is important to note that this is not a model but an exact expression for the fluctuating particle acceleration. We can now form the estimate for the correlation  $\langle A''_i v''_i \rangle$  as follows:

$$\langle A''_i v''_i \rangle_E = \frac{1}{N_p} \sum_{n=1}^{N_p} A''_i^{(n)} v''_i^{(n)}.$$

After substituting Eq. (D.2) into the above equation and performing some algebraic manipulations, we can write the evolution equation for the estimate of granular temperature as:

$$\frac{dT_E}{dt} = S - \Gamma \quad (\text{D.3})$$

where the source is,

$$S = -\frac{2}{3} \frac{1}{N_p} \sum_{n=1}^{N_p} \zeta_-^{(n)} v''_i^{(n)} v''_i^{(n)} \quad (\text{D.4})$$

and the dissipation is

$$\Gamma = \frac{2}{3} \frac{1}{N_p} \sum_{n=1}^{N_p} \zeta_+^{(n)} v''_i^{(n)} v''_i^{(n)}. \quad (\text{D.5})$$

In the above expressions for source and dissipation of particle granular temperature,

$$\zeta_+^{(n)} = \frac{1}{2} \left( \zeta^{(n)} + \left| \zeta^{(n)} \right| \right),$$

and,

$$\zeta_-^{(n)} = \frac{1}{2} \left( \zeta^{(n)} - \left| \zeta^{(n)} \right| \right).$$

From these equations, it is clear that the particles whose fluctuating acceleration is aligned with the fluctuating velocity contribute to the source in granular temperature. Particles with the fluctuating acceleration aligned in a direction opposite to that of the fluctuating velocity contribute to the dissipation in granular temperature. This can be easily visualized from the scatter plot shown in Fig. D.1. For illustration, in this figure we show the scatter plot of

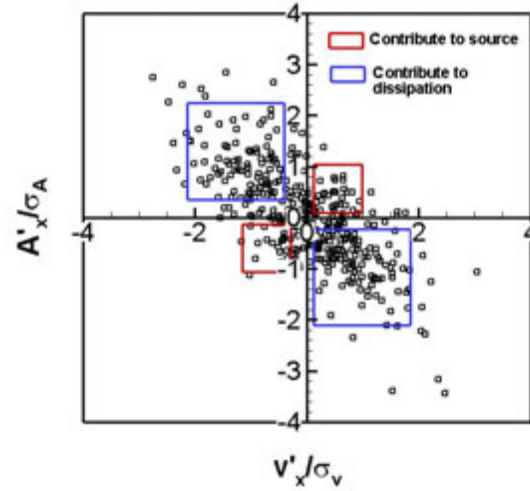


Figure D.1 Scatter plot showing the the fluctuating particle acceleration versus the fluctuating particle velocity obtained from the DNS of flow past a fixed particle assembly at a volume fraction of 0.2, mean flow Reynolds number of 20 and Reynolds number based on granular temperature of 16. From the analysis on the extraction of source and dissipation from the DNS, we can see that the symbols that lie in the first and the third quarter contribute to source and the symbols that lie in the second and the fourth quadrant contribute to the dissipation.

fluctuating particle acceleration and fluctuating particle velocity obtained from the DNS of flow past a fixed particle assembly ( $\phi = 0.2$ ,  $Re_m = 20$  and  $Re_T = 16$ ). The symbols that lie in the first and the third quadrants denote the particles whose fluctuating acceleration is aligned with the fluctuating velocity. Hence, these particles contribute to the source in granular temperature. Similarly, the symbols in the second and fourth quadrants contribute to the dissipation in granular temperature. Tenneti et al. (2010b) show that a simple extension of mean particle acceleration model applied to any particle velocity distribution does not produce any scatter in the first and third quadrants. They demonstrate that such instantaneous acceleration models do not produce any source in the granular temperature evolution equation. On the other hand, a stochastic acceleration model (cf. Eq. (6.2)) always results in a finite source term for the particle granular temperature for non-zero  $B$ .

We wish to know if the steady state attained by the suspension is a stable attractor. We can verify this by studying suspensions with different initial conditions. Using the formulae given by Eqs. (D.4) and (D.5), we extracted the source and dissipation from the DNS data and

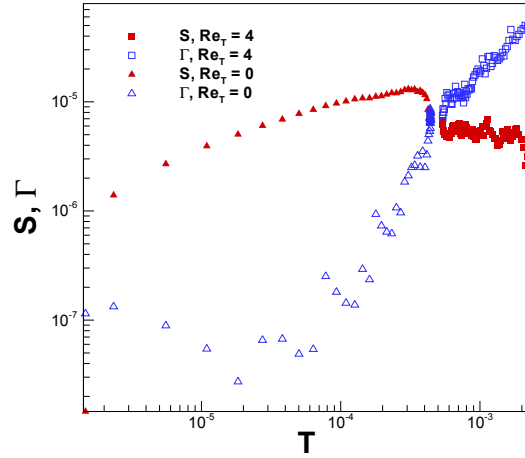


Figure D.2 Phase space plot showing the variation of source and dissipation with granular temperature. DNS data for two different suspensions is shown here. The volume fraction, mean flow Reynolds number and solid to fluid density ratio are 0.2, 20 and 100 respectively. Triangles denote the source (filled symbols) and dissipation (hollow symbols) and dissipation for a suspension initialized with zero granular temperature. Squares denote the data for a suspension initialized with a finite granular temperature corresponding to  $Re_T = 4$ .

plotted them versus the granular temperature in Fig. D.2 as a phase space plot. The state of the system is characterized by the granular temperature  $T$  and in phase space plots, the rate of change of the state variable  $\frac{dT}{dt}$  is plotted versus the state variable  $T$ . But the rate of change of granular temperature is simply the difference between the source ( $S$ ) and dissipation ( $\Gamma$ ). To understand the behavior of source and dissipation separately, we plot both  $S$  and  $\Gamma$  versus  $T$  in the plots shown in Fig. D.2. Source and dissipation are plotted for two sets of simulations differing only in their initial conditions. For both cases, the solid volume fraction is 0.2, mean flow Reynolds number is 20 and solid to fluid density ratio is 100. Triangular symbols are the data for a suspension where the particles initialized with zero granular temperature. In this case, the particles pick up energy from the fluid and hence we note that the source term is greater than dissipation at initial time. Square symbols show the source and dissipation data for a suspension initialized with a granular temperature corresponding to  $Re_T = 4$ . In this case, the particles have higher energy and thus they lose their energy to fluid. So for this case the dissipation is initially greater than the source term. A key observation from the figure is that

both suspensions attain the same steady granular temperature. This shows that the steady state behavior of a statistically homogeneous gas–solids suspension is independent of the initial temperature. Finally we note that for both suspensions, the source and dissipation are equal at steady state. These observations verify the expressions for the source and dissipation presented earlier and show that this is a viable approach to propose the acceleration model.

## APPENDIX E. Equations of motion for a polydisperse suspension in an accelerating frame of reference

Consider a two-phase flow in a finite flow volume  $\mathcal{V}$  in physical space as an ensemble of spherical particles. Let us assume that the solid phase consists of  $M$  discrete size classes. Each size class  $\alpha$  is characterized by the diameter  $D_\alpha$  and density  $\rho_\alpha$ . At time  $t$ , the  $n^{\text{th}}$  particle belonging to the size class  $\alpha$  is characterized by its position vector  $\mathbf{X}^{(n,\alpha)}(t)$  and its velocity vector  $\mathbf{V}^{(n,\alpha)}(t)$ . A Lagrangian description is used for the particles and an Eulerian description is used for describing the motion of the fluid.

Denoting the velocity and pressure fields of the fluid by  $\mathbf{u}(\mathbf{x}, t)$ ,  $p(\mathbf{x}, t)$  respectively, the governing equations of motion for the fluid phase in a reference frame  $E$  fixed in space (laboratory frame) are:

$$\frac{\partial u_i}{\partial x_i} = 0, \quad (\text{E.1})$$

$$\frac{\partial u_i}{\partial t} + u_j \frac{\partial u_i}{\partial x_j} = -\frac{1}{\rho_f} \frac{\partial p}{\partial x_i} + \nu_f \frac{\partial^2 u_i}{\partial x_j \partial x_j}. \quad (\text{E.2})$$

In the above equation,  $\rho_f$ ,  $\nu_f$  are the density and kinematic viscosity of the fluid respectively. These equations are to be solved with the boundary conditions  $\mathbf{u} = \mathbf{V}^{(n,\alpha)}(t)$  on  $\partial\mathcal{V}_s^{(n,\alpha)}(t)$ . Here,  $\partial\mathcal{V}_s^{(n,\alpha)}(t)$  is the surface of the  $n^{\text{th}}$  particle belonging to the size class  $\alpha$  whose spatial location changes with time because of the motion of the particle.

The objective here is to solve the equations of motion of both the phases in a reference frame such that we attain the desired mean slip Reynolds number. We first derive the equations of motion in an arbitrary accelerating frame of reference and then identify the frame acceleration that maintains the desired mean slip velocity. Since the particles will be accelerating in the laboratory frame, the new reference frame denoted  $\bar{E}$  will be a non-inertial frame of reference. Let the velocity and acceleration of  $\bar{E}$  with respect to the laboratory frame  $E$  be  $\mathbf{V}_f(t)$  and

$\mathbf{A}_f(t)$  respectively. The transformation rules between the two frames are :

$$\begin{aligned}\bar{\mathbf{u}} &= \mathbf{u} - \mathbf{V}_f, \\ \bar{\mathbf{x}} &= \mathbf{x} - \int_0^t \mathbf{V}_f(t') dt' \\ \bar{t} &= t.\end{aligned}\quad (\text{E.3})$$

Effecting the transformation rules defined above into Eq. E.2 the governing equations of motion for the fluid phase in  $\bar{E}$  are

$$\frac{\partial \bar{u}_i}{\partial \bar{x}_i} = 0, \quad (\text{E.4})$$

$$\frac{\partial \bar{u}_i}{\partial \bar{t}} + \bar{S}_i = -\frac{1}{\rho_f} \bar{g}_i + \nu_f \frac{\partial^2 \bar{u}_i}{\partial \bar{x}_j \partial \bar{x}_j} - A_{f,i} \quad (\text{E.5})$$

where  $\bar{\mathbf{S}}$  and  $\bar{\mathbf{g}}$  respectively are the convective and pressure gradient terms in  $\bar{E}$ . It is assumed that the particle assemblies are homogeneous at all times. If the particle configuration is homogeneous then the ensemble averaged quantities can be estimated by volume averaging. The flow quantities can be decomposed as a sum of the volumetric mean and a fluctuating part. For instance, the pressure gradient can be decomposed as  $\bar{\mathbf{g}} = \langle \bar{\mathbf{g}} \rangle_{\mathcal{V}} + \bar{\mathbf{g}}'$  where, the volumetric mean pressure gradient  $\langle \bar{\mathbf{g}} \rangle_{\mathcal{V}}$  is defined as

$$\langle \bar{\mathbf{g}} \rangle_{\mathcal{V}} = \frac{1}{V} \int_{\mathcal{V}} \bar{\mathbf{g}} d\mathcal{V}. \quad (\text{E.6})$$

In the above equation,  $V$  is the volume of the physical domain. Thus, E.5 can be rewritten as:

$$\frac{\partial \bar{u}_i}{\partial \bar{t}} + \bar{S}_i = -\frac{1}{\rho_f} \langle \bar{g}_i \rangle_{\mathcal{V}} - \frac{1}{\rho_f} \frac{\partial \psi'}{\partial \bar{x}_i} + \nu_f \frac{\partial^2 \bar{u}_i}{\partial \bar{x}_j \partial \bar{x}_j} - A_{f,i}. \quad (\text{E.7})$$

In the above equation,  $\bar{\mathbf{g}}'$  is written as the gradient of a fluctuating pressure  $\psi'$ . In a similar fashion averaged fluid velocity can be estimated by averaging the fluid velocity fields over the fluid volume i.e,

$$\langle \bar{u}_i^{(f)} \rangle = \frac{1}{V_f} \int_{\mathcal{V}_f} \bar{u}_i d\mathcal{V}_f. \quad (\text{E.8})$$

where  $V_f$  is the volume of the region occupied by the fluid. The evolution equation for the phasic averaged fluid velocity can be obtained by integrating Eq. E.7 over the fluid volume.

The resulting equation is:

$$\frac{d}{dt} \langle \bar{u}_i^{(f)} \rangle = -\frac{1}{\rho_f} \langle \bar{g}_i \rangle_{\mathcal{V}} + \frac{1}{\rho_f V_f} \int_{\partial \mathcal{V}_s} \psi' n_i^{(s)} dA - \frac{\nu_f}{V_f} \int_{\partial \mathcal{V}_s} \frac{\partial \bar{u}_i}{\partial x_j} n_j^{(s)} dA - A_{f,i} \quad (\text{E.9})$$

In the above equation  $\partial \mathcal{V}_s$  denotes the solid surface bounding the fluid volume and  $n_j^{(s)}$  denotes the component of normal vector pointing outward from the surface of the solid particles. This equation can be written in a simple notation as:

$$\frac{d}{dt} \langle \bar{u}_i^{(f)} \rangle = -\frac{1}{\rho_f} \langle \bar{g}_i \rangle_{\mathcal{V}} - \frac{1}{\rho_f V_f} \sum_{\alpha=1}^M \bar{\mathbf{F}}_{D-\alpha,i} - A_{f,i}. \quad (\text{E.10})$$

where,  $\bar{\mathbf{F}}_{D-\alpha}$  represents the sum of the surface forces acting on the particles belonging to the size class  $\alpha$ :

$$\bar{\mathbf{F}}_{D-\alpha,i} = \rho_f \sum_{n=1}^{N_\alpha} \left[ -\frac{1}{\rho_f} \int_{\partial \mathcal{V}_s^{(n,\alpha)}} \psi' n_i^{(n,\alpha)} dA + \nu_f \int_{\partial \mathcal{V}_s^{(n,\alpha)}} \frac{\partial \bar{u}_i}{\partial x_j} n_j^{(n,\alpha)} dA \right].$$

The equations of motion for the particles in the reference frame  $\bar{E}$  will be derived now. The equation of motion for the  $n^{\text{th}}$  particle belonging to size class  $\alpha$  is obtained as:

$$m_\alpha \frac{d\bar{V}_i^{(n,\alpha)}}{dt} = -\langle \bar{g}_i \rangle_{\mathcal{V}} V_\alpha + \bar{F}_{D,i}^{(n,\alpha)} - m_\alpha A_{f,i} + \sum_{\substack{k=1 \\ k \neq n}}^{N_\alpha} \bar{F}_{nk,i}^C + \sum_{\substack{\beta=1 \\ \beta \neq \alpha}}^M \sum_{k=1}^{N_\beta} \bar{F}_{nk,i}^C. \quad (\text{E.11})$$

In the above equation, the third term on the right hand side represents the contact force acting on the  $n^{\text{th}}$  particle due to collisions with other particles belonging to the same size class  $\alpha$ . The last term is the contact force acting on the  $n^{\text{th}}$  particle due to collisions with particles belonging to all other size classes.

We can define a mean solid velocity for each size class as follows:

$$\langle \bar{\mathbf{u}}^{(s,\alpha)} \rangle = \frac{1}{N_\alpha} \sum_{n=1}^{N_\alpha} \bar{\mathbf{V}}^{(n,\alpha)} \quad (\text{E.12})$$

where  $N_\alpha$  is the total number of particles in the size class  $\alpha$ . The evolution equation for the mean solid velocity in each size class can be derived by summing Eq. E.11 over all the particles belonging to that size class. The resulting equation is:

$$\frac{d}{dt} \langle \bar{u}_i^{(s,\alpha)} \rangle = -\frac{1}{\rho_\alpha} \langle \bar{g}_i \rangle_{\mathcal{V}} + \frac{1}{\rho_\alpha \phi_\alpha V} \left[ \bar{\mathbf{F}}_{D-\alpha,i} + \sum_{\substack{\beta=1 \\ \beta \neq \alpha}}^M \bar{\mathbf{F}}_{\alpha-\beta,i}^C \right] - A_{f,i} \quad (\text{E.13})$$

where  $\bar{\mathbf{F}}_{\alpha-\beta}^C$  is the total contact force acting on the size class  $\alpha$  due to collision with particles belonging to the size class  $\beta$ . From the above equation it is clear that the mean solid velocity whose evolution is not governed by the collisional forces is the mass weighted mixture mean velocity which can be defined as:

$$\langle \bar{\mathbf{u}}^{(s)} \rangle = \frac{\sum_{\alpha=1}^M \rho_{\alpha} \phi_{\alpha} \langle \bar{\mathbf{u}}^{(s,\alpha)} \rangle}{\sum_{\alpha=1}^M \rho_{\alpha} \phi_{\alpha}}. \quad (\text{E.14})$$

Using the above definition, evolution equation for the mixture mean solids velocity is

$$\frac{d}{dt} \langle \bar{u}_i^{(s)} \rangle = -\frac{\phi}{\sum_{\alpha=1}^M \rho_{\alpha} \phi_{\alpha}} \langle \bar{g}_i \rangle_{\mathcal{V}} + \frac{1}{\sum_{\alpha=1}^M \rho_{\alpha} \phi_{\alpha} V} \sum_{\alpha=1}^M \bar{F}_{D-\alpha,i} - A_{f,i}. \quad (\text{E.15})$$

Let us assume that all the size classes have the same density  $\rho_p$ . The equation for the mean slip velocity can now be obtained by subtracting (E.9) from (E.15):

$$\frac{d}{dt} \langle \bar{W}_i^{(s)} \rangle = \left( \frac{1}{\rho_f} - \frac{1}{\rho_p} \right) \langle \bar{g}_i \rangle_{\mathcal{V}} - \frac{1}{V} \left[ \frac{1}{\phi \rho_p} + \frac{1}{(1-\phi)\rho_f} \right] \sum_{\alpha=1}^M \bar{F}_{D-\alpha,i}. \quad (\text{E.16})$$

The mean pressure gradient sets the mean slip between the solid and the fluid phases. The frame acceleration can be chosen to be equal to the rate of change of the mixture mean solid velocity. This choice of the frame acceleration sets the level of both the solid and fluid velocity. The frame acceleration can be obtained as:

$$A_{f,i} = -\frac{1}{\rho_p} \langle \bar{g}_i \rangle_{\mathcal{V}} - \frac{d}{dt} \langle \bar{u}_i^{(s)} \rangle + \frac{1}{\phi \rho_p V} \sum_{\alpha=1}^M \bar{F}_{D-\alpha,i}. \quad (\text{E.17})$$

From equation E.13 it is clear that the slip velocity between the size classes evolves because of the imbalance between the fluid-particle force and the contact force due to collisions.

## BIBLIOGRAPHY

- Abanades, J. C., Anthony, E. J., Lu, D. Y., Salvador, C., and Alvarez, D. (2004). Capture of CO<sub>2</sub> from combustion gases in a fluidized bed of CaO. *Environmental and Energy Engineering*, 50(7):1614–1622.
- Acrivos, A., Hinch, E. J., and Jeffrey, D. J. (1980). Heat transfer to a slowly moving fluid from a dilute fixed bed of heated spheres. *J. Fluid Mech.*, 101(02):403–421.
- Agrawal, K., Loezos, P., Syamlal, M., and Sundaresan, S. (2001). The role of meso-scale structures in rapid gas-solid flows. *J. Fluid Mech.*, 445:151–181.
- Ahmadi, G. and Ma, D. (1990a). A thermodynamical formulation for dispersed multiphase turbulent flows: II simple shear flows for dense mixtures. *Intl. J. Multiphase Flow*, 16(2):341–351.
- Ahmadi, G. and Ma, D. (1990b). A thermodynamical formulation for dispersed multiphase turbulent flows: I basic theory. *Intl. J. Multiphase Flow*, 16(2):323–340.
- Amsden, A. A., O'Rourke, P. J., and Butler, T. D. (1989). KIVA-II: A Computer Program for Chemically Reactive Flows with Sprays. Technical Report LA-11560-MS, Los Alamos National Laboratory.
- Anderson, T. B. and Jackson, R. (1967). A fluid mechanical description of fluidized beds. *Ind. Eng. Chem. Fundam.*, 6:527–539.
- Apte, S., Martin, M., and Patankar, N. (2009). A numerical method for fully resolved simulation (frs) of rigid particle flow interactions in complex flows. *J. Comp. Phys.*, 228:2712–2738.

- Avidan, A. A. (1997). Fluid catalytic cracking. In Grace, J. R., Avidan, A. A., and Knowlton, T. M., editors, *Circulating fluidized beds*, pages 466–474. London: Blackie.
- Azar, C., Lindgren, K., Larson, E., and Mollersten, K. (2006). Carbon capture and storage from fossil fuels and biomass-costs and potential role in stabilizing the atmosphere. *Climatic Change*, 74(1-3):47–79.
- Bagchi, P. and Balachandar, S. (2003). Effect of turbulence on the drag and lift of a particle. *Phys. Fluids*, 15(11):3496–3513.
- Bagchi, P. and Balachandar, S. (2004). Response of the wake of an isolated particle to an isotropic turbulent flow. *J. Fluid Mech.*, 518:95–123.
- Balachandar, S. and Eaton, J. K. (2010). Turbulent dispersed multiphase flow. *Annu. Rev. Fluid Mech.*, 42:111–133.
- Balzer, G., Boelle, A., and Simonin, O. (1998). Eulerian gas–solid flow modelling of dense fluidized bed. In *Fluidization VIII*, pages 1125–1134. International Symposium of Engineering Foundation.
- Batchelor, G. K. (1988). A new theory of the instability of a uniform fluidized bed. *Journal of Fluid Mechanics*, 193:75–110.
- Beetstra, R., van der Hoef, M. A., and Kuipers, J. A. M. (2007). Drag force of intermediate Reynolds number flows past mono– and bidisperse arrays of spheres. *AIChE J.*, 53:489–501.
- Benyahia, S., Syamlal, M., and O’Brien, T. J. (2005). Evaluation of boundary conditions used to model dilute, turbulent gas/solids flows in a pipe. *Powder Technology*, 156:62–72.
- Boivin, M., Simonin, O., and Squires, K. D. (1998). Direct numerical simulation of turbulence modulation by particles in isotropic turbulence. *J. Fluid Mech.*, 375:235–263.
- Bokkers, G. A., Annaland, M. V. S., and Kuipers, J. A. M. (2004). Mixing and segregation in a bidisperse gas–solid fluidised bed: a numerical and experimental study. *Powder Technology*, 140:176–186.

- Bolio, E. and Sinclair, J. (1995). Gas turbulence modulation in the pneumatic conveying of massive particles in vertical tubes. *Intl. J. Multiphase Flow*, 21(6):985–1001.
- Bolio, E., Yasuna, J., and Sinclair, J. (1995). Dilute turbulent gas-solid flow in risers with particle-particle interactions. *AIChE J.*, 41(5):1375 – 1388.
- Breault, R. W. and Guenther, C. P. (2009). Mass transfer in the core-annular and fast fluidization flow regimes of a CFB. *Powder Technology*, 190(3):385 – 389.
- Breault, R. W., Guenther, C. P., and Shadle, L. J. (2008). Velocity fluctuation interpretation in the near wall region of a dense riser. *pt*, 182:137–145.
- Burton, T. M. and Eaton, J. K. (2005). Fully resolved simulations of particle-turbulence interaction. *J. Fluid Mech.*, 545:67–111.
- Carman, P. C. (1937). Fluid flow through granular beds. *Trans. Instn Chem. Engrs*, 15:150–166.
- Clift, R., Grace, J. R., and Weber, M. E. (1978). *Bubbles, Drops and Particles*. Academic Press.
- Cocco, R., Shaffer, F., Hays, R., Reddy Karri, S. B., and Knowlton, T. (2010). Particle clusters in and above fluidized beds. *Powder Technology*, 203(1):3–11.
- Cornish, R. J. (1928). Flow in a pipe of rectangular cross-section. *Proceedings of the Royal Society of London. Series A, Containing Papers of a Mathematical and Physical Character*, 120(786):691–700.
- Crowe, C. T. (2000). On models for turbulence modulation in fluid-particle flows. *Intl. J. Multiphase Flow*, 26:719–727.
- Crowe, C. T., Troutt, T. R., and Chung, J. N. (1996). Numerical models for two-phase turbulent flows. *Annu. Rev. Fluid Mech.*, 28:11–43.
- Cundall, P. A. and Strack, O. D. L. (1979). A discrete numerical model for granular assemblies. *Geotechnique*, 29:47–65.

- Daley, D. J. and Vere-Jones, D. (1988). *An Introduction to the Theory of Point Processes*. Springer-Verlag, New York.
- Drew, D. A. (1983). Mathematical modeling of two-phase flow. *Annu. Rev. Fluid Mech.*, 15:261–291.
- Drew, D. A. and Passman, S. L. (1998). *Theory of Multicomponent Fluids*. Springer.
- Elghobashi, S. E. and Truesdell, G. C. (1993). On the two-way interaction between homogeneous turbulence and dispersed solid particles. I: Turbulence modification. *Phys. Fluids A*, 5:1790–1801.
- Ergun, S. (1952). Fluid flow through packed columns. *Chem. Eng. Prog.*, 48:89–94.
- Ernst, M. H. (1981). Nonlinear model-Boltzmann equations and exact solutions. *Physics Reports*, 78(1):1–171.
- Feng, Z.-G. and Michaelides, E. E. (2008). Inclusion of heat transfer computations for particle laden flows. 20(4):040604.
- Fox, R. O. (2008). A quadrature-based third-order moment method for dilute gas-particle flows. *Journal of Computational Physics*, 227:6313.
- Garg, R. (2009). *Modeling and simulation of two-phase flows*. PhD thesis, Iowa State University.
- Garg, R., Galvin, J., Li, T., and Pannala, S. (2010a). Documentation of open-source mfix-dem software for gas-solids flows. Technical report, National Energy Technology Laboratory, Department of Energy.
- Garg, R., Tenneti, S., Mohd-Yusof, J., and Subramaniam, S. (2009). Direct numerical simulation of gas-solids flow based on the immersed boundary method. In Pannala, S., Syamlal, M., and O'Brien, T. J., editors, *Computational Gas-Solids Flows and Reacting Systems: Theory, Methods and Practice*. (in review).
- Garg, R., Tenneti, S., Mohd-Yusof, J., and Subramaniam, S. (2011). Direct numerical simulation of gas-solids flow based on the immersed boundary method. In Pannala, S., Syamlal, M.,

- and O'Brien, T. J., editors, *Computational Gas-Solids Flows and Reacting Systems: Theory, Methods and Practice*, pages 245–276. IGI Global.
- Garg, R., Tenneti, S., Pai, M. G., and Subramaniam, S. (2010b). Heat transfer in stokes flow past ordered and random assemblies of monodisperse spheres. In review.
- Garzo, V., Dufty, J. W., and Hrenya, C. M. (2007a). Enskog theory for polydisperse granular mixtures. I. Navier-Stokes order transport. *Physical Review E (Statistical, Nonlinear, and Soft Matter Physics)*, 76(3):031303.
- Garzo, V., Hrenya, C. M., and Dufty, J. W. (2007b). Enskog theory for polydisperse granular mixtures. II. Sonine polynomial approximation. *Physical Review E (Statistical, Nonlinear, and Soft Matter Physics)*, 76(3):031304.
- Gidaspow, D. (1986). Hydrodynamics of Fluidization and Heat Transfer: Supercomputer Modeling. *Appl. Mech. Rev.*, 39:1–23.
- Gidaspow, D. (1994). *Multiphase Flow and Fluidization*. Academic Press.
- Ginzburg, I. and d'Humières, D. (2003). Multireflection boundary conditions for lattice boltzmann models. *Phys. Rev. E*, 68(6):066614.
- Glowinski, R., Pan, T. W., Hesla, T. I., Joseph, D. D., and Périaux, J. (2001). A fictitious domain approach to the direct numerical simulation of incompressible viscous flow past moving rigid bodies: Application to particulate flow. *J. Comp. Phys.*, 169(2):363–426.
- Gunn, D. J. (1978). Transfer of heat and mass to particles in fixed and fluidized beds. *Intl. J. Heat Mass Transfer*, 21:467–476.
- Halvorsen, B., Guenther, C., and O'Brien, T. J. (2003). CFD calculations for scaling of a bubbling fluidized bed . In *Proceedings of the AIChE annual meeting*, pages 16–21, San Francisco, CA. AIChE.
- Hasimoto, H. (1959). On the periodic fundamental solutions of the Stokes equations and their application to viscous flow past a cubic array of spheres. *J. Fluid Mech.*, 5(2):317–328.

- Hill, R. J., Koch, D. L., and Ladd, A. J. C. (2001a). The first effects of fluid inertia on flows in ordered and random arrays of spheres. *J. Fluid Mech.*, 448:213–241.
- Hill, R. J., Koch, D. L., and Ladd, A. J. C. (2001b). Moderate–Reynolds–number flows in ordered and random arrays of spheres. *J. Fluid Mech.*, 448:243–278.
- Hinch, E. J. (1977). An averaged-equation approach to particle interactions in a fluid suspension. *J. Fluid Mech.*, 83:695–720.
- Holloway, W., Yin, X., and Sundaresan, S. (2010). Fluid-particle drag in inertial polydisperse gas-solid suspensions. *AIChE J.*, 56:1995–2004.
- Hrenya, C. M. and Sinclair, J. L. (1997). Effects of particle-phase turbulence in gas-solid flows. *AIChE Journal*, 43(4):853–869.
- Hu, H. H., Patankar, N. A., and Zhu, M. Y. (2001). Direct Numerical Simulations of Fluid-Solid Systems Using the Arbitrary Lagrangian-Eulerian Technique. *J. Comp. Phys.*, 169(2):427–462.
- Incropera, F. P., DeWitt, D. P., Bergman, T. L., and Lavine, A. S. (2006). *Fundamentals of Heat and Mass Transfer*. John Wiley & Sons Inc, New York, sixth edition.
- Jackson, R. (1963). The mechanics of fluidized beds: Part i: The stability of the state of uniform fluidization. *Trans. Inst. Chem. Eng.*, 41:13–28.
- Jenkins, J. T. and Savage, S. B. (1983). A theory for the rapid flow of identical, smooth, nearly elastic, spherical particles. *J. Fluid Mech.*, 130:187–201.
- Kashiwa, B. and Gaffney, E. (2003). Design Basis for CFDLib. Technical Report LA-UR-03-1295, Los Alamos National Lab.
- Kenning, V. M. and Crowe, C. T. (1997). On the effect of particles on carrier phase turbulence modulation in gas–particle flows. *Intl. J. Multiphase Flow*, 23(2):403–408.
- Kim, D. and Choi, H. (2006). Immersed boundary method for flow around an arbitrarily moving body. *J. Comp. Phys.*, 21(2):662–680.

- Kim, J. and Moin, P. (1985). Application of a fractional-step method to incompressible Navier-Stokes equations. *J. Comp. Phys.*, 59:308–323.
- Koch, D. L. (1990). Kinetic theory for a monodisperse gas–solid suspension. *Physics of Fluids*, A 2(10)(10):1711–1723.
- Koch, D. L. and Sangani, A. S. (1999). Particle pressure and marginal stability limits for a homogeneous monodisperse gas–fluidized bed: kinetic theory and numerical simulations. *J. Fluid Mech.*, 400:229–263.
- Ladd, A. J. C. (1994a). Numerical simulations of particulate suspensions via a discretized boltzmann-equation .1. theoretical foundation. *Journal of Fluid Mechanics*, 271:285–309.
- Ladd, A. J. C. (1994b). Numerical simulations of particulate suspensions via a discretized boltzmann-equation .2. numerical results. *Journal of Fluid Mechanics*, 271:311–339.
- Ladd, A. J. C. and Verberg, R. (2001). Lattice-boltzmann simulations of particle-fluid suspensions. *Journal of Statistical Physics*, 104(5):1191–1251.
- Leboreiro, J., Joseph, G. G., Hrenya, C. M., Snider, D. M., Banerjee, S. S., and Galvin, J. E. (2008). The influence of binary drag laws on mp-pic simulations of segregating gas–fluidized beds. *Powder Technology*, 184:275–290.
- Liboff, R. L. (2003). *Kinetic theory : Classical, Quantum, and Relativistic descriptions*. Springer-Verlag, New York, 3rd edition.
- Lucci, F., Ferrante, A., and Elghobashi, S. (2011). Is Stokes number an appropriate indicator for turbulence modulation by particles of Taylor–length–scale size? *Phys. Fluids*, 23(2):025101–025101–7.
- Lucci, F., Ferrante, A., and Elghobashi, S. (2010). Modulation of isotropic turbulence by particles of taylor length-scale size. *J. Fluid Mech.*, 650(5–55).
- Lun, C. K. K., Savage, S. B., Jeffrey, D. J., and Chepurniy, N. (1984). Kinetic theories for granular flow - inelastic particles in Couette-flow and slightly inelastic particles in a general flowfield. *J. Fluid Mech.*, 140:223–256.

- Mashayek, F. and Taulbee, D. B. (2002). Turbulent gas–solid flows, part I: Direct numerical simulations and Reynolds stress closures. *Numerical Heat Transfer, Part B: Fundamentals*, 41(1):1–29.
- Mehrabadi, M., Tenneti, S., and Subramaniam, S. (2012). Gas–phase velocity fluctuations in statistically homogeneous fixed particle beds and freely evolving suspensions using particle–resolved direct numerical simulation. In review.
- Miller, A. and Gidaspow, D. (1992). Size segregation of binary mixture of solid in bubbling fluidized beds. *AIChE J.*, 38(11):1801–1815.
- Modarress, D., Tan, H., and Elghobashi, S. E. (1984). Two–component LDA measurement in a two–phase turbulent jet. *AIAA Journal*, 22:624–630.
- Monin, A. S. and Yaglom, A. M. (1975). *Statistical Fluid Mechanics II*. MIT Press.
- Moran, J. C. and Glicksman, L. R. (2003). Mean and fluctuating gas phase velocities inside a circulating fluidized bed. *Chemical Engineering Science*, 58:1867–1878.
- Muldoon, F. and Acharya, S. (2008). A divergence–free interpolation scheme for the immersed boundary method. *Intl. J. for Numerical Methods in Fluids*, 56(10):1845–1884.
- Nomura, T. and Hughes, T. J. R. (1992). An arbitrary lagrangian–eulerian finite element method for interaction of fluid and a rigid body. *Comput. Meth. Appl. Mech. Eng.*, 95(1):115–138.
- Oguz, H. and Prosperetti, A. (2001). Physalis: A new  $o(n)$  method for the numerical simulation of disperse systems. part i: Potential flow of spheres. *J. Comp. Phys.*, 167:196–216.
- Pai, M. G. and Subramaniam, S. (2009). A comprehensive probability density function formalism for multiphase flows. *Journal of Fluid Mechanics*, 628:181–228.
- Passalacqua, A., Fox, R., Garg, R., and Subramaniam, S. (2010). A fully coupled quadrature–based moment method for dilute to moderately dilute fluidparticle flows. *Chemical Engineering Science*, 65(7):2267 – 2283.

- Patankar, N., Singh, P., Joseph, D. D., Glowinski, R., and Pan, T. W. (2000). A new formulation of the distributed Lagrange multipliers/fictitious domain method for particulate flow. *Intl. J. Multiphase Flow*, 26(9):1509–1524.
- Patankar, S. V. (1980). *Numerical heat transfer and fluid flow*. Hemisphere Pub. Corp.: McGraw-Hill.
- Patil, D. J., Annaland, M. V., and Kuipers, J. A. M. (2005). Critical comparisons of hydrodynamic models for gas–solid fluidized beds – part I: bubbling gas–solid fluidized beds operated with a jet. *Chem. Eng. Sci.*, 60:57–72.
- Peirano, E. and Leckner, B. (1998). Fundamentals of turbulent gas–solid flows applied to circulating fluidized bed combustion. *Prog. Energy Combust. Science*, 24:259–296.
- Peskin, C. S. (1981). The fluid dynamics of heart valves: experimental, theoretical, and computational methods. *Annu. Rev. Fluid Mech.*, 14:235–259.
- Pfeffer, R. and Happel, J. (1964). Analytical study of heat and mass transfer in multiparticle systems at low Reynolds numbers. *A.I.Ch.E. Journal*, 10(5):605 – 611.
- Pope, S. B. (2000). *Turbulent Flows*. Cambridge University Press, Port Chester, NY.
- Quintanilla, J. and Torquato, S. (1997). Local volume fraction fluctuations in random media. *The Journal of Chemical Physics*, 106(7):2741–2751.
- Richardson, J. and Zaki, W. N. (1954). Sedimentation and fluidization: part 1. *Trans. Instn Chem. Engrs*, 32:35–53.
- Sangani, A. S. and Acrivos, A. (1982). Slow flow through a periodic array of spheres. *Intl. J. Multiphase Flow*, 8:342–360.
- Sangani, A. S., Mo, G., Tsao, H.-K. W., and Koch, D. L. (1996). Simple shear flows of dense gas–solid suspensions at finite Stokes numbers. *J. Fluid Mech.*, 313(309-341).
- Scardovelli, R. and Zaleski, S. (1999). Direct numerical simulation of free–surface and interfacial flow. *Annu. Rev. Fluid Mech.*, 31:567–603.

- Schiller, L. and Naumann, A. (1935). A drag coefficient correlation. *V.D.I. Zeitung*.
- Sela, N. and Goldhirsch, I. (1998). Hydrodynamic equations for rapid flows of smooth inelastic spheres. *J. Fluid Mech.*, 361:41–74.
- Serero, D., Goldhirsch, I., Noskovicz, S. H., and Tan, M. L. (2006). Hydrodynamics of granular gases and granular gas mixtures. *J. Fluid Mech.*, 554:237–258.
- Shah, R. K. and London, A. L. (1978). *Laminar flow force convection in ducts*. Academic Press, New York.
- Sharma, N. and Patankar, N. (2005). A fast computation technique for the direct numerical simulation of rigid particulate flows. *J. Comp. Phys.*, 205(2):439–457.
- Shen, L., Zheng, M., Xiao, J., and Xiao, R. (2008). A mechanistic investigation of a calcium-based oxygen carrier for chemical looping combustion. *Combustion and Flame*, 154(3):489 – 506.
- Sherman, J. and Morrison, W. J. (1950). Adjustment of an inverse matrix corresponding to a change in one element of a given matrix. *Ann. Math. Statist*, 21(1):124–127.
- Simonin, O. (1995). Two-fluid model approach for turbulent reactive two-phase flows. *Summer school on numerical modelling and prediction of dispersed two-phase flows. IMVU, Meserburg, Germany*.
- Snyder, L. J. and Stewart, W. E. (1966). Velocity and pressure profiles for Newtonian creeping flow in regular packed beds of spheres. *AIChE J.*, 12(1):167–173.
- Sorensen, J. P. and Stewart, W. E. (1974a). computation of forced-convection in slow flow through ducts and packed-beds .2. Velocity profile in a simple cubic array of spheres. *Chem. Eng. Sci.*, 29(3):819–825.
- Sorensen, J. P. and Stewart, W. E. (1974b). Computation of forced-convection in slow flow through ducts and packed-beds .3. Heat and mass-transfer in a simple cubic array of spheres. *Chemical Engineering Science*, 29:827–832.

- Squires, K. D. and Eaton, J. K. (1991). Measurements of particle dispersion obtained from direct numerical simulations of isotropic turbulence. *J. Fluid Mech.*, 226:1–35.
- Stoyan, D., Kendall, W. S., and Mecke, J. (1995). *Stochastic Geometry and its Applications*. Wiley Series in Probability and Mathematical Statistics. John Wiley and Sons, New York, 2nd edition.
- Stoyan, D. and Stoyan, H. (1995). *Fractals, Random Shapes and Point Fields*. Wiley Series in Probability and Mathematical Statistics. John Wiley and Sons, New York.
- Subramaniam, S. (2000). Statistical representation of a spray as a point process. *Phys. Fluids*, 12(10):2413–2431.
- Subramaniam, S. (2001). Statistical modeling of sprays using the droplet distribution function. *Phys. Fluids*, 13(3):624–642.
- Sun, J., Battaglia, F., and Subramaniam, S. (2007). Hybrid two-fluid dem simulation of gas-solid fluidized beds. *Journal of Fluid Engineering*, 129(11):1394–1403.
- Sundaram, S. and Collins, L. R. (1994). Spectrum of density fluctuations in a particle–fluid system—I. Monodisperse spheres. *Intl. J. Multiphase Flow*, 20(6):1021–1037.
- Sundaram, S. and Collins, L. R. (1999). A numerical study of the modulation of isotropic turbulence by suspended particles. *J. Fluid Mech.*, 379:105–143.
- Syamlal, M. and O’Brien, T. J. (1987). A generalized drag correlation for multiparticle systems. Technical report, Morgantown Energy Technology Center DOE Report.
- Syamlal, M., Rogers, W., and O’Brien, T. J. (1993). MFIx Documentation: Theory Guide. Technical Report DOE/METC-95/1013, NTIS/DE95000031, National Energy Technology Laboratory, Department of Energy. See also URL <http://www.mfix.org>.
- Takagi, S., Oguz, H., Zhang, Z., and Prosperetti, A. (2005). Physalis: A new method for particle simulation. part ii: Two-dimensional navier-stokes flow around cylinders. *J. Comp. Phys.*, 187:371–390.

- Ten Cate, A., Derksen, J. J., Portela, L. M., and van den Akker, H. E. A. (2004). Fully resolved simulations of colliding monodisperse spheres in forced isotropic turbulence. *J. Fluid Mech.*, 519:233–271.
- Tenneti, S., Fox, R. O., and Subramaniam, S. (2010a). Instantaneous particle acceleration model for gas-solid suspensions at moderate reynolds numbers particle-laden flows. In *Proceedings of the International Conference on Multiphase Flow*.
- Tenneti, S., Garg, R., Hrenya, C. M., Fox, R. O., and Subramaniam, S. (2010b). Direct numerical simulation of gas–solid suspensions at moderate reynolds number: quantifying the coupling between hydrodynamic forces and particle velocity fluctuations. *Powder Technology*, 203(1):57–69.
- Tenneti, S., Garg, R., and Subramaniam, S. (2011). Drag law for monodisperse gas–solid systems using particle–resolved direct numerical simulation of flow past fixed assemblies of spheres. In review.
- Tenneti, S., Garg, R., and Subramaniam, S. (2012). Gas–phase velocity fluctuations in statistically homogeneous fixed particle assemblies from particle–resolved direct numerical simulation. In preparation.
- Torquato, S. and Stell, G. (1982). Microstructure of two-phase random media. i. the n-point probability functions. *The Journal of Chemical Physics*, 77(4):2071–2077.
- Tsuji, Y., Morikawa, Y., and Shiomi, H. (1984). LDV measurements of an air–solid two–phase flow in a vertical pipe. *J. Fluid Mech.*, 139:417–434.
- Uhlmann, M. (2005). An immersed boundary method with direct forcing for the simulation of particulate flows. *J. Comp. Phys.*, 209:448–476.
- Uhlmann, M. (2008). Interface–resolved direct numerical simulation of vertical particulate channel flow in the turbulent regime. *Phys. Fluids*, 20(5):053305–053305–27.

- van der Hoef, M. A., Beetstra, R., and Kuipers, J. A. M. (2005). Lattice-Boltzmann simulations of low-Reynolds-number flow past mono- and bidisperse arrays of sphere: results for the permeability and drag force. *J. Fluid Mech.*, 528:233–254.
- Wakao, N. and Kaguei, S. (1982). *Heat and mass transfer in packed beds*, volume 1 of *Topics in chemical engineering*. Gordon and Breach science.
- Wall, T. F. (2007). Combustion processes for carbon capture. *Proceedings of the Combustion Institute*, 31(1):31 – 47.
- Wang, Q., Squires, K. D., and Simonin, O. (1998). Large eddy simulation of turbulent gas–solid flows in a vertical channel and evaluation of second–order models. *Intl. J. Heat and Fluid Flow*, 19:505–511.
- Wen, C. Y. and Yu, Y. H. (1966). Mechanics of fluidization. *Chem. Eng. Prog. Symp. Series*, 62:100–111.
- Williams, F. A. (1958). Spray combustion and atomization. *Phys. Fluids*, 1(6):541–545.
- Wylie, J. J., Koch, D. L., and Ladd, A. J. (2003). Rheology of suspensions with high particle inertia and moderate fluid inertia. *Journal of Fluid Mechanics*, 480:95 – 118.
- Xu, Y. and Subramaniam, S. (2006). A multiscale model for dilute turbulent gas-particle flows based on the equilibration of energy concept. *Phys. Fluids*, 18:033301.
- Xu, Y. and Subramaniam, S. (2010). Effect of particle clusters on carrier flow turbulence: A direct numerical simulation study. *Flow, Turbulence and Combustion*, 85:735–761. 10.1007/s10494-010-9298-8.
- Yarin, L. and Hetsroni, G. (1994). Turbulence intensity in dilute two-phase flows–1: Effect of particle-size distribution on the turbulence of the carrier fluid. *International Journal of Multiphase Flow*, 20(1):1–15.
- Yi, C. K., Jo, S. H., Seo, Y., Lee, J. B., and Ryu, C. K. (2007). Continuous operation of the potassium-based dry sorbent CO<sub>2</sub> capture process with two fluidized-bed reactors. *International Journal of Greenhouse Gas Control*, 1(1):31 – 36.

- Yin, X. and Koch, D. L. (2007). Hindered settling velocity and microstructure in suspensions of spheres with moderate reynolds number. *Physics of Fluids*, 19:093302.
- Yin, X. and Sundaresan, S. (2009a). Drag law for bidisperse gas-solid suspensions containing equally sized spheres. *Industrial & Engineering Chemistry Research*, 48(1):227–241.
- Yin, X. and Sundaresan, S. (2009b). Fluid–particle drag in low–reynolds–number polydisperse gas-solid suspensions. *AIChE J.*, 55(6):1352–1368.
- Ying, X. and Subramaniam, S. (2007). Consistent modeling of interphase turbulent kinetic energy transfer in particle-laden turbulent flows. *Physics of Fluids*, 19(8):085101.
- Yuan, Z. and Michaelides, E. E. (1992). Turbulence modulation in particulate flows—a theoretical approach. *International Journal of Multiphase Flow*, 18(5):779–785.
- Yusof, J. M. (1996). *Interaction of Massive Particles with Turbulence*. PhD thesis, Cornell University.
- Zhang, D. Z. and Prosperetti, A. (2003). A method for particle simulations. *J. Appl. Mech.*, 70:64–74.
- Zhang, D. Z. and Prosperetti, A. (2005). A second-order method for three-dimensional particle flow simulations. *J. Comp. Phys.*, 210:292–324.
- Zhang, Y. H. and Reese, J. M. (2003). Gas turbulence modulation in a two–fluid model for gas–solid flows. *AIChE J.*, 49(12):3048–3065.
- Zick, A. A. and Homsy, G. M. (1982). Stokes flow through periodic arrays of spheres. *J. Fluid Mech.*, 115:13–26.